Structural analysis of dilute bismide alloys by means of high resolution scanning transmission electron microscopy

Dissertation

zur
Erlangung des Doktorgrades
der Naturwissenschaften
(Dr. rer. nat.)

dem

Fachbereich Physik
der Philipps-Universität Marburg

vorgelegt von

Nikolai Knaub, M. Sc.

aus

Nischni Tagil (Russland)

Marburg/Lahn, 2016

Vom Fachbereich Physik der Philipps-Universität Marburg
als Dissertation angenommen am: 20.06.2016
Erstgutachter: Prof. Dr. Kerstin Volz
Zweitgutachter: Dr. Ralf Tonner
Tag der mündlichen Prüfung: 23.06.2016
Hochschulkennziffer: 1180

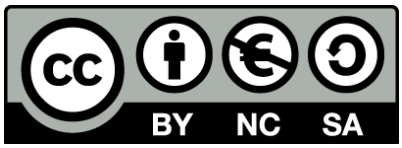

Contents

CHAPTER 1

Introduction

Semiconductor materials have gained an enormous influence on our everyday lives since their appearance in industry in the mid of the last century. Moreover, semiconductors still have a promising future which is not least expressed by the Nobel Prize in Physics in 2014 "*for the invention of efficient blue light-emitting diodes which has enabled bright and energy-saving white light sources*"[1]. The research and optimization of a gallium nitride (GaN) based blue light-emitting diode[2] (LED) was a milestone for the realization of an energy-efficient "white" LED. Nowadays "white" LEDs can be found in almost every household and therefore the LED is dubbed as "light bulb of the 21st century".
Environment protection plays a key role for the realization of new semiconductor materials, especially in the increasing field of internet data transfer via fiber networks (telecommunication network) operating at a wavelength of 1.55 µm. Common used semiconductor laser (Light Amplification by Stimulated Emission of Radiation) devices, which operate at this wavelength are based on gallium indium arsenide phosphide ((GaIn)(AsP)). However, these semiconductor laser suffer from non-radiative Auger recombination that leads to heating of the devices and thus to a shift of the wavelength, due to temperature sensitivity of the (GaIn)(AsP) band gap. Therefore additional cooling units are mandatory to ensure a constant emitting wavelength of the laser devices. The consequence is an immense power consumption that comes along with the operation of these devices, and this shows a rising demand of energy efficient semiconductor devices not only in the field of telecommunication network.
A promising semiconductor alloy which addresses the energy efficiency is the dilute bismide compound gallium arsenide bismide (Ga(AsBi)). This alloy offers the opportunity of new generation 1.55 µm devices, requiring a Bi fraction of about 10% in Ga(AsBi). In contrast to the (GaIn)(AsP) based devices, dilute bismides reveal a suppression of the non-radiative loss mechanisms and a much lower temperature dependency of the emission wavelength[3–8], which end up in a higher energy efficiency. So far, Ga(AsBi) alloys with Bi fractions above 10% could be realized using molecular beam epitaxy (MBE)[3], whereas much effort was made to deposit Ga(AsBi)-layers with Bi fractions up to 7% using metal organic vapour

phase epitaxy (MOVPE)[9]. Despite Ga(AsBi), the additional incorporation of nitrogen (N) and phosphorus (P) allows a realization of the quaternary material systems gallium nitride arsenide Ga(NAsBi) and gallium phosphide arsenide bismide Ga(PAsBi), respectively. Furthermore, the incorporation of N involves a further decrease of the GaAs bandgap, and in addition strain compensation in respect to the incorporation of Bi can be achieved. Thus, Ga(NAsBi) alloys allow the realization of 1.55 µm laser devices with Bi-fractions below much lower than 10%. Moreover, Ga(PAsBi) seems to be a promising candidate for multi-junction solar cell applications, since it can be grown lattice matched on germanium (Ge) and exhibiting a bandgap energy of 1 eV. Nevertheless, characterization processes of semiconductor materials are indispensable and thus very important, whereby transmission electron microscopy (TEM) is one of the most powerful methods for investigation in the nanometer and atomic regions. Characterizations by means of TEM could reveal atomic ordering[10,11] and clustering effects[12–15] in Ga(AsBi)-layers with Bi fractions below 5%.
The present work describes the studies of ordering effects in MOVPE grown Ga(AsBi) extracted from scanning TEM (STEM) measurements. Thereby it will be shown that STEM investigations at atomic resolution verify the presence of Bi ordering below 1 nm scale in high quality Ga(AsBi)-layers, even though they exhibit a homogeneous Bi distribution which was detected with low resolution STEM measurements. The evaluation of the measurements is accompanied by data mining concepts which have been performed by means of the MATLAB-software. Furthermore, STEM investigations were also carried out on MOVPE grown Ga(NAsBi)- and Ga(PAsBi)-layers, whereby first clustering effects could be detected in Ga(PAsBi). The investigation and characterization of dilute Bi alloys was part of the research training group *GRK1782* founded by the *German Research Foundation (DFG, Deutsche Forschungsgemeinschaft).*
This Ph.D thesis is written in cumulative form and has the following structure: Chapter 2 will introduce the basic physical properties of the investigated materials as well as the Rutherford-scattering which is fundamental for the understanding of electron scattering processes in STEM. Furthermore, Chapter 3 summarizes the concepts of the experimental techniques which were applied in this work. Research results, which have not been published, can be found in Chapter 4, whereby detailed discussions of Bi ordering and distribution in Ga(AsBi) were published and are printed in full length in Chapter 6. Finally, the presented results are summed up in Chapter 5.

List of publications:

- N. Knaub, A. Beyer, T. Wegele, P. Ludewig, K. Volz, *Quantification of Bi distribution in MOVPE-grown Ga(AsBi) via HAADF STEM*, Journal of Crystal Growth **433**, 89 (2016). DOI: 10.1016/j.jcrysgro.2015.10.007 (Ref. 16, Section 6.1)

- N. Knaub, A. Beyer, P. Rosenow, K. Jandieri, P. Ludewig, L. Bannow, S.W. Koch, R. Tonner, K. Volz, *Local Bi ordering in MOVPE grown Ga(As,Bi) by high resolution scanning transmission electron microscopy*, *submitted (2016)* in Journal of Physics D: Applied Phyics (Ref. 17, Section 6.2)

- E. Sterzer, N. Knaub, P. Ludewig, R. Straubinger, A. Beyer, K. Volz, *Investigation of the microstructure of metallic droplets on Ga(AsBi)/GaAs*, Journal of Crystal Growth **408**, 71 (2014). DOI: 10.1016/j.jcrysgro.2014.09.006 (Ref. 18, Section 6.3)

- P. Ludewig, N. Knaub, W. Stolz, K. Volz, *MOVPE growth of Ga(AsBi)/GaAs multi quantum well structures*, Journal of Crystal Growth **370**, 186 (2013). DOI: 10.1016/j.jcrysgro.2012.07.002. (Ref. 19, Section 6.4)

- P. Ludewig, N. Knaub, N. Hossain, S. Reinhard, L. Nattermann, I. P. Marko, S.R. Jin, K. Hild, S. Chatterjee, W. Stolz, S.J. Sweeney, K. Volz, *Electrical injection Ga(AsBi)/(AlGa)As single quantum well laser*, Applied Physics Letters **102**, 242115 (2013). DOI: 10.1063/1.4811736. (Ref. 20, Section 6.5)

- Z. L. Bushell, P. Ludewig, N. Knaub, Z. Batool, K. Hild, W. Stolz, S. J. Sweeney, K. Volz, *Growth and characterisation of GaNAsBi alloy by metal organic vapour phase epitaxy*, Journal of Crystal Growth **396**, 79 (2014). DOI: 10.1016/j.jcrysgro.2014.03.038. (Ref. 21, Section 6.7)

- P. Ludewig, Z. L. Bushell, L. Nattermann, N. Knaub, W. Stolz, K. Volz, *Growth of Ga(AsBi) on GaAs by continuous flow MOVPE*, Journal of Crystal Growth **396**, 95 (2014). DOI: 10.1016/j.jcrysgro.2014.03.041. (Ref. 22, Section 6.6)

CHAPTER 2

Physical Principles

This chapter outlines the physical properties of III-V semiconductors on the basis of *gallium arsenide* (GaAs) and exemplifies how the incorporation of bismuth (Bi) in GaAs influences the band- and crystal structure. Besides the quaternary material systems *gallium nitride arsenide bismide* Ga(NAsBi) and *gallium phosphide arsenide bismide* Ga(PAsBi) will be introduced. Furthermore the Rutherford scattering will be elaborated, which is necessary for a further description of scanning transmission electron microscopy (STEM) in the subsequent chapter.

2.1 III-V Semiconductors

III-V semiconductors consist stoichiometrically of group III and group V elements, hence they correspond to the group of the so-called compound semiconductors. The most prominent semiconductor of this group is the binary compound GaAs. It has gained huge popularity due to its direct bandgap ($E_g = 1.42\,\mathrm{eV}$ at $300\,\mathrm{K}$ [23]) and for this reason it serves frequently as a host material for optical and electronical applications. GaAs crystallizes, as many other III-V semiconductors, in the zinc blende crystal structure which is composed of two face centered cubic (fcc) sublattices (Figure 2.1) where each element occupies one sublattice.

Due to the sp^3 hybridization of the group III and group V elements, the atoms arrange in a tetrahedral coordination. The sublattices are shifted by one quarter of the space diagonal and generate a lattice basis at (0,0,0) and $(\frac{1}{4},\frac{1}{4},\frac{1}{4})$. Furthermore, the crystal periodicity is described by the translation vector:

$$\vec{T} = n_1\vec{a}_1 + n_2\vec{a}_2 + n_3\vec{a}_3 \tag{2.1}$$

where n_1, n_2, n_3 are integers and $|\vec{a}_1| = |\vec{a}_2| = |\vec{a}_3|$ is the lattice constant of the cubic unit cell, which is a_{GaAs}= 0.5653 nm for GaAs [24]. Following this, the periodicity of the reciprocal lattice (Fourier transform of the lattice in real space) is described by the reciprocal lattice vector:

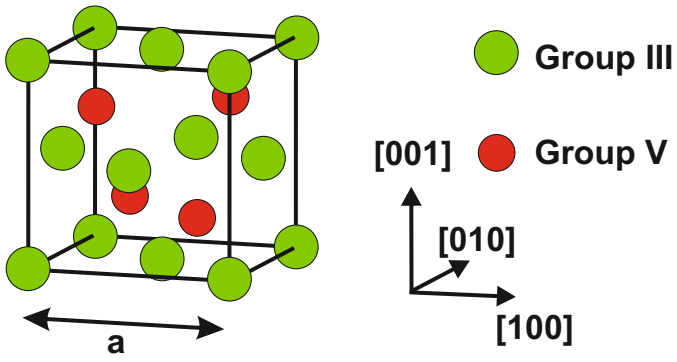

Figure 2.1: Unit cell of the zinc blende crystal structure with lattice constant a. Each fcc sublattice is either occupied by group III (green) or by group V atoms (red).

$$\vec{g}_{hkl} = h\vec{b}_1 + k\vec{b}_2 + l\vec{b}_3 \tag{2.2}$$

where $\vec{b}_1, \vec{b}_2, \vec{b}_3$ define the basis in the reciprocal space and integers h, k and l are the so-called *Miller-indices*. Thus, the triple (hkl) represents a crystal lattice plane, which is orthogonal to the reciprocal lattice vector in (2.2) and intercepts at $(\frac{\vec{a}_1}{h}, \frac{\vec{a}_2}{k}, \frac{\vec{a}_3}{l})$. Consequently, the notation [hkl] represents the direction (zone axis) of the direct lattice vector $h\vec{a}_1 + k\vec{a}_2 + l\vec{a}_3$, which is the normal to the lattice planes (hkl) in a cubic lattice.

2.2 Ga(AsBi)

The ternary dilute Bi compound *gallium arsenide bismide* Ga(AsBi) has gained a lot of attention over the last decade, due to the significant influence of Bi on the GaAs band- and crystal structure. The main properties of these influences will be introduced in this section.

2.2.1 The Influence of Bi on the GaAs Band Structure

The incorporation of dilute amounts of Bi into GaAs causes a large band gap reduction, namely 80-90 meV/% Bi, and in addition to that the band gap is less temperature dependent than in other III-V semiconductors e.g. GaAs which was demonstrated by photoluminescence studies in different experiments[3–8] of Ga(AsBi) compounds. A first theoretical description of the band structure behavior was given with a valence band anti crossing model (VBAC) by Alberi et al.[25,26], however the VBAC model is only valid for dilute Bi fractions. This model treats the Bi atoms as metallic isovalent impurities in the host semiconductor (GaAs), which introduce localized defect states and thus a perturbation of the electronic structure. Furthermore, the defect states are localized near the valence band edge due to a lower electronegativity of Bi compared to the one of As.

This leads to a restructuring of the the heavy-hole (HH), light-hole (LH) and spin-orbit split-off (SO) bands into E_+ and E_- subbands, respectively (Figure 2.2).

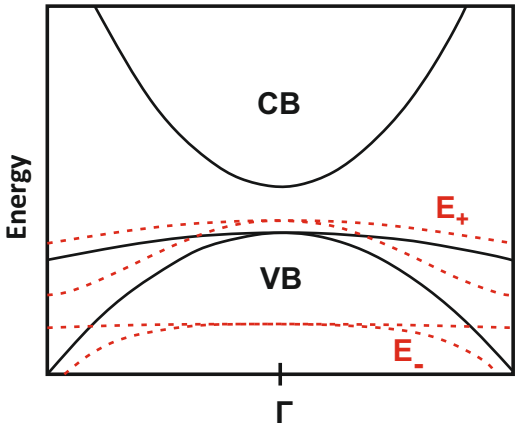

Figure 2.2: Influence of Bi on the band structure of GaAs (solid lines) in the VBAC model. The incorporation of Bi leads to valence band restructuring into E_+ and E_- subbands (adapted from Ref. 27).

Thus, the energetically upward shift of the HH- and LH-E_+ subbands is the reason for the observed band gap bowing in Ga(AsBi), whereby the resulting valence band edge can be calculated by:

$$E_+^{HH}(k) = \frac{1}{2}\left[E_{HH}(k) + E_{Bi} - \sqrt{(E_{HH}(k) + E_{Bi})^2 + 4V_{Bi}^2(x)}\right] \tag{2.3}$$

where $E_{HH}(k)$ is the energy dispersion of the HH band of GaAs, E_{Bi} is the non dispersal Bi induced energy level relative to the GaAs valence band edge and V_{Bi} describes the coupling between the band states of GaAs and the localized Bi states. An additional effect of the Bi incorporation is the increased spin-orbit-splitting (Δ_{SO}), which is known to increase as a function of the atomic number Z and hence has the largest value for Bi in III-V semiconductors[28]. Large Δ_{SO} are desirable in various semiconductor devices, because present laser devices with an emission wavelength of 1.55 µm suffer from loss mechanisms like the CHSH (hot hole) Auger recombination[29–31]. This is an electron-hole recombination from CB to HH band and a subsequent hole excitation from the HH band to the SO band. It leads to a heating of the device, since it is an non-radiative recombination process (Figure 2.3). However, calculations have shown that in case of Ga(AsBi) $\Delta_{SO} > E_G$ occurs at Bi fractions above 10%[32] which would lead to a suppression of the CHSH Auger recombination and therefore to higher device efficiencies and decreased heating.

2.2.2 The Influence of Bi on the GaAs Crystal Structure

Besides the enormous impact of dilute Bi amount on band structure of GaAs, there also exists a significant influence on the crystal structure. The incorporation of Bi in GaAs

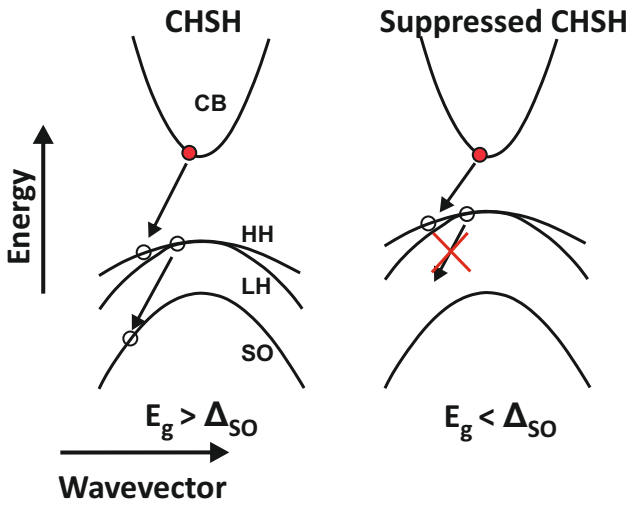

Figure 2.3: Sketch of the CHSH process, which occurs in conventional semiconductor devices (left) due to non-radiative electron-hole recombination and therefore leads to heating of the device. This process is suppressed (right) for Ga(AsBi) with $x_{Bi} > 10\%$ due to $\Delta_{SO} > E_G$ (adapted from Ref. 33).

leads to a change of the crystal lattice constant, which can be estimated using Vegard's law:

$$a_{Ga(As_{1-x}Bi_x)} = x \cdot a_{GaBi} + (1 - x) \cdot a_{GaAs} \tag{2.4}$$

where x is the Bi fraction and a_{GaBi} is the theoretical zinc blende lattice constant of the binary compound GaBi, which could not be realized so far since Ga and Bi are phase separated in the solid state[34]. Nevertheless, theoretical calculations predicted a GaBi lattice constant of 0.633 nm[28,35], which was confirmed in experiment by extrapolating Rutherford backscattering (RBS) and x-ray diffraction (XRD) data[5].
Due to different atomic parameters of As and Bi, namely electronegativity and covalent radius (see Table 2.1), the so-called *static atomic displacements*[36] (SAD) have to be taken into account, especially for STEM image simulations of Ga(AsBi) supercells. The SADs in Ga(AsBi) occur due to the incorporation of Bi atoms on group V lattice sites and imply local strain as well as shifting of the surrounding Ga atoms away from the Bi atoms (Figure 2.4), which is about 7.1% on the average of the original bond length. The concept of SADs is important and has to be considered when comparing experimental STEM results with image simulations, which is associated with a valence force field[37] (VFF) relaxation of the supercell.

In addition to the effects mentioned above, the large atomic parameter differences between As and Bi can also lead to atomic ordering, clustering and phase separation. In the publication of Zhang and Zunger[40] substitution energies were calculated, including the substitution of As atoms by larger group V atoms (e.g. Sb or Bi). It was found that

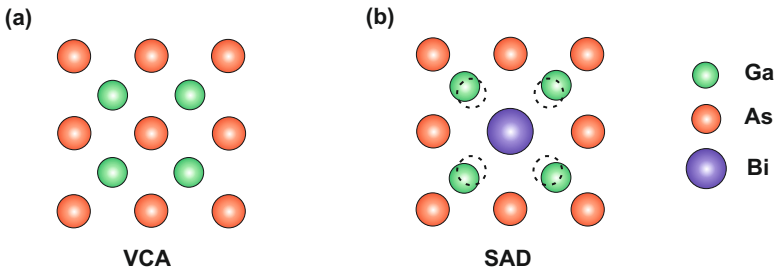

Figure 2.4: Depiction of perfect crystal structure in the virtual crystal approximation (VCA) (a) and the influecne of SAD due to an impurity atom (b). The dashed circles mark the undistorted Ga positions.

Element	Atomic number Z	Covalent radius[38] $[nm]$	Electronegativity[39]
N	7	0.074	3.04
P	14	0.110	2.19
As	33	0.121	2.18
Bi	83	0.152	2.02

Table 2.1: Atomic parameter of group V elements, which were incorporated in the investigated samples. Especially the electronegativities of N and Bi show a significantly different value from the As one, which is a major reason for SAD.

substitution energy increases and solubility reduces which results in clustering or phase separation, whereas the opposite is the case at a dimerized, reconstructed surface. The latter case leads to CuPt-type ordering which is the ordering of cations on alternating {111} planes (Figure 2.5). Both, CuPt-type ordering and phase separation, were observed in MBE grown $Ga(As_{1-x}Bi_x)$ alloys by means of (S)TEM[10], where CuPt$_B$-type ordering was detected for compositions up to $x = 10\%$ and on the other hand phase separation was observed at higher Bi concentration ($x \approx 13\%$).

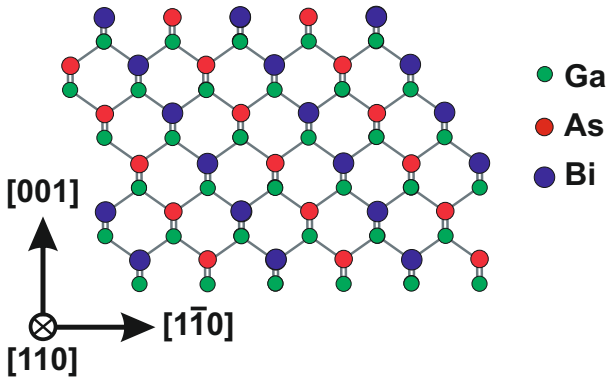

Figure 2.5: Model of CuPt$_B$-type ordering in Ga(AsBi), where As (red) and Bi (blue) are alternating on $\{\bar{1}11\}$ planes.

Other experiments have shown the evidence of small Bi clusters and Bi pairs, which where detected either by extended x-ray absorption fine structure spectroscopy measurements[12,13]

or by means of STEM[14]. Moreover, Bi clustering becomes more dominant after annealing of Ga(AsBi) alloys that was investigated in subsequent TEM experiments[15].

2.3 Ga(NAsBi) and Ga(PAsBi)

2.3.1 Ga(NAsBi)

The incorporation of dilute amounts of Nitrogen (N) in GaAs leads to a band gap reduction of the host material, which is in the range of 130 - 150 meV/% N[41]. While incorporating Bi has an influence on the GaAs valence band structure, N has an impact on the conduction band structure of the host material. This influence can be described by the conduction band anti crossing model (CBAC) where N is treated as an isoelectric impurity, which induces a separation of the conduction band into an energetically higher E_+ and an energetically lower E_- subband. Thus, the resulting band edge can be calculated similar as in (2.3):

$$E_-(k) = \frac{1}{2}\left[E_{CB}(k) + E_N - \sqrt{(E_{CB}(k) - E_N)^2 + 4V_N^2(x)}\right] \tag{2.5}$$

where $E_{CB}(k)$ is the energy dispersion of the lowest conduction band of GaAs, E_N is the non dispersal N induced energy level in relation to the top of the GaAs valence band and V_N describes the coupling between the band states of GaAs and the localized N states.

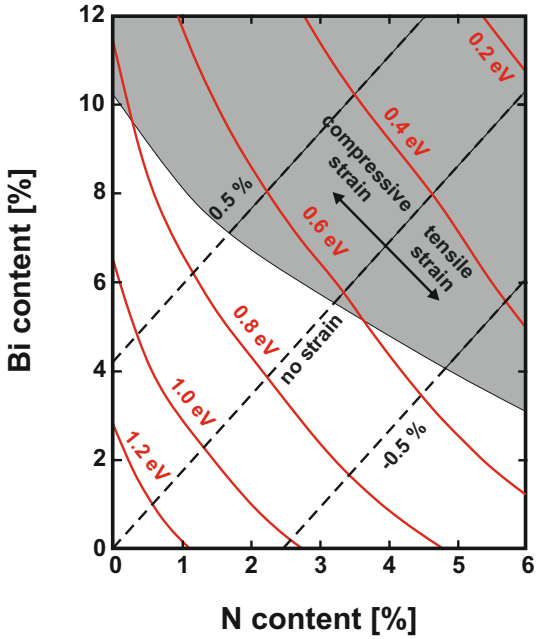

Figure 2.6: Band gap calculations (red lines) for Ga(NAsBi) on GaAs in dependence of strain (dashed lines), Bi and N fraction. The gray region represents the Bi and N fractions with $\Delta_{SO} > E_G$ (adapted from Ref. 32).

Incorporating both, N as well as Bi, in GaAs and thus obtaining the quaternary compound Ga(NAsBi) has two main advantages. First of all, since N induces tensile and Bi induces compressive strain in GaAs, it is possible to deposit Ga(NAsBi) lattice matched on GaAs. Secondly, both reduce independently the band gap in GaAs due to CBAC and VBAC, whereby the resulting Ga(NAsBi) band gap can be calculated by (2.3) and (2.5). Therefore it is possible to create a lattice matched Ga(NAsBi) compound on GaAs (Figure 2.6) which covers a wide band gap range (up to 1.42 eV) and hence can be applied for miscellaneous photonic devices.

2.3.2 Ga(PAsBi)

Despite the enormous advantages and possibilities which are offered by Ga(NAsBi), the growth of dilute nitrides (e.g. Ga(NAs)) is not less demanding than the growth of Ga(AsBi). Thus, different results have shown suffering of dilute nitrides' crystalline quality due to N induced defects, and which is the reason why dilute nitrides have to undergo thermal annealing processes[42–44]. Therefore, a possible alternative to Ga(NAsBi) alloys is the growth of the rather new Ga(PAsBi) alloy. It has the advantage that growth and device performances of Ga(PAs) are well-established. Furthermore, Ga(PAs) grown on GaAs is tensile strained and the incorporation of Bi in Ga(PAs) offers the possibility to tune the band gap as well as to compensate strain and to grow lattice matched on GaAs. So far, first Ga(PAsBi) alloys grown lattice matched on GaAs could be realized by MOPVE[45], with nominal Bi fractions ranging between 0.7-8.5% and nominal P fractions of 23-27%. The estimated room temperature band gap energies were in the range of 1.19-1.01 eV. These first results of experimentally grown Ga(PAsBi) make this alloy a promising material for a wide field of electronic devices, especially in solar cell applications, where Ga(PAsBi) could serve as a lattice matched 1 eV device in multi-junction solar cells.

2.4 Rutherford and Thermal Diffuse Scattering

Since sample investigation was performed via STEM in this thesis, where a narrow electron beam (probe) interacts with a periodic crystal, fundamentals of elastic electron scattering are required. The very basic description of elastic electron scattering is done by scatter from isolated atoms, where either electron-electron (mainly inelastic scattering) or electron-nucleus interaction (mainly elastic scattering) could occur (Figure 2.7). The probability of a electron-nucleus scattering event is expressed by the electron-nucleus cross section:

$$\sigma_{nucleus} = \pi r_n^2 = \pi \left(\frac{Ze}{E_0 \theta} \right)^2 \tag{2.6}$$

where Z is the atomic number of the target nucleus, e the elementary charge, E_0 the incident electron energy and θ is the scattered angle.

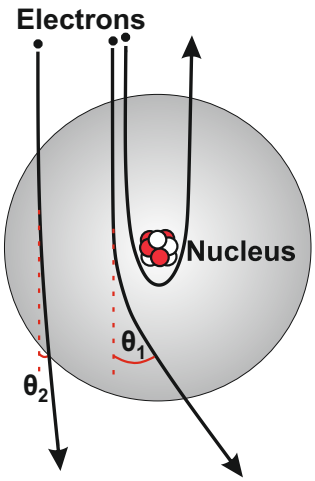

Figure 2.7: Depiction of electron scattering by an atom. Electron-nucleus interaction leads either to backscattering of the electrons or to scattering in high angles (θ_1), whereas the interaction with the electron cloud (gray sphere) leads to scattering in low angles (θ_2).

The first description of electron-nucleus interaction in vacuum and in particular the backscattering of α particles from a thin gold foil was carried out by Rutherford (1911)[46], who derived a formula for the differential cross section:

$$\frac{d\sigma_{nucleus}(\theta)}{d\Omega} = \frac{e^4 Z^2}{16(4\pi\varepsilon_0 E_0)} \frac{1}{\sin^4 \frac{\theta}{2}} \tag{2.7}$$

where ε_0 is the electric constant and Z, e, E_0, and θ are the same as described in (2.6). In a first rough approximation (2.7) describes the interaction of the probe with the investigated sample in STEM. For a more detailed description (2.7) has to be modified in a manner that on the one hand the screening parameter has to be taken into account:

$$\theta_0 = \frac{0.117 Z^{1/3}}{E_0^{1/2}} \tag{2.8}$$

which is mandatory when the electrons interact only with the atom electron cloud and hence the scattering angle will be small ($< 3°$). On the other hand, due to high acceleration voltages (>100 kV) in the STEM, relativistic correction of the electrons has to be applied. These modifications rearrange (2.7) into:

$$\frac{d\sigma_{nucleus}(\theta)}{d\Omega} = \frac{\lambda_r^4 Z^2}{64\pi^4 a_0^2} \frac{1}{\left[\sin^2\left(\frac{\theta}{2}\right) + \frac{\theta_0^2}{4}\right]^2} \tag{2.9}$$

where λ_r is the relativistically corrected electron wavelength and a_0 is the Bohr radius of the scattering atom. Thus, in case of $\theta < \theta_0$, the screening parameter θ_0 is dominant in (2.9) describing the electron-electron interaction with the atom electron cloud and therefore scattering in small angles. Whereas for the electron-nucleus interaction ($\theta > \theta_0$), θ_0 can be neglected and (2.9) results in a relativistic corrected Rutherford scattering formula.

Furthermore, $\frac{d\sigma_{nucleus}(\theta)}{d\Omega}$ is related directly to the atomic-scattering factor $f(\theta)$, which is a measure for how strong an electron wave is scattered by an isolated atom (Figure 2.8), via:

$$|f(\theta)|^2 = \frac{d\sigma_{nucleus}(\theta)}{d\Omega} \tag{2.10}$$

Since $|f(\theta)|^2$ is proportional to the scattered intensity I and due to the given relations in (2.10) and (2.9), I is directly proportional to Z^2. The $I \propto Z^2$ proportionality is the reason why the investigation via STEM is often called *Z-contrast* in literature[47,48].

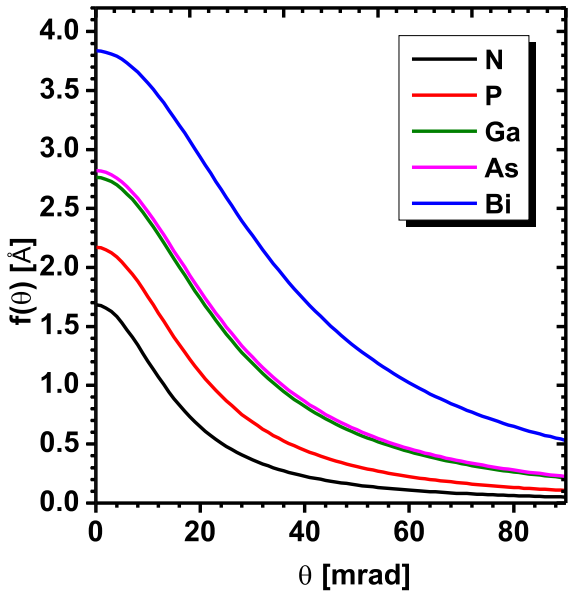

Figure 2.8: Diagram of the atomic form factor dependence on the scattering angle θ for different group V elements, which shows a Z-proportionality for $f(\theta)$ and thus for the intensity $I \propto |f(\theta)|^2$.

However, the Z^2 proportionality of the intensity is derived from a simplified model and thus very theoretical. STEM image simulations have shown that the exponent "c" of the atomic number Z^c is reduced and ranges between 1.6 and 1.9, since the screening of the atomic electron cloud has to be taken into account[49]. Furthermore, the scattered intensity is detected with an annular detector (see Section 3.2.3). Therefore, the choice of the detector acceptance angle ϑ_{min} has also an influence on the exponent "c", whereby a small exponent value is accompanied by a small ϑ_{min}.

Besides the electron scattering on localized atoms, there also exists an electron-phonon scattering process which contributes to STEM image formation. Since STEM measurements are usually performed at room temperature (300 K), electrons interact with vibrating atoms and cause an additional so-called *thermal diffuse scattering* (TDS). This scattering process is uncorrelated and therefore STEM images exhibit an additional background intensity. Furthermore, the amount of TDS and therefore the background intensity increases with the TEM sample thickness due to an increasing amount of electron-phonon interactions.

There are different approaches of the calculation of TDS in STEM image simulations which will be discussed in Section 3.3.

CHAPTER 3

Experimental Methods

This chapter summarizes the methods which were necessary for the obtaining of experimental results within this thesis. Since all investigated samples were grown by MOVPE, principles of this technique will be introduced. Furthermore, the basics of scanning transmission electron microscopy will be discussed in more detail. Finally, basic concepts of STEM image simulation will be introduced which is mandatory for the evaluation of experimental results.

3.1 Metal Organic Vapor Phase Epitaxy

The investigated ternary and quaternary III-V semiconductors were produced by metal organic vapor phase epitaxy (MOVPE) which is a common technique for the manufacturing of semiconductor materials, particularly metastable materials such as Ga(AsBi) which can be grown under non-equilibrium conditions. The source materials (*precursors*) are metal organic molecules that are stored in stainless steel tanks (*bubblers*) mostly in the liquid state. Highly purified hydrogen carrier gas transports the saturated gas phase of the metal organic molecules to the surface of a heated substrate which is a single crystal wafer (e.g. GaAs). The transport of group III and group V precursor chemicals takes place via separated stainless steel pipe systems in order to avoid chemical reactions before reaching the reactor system where crystal growth takes place. The decomposition of the molecules occurs due to the high substrate temperature at the surface which should result ideally in a single metal atom incorporating into the crystal and the organic group not affecting the crystal growth (Figure 3.1). Furthermore, the amount of different precursor chemicals can be adjusted by their partial pressure.
The growth of Ga(AsBi), Ga(NAsBi) and Ga(PAsBi) on GaAs substrates was performed on a AIX 200 gas flow rotation system including a 2" horizontal reactor system; moreover, the all-liquid precursors triethylgallium (TEGa), tertiarybutylarsine (TBAs), trimethylbismuth (TMBi), tertiarybutylphosphine (TBP) and unsymmetric dimethylhydrazine (UDMHy) were also used. At this point it has to be mentioned that growth of the investigated

samples via MOVPE was not part of this work, hence a detailed description of growth and characterization of Ga(AsBi) and Ga(NAsBi) can be found in Ref. 9. Additional information on the precursor chemicals characteristics and MOVPE are given in Ref. 50,51.

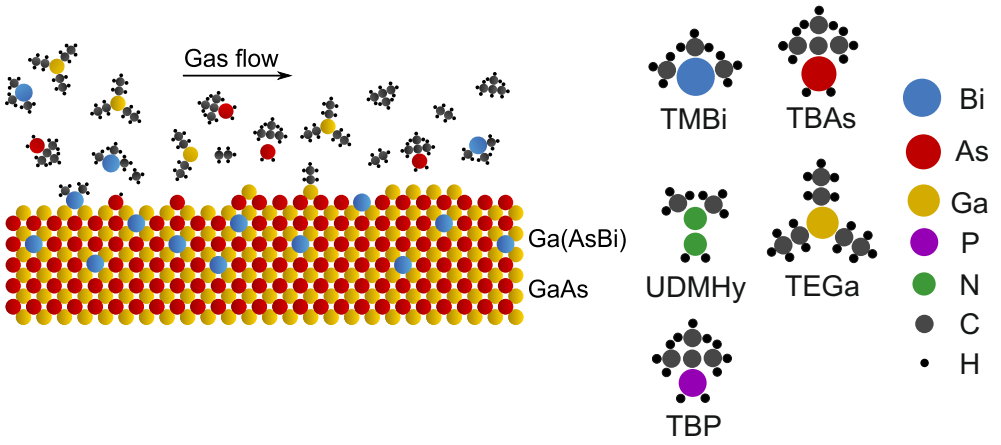

Figure 3.1: Scheme of the MOVPE growth as it takes place in a horizontal reactor system. The precursors which were used for the growth of Ga(AsBi), Ga(NAsBi) and Ga(PAsBi) are depicted on the right hand side. Adapted from Ref. 9.

3.2 Scanning Transmission Electron Microscopy

Transmission electron microscopy is a well established method in material sciences as well as in life sciences. It is therefore a very suitable tool for the investigation and characterization of novel semiconductor materials.

Since the size of investigated semiconductor materials is in the range of a few 10 nm, conventional light microscopes are inappropriate for the characterization of those. The reason for this is described by the *Abbe* diffraction limit formula:

$$\delta = \frac{\lambda}{2n \sin\theta} \tag{3.1}$$

where δ is the diffraction limit, λ the corresponding wavelength and $2n \sin\theta$ is called numerical aperture. Hence, typical light microscopes' resolution is in the range of a few 100 nm, whereas wavelengths below nanometer range are desirable for sub-nanometer (atomic) resolution. This is the main advantage of electron microscopes, since the relativistic *de Broglie* wavelength for electrons is expressed by:

$$\lambda_{el} = \frac{h}{\sqrt{2m_0 eU_0 \left(1 + \sqrt{\frac{eU_0}{2m_0 c^2}}\right)}} \tag{3.2}$$

with the Planck constant h, the electron mass m_0, the acceleration voltage U_0 and the speed of light c. Based on this equation, the electron wavelength equals to 2.5 pm in a TEM

provided with an acceleration voltage of 200 kV and due to (3.1) the theoretical resolution would be in the range of some picometer. Furthermore, the optics in electron microscopy is analogous to light microscopy and can be treated by the ray model. Therefore, the image formation in electron microscopy is provided with the help of electromagnetic round lenses (glass lenses in light microscopy). Additionally, TEM samples have to undergo a sample preparation process where the transmitted sample has a typical final thickness below 50 nm, due to the strong electron-matter interaction (see Section 2.4). The main steps of the conventional sample preparation which was applied in this work can be found in the appendix of this thesis (Figure 6.1).

3.2.1 Construction and Function of (S)TEM

Since the main experiments were performed in an aberration corrected *JEOL-JEM 2200FS* field emission (S)TEM operating at 200 kV. The instrument will be described based on a scheme of this device depicted in Figure 3.2. In the following, the microscope is described from top to bottom in the scanning mode.

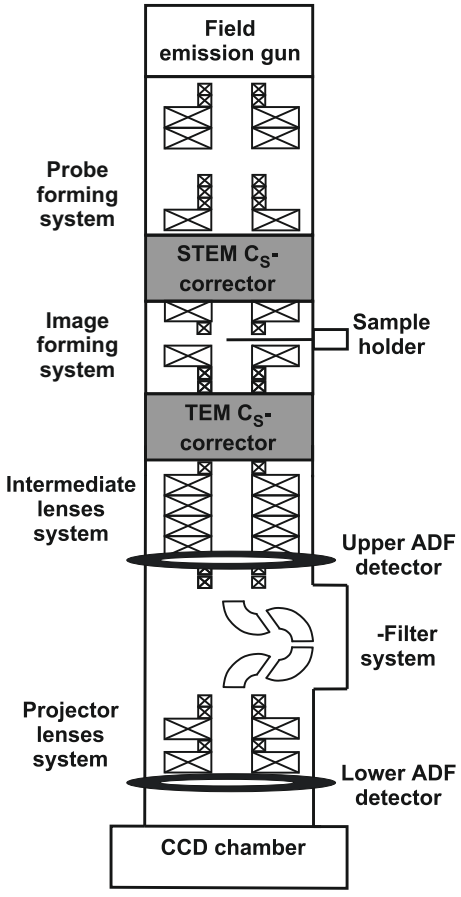

Figure 3.2: Schematic construction of the double C_S corrected JEOL-JEM 2200FS which was used for the investigation in this work.

At the top of the microscope is an electron source (electron gun) which is a *Schottky* type field emission gun (FEG) in the *JEOL-JEM 2200FS* (S)TEM. The main advantages of FEGs in contrast to conventional thermionic guns are the higher coherence and the greater brightness which not only leads to an improved signal-to-noise ratio but also to an improved spatial resolution in addition to a decreased energy width ΔE (below 1 eV). Moreover, *Schottky* type FEGs exhibit a higher current stability compared to so-called cold FEGs. These improvements are indispensable for the formation of a narrow electron beam (probe) with a size below 0.1 nm which is necessary for atomic resolution.
Electrons are accelerated up to 200 keV after the emission and pass the illumination system where they first enter the condenser lenses (CL) system (probe forming system in Figure 3.2). The CL system is the most important lenses system in STEM, since it is the probe forming system and therefore ensures a convergent illumination. Additional scan coils enable the scanning operation over the investigated sample and an aperture above the sample defines the so-called convergence semi-angle α. The aperture is mandatory because it truncates the off-axis rays which are responsible for an increased spherical and chromatic aberration Figure 3.3. An additional spherical aberration C_S-corrector provides an almost aberration free electron wavefront which is focused afterward and supplementary scan coils enable the scanning of the focused probe over the sample. Basics of C_S-correction in STEM will be given in Section 3.2.2. The sample is mounted on a special sample holder in the goniometer stage and is located within the ultra-high-resolution (UHR) polepiece, in the heart of the objective lenses (OL) system (image forming system in Figure 3.2). The objective lens is the most important lens in conventional TEM and is responsible for the biggest part of magnification and therefore providing the resolving power. However, like in the CL system the OL system suffers from spherical aberration as well. Therefore, another C_S-corrector is installed below the OL system which corrects spherical aberration in the image plane and hence enables atomic resolution in TEM mode. Due to subsequent intermediate lenses (IL) system, the possibility is given to select either the diffraction plane or the image plane of the investigated sample region by variation of IL currents. In STEM mode these lenses are necessary for the camera length variation that allows different signal detection (see Section 3.2.3) with an annular dark field (ADF) detector. Furthermore, variation of IL currents allow the imaging of both ADF detectors which can be used for intensity normalization in quantitative STEM measurements[52].
In-between IL system and the upper ADF detector is an energy filter (e.g. Ω filter) that disperses spatially electrons which exhibit different energies due to energy loss processes during the sample interaction. An additional slit gives the opportunity to choose a specific electron energy that either contributes to a filtered image, or can be used for electron energy loss spectroscopy (EELS) in combination with the lower ADF detector. The projection lenses (PL) system enables a further magnification of the final image, before it can be recorded by a charge-coupled device (CCD) camera in TEM mode, whereas PL

system is additionally used for camera length variation as well as central alignment of the measured ADF signal with respect to lower detector in STEM mode.

3.2.2 Spherical Aberration Correction in STEM

In electron microscopy (as well as in light microscopy), the resolution is strongly affected by miscellaneous lens system aberrations. Therefore, the probe function close to the sample surface in the reciprocal space is given by:

$$\psi_p(\vec{k},\vec{r}_p) = A(\vec{k}) \exp\left[-i\chi(\vec{k}) - 2\pi\vec{k}\vec{r}_p\right] \tag{3.3}$$

where $\vec{r}_p$ is the position of the probe, A($\vec{k}$) is the aperture function, which is 1 inside and 0 outside the convergence semi-angle α, and $\chi(\vec{k})$ is the aberration function (here: only the main rotationally symmetric aberrations):

$$\chi(\vec{k}) = \frac{2\pi}{\lambda}\left[\frac{1}{2}\Delta f\lambda^2k^2 + \frac{1}{4}C_S\lambda^4k^4 + \frac{1}{6}C_5\lambda^6k^6 + ...\right] \tag{3.4}$$

where λ is the electron wavelength, C_S and C_5 are the spherical aberration and the fifth order spherical aberration coefficients. Therefore, the minimization of $\chi(\vec{k})$ leads to a minimal probe size in STEM and thus, to the highest resolution.
The two dominant aberrations are the spherical (C_S) and the chromatic (C_C) aberration (Figure 3.3), whereby C_S is the dominating aberration in high kV (S)TEM. In contrast to glass lenses, electromagnetic round lenses are always convergent due to the *Lorentz force*. Thus, it is impossible to create a single divergent electromagnetic round-lens and hence to correct the aberrations which is explained by the *Scherzer-theorem*[53,54].

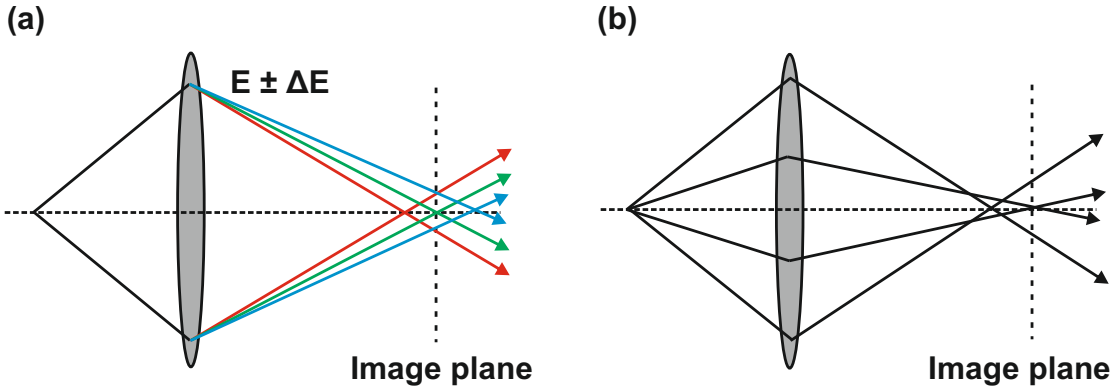

Figure 3.3: Simplified depiction of the chromatic (a) and spherical aberration (b). While the chromatic aberration occurs due to different electron energy, e.g. due to energy loss after sample transmission, the occurrence of spherical aberration is due to the anisotropy of the round lenses' magnetic fields. Both aberrations lead to many different foci which end up in a so-called disk of least confusion and lead to a reduced resolution.

Nevertheless, multi-pole corrector systems for TEM[55] as well as STEM[56] allow to compensate the spherical aberration nowadays. An optimization of (3.4) was elaborated by Haider et al.[57] Thereby defocus (Δf) and C_S are optimized in a way that (3.4) is minimized for a given C_5 and convergence semi-angle α with the optimized Δf:

$$\Delta f = 0.144 \cdot \alpha^4 C_5 \tag{3.5}$$

and the minimized C_S:

$$C_S = -0.92 \cdot \alpha^2 C_5 \tag{3.6}$$

thus, C_S corrector systems provide achievable resolutions below 50 pm in STEM[58]. Besides spherical aberration, chromatic aberration has an influence on the resolution as well, because it is the result of a finite energy width of an electron source. Therefore, a suggestion for a modification of the defocus value Δf is made in Ref. 57:

$$\Delta f_C = \Delta f + C_C \Delta E \tag{3.7}$$

where ΔE is the energy width of the given electron source. Despite the influence on the defocus Δf_C chromatic aberration has no influence on the optimized defocus value in (3.5). However, the product $C_C \Delta E$, which is named energy length, affects the Gaussian probe size's FWHM. Based on these characteristics, in Ref. 57 an optimum convergence semi-angle α of 25 mrad for a 200 keV probe and an energy length of 1.25 eVmm was found, achieving a resolution of 80 pm which is related to the *JEOL-JEM 2200FS* instrument used in this work. Otherwise, a smaller α limits the resolution by diffraction, whereas a larger one limits the resolution by the more dominant axial chromatic aberration.

3.2.3 Annular Dark Field Imaging

Annular dark field STEM has gained huge interest over the last two decades which is mainly attributed to a rather intuitive intensity interpretation in contrast to conventional TEM. This is mainly due to incoherent imaging and a Z^c $(1 < c < 2)$ proportionality of the detected intensity[47,48]. Furthermore, aberration correction provides a possibility of quantitative atom column analysis[59].

The basic difference to conventional TEM is a converged electron beam that is realized by the CL system (objective lenses in STEM). However, the choice of the condenser lens aperture size is important, since it influences the current density on the sample and therefore the signal-to-noise ratio. Based on the results given in Ref. 57, the convergence semi-angle was set to 24 mrad for HR-STEM measurements in this work.

Various signals arise during probe-specimen interaction, whereas the elastic scattering signal in high angles can be detected with an annular detector (scintillator) below the specimen. Therefore, the probe produced signal on sample position (X_s,Y_s) is assigned

to an image position (x_i,y_i) by the detector. The result is a dark field image, since only scattered electrons are detected, whereas undisturbed or weakly scattered electrons ($\vartheta_{min} < 20\,\mathrm{mrad}$) can be detected by an annual bright field (ABF) detector[60]. The latter is advantageous for the detection of light elements, such as hydrogen (H) as demonstrated in Ref. 61.

A huge difference to conventional TEM is the lack of further lenses behind the specimen. The achievable resolution in STEM depends only on the probe size. Moreover, the IL system ensures the (virtual) variation of the camera length (distance between sample and detector) what is correlated to a variation of the detector acceptance angle ϑ_{min} via:

$$\tan \vartheta_{min} = \frac{r_i}{L} \tag{3.8}$$

with inner detector radius r_i and camera length L which is depicted in a simplified model of the ADF imaging mode in Figure 3.4. This allows not only high angle annular dark field (HAADF, ϑ_1 in Figure 3.4) but also low angle annular dark field (LAADF, ϑ_2 in Figure 3.4) imaging.

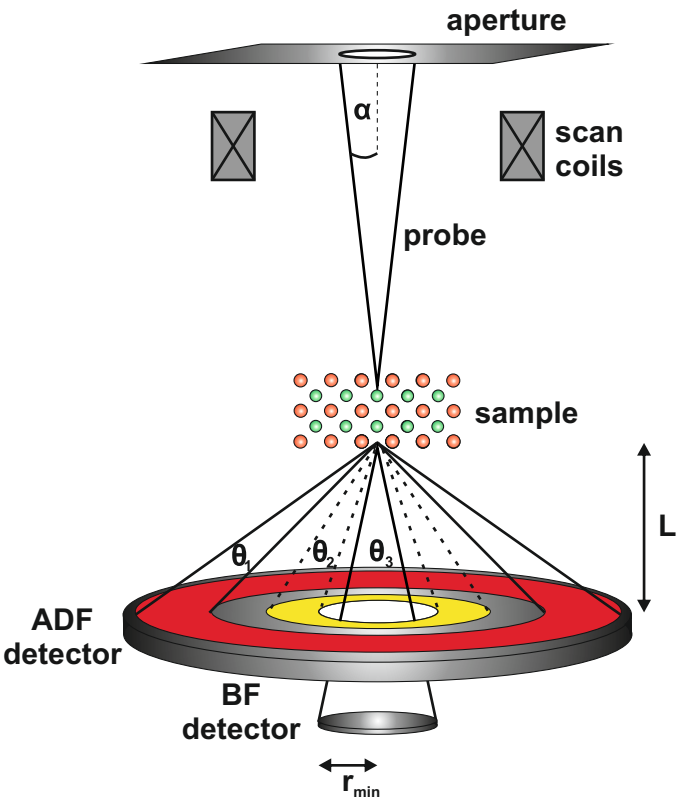

Figure 3.4: Simplified depiction of the signal detection in ADF imaging mode. The "variation" of the camera length L induces the possibility to detect either scattering in high angles (ϑ_1) or scattering in low angles (ϑ_2). Furthermore, an ABF detector allows the detection of undisturbed or weakly scattered electrons.

Basics of the intensity distribution in ADF images (especially in HR images) is described by the so-called *channeling* theory[62,63], whereby the electrons interact with the sample's 1s atomic orbitals which leads to a strong localization of the electron beam and hence a "channeling" through the atom columns. Therefore, the local intensity peaks in the resulting image correspond to the atom column positions. In addition to this, the interaction of the probe with thermal induced atom vibrations cause TDS (see Section 2.4) which is also pronounced in ADF measurements. Apart from the *channeling* theory and TDS there exist an additional scattering contribution that occurs due to local disordering of the crystal structure (SAD or defects). It is named *Huang-scattering* and was first observed by Huang in X-ray diffraction experiments of doped crystals[64]. Since this is rather an elastic scattering process, it is more pronounced in the LAADF scattering regime. Therefore, LAADF is often called strain-sensitive ADF imaging, because the additional *Huang-scattering* makes it is easier to detect strain at crystal defects or interfaces[65].

3.2.4 Energy Dispersive X-ray Spectroscopy

Due to the probe-specimen interaction and an associated electron energy loss, originating characteristic X-rays of the sample can be detected and result in a corresponding X-ray spectrum. Therefore, it is possible to analyze chemical composition of the investigated sample because the energy of characteristic X-rays is element-specific. Moreover, there exists the possibility of elemental mapping since STEM is an incoherent process. Thus, each pixel (x-y position of the probe at the sample) includes a corresponding X-ray spectrum. Since EDX is a surface sensitive method, the signal is generated near the sample surface, therefore the EDX-detector is located above the sample (see Figure 3.5).
EDX was used for the investigation of element distribution in Ga(PAsBi) layers (Section 4.3) in this work. For EDX measurements, a so-called silicon drift detector (*XFlash 5060 detector, Bruker*) was used providing a X-ray energy resolution of 129 eV.

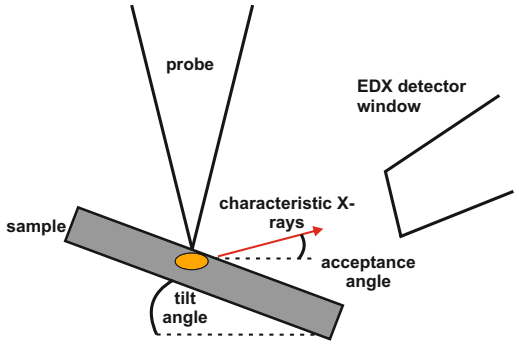

Figure 3.5: Simplified representation of the detector arrangement for EDX measurements in STEM. The detector is located at an acceptance angle above the sample and detectes the characteristic X-rays. The sample can be tilted which allows a maximization of the X-ray detection.

3.3 STEM Image Simulation

The simulation of STEM ADF images is indispensable for quantitative evaluation of experimental ADF images. There exist two established (S)TEM simulation methods, namely the Bloch-wave and the multislice algorithm[66]. Since the performed ADF image simulations in this work are based on the multislice algorithm it will be explained in more detail in this section.
The multislice algorithm was first introduced by Cowley and Moodey[67] for conventional TEM simulation and further developed for STEM image simulation by Kirkland[68]. The basic concept of this method is a division of the simulated supercell in commensurate cells (slices) with identical thicknesses Δz (usually the thickness of a unit cell or thinner). Each atomic potential in a single slice is projected perpendicular to the probe direction on a x-y plane (projected potential). Thus, probe-slice-interactions can be calculated independently and summed up afterwards (incoherent modeling). The scattering from atoms in j-th slice and propagation to the next (j+1) slice is given by the following expression:

$$\psi_{j+1}(x,y) = t_j(x,y)\,[\psi_j(x,y) \otimes p(x,y)] \tag{3.9}$$

where $\psi_j(x,y)$ is the electron wave function before the j-th slice at position (x,y), p(x,y) the propagator function and $t_j(x,y)$ is the transmission function (or phase grating) at slice j. The latter is an element specific function depending on the projected atomic potential of j-th slice $V_j(x,y)$:

$$t_j(x,y) = \exp\left\{\frac{2\pi i}{E_0}\underbrace{\left[\phi_j(x,y) + i\phi_j(x,y)'\right]}_{V_j(x,y)}\right\} \tag{3.10}$$

with the relativistic corrected electron energy E_0 and the projected potential's imaginary part $\phi_j(x,y)'$. The imaginary part is used in the so-called *absorptive potential* (AP) method[69] as an additional potential that takes into account the atoms' thermal vibrations around their equilibrium position (TDS). The AP approach is a rough approximation because electrons, scattered by $\phi_j(x,y)'$, do not contribute to further scattering processes in subsequent slices, but are "absorbed" and added to the final calculated intensity. Nevertheless, this approach is valid for thin samples ($< 20\,\mathrm{nm}$) and for LAADF measurements, where TDS is not as pronounced as in HAADF STEM. However, a more realistic treatment of TDS is given in the *frozen phonon* (FP) approximation[70–72] with a time-dependent crystal potential:

$$V(\vec{r},t) = V_0(\vec{r}) + \Delta V(\vec{r},t) \tag{3.11}$$

where $V_0(\vec{r})$ is the time averaged crystal potential and $\Delta V(\vec{r},t)$ is the perturbation part of the crystal potential (TDS) due to thermal vibrations. It is defined as:

$$\Delta V(\vec{r},t) = \sum_n \left[V_n(\vec{r} - \vec{r}_n - \vec{u}_n(t)) - V_{n,0}(\vec{r} - \vec{r}_n)\right] \tag{3.12}$$

where $\vec{r}_n$ is the equilibrium position of the n-th atom and $\vec{u}_n(t)$ is the time-dependent atom displacement from $\vec{r}_n$, that is connected to the *Debye-Waller* factor via:

$$M_n = 2\pi^2 \left\langle \vec{u}_n^2 \right\rangle . \tag{3.13}$$

The basic step in FP approach is the calculation of different atomic vibration (phonon) configurations, i.e. $\vec{u}_n(t)$, while (3.13) is calculated once for each atom in the AP approach. This approximation is valid, because electrons reach about 70% the speed of light (at 200 kV) and therefore the electron-sample interaction is in the order of 10^{-16} s, whereas atomic vibration periods are in the order of 10^{-13} s[73]. Furthermore, electrons are temporarily and spatially separated, due to an extremely low current. Thus, every electron does not "see" any thermal vibration but only a random snapshot of an apparently fixed atom. In contrast to AP simulation, the FP approach provides multiple scattering, since thermal diffuse scattered electrons are not absorbed and therefore can interact with subsequent slices. On the other hand, the FP approach demands a large computation time in contrast to the AP approach since N (usually 20) phonon configurations, and therefore N probe-slice interactions, have to be calculated for each slice.
The STEM ADF simulations in this work were performed with the STEMSIM software package[74] in the AP and *frozen lattice* multislice approach. The latter is similarly treated as the FP approach but implies an uncorrelated thermal motion of crystal atoms (Einstein model). Furthermore, *Debye-Waller* factors for the simulation of Ga(AsBi) and GaAs were taken from Ref. 75.

CHAPTER 4

Results

The following chapter presents the results of Ga(AsBi), Ga(NAsBi) and Ga(PAsBi) characterizations obtained with STEM measurements which were not published. The first part is focused on the results of Ga(AsBi) ADF simulations, which are indispensable for the interpretation of experimental images and their quantification. Furthermore, a method for the investigation of quantum well (QW) composition homogeneity will be explained, based on Ga(NAsBi) and Ga(PAsBi) HAADF measurements. The second part of this chapter includes HAADF measurements of Ga(PAsBi). Additional EDX measurements of Ga(PAsBi) were carried out, since a composition fluctuation was assumed. Moreover, cluster-like features were detected whose chemical composition was investigated via EDX. The results will show besides a qualitatively good chemical composition of Bi containing Ga(AsBi), Ga(NAsBi) and Ga(PAsBi) on large length scales, atomic ordering in the nanometer regime and cluster formation due to annealing processes can be revealed.

4.1 ADF Simulation of Ga(AsBi)

This section describes the results of STEM ADF simulations of a VFF relaxed Ga(AsBi) supercell. The performance and evaluation of the simulation is representative for the other simulations, which were carried out in this work.
The supercell has a Bi concentration of $x = 3.8\%$, a size of $\approx 4\,\text{nm} \times 4\,\text{nm}$ in x-y plane and a thickness of t$\approx 5.1\,\text{nm}$ (probe direction). In order to investigate the measured ADF signal in dependence on the detector acceptance angle ϑ_{min}, simulations of the supercell were performed in the low angle (33 mrad) as well as in the high angle (73 mrad) scattering region. The STEMSIM package allows STEM image simulation either in the absorptive potential or in the frozen lattice approach. In this case the absorptive potential approach was used, since the supercell thickness is rather small and multiple scattering can be neglected. The convergence semi-angle of the condenser lens aperture was set to 24 mrad to achieve comparable results to the experiment. Furthermore, a spherical aberration

corrected probe was assumed with a C_S value of -2.32 µm. The result of $\vartheta_{min} = 73$ mrad simulation in [010] direction is depicted in Figure 4.1(a) where one can see clearly the intense Bi containing group V columns.

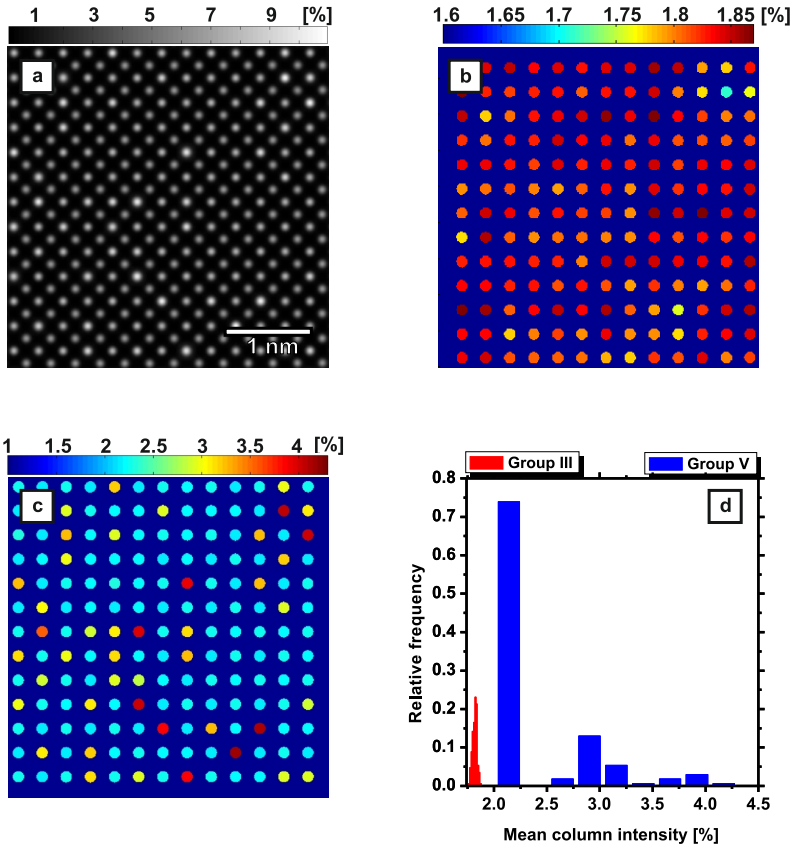

Figure 4.1: (a) HAADF absorptive potential simulation of Ga(AsBi) supercell and the separated group III (b) and group V (c) mean column intensity maps. The color and grayscale bars represent the scattered intensity in % of the impinging probe's intensity. (d) Histogram depiction of column intensities of each sublattice.

In further steps the peak pairs analysis software[76] was used to detect atomic column peaks and a self written MATLAB algorithm allowed to separate the two sublattices. In order to analyze properly the atomic column intensities, an intensity integration radius of 1/3 next neighbor distance was chosen around each column peak which allows a generation of the mean column intensity map of each sublattice, depicted in Figure 4.1(c) and (d). The choice of this radius is due to a reasonable signal-to-noise ratio without introducing too much crosstalk between atomic columns, and furthermore it corresponds to the atomic columns' full width of half maximum (FWHM). Finally, histogram plots are used to visualize the integrated (mean) column intensity distribution of each sublattice (Figure 4.1(d)) in fractions of the probe's intensity. The bin size of each distribution is determined individually by taking into account the Freedman-Diaconis rule[77].

4.1.1 Group V Column Intensities

The following subsection focuses on the interpretation of group V intensity distribution, which is depicted in a histogram plot in Figure 4.1(d). Thereby the amount of equal mean column intensities within a bin is given by the relative frequency. The depicted intensity distribution shows the highest relative frequency at a mean column intensity value of 2.1% and two local maximums around 2.9% and 3.9%. While the lowest mean column intensity value corresponds to Bi-free As columns, the other two values are the result of Bi incorporation into the group V sublattice. Since the location of Bi atoms is known in the given supercell, the two intensity maximums are related to group V columns containing one and two Bi atoms respectively. Furthermore, these results demonstrate the atomic number dependency of the scattered intensity in HAADF imaging. In contrast to the pure As column intensities, Bi containing group V columns exhibit an intensity spread, which is $\Delta I = 0.8\%$ for both local maximums. For a more accurate analysis of the intensity spread, the bin size was manually reduced which ensures a higher resolution of the intensity distribution (Figure 4.2(a)).

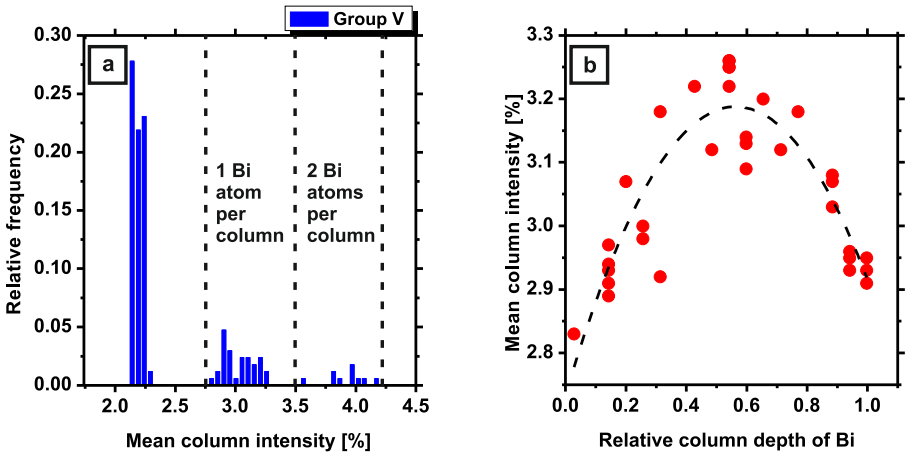

Figure 4.2: Histogram plot of mean group V column intensities with a reduced bin size (a). The dashed lines define the intensity ranges of columns containing one and two Bi atoms. (b) Plot of the group V column intensities containing one Bi atom versus the Bi atom depth within the column. An intensity maximum is pronounced when the Bi atom is located at the columns' mid-position. The variance of the mean column intensity at a fixed depth is likely due to different chemical environment. The dashed curve is a polynomial fit of the data points.

Thus, the histogram shows slightly different intensities for single Bi containing group V columns. For a further examination of this behavior, the column intensity is plotted over the corresponding Bi atom depth (z-position) in column. Figure 4.2(b) depicts a non constant column intensity dependency of the Bi atom depth with a maximum intensity value for group V columns, where the Bi atom is located at the column's mid-position. Similar simulation results have been found in Ref. 78 where an intensity oscillation in dependence on the depth of an antimony (Sb) atom in a silicon (Si) column could be revealed, due to electron probe channeling. Furthermore, the non-constant intensity of

Bi containing group V columns could be related to the probe focus which is located at the center of the supercell thickness (depth) during the simulation. Therefore, group V columns where Bi atoms are located at the center reveal the highest mean column intensities. Hence, the mean column intensities decrease with an increasing defocus of the probe (at the supercell edges). These results show a dependence of the column intensity on the Bi atom position and therefore an existing measurement uncertainty, which is also expected in the experiment. However, such a clear distinction between the group V intensities, especially a clear allocation of Bi atom position and column intensity, is expected to be much more challenging in the experiment. The reasons for this are on the one hand scan artifacts (scan noise and sample drift) which are unavoidable during STEM measurements, and on the other hand chromatic aberration which becomes more crucial with an increasing sample thickness. Especially the influence of chromatic aberration, which was not considered for this simulation, will lead to an overlap of the mean group V column intensities in Figure 4.2(a).

4.1.2 Group III Column Intensities

In addition to group V intensity distribution, group III (Ga) intensity distribution was properly examined as well. For this reason a smaller bin size was chosen than it is depicted in Figure 4.1(d) Furthermore, the Ga intensity distribution was investigated for LAADF (ϑ_{min} = 33 mrad) as well as for HAADF (ϑ_{min} = 73 mrad) simulations. The intensity histograms of both simulations are depicted in Figure 4.3(a) and (b), respectively. The histograms show clearly a non-constant Ga column intensity, as one would expect, but rather a certain width of intensity distribution.

Moreover, despite the peak values 1.83% and 5.84% for HAADF and LAADF intensities respectively, there exist a shoulder-like feature in the lower intensity range [1.75%;1.81%] for HAADF simulation as well as in the higher intensity range [5.96%;6.30%] for LAADF simulation.

For further analysis, corresponding positions of Ga intensities were highlighted from the intensity ranges which were named before and plotted together with the Bi containing group V columns in a mean column intensity map. The presented mean intensity map of LAADF simulation Figure 4.3(c) shows all Bi-containing group V columns and group III columns corresponding to the intensity range [5.96%;6.30%]. One can see a clear tendency that most of Bi-containing group V columns are surrounded by the highlighted group III columns. Thereby, the yellow and white colored group V columns represent group V columns containing one and two Bi atoms, respectively. This result is a consequence of displaced Ga atoms (SADs) by the strain field inducing Bi atoms that are derived from VFF supercell relaxation. Moreover, the higher intensity of these group III columns occurs due to additional *Huang-scattering* that arises because of local disorder in crystals and can be detected in LAADF imaging mode. On the other side the depicted mean

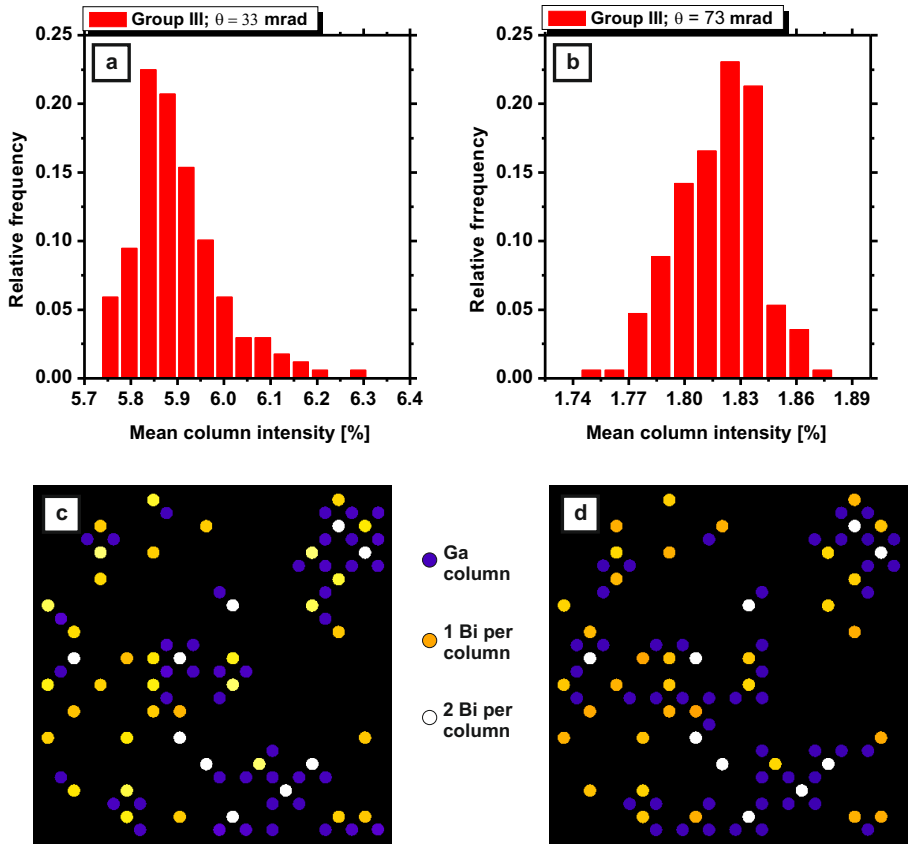

Figure 4.3: Group III mean column intensity distributions for LAADF (a) and HAADF (b) simulation. (c) and (d) are the corresponding mean column intensity maps. Whereby the intensity range $[5.96\%; 6.30\%]$ in (a) was used to highlight Ga columns (violet) in (c) and the intensity range $[1.75\%; 1.81\%]$ was used to highlight Ga columns in (d).

intensity map of HAADF simulation (Figure 4.3(d)) shows most of the Bi-containing group V columns surrounded by less intense group III columns which have similar position as shown in LAADF simulation. The lack of intensity, in contrast to other group III columns' intensity, is again a consequence of displaced Ga atoms from their mean position and can be explained with the *de-channelling*[63] effect. This effect describes the loss of probe intensity at the column position due to column distortion by the strain fields that arise because of incorporated Bi atoms.

Both results originate from the same physical behavior, namely the local lattice distortion due to impurity atoms. Thus, it could be shown by means of ADF simulations that there exists a possibility to detect local lattice distortions in HR-STEM via the measured ADF intensity.

4.2 Composition Homogeneity Analysis of Ga(PAsBi) and Ga(NAsBi)

Another topic of this work is the investigation of quaternary Bi containing materials Ga(PAsBi) and Ga(NAsBi), especially whether Bi incorporates homogeneously or not. A

homogeneous Bi incorporation is required in particular for devices based on Bi containing semiconductor alloys. Therefore, a Ga(PAsBi)-QW with a Bi fraction of 4.4% and P fraction of 20.2% as well as a Ga(NAsBi)-QW with a N fraction of 2.5% and Bi fraction of 4.8% were investigated by means of STEM HAADF imaging.
Therefore, $\vartheta_{min} = 73\,\text{mrad}$ was set for the HAADF measurements which allows chemical contrast imaging, thus a fluctuation of the intensity can be directly interpreted with a composition fluctuation. The HAADF measurements of Ga(PAsBi) and Ga(NAsBi) are depicted in Figure 4.4 (a) and (b), respectively. One can see that the Bi containing QW appears less intense in Figure 4.4(a) than in Figure 4.4(b) where the Ga(NAsBi)-QW has even a higher intensity than GaAs. This is related to the mean atomic number Z of the QW which is lower in Ga(PAsBi) than in GaAs due to the high P fraction, and higher in Ga(NAsBi) than GaAs because of a Bi fraction of 4.8% and a relatively low N fraction of 2.5%.

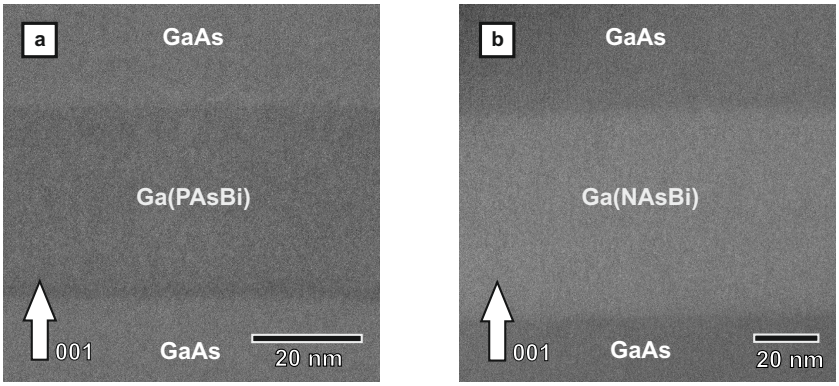

Figure 4.4: Normalized and background subtracted HAADF overview of Ga(PAsBi)-QW (a) and Ga(NAsBi)-QW (b) in [010] zone-axis for intensity fluctuation analysis.

Furthermore, the images were normalized to the impinging electron beam and background subtracted due to sample preparation geometry. In the next steps a method was applied which was developed by Wegele et al.[79] and which allows the determination of the composition fluctuation in the QWs. The image size was reduced to one third of the original size for both measurements which ensures a filtering of the high resolution part in the image. Finally, intensity fluctuation was determined as described in Section 6.1, i.e. pixel intensities were normalized to the mean QW-intensity value I_{mean}. The result is an intensity fluctuation map where each pixel intensity value is related to the deviation from I_{mean}. Figure 4.5 (a) and (b) depicts the intensity fluctuation map of Ga(PAsBi) and Ga(NAsBi), respectively.

The resulting mean σ_{norm} about 2.2% for the Ga(NAsBi)-QW and 2.4% for the Ga(PAsBi)-QW. A comparison with the intensity fluctuation results of Ga(AsBi)-QWs, which are presented in Section 6.1, is depicted in Figure 4.5(c). The diagram shows the mean σ_{norm} in dependence on the Bi fraction. One can see that an increasing Bi fraction does not influence the mean σ_{norm} and moreover, the mean σ_{norm} is almost

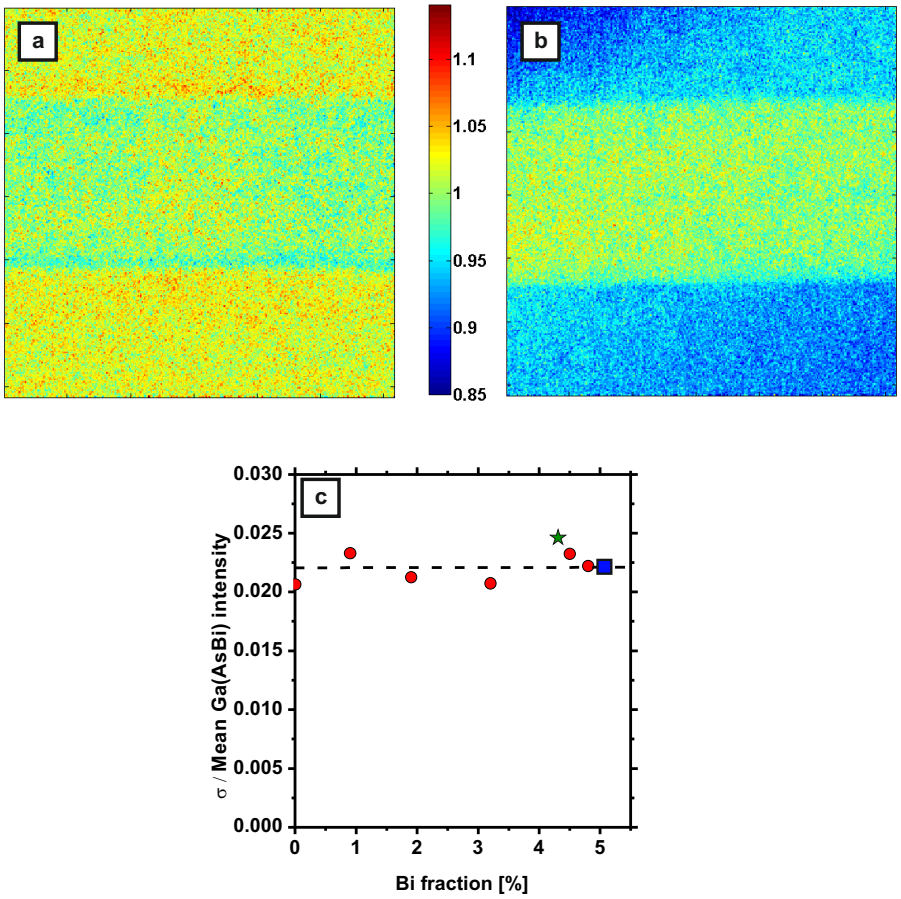

Figure 4.5: Intensity fluctuation maps (a) and (b) of the corresponding Ga(PAsBi)- and Ga(NAsBi)-QW from HAADF measurements in Figure 4.4 (a) and (b). (c) Plot of the mean σ_{norm} versus the Bi fraction. The red dots are taken from investigated Ga(AsBi)-QWs. The green star and the blue square correspond to the mean σ_{norm} measured in (a) and (b), respectively. The dashed line is a guide to the eye that marks a constant σ_{norm} value of 0.022. The diagram shows a homogeneous Bi incorporation in the investigated QWs since the mean σ_{norm} of the QWs do not differ much from the one of GaAs (0.02).

constant for all Bi fractions and is as low as for pure GaAs. These results lead to the interpretation of a homogeneous Bi incorporation and thus of good chemical quality of Bi containing-QWs. The slightly higher mean σ_{norm} of the Ga(PAsBi)-QW is potentially connected to the composition fluctuation at the lower and upper interface and therefore, a further optimization of the Ga(PAsBi) growth via MOVPE is required. These results show the good homogeneity of Bi containing materials on length scales above 10 nm. However, inhomogeneous Bi incorporation or ordering effects can occur on much smaller length scales which is why it will be discussed in the subsequent section.

4.3 Investigations of the Composition Fluctuation in Ga(PAsBi)

Additionally to the ternary Ga(AsBi) alloy the rather new quaternary material Ga(PAsBi) was part of ADF investigations in this work. Therefore, so-called *Secondary ion mass spectrometry* (SIMS) samples for further SIMS measurements (not part of this work) were realized. A typical sample overview, prepared in [010] zone axis, is depicted in Figure 4.6.

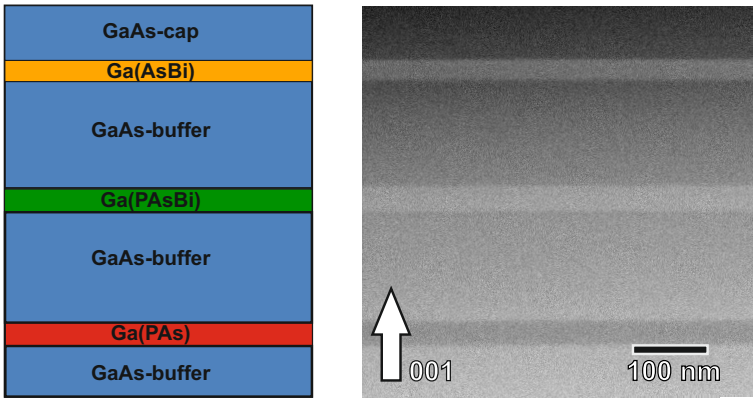

Figure 4.6: Sketch of a SIMS sample structure (left) and corresponding HAADF overview (right).

The sample consists of a Ga(PAs)-, a Ga(PAsBi)-, and a Ga(AsBi)-QW, from bottom to top. The layers are separated by a GaAs-buffer in each case, whereas the subsequent discussion is focused only on the Ga(PAsBi)-layer with a nominal Bi and P fraction of 4.4% and 20.3% respectively, derived from additional SIMS measurements. An explicit HAADF (73 mrad) measurement of the Ga(PAsBi)-layer is shown in Figure 4.7.

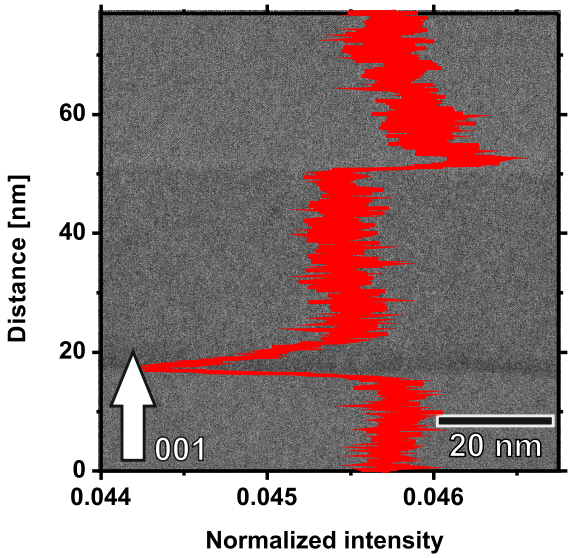

Figure 4.7: Normalized and background subtracted HAADF overview of Ga(PAsBi) and a corresponding integrated intensity profile (red diagram). The intensity profile depicts clearly a decreased intensity at the lower interface and an increased intensity at the upper interface.

In addition, the measurement was undergone further processing steps which include a normalization and a background subtraction step, as described in Section 6.1. Furthermore, an integrated HAADF intensity profile (red) of the layer is given as an inset. Thus, a layer width of 40 nm was determined and moreover, a decreasing as well as increasing intensity can be seen at the lower and upper Ga(PAsBi) interface, respectively. Due to the Z-dependency of the intensity, a composition fluctuation is assumed in these regions. Therefore, additional EDX measurements were carried out whose results are depicted in Figure 4.8.

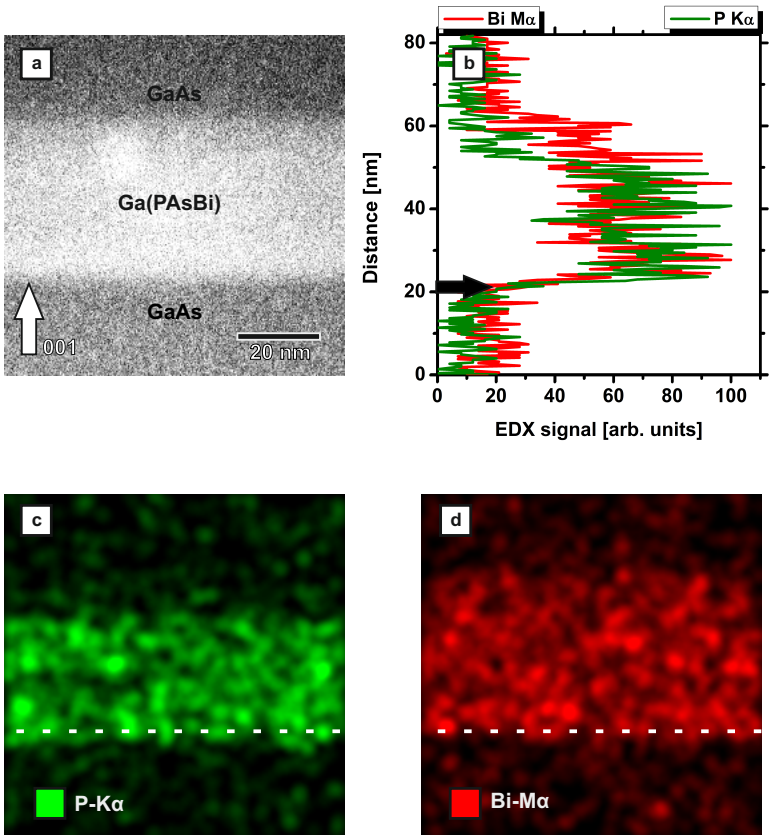

Figure 4.8: HAADF overview of Ga(PAsBi)-QW (a) and corresponding integrated EDX Bi-Mα and P-Kα signal line scans (b) as well as the corresponding P (c) and Bi (d) EDX element maps in false colors.

It includes a HAADF overview of the measured region (a), an integrated EDX signal line scan (b) and the measured EDX element maps of P (c) and Bi (d). The EDX line scan in Figure 4.8(b) shows qualitatively that P incorporation takes place earlier than Bi incorporation during the growth of Ga(PAsBi) which is marked with a black arrow. This effect becomes more visible by comparing the corresponding element maps of P and Bi in Figure 4.8(c) and (d). These element maps show the detected P-Kα and Bi-Mα EDX signals, and hence the spatial distributions of P and Bi in the Ga(PAsBi)-QW. The white dashed line in Figure 4.8(d) marks the beginning of Bi-Mα signal detection at the lower Ga(PAsBi) interface and therefore the beginning of Bi incorporation. A comparison with

the detected P-Kα signal at the same position (white dashed line) in Figure 4.8(c) depicts that P incorporation starts slightly earlier. However, one can see that Bi-Mα signal is present at the upper interface in Figure 4.8(d) whereas P-Kα signal can not be detected anymore (depicted in Figure 4.8(c)). Thus, a Bi-poor and a Bi-rich region is present at the lower and at the upper Ga(PAsBi) interface. This characteristic is well known for MOVPE-grown Ga(AsBi) (see Ref. 9): the supply of Bi does not lead to an immediate incorporation into GaAs but demands a certain surface coverage. On the other side, the melting point of Bi (271.4 °C) is beyond the typical MOVPE growth temperature of Bi containing alloys (usually 400 °C). Therefore, the liquid Bi part remains at the surface and incorporates further on into the GaAs barriers even though no Bi is offered anymore. Besides the mentioned effects at the lower and upper interfaces, bright round-shaped regions were detected in the Ga(PAsBi)-layer. These regions were especially pronounced in Ga(PAsBi)-layers which were thermally annealed after the growth process, depicted in Figure 4.9(a). In addition, EDX-spectra inside (black dashed circle) and outside (red dashed circle) the round-shaped region were recorded (depicted in Figure 4.9(b)). A comparison of both spectra shows a higher Bi-Mα peak in the EDX-spectrum of the round-shaped region, thus a higher Bi-amount is assumed. This leads to the conclusion that the round-shaped regions are Bi-rich Ga(PAsBi)-cluster which are formed due to thermal annealing processes. One possible description of the cluster formation is related to a high amount of Ga-vacancies that can occur due to relatively low growth temperatures of Bi containing materials. Furthermore, it could be shown by means of theoretical calculations that Bi has the tendency to diffuse into to Ga-vacancies during annealing processes [80].

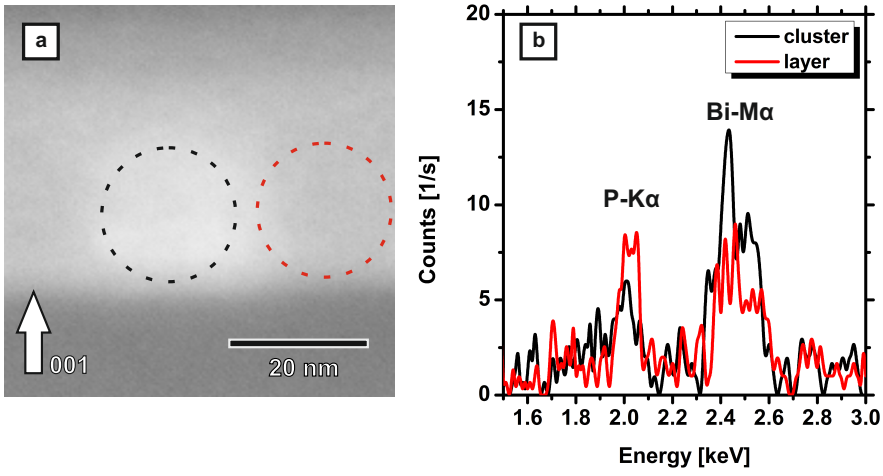

Figure 4.9: HAADF overview of a Ga(PAsBi)-QW after thermal annealing at 625 °C (a). The black and the red dashed circles mark a cluster-like feature and a region outside the cluster-like feature, respectively. (b) EDX spectra of a cluster (black spectrum) and a region of the Ga(PAsBi)-QW outside the cluster-like feature (red spectrum). The EDX measurement of the cluster reveals a slightly higher Bi content and a slightly lower P content than the EDX measurement outside the cluster.

4.3.1 Atomic Ordering in Ga(PAsBi)

The following subsection focuses on the atomic ordering in the investigated Ga(PAsBi)-QWs. For this reason, similar samples as shown in Section 4.3 were prepared in [110] and $[1\bar{1}0]$ zone axis. For the investigation of atomic ordering, HR-HAADF measurements were carried out. The resulting HR image is depicted in Figure 4.10(a) and shows the Ga(PAsBi)-layer in $[1\bar{1}0]$ zone-axis. The fast Fourier transformation (FFT) of the measurement is depicted in Figure 4.10(b).

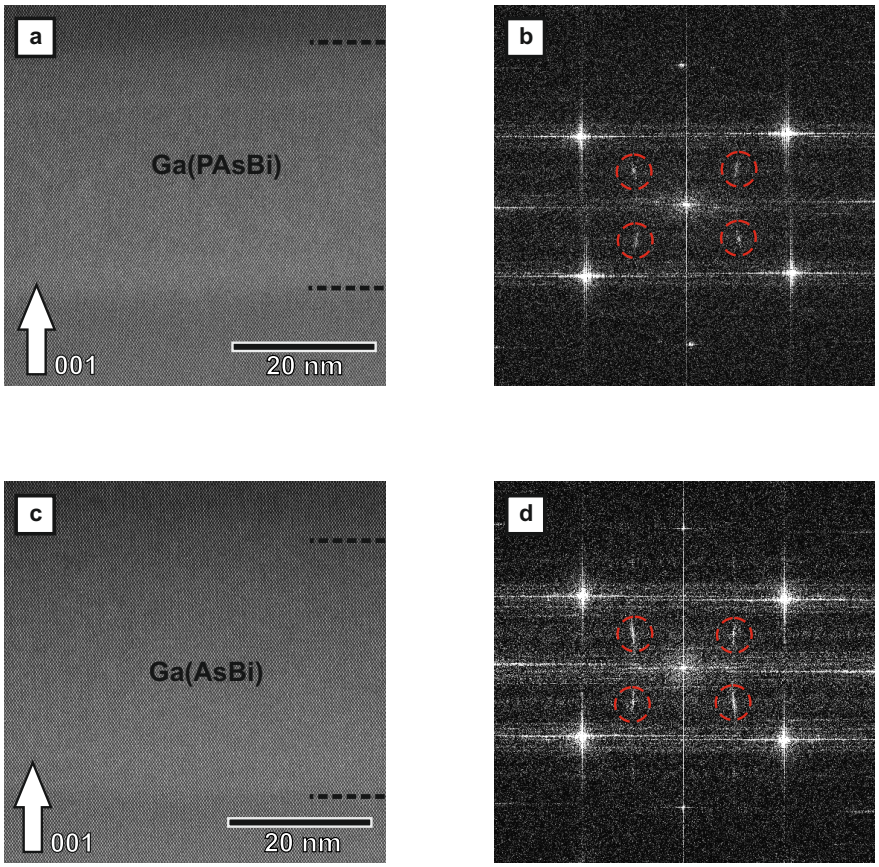

Figure 4.10: High resolution HAADF measurement of Ga(PAsBi)- and Ga(AsBi)-QW (a) and (c) in $[1\bar{1}0]$ zone-axis. Their corresponding FFT (b) and (d) exhibit superlattice spots (dashed red circles) which is related to CuPt-ordering. The black dashed lines mark the upper and lower interface of Ga(PAsBi)-QW (a) and Ga(AsBi)-QW (c).

Besides the typical zinc-blende $[1\bar{1}0]$ diffraction pattern, additional 1/2 {111} superlattice spots are weakly visible which are related to CuPt-ordering (Figure 2.5). However, similar results were revealed in the Ga(AsBi)-layer with a Bi fraction of 4.1% (Figure 4.10(c) and (d)), thus one can say that atomic ordering in Ga(PAsBi) is induced due to the presence of Bi. Furthermore, $CuPt_B$-type ordering is known to appear in Ga(AsBi)-alloys with Bi fractions up to 10%[10]. Nevertheless, these are the first observations of $CuPt_B$-type ordering in Ga(PAsBi). Since there exist also the possibility of $CuPt_A$-type ordering, investigation of the same sample was carried out in [110] zone-axis. The resulting HAADF

measurement, which is depicted in Figure 4.11(a), does not show any superlattice structure in a corresponding FFT (not shown here). However, the lower Ga(PAsBi)-interface shows a certain roughness which could not be detected in $[1\bar{1}0]$ zone-axis.

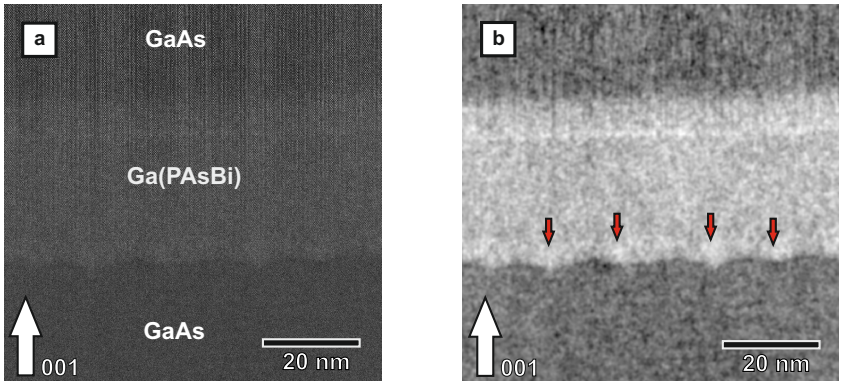

Figure 4.11: HAADF image of Ga(PAsBi)-QW in [110] zone-axis after background subtraction (a). Corresponding low pass filtered image (b) for a better visualization. The red arrows point on intense round-shaped regions which are possibly Bi-rich regions.

Moreover, intense round-shaped regions with the size of about $20\,nm^2$ appear every 15-18 nm at the lower interface (red arrows in Figure 4.11(b)). Similar pronounced phase-separation was also revealed in Ga(AsBi) by Ref. 10 where intense Bi regions in Ga(AsBi) and less intense Bi-free GaAs regions could be detected by means of STEM measurements in combination with EDX.

Finally, these results show the evidence of Bi ordering effects in Ga(PAsBi) and furthermore inhomogeneous incorporation of Bi and the formation of Bi-rich clusters, especially after thermal annealing of the samples. Nevertheless, the homogeneous Bi incorporation in Ga(AsBi), Ga(NAsBi) and Ga(PAsBi), which was shown in Section 4.2, can be related to the well known surfactant effect of Bi[81–83], among others, Bi as surfactant reduces the density of crystal defects which leads to an increasing crystal quality.

CHAPTER 5

Summary and Outlook

Energy efficiency plays a key role in the development of new industrial as well as daily life applications. There exists a strong demand for a new energy efficient generation of optoelectronic devices, especially in the growing market of internet data transfer where devices operate in the 1.55 µm wavelength regime. A promising material system that could face the challenge of efficient devices is the dilute Bi containing Ga(AsBi) and the dilute bismides in general. The novel material system Ga(AsBi) has been proven that the incorporation of dilute Bi amounts reduces the bandgap energy. Furthermore, a suppression of non-radiative loss mechanisms and a decreased temperature-dependency of the emission wavelength could be verified which can be described by the valence band anti crossing model. Moreover, first electrically pumped Ga(AsBi) based laser devices could be fabricated which reveal once more the huge potential of dilute bismides.

In this work structural analysis of MOVPE grown Ga(AsBi), Ga(PAsBi) and Ga(NAsBi) on GaAs substrates were carried out by means of spherical aberration corrected STEM. In addition to STEM ADF measurements, ADF image simulations of Ga(AsBi) supercells were performed which allowed the interpretation of the measurements as well as the Bi quantification in Ga(AsBi)-QWs. Despite STEM measurements, image processing was applied for further analysis, i.e., determination and separation of the crystal sublattices in HR measurements via the MATLAB software. Image processing is mandatory since it allows on the one hand a quantification of the Bi fraction in Ga(AsBi), and on the other hand a further statistical evaluation of the atomic column intensities is possible.

First Ga(AsBi) samples, which were investigated with TEM in [010] zone-axis, were grown via MOVPE under non-optimized conditions (see Section 6.3). They exhibited a huge amount of metallic droplets on the surface, whereby their crystal structure could be analyzed by means of TEM diffraction pattern evaluation. It turned out that many of the droplets are Bi single crystals and moreover a preferred alignment of Bi-$\{10\bar{1}\}$ lattice planes parallel to GaAs-$\{202\}$ with the formation of a coincidence lattice could be revealed. Thereby the lattice mismatch between droplet and surface can be reduced from 12% to 0.6%. However, supposed high quality (chemically homogeneous) Ga(AsBi)-QWs

with different Bi fractions ($0.9\% \leqslant x \leqslant 4.8\%$) were investigated in [010] zone-axis as well (see Section 6.1). Additional STEM HAADF simulations of Ga(AsBi) supercells with different amount of Bi were carried out which served for the Bi quantification of the investigated Ga(AsBi)-QW. The Bi quantification was carried out with the help of low resolution STEM HAADF measurements of the particular Ga(AsBi)-QW. Thus, the derived Bi fractions are in excellent agreement with the ones derived from SIMS and HR-XRD measurements. Furthermore, the comparison with corresponding STEM HAADF simulations revealed rather a $Z^{1.6}$ proportionality of the detected intensity, than an often assumed Z^2 dependency. Moreover, a method for the measurement of the STEM HAADF intensity fluctuation within the Ga(AsBi)-QWs was applied which served as an indicator for the particular Bi distribution. The results exhibit homogeneous Bi distributions for all investigated Ga(AsBi)-QWs, since the intensity fluctuations were comparable with the one from pure GaAs that occurs due to measuring processes in STEM (specimen drift, scan noise and sample thickness fluctuation due to sample preparation). In conclusion, the investigated high quality Ga(AsBi)-QWs revealed homogeneous Bi distributions in the 10 nm range and above. For the detection of Bi ordering effects or composition fluctuation on the nm scale and below, HR-STEM HAADF measurements of Ga(AsBi)-QWs in [010] zone-axis in combination with a frozen-lattice simulation of a Ga(AsBi) supercell and a Bi fraction of 4.8% were carried out (see Section 6.2). Thereby, high resolution investigations were performed by measuring the same region of interest seven times in a row with a fast acquisition time. Afterward, the measurements were aligned with the MATLAB based non-rigid image alignment tool *SmartAlign*. This allowed final images with an improved signal-to-noise ratio and less scanning artifacts. A statistical evaluation of HR measurement of the Ga(AsBi)-QW with the highest Bi fraction revealed good agreement with a corresponding Ga(AsBi) STEM simulation. Moreover, the simulation allowed a quantification of the integer amount of Bi atoms per group V column and their corresponding intensity. Based on the simulation results, group V intensity regions were chosen in the experiment which correspond to atomic columns with a high amount of Bi atoms (three or more). A corresponding map plot of the positions in combination with the so-called *Hough transform* enables the detection of chain-like Bi ordering along the $\langle 100 \rangle$ and $\langle 101 \rangle$ crystallographic directions. It turns out that this is a non statistical distribution of Bi on the sub-nanometer scale, since a significantly lower amount of this ordering could be detected in a corresponding Ga(AsBi) HAADF simulation which exhibits a random Bi distribution within the supercell. These outcomes show the existence of Bi ordering below the nanometer scale in Ga(AsBi)-QWs exhibiting an apparently homogenous Bi distribution.

Beside Ga(AsBi), intensity fluctuation was also investigated in the quaternary material systems Ga(NAsBi) and Ga(PAsBi). The results were as similar as in Ga(AsBi) but with a slightly higher intensity fluctuation in Ga(PAsBi). STEM HAADF measurements of Ga(PAsBi) in combination with EDX show the presence of a P free Ga(AsBi)-layer above

the Ga(PAsBi)-QW that emerges probably after the growth of Ga(PAsBi). Additional HR-STEM investigations revealed $CuPt_B$-type ordering in Ga(PAsBi)-QWs, and moreover the presence of cluster formation could be detected in Ga(PAsBi) containing samples which have undergone thermal annealing processes. Further EDX measurements indicated these clusters as Bi-rich whose origin could be Bi-rich islands which were found close to the lower Ga(PAsBi) interface. The additional energy, that is accompanied with thermal annealing, could be the driving force for the formation of clusters inside the Ga(PAsBi)-QW.
Additional studies have to be carried out in the field of optimizing the MOVPE growth conditions for Ga(PAsBi) which could lead to high quality layers without any phase-separation. More detailed TEM studies should be focused on the Bi-rich regions in Ga(PAsBi). The knowledge of their formation could prevent the clustering processes and moreover it could help to find the optimal MOVPE growth parameters for Ga(PAsBi) with a homogenous distribution of all elements. Furthermore, STEM ADF simulations of a thin Ga(AsBi) supercell (5 nm) in combination with a statistical evaluation of the ADF intensities could reveal the influence of the local strain on Ga columns, due to the presence of neighbouring Bi atoms in group V columns. This shows the possibility of detecting and quantifying local strain via a statistical evaluation of HR-STEM ADF measurements. However, this requires sample preparation methods where TEM sample thicknesses of 5 nm can be achieved and an absence of impurity atoms is ensured. Conventional sample preparation, as it was applied in this work, does not fulfil these requests, since typical sample thicknesses are in the range of 15 to 30 nm that can be achieved with this method. Furthermore, Ar-ion sputtering is an important part of this preparation method but it introduces impurity atoms in the sample as well as their surface amorphization. A preparation method which could address the requirements is the so-called *Allied MultiPrep* polishing system which deals only with mechanical grinding and polishing, even though it is very challenging and a lot of experience is required to achieve TEM sample thicknesses in the nanometer regime. Nevertheless, the results of this work show that STEM is inevitable for the characterization of novel semiconductors as well as for the detection of atomic ordering. Finally, Bi has the ability to distribute homogeneously in dilute Bi-containing materials, when MOVPE takes place under optimized growth conditions which is very promising for the realization and fabrication of new energy efficient semiconductor devices.

CHAPTER 6

Publications

6.1 Quantification of Bi distribution in MOVPE-grown Ga(AsBi) via HAADF STEM[1]

N. Knaub, A. Beyer, T. Wegele, P. Ludewig, K. Volz, Journal of Crystal Growth **433**, 89 (2016). DOI: 10.1016/j.jcrysgro.2015.10.007.

Abstract

The importance of dilute bismide III/V semiconductors increases and their physical properties open up a wide range for applications. Therefore, high quality layers are required, what is difficult to achieve, as these alloys are highly metastable and phase separation can occur. We use HAADF (high angle annular dark field) imaging in aberration-corrected STEM (scanning transmission electron microscopy) to quantify the Bi distribution in MOVPE (metal organic vapor phase epitaxy) grown material at large length scales as well as down to the nanoscale. This is done for different Bi fractions in the solid, which are achieved by changing the MOVPE growth conditions. The composition of the Ga(AsBi) was determined by comparing frozen lattice annular dark field simulations of different Ga(AsBi) supercells with the experimental HAADF STEM images. The derived compositions are in quantitative agreement with results of HR-XRD (high resolution X-ray diffraction) and SIMS (secondary ion mass spectroscopy) of the same samples. We furthermore show a homogeneous Bi distribution for the investigated samples, which contain up to 5% Bi. By separating the group III intensities from the group V intensities in high resolution HAADF STEM images, we can investigate the group V intensity distribution only. Moreover from the statistical evaluation, we conclude that the Bi is distributed homogeneously across the group V lattice positions, confirming the excellent structural quality of the layers. This

1 Reprinted from *Journal of Crystal Growth **433** (2016) 89-96*, Copyright 2015, with permission from Elsevier.

result is also important for device applications of dilute bismide alloys, as homogeneous layers are a prerequisite for optimizing optoelectronic applications.

The Authors contribution

My contribution to this work was the execution of the STEM experiments, including sample preparation and the ADF *frozen lattice* simulations of Ga(AsBi) supercells as well as the Bi quantification of the investigated Ga(AsBi)-QWs. The growth of the Ga(AsBi) sample via MOVPE was performed by Peter Ludewig. Furthermore, Peter Ludewig carried out and evaluated the SIMS and HR-XRD measurements. Measurements of the HAADF intensity fluctuations as well as their interpretation was performed by Tatjana Wegele in close collaboration with me. Besides the interpretation of the data, all co-authors helped me to improve the first draft of the manuscript.

Journal of Crystal Growth 433 (2016) 89–96

Contents lists available at ScienceDirect

Journal of Crystal Growth

journal homepage: www.elsevier.com/locate/jcrysgro

Quantification of Bi distribution in MOVPE-grown Ga(AsBi) via HAADF STEM

Nikolai Knaub*, Andreas Beyer, Tatjana Wegele, Peter Ludewig, Kerstin Volz

Materials Science Center and Faculty of Physics, Philipps-Universität Marburg, 35032 Marburg, Germany

ARTICLE INFO

Article history:
Received 30 July 2015
Received in revised form
25 September 2015
Accepted 10 October 2015
Communicated by T.F. Kuech
Available online 23 October 2015

Keywords:
A1. Characterization
A1. Scanning transmission electron microscopy
A3. Metalorganic vapor phase epitaxy
B1. Bismuth compounds
B2. Semiconducting III–V materials

ABSTRACT

The importance of dilute bismide III/V semiconductors increases and their physical properties open up a wide range for applications. Therefore, high quality layers are required, what is difficult to achieve, as these alloys are highly metastable and phase separation can occur. We use HAADF (high angle annular dark field) imaging in aberration-corrected STEM (scanning transmission electron microscopy) to quantify the Bi distribution in MOVPE (metal organic vapor phase epitaxy) grown material at large length scales as well as down to the nanoscale. This is done for different Bi fractions in the solid, which are achieved by changing the MOVPE growth conditions. The composition of the Ga(AsBi) was determined by comparing frozen lattice annular dark field simulations of different Ga(AsBi) supercells with the experimental HAADF STEM images. The derived compositions are in quantitative agreement with results of HR-XRD (high resolution X-ray diffraction) and SIMS (secondary ion mass spectroscopy) of the same samples. We furthermore show a homogeneous Bi distribution for the investigated samples, which contain up to 5% Bi. By separating the group III intensities from the group V intensities in high resolution HAADF STEM images, we can investigate the group V intensity distribution only. Moreover from the statistical evaluation, we conclude that the Bi is distributed homogeneously across the group V lattice positions, confirming the excellent structural quality of the layers. This result is also important for device applications of dilute bismide alloys, as homogeneous layers are a prerequisite for optimizing optoelectronic applications.

1. Introduction

The ternary bismuth (Bi) containing alloy $Ga(As_{1-x}Bi_x)$ gained significant interest in the semiconductor technology in the past years. Due to the strong influence of Bi on the gallium arsenide (GaAs) band structure [1–3], Ga(AsBi) becomes interesting for photonic devices emitting in the infrared region [4–7]. Alloys with Bi fractions above 10% have been grown mainly by molecular beam epitaxy (MBE) [8,9]. High Bi concentrations are more challenging to be achieved by metal organic vapor phase epitaxy (MOVPE). The reason for this is the metastability of the alloy, which can lead to phase separation at higher growth temperatures [10], which however have to be applied during MOVPE growth due to the requirement of sufficient decomposition of the precursor chemicals [11–14]. The metastability of Ga(AsBi) originates from the highly different covalent radius of the arsenic (As) and Bi atoms, resulting in local strain when incorporating Bi in GaAs and hence a large miscibility gap. In addition, biaxial strain might influence the (meta)stability of the alloy [15].

From the technological point of view, a homogeneous, i.e. statistical, distribution of the Bi atoms is preferred but not automatically given, first of all, as phase separation due to metastability has to be considered; secondly as due to low-temperature growth other structure formation processes could occur due to the limited diffusivity of the deposited atoms on the growth surface. Investigations of the structural quality of Ga(AsBi), also in dependence on the growth conditions, are hence mandatory.

Early electron-spin resonance (ESR) studies of Bi doped GaAs (grown by the liquid encapsulation Czochralski technique from a Bi-doped melt) showed that a fraction, about 10%, of the total Bi content ($2.6 \times 10^{16}\,cm^{-3}$) occupies the gallium (Ga) site [16]. These findings underline the difficulty to grow dilute bismide alloys under thermodynamic equilibrium conditions. Later, extended X-ray absorption fine structure spectroscopy (EXAFS) studies of MBE grown Ga(AsBi) samples with Bi concentrations of 1.9% and 2.4% could verify Bi clustering in form of Bi pairs and Bi tetramers [17,18]. Investigations of MBE grown Ga(AsBi) samples, containing 2.65% Bi, by scanning transmission electron microscopy (STEM) high angle annular dark field (HAADF) in [110] direction

* Corresponding author.
E-mail address: nikolai.knaub@physik.uni-marburg.de (N. Knaub).

http://dx.doi.org/10.1016/j.jcrysgro.2015.10.007
0022-0248/

could also show hints for nanoclustering in form of Bi pairs [19]. Furthermore, STEM HAADF evaluation with additional X-ray diffraction (XRD) of MBE grown Ga(AsBi) films allowed to analyze Bi concentration profiles quantitatively [20] and derive a model for the Bi incorporation in MBE grown material. It was shown that the incorporated Bi fraction fluctuates between 1.5% and 5% over a nominal film thickness of 250 nm. These results underline the importance of in-depth structural characterization, which should go in-line with epitaxial growth. Only when the structure and the Bi depth profile of Ga(AsBi) is known, meaningful conclusions on the optoelectronic properties can be drawn and correlations between both of them as well as the growth conditions can be established. Also Bi concentration profiles of MOVPE grown GaAs/$Ga(As_{1-x}Bi_x)$ superlattices with Bi fractions of 1.4% and 2.7% were investigated via STEM quantitatively [21] in combination with high resolution X-ray diffraction (HR-XRD) rocking curves, where both methods show a highly non-uniform Bi concentration profile in growth direction.

In this report, we examine MOVPE grown samples also systematically in dependence on the Bi composition of the alloy. This can be performed down to the atomic scale by using aberration (C_S) corrected STEM [22]. The HAADF STEM signal of incoherent electron scattering in high angles (Rutherford-like scattering) is well known as the so-called Z-contrast [23,24] and can be applied rather straightforwardly to dilute bismides due to the large difference in the atomic number of Bi with respect to As and Ga. In this paper we present our results obtained using HAADF STEM measurements, performing low resolution as well as high resolution.

2. Materials and methods

The investigated sphalerite type Ga(AsBi) sample consists of five Ga(AsBi) layers with different Bi fractions and one Ga(NAsBi) layer (which will not be discussed here) grown by metal organic vapor phase epitaxy (MOVPE) on GaAs (001) substrate in a commercially available AIX 200-GFR reactor. The Ga(AsBi) quantum wells (QWs) are separated by GaAs barriers with a thickness of 100 nm. This sample was specifically grown for STEM investigation, and is schematically depicted in Fig. 1. The growth conditions of each single layer were calibrated with separately grown Ga(AsBi) multi-quantum well (MQW) structures. Intentionally no specific (composition) stacking sequence was chosen for this sample to not erroneously misinterpret any structural characteristics, which might escalate with increasing number of quantum wells, as Bi is known for segregate to the surface. Triethylgallium (TEGa) was used as Ga precursor, tertiarybutylarsine (TBAs) and trimethylbismuth (TMBi) were applied as group V precursors. The growth temperature of the Ga(AsBi) was chosen between 375 °C (topmost QW) and 400 °C (all other QWs), while the GaAs barrier growth temperature was set to 625 °C to desorb surface-segregated Bi from the growth surface prior to GaAs barrier growth. The Bi incorporation into the Ga(AsBi) alloys was adjusted by variation of TMBi/TBAs. Details of the MOVPE growth procedure of Ga(AsBi) are summarized in [13,14]. The width and nominal Bi composition of each Ga(AsBi) layer were determined (for the calibration samples) by fitting the experimental results from (004) HR-XRD $\omega/2\theta$-scans with a dynamic model. The composition was calculated assuming 0.633 nm [25] as lattice constant for GaBi. For electron microscopy investigation, a wedge-shaped TEM sample in [010] cross-section was prepared conventionally by mechanical grinding, followed by Ar-ion milling with a Gatan PIPS. STEM was performed in a double-C_S corrected JEOL JEM 2200 FS field emission transmission electron microscope operating at 200 kV. For the STEM measurements we used the HAADF method with an inner detector angle of 75 mrad and a semi angle of beam convergence of 24 mrad. To evaluate our results quantitatively, we performed HAADF-simulations of Ga(AsBi) in the frozen lattice multislice approach [26] in virtual crystal approximation (VCA) by using the STEMSIM software-package [27]. Since normalizing of the intensities is necessary for a quantitative interpretation of the measurements, we normalized our background-corrected HAADF images to the incident beam by using a similar method as it is described in [28], where the beam's current is measured with the CCD camera. Additional secondary ion mass spectroscopy (SIMS) measurements were carried out on the multi-layer sample, first of all to control the XRD data, secondly to also confirm that the transfer from the calibration sample to the multi-layer sample resulted in the intended Bi fraction in the individual layers.

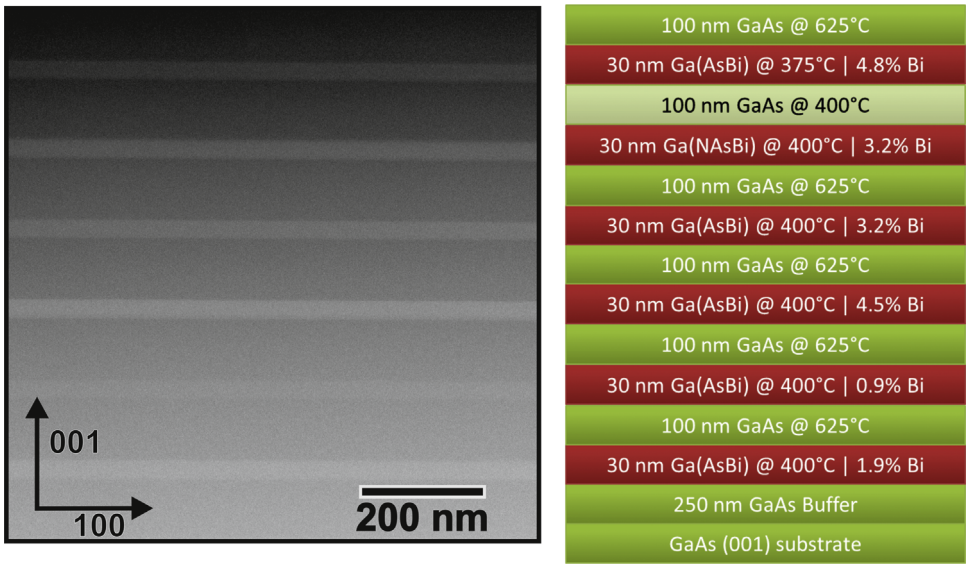

Fig. 1. STEM HAADF micrograph overview of the investigated sample, prepared in [010] zone axis. One can see clearly the intense Ga(AsBi) QW with different Bi fractions. The schematic on the right displays the investigated sample with growth temperature, nominal layer width and Bi fraction obtained from HR-XRD measurements.

3. Results and discussion

The paper is organized as follows: first we show that we can quantitatively determine the Bi fraction in the Ga(AsBi) QWs from STEM HAADF measurements in combination with electron scattering simulations. These results are in agreement with HR-XRD and SIMS results, also giving confidence to the unknown parameters (especially for dilute bismide materials) that go into the evaluation of these two techniques, which are frequently used in the growth community. Second, the intensity fluctuation in low resolution measurements will be evaluated to address any Bi composition fluctuations in the alloy, also in dependence on composition and growth temperature. Finally these results will be compared to a statistical evaluation of atomic resolution STEM HAADF measurements.

3.1. Ga(AsBi) composition quantification

A HAADF overview of the Ga(AsBi) sample containing QWs grown at different temperatures as well as containing different Bi fractions and a schematic of the intended sample structure are depicted in Fig. 1. The Bi containing layers can be clearly seen from their bright contrast with respect to the GaAs barriers. The given values for bulk thickness and Bi fraction, shown in schematic, are obtained from HR-XRD measurements of the reference MQW structures. There are several uncertainties in Bi fractions from HR-XRD measurements as well as SIMS measurements. First of all, in HR-XRD one measures a tetragonally distorted lattice constant. The input parameters which influence the evaluation in XRD are the material constants of the binary GaBi, i.e. the lattice constant and the elastic constants, of which theoretical values exist only [25], as this alloy does not exist in nature. Small deviations of these values could result in large errors of the calculated Bi fraction. Moreover the validity of the simple linear interpolation of lattice constants of mixed alloys between the lattice constant of the two binary endpoints (Vegard's law) has not been proven yet for dilute bismide III/V semiconductors. Furthermore, it is assumed that Bi incorporates on the group V lattice positions only. If this is not true, again a shift in lattice constant and hence an error in the evaluated Bi fraction follows. Quantitative SIMS measurements of the composition might also be error-prone, as Ga(AsBi) standards do not exist and have to be produced by ion implanting Bi in GaAs. Also the presence of antisites would cause some error to the composition. Therefore we quantified the Bi composition of the different alloys by means of STEM HAADF.

In the following part, we will explain the evaluation steps which were performed to determine the mean Bi fraction from the measured HAADF intensity for each Ga(AsBi) layer.

Since every layer was evaluated in the same manner, we will explain the procedure by taking the example of one Ga(AsBi) layer only. Fig. 2a depicts a low resolution HAADF measurement of the topmost Ga(AsBi) layer with a nominal Bi fraction of 4.8%. Here one can see the intense Bi containing layer embedded in GaAs barriers, which serve as reference regions for our TEM sample

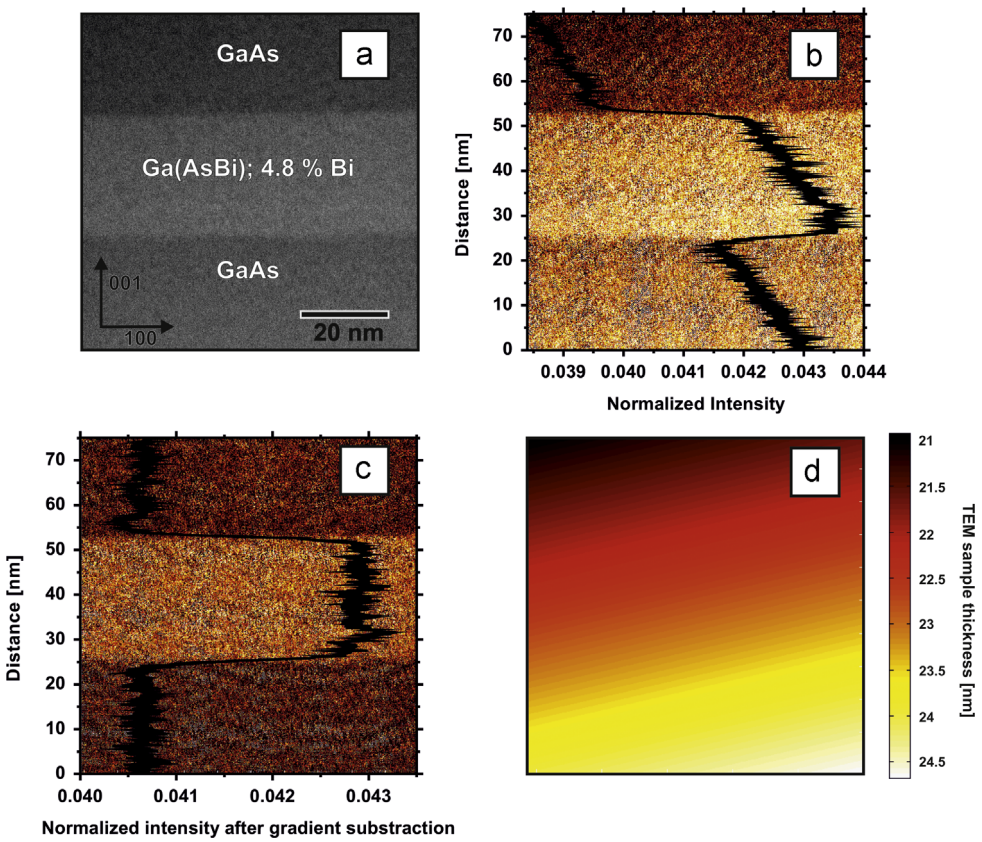

Fig. 2. (a) STEM HAADF low resolution measurement of the topmost Ga(AsBi) QW with a nominal Bi fraction of 4.8%. The measured layer width of the layer is about 28 nm. (b) False color image of the low resolution measurement depicted in (a), normalized to the impinging electron probe (after background subtraction). The inset diagram is an integrated intensity plot over the measurement distance. It reflects the thickness originating from sample preparation. (c) Same false color image as in(b) but after thickness gradient correction. The inset diagram depicts a mean normalized intensity value of 4.3% of the electron probe's intensity for the Ga(AsBi) layer. (d) Interpolated GaAs thickness gradient (false color plot) of the measurement displayed in (a). The scale bar displays the corresponding TEM sample thickness in nm. Here, the determination yields a mean thickness value of 22.7 nm for the Ga(AsBi) QW. (For interpretation of the references to color in this figure legend, the reader is referred to the web version of this article.)

thickness estimation. In the next step, we normalized our images-after correcting them for the background intensity-to the impinging beam's current by using a similar procedure as described in [28]. Thus we obtain a normalized image with absolute intensity values, as depicted in Fig. 2b. The inset graph is an integrated line profile over the whole image and it describes clearly a thickness gradient, which is a side effect of the conventional sample preparation. We performed a gradient correction, where the GaAs intensity from the barriers only was taken into account and a two dimensional surface interpolation as well as a thickness gradient subtraction of the original image was carried out. Both, the result of the gradient corrected image and the integrated line profile (inset) are shown in Fig. 2c. The line profile now clearly displays a constant GaAs intensity level and a higher Ga(AsBi) layer intensity. It is remarkable that the interfaces of the Ga(AsBi) layer with the GaAs barriers are abrupt, which is a consequence of the high growth temperature of the GaAs barrier [14]. If the barriers are grown at the same temperatures as the QWs, there is a significant Bi-segregation into the GaAs barriers observable [13] and the interfaces are not nearly as sharp. From the line profile, which is shown in the inset, we determine the QW layer thickness to 28 nm, what is in a good agreement with the layer thickness of the calibration samples deduced from HR-XRD. The thickness gradient correction provides additionally an interpolated GaAs signal, from which we can calculate the TEM sample thickness, which is needed as input for quantification of the Bi content. The STEMSIM package was used in the frozen lattice multislice approach [26] to simulate the GaAs HAADF intensity in dependence on the TEM sample thickness. Comparing the experimental GaAs intensity with the simulated GaAs intensity yields a thickness value for each pixel (as described in [29]) and thus allows us to create a thickness map at low resolution, as depicted in Fig. 2d. Thus we get a mean sample thickness of approximately 22.7 ± 0.6 nm at the position of the Ga(AsBi) QW for this particular sample. The normalized HAADF Ga(AsBi) intensity in this image was 4.3% of the impinging beam. Further frozen lattice multislice simulations of Ga(AsBi) supercells with Bi concentrations of 1%, 2%, 3% and 5% were carried out to determine the Bi fraction from this data. As a result of the simulation we get the HAADF intensity dependence on the Bi concentration for different TEM sample thicknesses, depicted in Fig. 3a there is an estimated thickness of 22.7 nm. The black points are the calculated values, which were interpolated assuming a linear dependence of the scattered intensity of the Bi fraction. At this point it is worth noting that the distribution of doping atoms in the direction of the electron beam can severely influence the measured HAADF intensity [30]. In our case the deviation of some calculated data points (e.g. 2% Bi) from the linear interpolation can be explained by the crystal model used for the simulation: the Bi was distributed statistically on the group V positions. As the TEM sample is very thin, the Bi in the crystal models might be at different positions (depths) in the TEM sample for each calculated data point. This results in different intensities. We estimate the difference of the scattered intensity for a given Bi concentration, where the Bi is placed at different positions in the crystal model to about 1% of the value. This is included as “error bars” in the figure. However, it should be emphasized that this is not the error of the method, but rather a feature which also occurs in experiment [31]. Comparing the simulated data with the experimental intensity yields a mean Bi fraction of 4.6%, what is in good agreement with the reference value of 4.8% from HR-XRD. It also should be noted at this point that there is no “simple”- Z^2-dependence of the scattered intensity, which is often used to calculate compositions in a hand-waiving way. The calculated intensities rather follow a $Z^{1.6}$-dependence, which confirms the $Z^{1.7}$ proportionality suggested in [32]. This is depicted in Fig. 3b, where the mean Ga(AsBi) intensity is normalized to the GaAs intensity

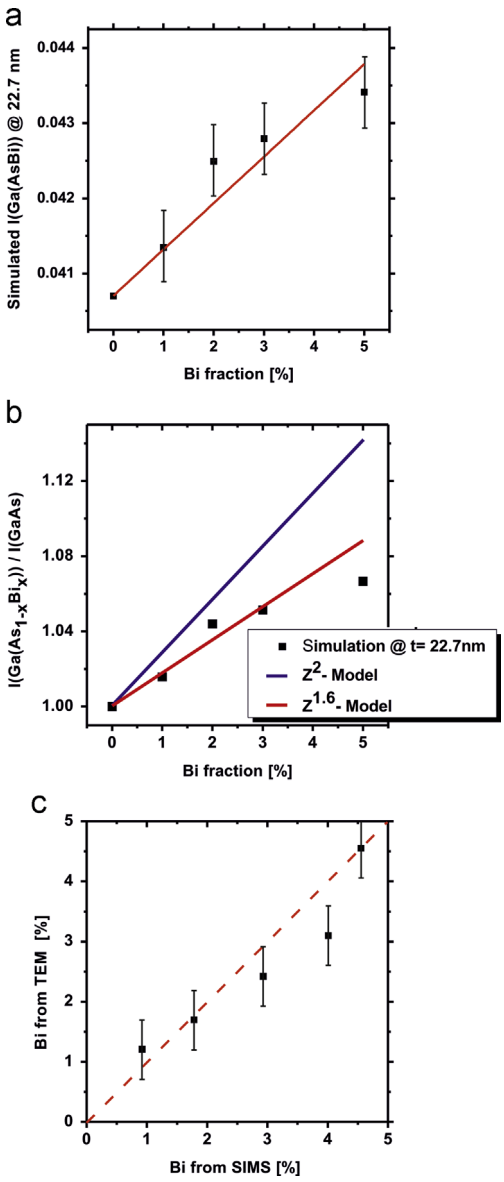

Fig. 3. (a) Dependency of image simulation with frozen lattice approach obtained Ga(AsBi) HAADF intensity on the Bi fraction for a constant TEM sample thickness of 22.7 nm. The red line is a linear fit to the calculated values. Thus it is possible to derive a mean Bi fraction from the measured intensity. (b) Dependency of Ga($As_{1-x}Bi_x$) HAADF STEM intensity normalized on GaAs intensity on the Bi fraction for a Z^2 (red line)- and a $Z^{1.6}$- proportionality (blue line) of the intensity. The black squares are the simulated values from (a). It can be seen that the simulation follows the $Z^{1.6}$- proportionality instead of Z^2. (c) Comparison of the Bi fraction determined by our HAADF measurements and the Bi fraction determined by SIMS in percent. The dashed line is a guide to the eye, which represents an exact agreement of both methods. (For interpretation of the references to color in this figure legend, the reader is referred to the web version of this article.)

and is plotted versus the Bi fraction for the different Z-dependencies mentioned above. Therefore a Bi fraction estimation by assuming a simple Z^2 proportionality of the measured intensity would lead to significantly wrong Bi fractions in experimental investigated Ga(AsBi) layers, for example, the error would be already a factor of two for a Bi concentration of 5%. It should also be noted that comparison to calculations using a VCA crystal model are only justified if the inner angle of the HAADF detector is set to rather large values as in this study. Setting the inner angle to lower values can result in a significant local strain distribution to the material's intensity and would have to be taken into account

by relaxing the atom positions in the crystal model as shown in [29] for Ga(NAs). In a further study we will show, how this can influence image intensity also at an atomic scale.

The procedure just described was applied to the other Ga(AsBi) layers. The results are depicted in Fig. 3c. Here the Bi fraction from quantitative STEM HAADF is plotted versus the estimated Bi fraction obtained by SIMS measurements from the multi-layer sample. The dashed line corresponds to equality between SIMS and quantitative STEM HAADF. The agreement between the quantitative STEM HAADF evaluation and the SIMS data (as well as the HR-XRD data, which is incorporated in the schematic of Fig. 1, but not shown here anymore) shows that there is excellent agreement between the three methods.

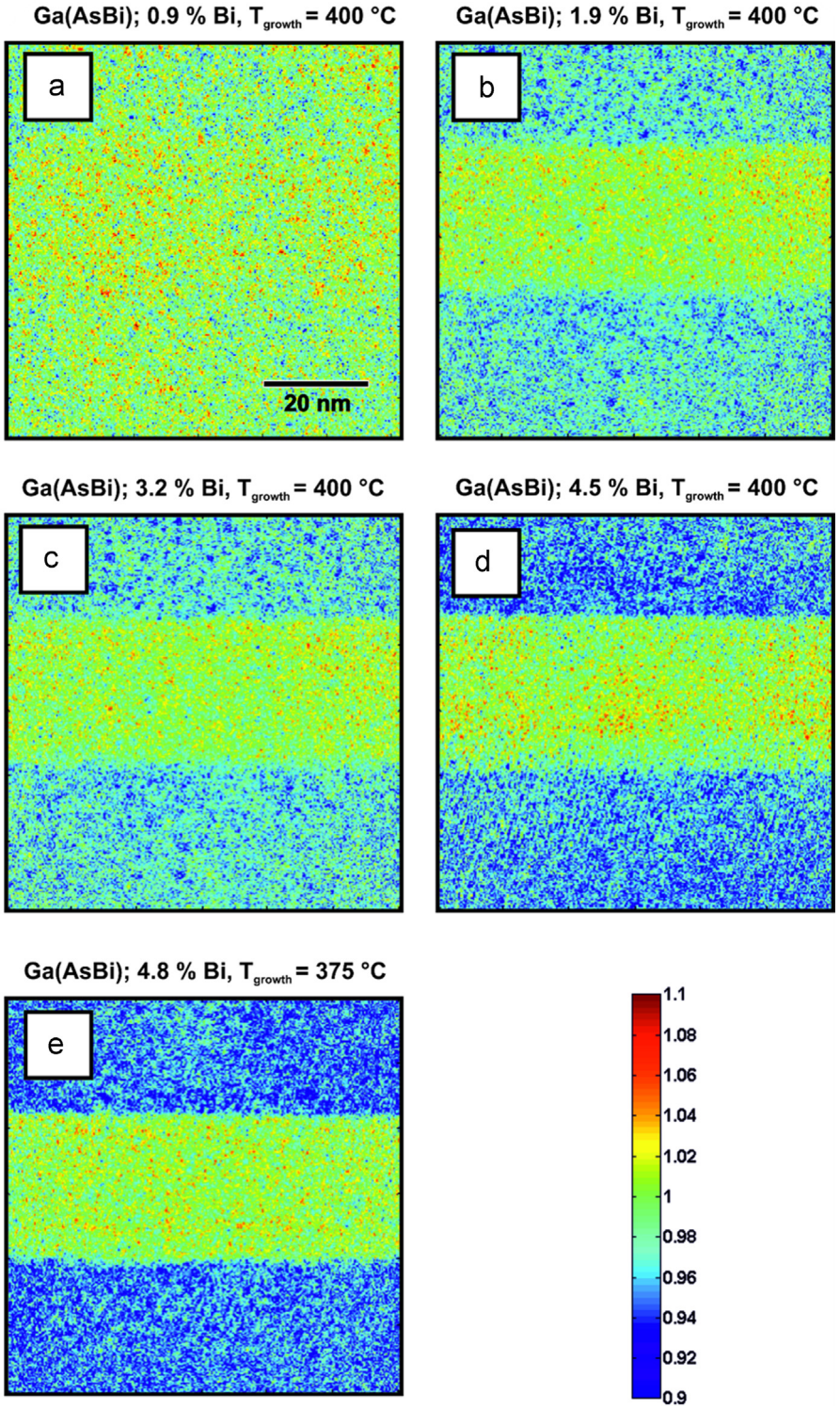

Fig. 4. (a)–(e) Determination of the QWs intensity fluctuation with increasing Bi fraction. The false color plots display the relative standard deviation σ_{rel} of each Ga(AsBi) layer's mean intensity, which serves as a goodness for the layers' homogeneity. One can see almost the same homogeneity for all investigated Ga(AsBi) QWs. (For interpretation of the references to color in this figure legend, the reader is referred to the web version of this article.)

This not only confirms that STEM HAADF is a good method to address the composition quantitatively-what might become important if there are nanoscale fluctuations of the compositions-but also indicates that the potential sources of errors of HR-XRD and SIMS measurements-enumerated above-can be excluded for this material.

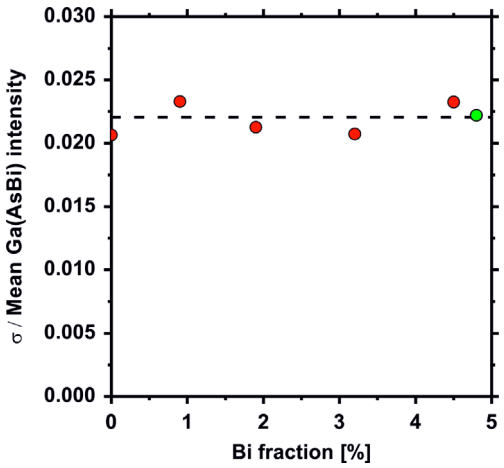

Fig. 5. Comparison of the relative standard deviation σ_{rel} values from Fig. 4 with the Bi fraction in the QWs. The dashed line is a guide to the eye, which shows that all investigated layers are equally homogeneous. The value of the Ga(AsBi) QW grown at 375 °C is green colored. (For interpretation of the references to color in this figure legend, the reader is referred to the web version of this article.)

3.2. Composition homogeneity by low resolution HAADF measurements

Since dilute Bi III/V alloys are metastable and are grown at low temperatures, phase separation into Bi-rich and Bi-poor regions could occur. Therefore, we also analyzed the homogeneity of the investigated Ga(AsBi) layers. Thereto, each pixel intensity in the Ga(AsBi) structure was normalized to the mean intensity of the same QW, which was determined over an area of 2000 nm². As a result we create false color images of each Ga(AsBi) layer (Fig. 4), where the intensity deviation from the mean intensity value is visible, which represents a goodness for the homogeneity. Fig. 4 shows that all Ga(AsBi) layers we investigated exhibit a maximum fluctuation in intensity of only about 2.5% from their mean intensity value. These findings are summarized in Fig. 5, where the standard deviation σ_{rel} of the mean intensity normalized to the mean intensity is plotted in dependence on the Bi fraction in the layers. It is remarkable that all Ga(AsBi) layers have the same low relative standard deviation of intensity irrespective of their composition. Their homogeneity is same as for GaAs, i.e. about 2%, and can be explained by experimental effects due to measuring process in STEM, such as scan noise, specimen drift and TEM sample thickness fluctuation. It should be noted that in order to derive statistical information for the barrier, the GaAs intensity was normalized to the mean GaAs intensity. This means that there are no detectable composition fluctuations in the Ga(AsBi) material in the 10 nm range and above. This is a very important result for the correlation to optical data of the samples, as the length scale, where composition fluctuations would alter for example PL (photoluminescence) characteristics is typically in the range of 10 nm. Smaller scale compositions fluctuations cannot be excluded

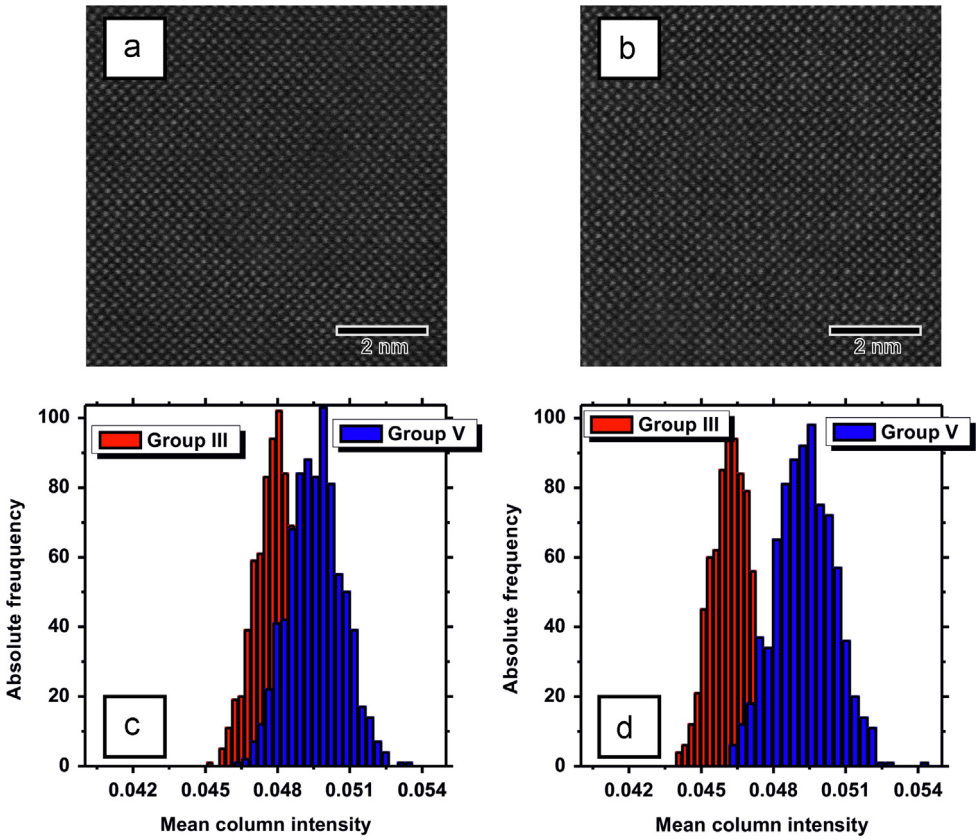

Fig. 6. STEM HAADF high resolution micrographs of the Ga(AsBi) QWs with a nominal Bi fraction of 0.9% (a) and 4.8% (b). The displayed histograms (c) and (d) depict the group III (red) and group V (blue) column intensity distribution corresponding to the high resolution measurements (a) and (b). One can see that the group III and group V intensities separation is more pronounced with increasing Bi fraction. (For interpretation of the references to color in this figure legend, the reader is referred to the web version of this article.)

as the TEM samples shown here had all thicknesses around 25 nm. Hence, extreme short range composition fluctuations could be averaged by projection effects and will be a topic of a separate paper. In the following we will present a method to derive composition fluctuations also from high resolution STEM measurements to address composition fluctuations at an atomic scale.

3.3. Composition homogeneity by high resolution HAADF measurements

Further investigations at an atomic scale are necessary to decide if Bi clustering is present or not in the nanometer range. Therefore we performed additional high resolution HAADF measurements of the Ga(AsBi) layers. Intentionally thick sample regions were chosen to be able to derive statistical data from the high resolution measurements. Even for the sample with the lowest Bi content, each group V column should contain at least one Bi atom, which leads to a required sample thickness of around 25 nm. All high resolution measurements were normalized to the incident beam in the same way as the low resolution measurements in Section 3.1. Fig. 6a and b depicts exemplarily two high resolution HAADF measurements of Ga(AsBi) layers, containing a nominal Bi fraction of 0.9% and 4.8%. The group III and group V sublattices were separated in the images. For the sublattice separation, column peak positions had to be found first. This was carried out with the help of the peak pairs software [33]. Afterwards we separated the group III from the group V sublattice and integrated the pixel intensities of each column within a radius which was defined as one third of the nearest neighbor distance. We have chosen this integration radius because of a reasonable signal to noise ratio without introducing too much crosstalk between the atomic columns. The respective column intensity distribution is plotted in histograms for each sublattice. The intensity distributions depicted in Fig. 6c and d correspond to the high resolution measurements (Fig. 6a and b). The bin size of each histogram was calculated by using the Freedman–Diaconis rule [34]:

$$\text{Bin size} = 2 * \text{IQR}(x) n^{-\frac{1}{3}} \quad (1)$$

where IQR(x) is the interquartile range of the intensity distribution x and n is the number of the intensities within the distribution x.

The histogram depiction of the intensities is helpful for a further analysis. A first comparison of the histograms shows that the intensities of group III and group V sublattices separate the more from each other, the more Bi is incorporated. This seems to be obvious and expectable, since the measured HAADF intensity is proportional to the atomic number $Z^{1.6}$. Furthermore, a more exact analysis of group V column intensities allows to decide whether a specific Bi clustering is present or not. Therefore, the group V histograms were fitted by assuming a Gaussian distribution, which provide us the distributions' mean value μ and their standard deviation σ. The fitted group V column intensities from Fig. 6c and d are depicted in Fig. 7a and b respectively. In addition, also the σ, 2σ and 3σ confidence interval are colored in green, red and yellow. The intensity distribution follows the Gaussian distribution fit (dashed curve) in both cases, which means that no specific Bi clustering could be identified and the Bi is homogenously distributed over the measured region. Otherwise we would expect a significantly larger number of higher group V column intensities in the histogram which would not follow the Gaussian distribution.

Since the standard deviation σ of the Gaussian distribution is a goodness for group V intensity distribution and therefore for the Ga(AsBi) layer quality, we compared each standard deviation of the Ga(AsBi) high resolution measurements containing different Bi fractions. The result is depicted in Fig. 7c, where the standard deviation is plotted versus the Bi fraction. As for the low resolution case (Fig. 5), we see the same standard deviation for each group V

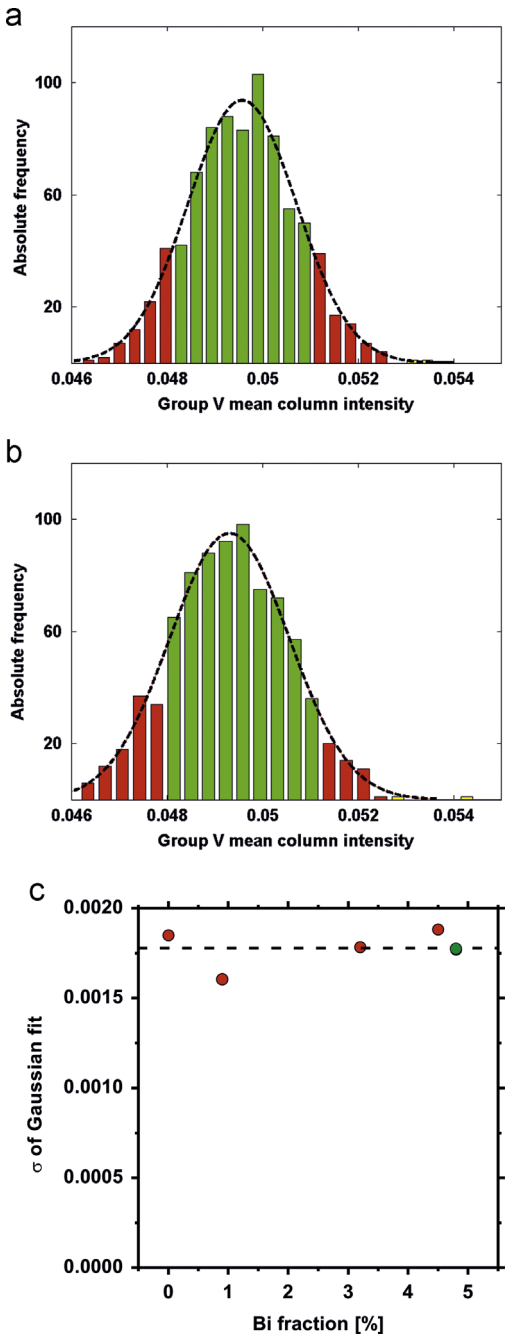

Fig. 7. (a, b) Histogram plot of the group V intensities. The dashed curve corresponds to a Gaussian distribution fit. The colored regions represent the standard deviation σ of the dashed line, where green is the σ, red the 2σ and yellow the 3σ confidence interval. Both histograms show a Gaussian distribution of the group V intensities and therefore Bi clustering cannot be found in the investigated Ga(AsBi) QWs. The diagram in (c) shows the determined standard deviations σ of the group V column intensity distribution measured for each Ga(AsBi) QW. The green colored value is again from the QW grown at 375 °C. The dashed line serves as a guide to the eye and shows an almost equal group V intensity distribution. (For interpretation of the references to color in this figure legend,the reader is referred to the web version of this article.)

intensity distribution (dashed line) in the high resolution measurements. The standard deviation has also the same value for the GaAs. From the structural point of view this means that the Bi atoms are homogeneously (statistically) distributed and all grown Ga(AsBi) layers exhibit a good quality, irrespective of the Bi concentration up to 5% and the growth temperature between 375 °C and 400 °C.

If possible Bi clustering in the nearest neighbor size range should be detected, much thinner TEM samples (5 nm) are required and results will be presented elsewhere.

4. Conclusions

We have shown by means of HAADF measurements how the obtained data can be used, in order to analyze the Bi fraction of dilute Bi material Ga(AsBi) quantitatively. There is excellent agreement of the Bi-composition derived from STEM with the one from HR-XRD and SIMS, making this method very useful to also address composition fluctuations quantitatively. Hence, the Ga(AsBi) layers' homogeneity was analyzed. As a result we find a homogeneous intensity distribution in the Ga(AsBi) layer, meaning that no Bi clustering can be detected for samples containing up to 5% Bi and grown at 375 °C and 400 °C, respectively.

Furthermore, high resolution measurements of the Ga(AsBi) layers were performed for analyzing the occurrence of possible Bi clustering. The group V column intensity histogram could be described well by a Gaussian distribution, proving that the group V intensities of all investigated Ga(AsBi) layers exhibit the same standard deviation σ. Hence, also from high resolution measurements, no Bi clustering becomes evident pointing towards an excellent quality of the metastable Ga(AsBi) material grown by MOVPE. These findings also prove that correlation of optical data to composition from HR-XRD is justified, as no Bi-composition fluctuations at length scales, which would influence optical characteristics, takes place.

Acknowledgments

This work was supported by the German Science Foundation (DFG) in the framework of the Research Training Group "Functionalization of Semiconductors" (GRK 1782) and the European Union Project BIANCHO (FP7-257974).

References

[1] S. Francoeur, M.J. Seong, A. Mascarenhas, S. Tixier, M. Adamcyk, T. Tiedje, Band gap of $GaAs_{1-x}Bi_x$, $0 < x < 3.6\%$, Appl. Phys. Lett. 82 (2003) 3874, http://dx.doi.org/10.1063/1.1581983.

[2] K. Alberi, O.D. Dubon, W. Walukiewicz, K.M. Yu, K. Bertulis, A. Krotkus., Valence band anticrossing in $GaBi_xAs_{1-x}$, Appl. Phys. Lett. 91 (2007) 051909, http://dx.doi.org/10.1063/1.2768312.

[3] S. Imhof, C. Bückers, A. Thränhardt, J. Hader, J.V. Moloney, S.W. Koch, Microscopic theory of the optical properties of Ga(AsBi)/GaAs quantum wells, Semicond. Sci. Technol. 23 (2008) 125009, http://dx.doi.org/10.1088/0268-1242/23/12/125009.

[4] C.A. Broderick, M. Usman, S.J. Sweeney, E.P. O'Reilly, Band engineering in dilute nitride and bismide semiconductor lasers, Semicond. Sci. Technol. 27 (2012) 094011, http://dx.doi.org/10.1088/0268-1242/27/9/094011.

[5] S. Imhof, C. Wagner, A. Thränhardt, A. Chernikov, M. Koch, N.S. Köster, S. Chatterjee, S.W. Koch, O. Rubel, X. Lu, S.R. Johnson, D.A. Beaton, T. Tiedje, Luminescence dynamics in Ga(AsBi), Appl. Phys. Lett. 98 (2011) 161104, http://dx.doi.org/10.1063/1.3580773.

[6] P. Ludewig, N. Knaub, N. Hossein, S. Reinhard, L. Nattermann, I.P. Marko, S.R. Jin, K. Hild, S. Chatterjee, W. Stolz, S.J. Sweeney, K. Volz, Electrical injection Ga(AsBi)/(AlGa)As single quantum well laser, Appl. Phys. Lett. 102 (24) (2013) 242115, http://dx.doi.org/10.1063/1.4811736.

[7] T. Fuyuki, K. Yoshida, R. Yoshioka, M. Yoshimoto, Electrically pumped room-temperature operation of $GaAs_{1-x}Bi_x$ laser diodes with low-temperature dependence of oscillation wavelength, Appl. Phys. Express 7 (2014) 082101, http://dx.doi.org/10.7567/APEX.7.082101.

[8] X. Lu, D.A. Beaton, R.B. Lewis, T. Tiedje, M.B. Whitwick, Effect of molecular beam epitaxy growth conditions on the Bi content of $GaAs_{1-x}Bi_x$, Appl. Phys. Lett. 92 (2008) 192110, http://dx.doi.org/10.1063/1.2918844.

[9] A.J. Ptak, R. France, D. Beaton, K. Alberi, J. Simon, A. Mascarenhas, C.-S. Jiang, Kinetically limited growth of GaAsBi by molecular-beam epitaxy, J. Cryst. Growth 338 (2012) 107–110, http://dx.doi.org/10.1016/j.jcrysgro.2011.10.040.

[10] E. Sterzer, N. Knaub, P. Ludewig, R. Straubinger, A. Beyer, K. Volz, Investigation of the microstructure of metallic droplets on Ga(AsBi)/GaAs, J. Cryst. Growth 408 (2014) 71–77, http://dx.doi.org/10.1016/j.jcrysgro.2014.09.006.

[11] K. Forghani, A. Anand, L.J. Mawst, T.F. Kuech, Low temperature growth of $GaAs_{1-y}Bi_y$ epitaxial layers, J. Cryst. Growth 380 (2013) 23–27, http://dx.doi.org/10.1016/j.jcrysgro.2013.05.033.

[12] K. Forghani, Y. Guan, A.W. Wood, A. Anand, S.E. Babcock, L.J. Mawst, T.F. Kuech, Self-limiting growth when using trimethyl bismuth (TMBi) in the metal-organic vapor phase epitaxy (MOVPE) of $GaAs_{1-y}Bi_y$, J. Cryst. Growth 395 (2014) 38–45, http://dx.doi.org/10.1016/j.jcrysgro.2014.03.014.

[13] P. Ludewig, N. Knaub, W. Stolz, K. Volz, MOVPE growth of Ga(AsBi)/GaAs multi quantum well structures, J. Cryst. Growth 370 (2013) 186–190, http://dx.doi.org/10.1016/j.jcrysgro.2012.07.002.

[14] P. Ludewig, Z. Bushell, L. Nattermann, N. Knaub, W. Stolz, K. Volz, Growth of Ga(AsBi) on GaAs by continuous flow MOVPE, J. Cryst. Growth 396 (2014) 95–99, http://dx.doi.org/10.1016/j.jcrysgro.2014.03.041.

[15] H. Jacobsen, B. Puchala, T.F. Kuech, D. Morgan, Ab initio study of the strain dependent thermodynamics of Bi doping in GaAs, Phys. Rev. B 86 (2012) 085207, http://dx.doi.org/10.1103/PhysRevB.86.085207.

[16] M. Kunzer, W. Jost, U. Kaufmann, H.M. Hobgood, R.N. Thomas, Identification of the Bi_{Ga} heteroantisite defect in GaAs:Bi, Phys. Rev. B 48 (1993) 4437, http://dx.doi.org/10.1103/PhysRevB.48.4437.

[17] G. Ciatto, E.C. Young, F. Glas, J. Chen, R. Alonso Mori, T. Tiedje, Spatial correlation between Bi atoms in dilute $GaAs_{1-x}Bi_x$: from random distribution to Bi pairing and clustering, Phys. Rev. B 78 (2008) 035325, http://dx.doi.org/10.1103/PhysRevB.78.035325.

[18] G. Ciatto, M. Thomasset, F. Glas, X. Lu, T. Tiedje, Formation and vanishing of short range ordering in $GaAs_{1-x}Bi_x$ thin films, Phys. Rev. B 82 (2010) 201304, http://dx.doi.org/10.1103/PhysRevB.82.201304 (R).

[19] D.L. Sales, E. Guerrero, J.F. Rodrigo, P.L. Galindo, A. Yáñez, M. Shafi, A. Khatab, R. H. Mari, M. Henini, S. Novikov, M.F. Chisholm, S.I. Molina, Distribution of bismuth atoms in epitaxial GaAsBi, Appl. Phys. Lett. 98 (2011) 101902, http://dx.doi.org/10.1063/1.3562376.

[20] A.W. Wood, S.E. Babcock, J. Li, A.S. Brown, Increased bismuth concentration in MBE $GaAs_{1-x}Bi_x$ films by oscillating III/V flux ratio during growth, J. Vac. Sci. Technol. A 33 (2015) 031506, http://dx.doi.org/10.1116/1.4916575.

[21] A.W. Wood, Y. Guan, K. Forghani, A. Anand, T.F. Kuech, S.E. Babckock, Unexpected bismuth concentration profiles in metal-organic vapor phase epitaxy-grown $Ga(As_{1-x}Bi_x)$/GaAs superlattices revealed by Z-contrast scanning transmission electron microscopy imaging, Appl. Phys. Lett. Mater. 3 (2015) 036108, http://dx.doi.org/10.1088/1742-6596/522/1/012017.

[22] M. Haider, H. Rose, S. Uhlemann, E. Schwan, B. Kabius, K. Urban, A spherical-aberration-corrected 200 kV transmission electron microscope, Ultramicroscopy 75 (1) (1998) 53–60, http://dx.doi.org/10.1063/1.4915301.

[23] S.J. Pennycook, Z-contrast stem for materials science, Ultramicroscopy 30 (1–2) (1989) 58–69, http://dx.doi.org/10.1016/0304-3991(89)90173-3.

[24] S.J. Pennycook, D.E. Jesson, High-resolution Z-contrast imaging of crystals, Ultramicroscopy 37 (1–4) (1991) 14–38, http://dx.doi.org/10.1016/0304-3991(91)90004-P.

[25] S. Tixier, M. Adamcyk, T. Tiedje, S. Francoeur, A. Mascarenhas, P. Wei, F. Schiettekatte, Molecular beam epitaxy growth of $GaAs_{1-x}Bi_x$, Appl. Phys. Lett. 82 (14) (2003), http://dx.doi.org/10.1063/1.1565499 2245-2247.

[26] E.J. Kirkland, Advanced Computing in Electron Microscopy, Plenum Press, New York (1998) http://dx.doi.org/10.1007/978-1-4419-6533-2.

[27] A. Rosenauer, M. Schowalter, STEMSIM- a new software tool for simulation of STEM HAADF Z-contrast imaging, in: A.G. Cullis, P.A. Midgley (Eds.), Microscopy of Semiconducting Materials (Proceedings in Physics), 120, Springer, Netherlands, 2007, pp. 169–172.

[28] D.S. He, Z.Y. Li, A practical approach to quantify the ADF detector in STEM, J. Phys.: Conf. 522 (2014) 012017, http://dx.doi.org/10.1088/1742-6596/522/1/012017.

[29] T. Grieb, K. Müller, R. Fritz, M. Schowalter, N. Neugebohrn, N. Knaub, K. Volz, A. Rosenauer, Determination of the chemical composition of GaNAs using STEM HAADF imaging and STEM strain state analysis, Ultramicroscopy 117 (2012) 15–23, http://dx.doi.org/10.1016/j.ultramic.2012.03.014.

[30] P.M. Voyles, J.L. Grazul, D.A. Muller, Imaging individual atoms inside crystals with ADF-STEM, Ultramicroscopy 96 (2003) 251–273, http://dx.doi.org/10.1016/S0304-3991(03)00092-5.

[31] P.M. Voyles, D.A. Muller, E.J. Kirkland, Depth-dependent imaging of individual dopant atoms in silicon, Microsc. Microanal. 10 (02) (2004) 291–300, http://dx.doi.org/10.1017/S1431927604040012.

[32] O.L. Krivanek, M.F. Chisholm, V. Nicolosi, T.M. Pennycook, G.J. Corbin, N. Dellby, M.F. Murfitt, C.S. Own, Z.S. Szilagyi, M.P. Oxley, S.T. Pantelides, S.J. Pennycook, Atom-by-atom structural and chemical analysis by annular dark-field electron microscopy, Nature 464 (2010) 571–574, http://dx.doi.org/10.1038/nature08879.

[33] P.L. Galindo, S. Kret, A.M. Sanchez, J.-Y. Laval, A. Yáñez, J. Pizarro, E. Guerrero, T. Ben, S.I. Molina, The Peak pairs algorithm for strain mapping from HRTEM images, Ultramicroscopy 107 (12) (2007) 1186–1193, http://dx.doi.org/10.1016/j.ultramic.2007.01.019.

[34] D. Freedman, P. Diaconis, On the histogram as a density estimator: L_2 theory, Probab. Theory Relat. Fields 57 (4) (1981) 453–476, http://dx.doi.org/10.1007/BF01025868.

6.2 Local Bi ordering in MOVPE grown Ga(As,Bi) by high resolution scanning transmission electron microscopy

N. Knaub, A. Beyer, P. Rosenow, K. Jandieri, P. Ludewig, L. Bannow, S.W. Koch, R. Tonner, K. Volz, *submitted (2016)* in Journal of Physics D: Applied Phyics

Abstract

The incorporation of Bismuth (Bi) into GaAs allows the fabrications of new optoelectronic devices, e.g. lasers and solar cells due to the strong influence of the Bi on the band gap. In such devices, not only the amount of Bi incorporated but also its lateral distribution within the crystal has a significant influence on the optic properties. We use aberration corrected high angle annular dark field imaging to investigate the distribution of Bi atoms in Ga(As,Bi) samples on an atomic scale. With the help of statistical evaluations, we show that the Bi atoms are not randomly distributed. Utilizing a Hough transformation, we detect Bi ordering along the <100> and <101> crystallographic directions with chain lengths of up to 5 atoms. Electronic structure calculations reveal the chain-like arrangement of Bi is energetically favoorable compared to isolated Bi atoms due to the stabilization by stronger bonds to shared Ga atoms and to in-plane Ga atoms.

The Authors contribution

My contribution to this work was the execution of the STEM experiments including the sample preparation, the *frozen lattice* simulations and the evaluation procedure. The growth of the sample via MOVPE was carried out by Peter Ludewig, while VFF relaxation of the Ga(AsBi) supercell was performed by Kakhaber Jandieri. Furthermore, Andreas Beyer helped me with the interpretation of the gained results. This work was in close collaboration with Phil Rosenow from the chemistry department of the Philipps Universität Marburg. He performed electronic structure calculations of Ga-Bi bond strengths in Ga(AsBi), whose results are published in this work. All co-authors also helped to interpret the data and to improve the first draft of the manuscript.

Local Bi ordering in MOVPE grown Ga(As,Bi) by high resolution scanning transmission electron microscopy

Nikolai Knaub[1], Andreas Beyer[1], Phil Rosenow[2], Kakhaber Jandieri[1], Peter Ludewig[1], Lars Bannow[1], Stephan W. Koch[1], Ralf Tonner[2] and Kerstin Volz[1]

[1]*Materials Science Center and Faculty of Physics, Philipps-Universität Marburg, 35032 Marburg, Germany*

[2]*Materials Science Center and Faculty of Chemistry, Philipps-Universität Marburg, 35032 Marburg, Germany*

*andreas.beyer@physik.uni-marburg.de

Abstract

The incorporation of Bismuth (Bi) into GaAs allows the fabrications of new optoelectronic devices, e. g. lasers and solar cells due to the strong influence of the Bi on the band gap. In such devices, not only the amount of Bi incorporated but also its lateral distribution within the crystal has a significant influence on the optic properties. We use aberration corrected high angle annular dark field imaging to investigate the distribution of Bi atoms in Ga(As,Bi) samples on an atomic scale. With the help of statistical evaluations, we show that the Bi atoms are not randomly distributed. Utilizing a Hough transformation, we detect Bi ordering along the <100> and <101> crystallographic directions with chain lengths of up to 5 atoms. Electronic structure calculations reveal the chain-like arrangement of Bi is energetically favorable compared to isolated Bi atoms due to the stabilization by stronger bonds to shared Ga atoms and to in-plane Ga atoms.

Introduction

Bismuth (Bi) containing III-V semiconductors, e.g. Ga(As,Bi), have raised significant attention in recent years due to the unique band structure formation in these alloys, which also allows for the realization of novel devices. It is well known that even the incorporation of dilute amounts of Bi in GaAs leads to a strong reduction of the band gap of up to 84 meV per % Bi[1,2] and shifts the spin-orbit split-off band towards lower energies. The great potential of dilute Bi alloys has also been underlined by the realization of first Bi containing lasers, emitting in the infrared region[3–6].

Besides the huge effect on the III-V semiconductors' band structure, the large covalent radius of the Bi atoms is a challenging property for the incorporation of significant amounts of Bi into the host material (e.g. GaAs). While $Ga(As_{1-x}Bi_x)$ layers with Bi fractions above x = 0.1 have been realized using molecular beam epitaxy (MBE)[7,8], the growth of $Ga(As_{1-x}Bi_x)$

by metalorganic vapor phase epitaxy (MOVPE) is more challenging since it has to take place at higher temperatures (compared to MBE growth) to ensure a sufficient decomposition of the precursor chemicals. Nevertheless, high quality $Ga(As_{1-x}Bi_x)$ layers with Bi fractions up to x = 0.07 have been realized using MOVPE under optimized growth conditions[9–12].

Earlier reports showed the occurrence of $CuPt_B$ atomic ordering in MBE grown $Ga(As_{1-x}Bi_x)$ layers with x = 0.1[13] and with lower Bi fractions of x = 0.042[14], respectively, by means of scanning transmission electron microscopy (STEM) and conventional TEM. Whereas quantitative [110] high resolution (HR) STEM investigations of MBE grown $Ga(As_{1-x}Bi_x)$ samples (x = 0.0265)[15] provided hints for nanoclustering in form of Bi pairs, recent (S)TEM investigations of MBE grown $Ga(As_{1-x}Bi_x)$ layers[16] ($0.015 \leq x \leq 0.029$), have shown the ordering of Bi atoms in triple-period (TP) sequences (TP-A and TP-B). Other (S)TEM measurements[17,18] described the evidence of Bi clustering in MBE grown $Ga(As_{1-x}Bi_x)$ ($x \leq 0.047$) samples after annealing processes up to temperatures of T_a = 800 °C. Furthermore, Mingjang et al.[18] proposed a model which describes the formation of Bi-rich Ga(As,Bi) clusters of zinc-blende structure and the phase transformation to rhombohedral Bi clusters. Moreover, Punkkinen et al.[19] addressed the formation of Bi clusters in $Ga(As_{1-x}Bi_x)$ crystal models ($0.0078 \leq x \leq 0.063$) theoretically using density functional theory (DFT) calculations. It was shown that Ga vacancies in the alloy are the most probable reason for the occurrence of Bi clustering.

Recent results on the optoelectronic properties of MOVPE grown $Ga(As_{1-x}Bi_x)$/GaAs heterostructures ($0.029 \leq x \leq 0.045$) show that there is a non-monotonous dependence of the energy scale of disorder and thus a variation of the hole effective mass on the Bi content[20]. These results have been obtained by evaluating the temperature-dependent photoluminescence (PL) of the samples. These findings show very well the significant impact of compositional disorder in Ga(As,Bi)/GaAs alloys on the band structure and therefore on its optoelectronic properties. Moreover, recent theoretical studies highlight the influence of the Bi-arrangement on the band gap of the material[21].

In the present paper we examine MOVPE grown material and correlate structural properties to theoretical predictions on the stability of certain Bi clusters. We introduce chain-like ordering of Bi atoms in different crystallographic directions on the nanometer scale, which can be detected by high resolution (HR) STEM high angle annular dark field (HAADF) investigations combined with an image evaluation using the Hough-transform[22,23]. This allows – especially in comparison with HAADF STEM simulations using crystal models where the Bi atoms have been placed randomly in the GaAs matrix - to have an objective criterion to decide whether ordering or clustering is present or not. The samples used for this study were grown by MOVPE under optimized conditions[11], where metallic Bi droplets do not occur on the sample's surface. In a previous study, we examined the average composition of the Quantum Wells (QW) and the composition homogeneity on length scales above 10 nm by HAADF STEM imaging[24]. It was shown that on these long length scales the Bi is

distributed homogeneously. By means of the detailed statistical evaluation applied in the present study, as well as with an enhanced image acquisition method (improved signal to noise) we can, however, show that there is a deviation from statistical distribution on much shorter length scales (in the nanometer range) than previously investigated. In combination with electron structure calculation, especially the bond strength calculation of Ga-Bi bonds in Ga(As,Bi), we will support the HR HAADF imaging results.

Methods

The Ga(As,Bi)/GaAs sample studied in this work was grown by MOVPE on GaAs (001) substrates in a commercially available AIX 200-GFR reactor. Triethylgallium (TEGa) was used as Ga precursor together with tertiarybutylarsine (TBAs) and trimethylbismuth (TMBi) as group V precursors, respectively. The growth temperature (T_G) range of the Ga(As,Bi) QWs was set between 375 °C and 400 °C, whereas the GaAs barriers' T_G was set to 625 °C. By doing this, a sufficient desorption of the surface segregated Bi of the previously grown Ga(As,Bi) QW is ensured before the GaAs barrier is grown. At this point we refer to a more detailed description of the MOVPE growth procedure of Ga(As,Bi), which is summarized thoroughly by Ludewig et al.[9,11].

The sample used for the present study consists of five $Ga(As_{1-x}Bi_x)$ QWs with different Bi fractions x ($0.009 \leq x \leq 0.048$), separated by GaAs barriers with a nominal thickness of 100 nm. The sample was especially deposited for STEM analysis and the composition of each QW was calibrated with test samples prior to the growth of the TEM sample. The nominal Bi fraction and layer width of each Ga(As,Bi) QW was determined by high resolution X-ray diffraction (HR-XRD), where experimental (004) $\omega/2\theta$-scans were fitted with a dynamical scattering model. Since there is no proven existence of GaBi as a binary III-V semiconductor, we assumed a the value of 0.633 nm, which was obtained from theoretical predictions[25,26], as lattice constant for GaBi. Thus it is possible to estimate the composition in Ga(As,Bi) via Vegard's rule. In a previous study it has been shown that the expected Bi concentrations match well with the actual ones derived from quantitative HAADF STEM analysis[24].

HR STEM investigations were performed in a double-C_S corrected JEOL JEM 2200 FS field emission transmission electron microscope (TEM) operating at 200 kV. A wedge-shaped TEM sample in [010] cross section was prepared conventionally by mechanical grinding, followed by Ar-ion milling with a Gatan PIPS. The measurement itself was carried out in the HAADF-mode, which is also known as Z-contrast[27] mode due to the Rutherford-like distribution of the scattered electrons. Hence, the detected intensity is proportional to $Z^{1.6\text{-}2}$. For the HAADF intensity measurement, we used an annular detector with an inner detector angle of 73 mrad. The electron beam had a semi angle of convergence of 24 mrad.

The evaluated HR images are not one single measurement but the result of seven measurements of the same sample position. An acquisition time of 3.4 s for one single measurement (7.9 nm × 7.9 nm) was set to acquire the seven images in a row. A non-rigid image alignment was carried out afterwards by using the free available Smart Align[28] tool for MATLAB. Hence, we obtain an image with an improved signal to noise ratio as well as less scanning artefacts (figure 1a), since sample drift and scan distortions do not have such a large effect on the measurement compared to an image with a significantly longer acquisition time. To compare the experimental results with simulation and thus for a quantitative interpretation, intensity normalization is necessary. Therefore we normalize our HR images to the impinging beam's current as described by He et al.[29].

HAADF image simulation was carried out in the frozen lattice approach[30] by using the STEMSIM software-package[31]. We performed the simulation on a Valence Force Field (VFF) relaxed $Ga(As_{1-x}Bi_x)$ supercell with the highest Bi content also deposited in experiment (x = 0.048). The Bi atoms were placed in this supercell randomly.

Computational Details

Electronic structure calculations were performed using the *Vienna ab initio simulation package* (VASP)[32–35] 5.3.5 with the TB09 (mBJLDA)[36,37] functional based on structures optimized with the PBE-D3(BJ) functional.[38–41] A plane wave basis with a cut-off energy of 510 eV was used in conjunction with the projector augmented wave method.[42,43] Sampling of the k-space was performed using a Γ-centered Monkhorst-Pack grid[44] with three points per direction for a $3 \times 3 \times 3$ supercell. The electronic energy was converged to 10^{-5} eV. The bonding properties were analyzed with the crystal orbital Hamilton population (COHP) method as implemented in Lobster 2.0.0[45–47] with the default Koga local basis set.[48,49]

Results and Discussion

This paper is organized as follows: in the first part we will explain the atom columns' intensity evaluation of HR HAADF measurements by means of statistics. This routine is also applied to the simulated image. In the second part we will present the Bi ordering detection procedure using the so-called Hough transform[22,23]. Finally, a detailed analysis of the detected Bi ordering in experimental images as well as in the simulation will be summarized and the results will be compared. It is concluded that the Bi atoms in the experimental sample are distributed non-statistically on very short length scales in the nanometer range. The ordering predominantly takes place along the <100> and <101> directions.

Intensity distribution of HR HAADF measurements

In the following, the procedure of extracting the intensity distribution of a HR HAADF measurement, which includes the intensities of 1494 atom columns, is exemplarily described. The procedure was performed in the same manner for all other HR images.

Figure 1a depicts a HR HAADF image of a Ga($As_{0.952}Bi_{0.048}$) QW. After measurement the group III and group V sublattices were separated to investigate their intensities separately. This procedure as well as the sample thickness determination was performed as explained in our earlier studies[24]. For the chosen example we obtain a sample thickness of 28 ± 0.5 nm and an intensity integration width of 120 pm (15 pixels) for each atom column. This value corresponds to the mean full width at half maximum (FWHM) of the group III and group V atom columns, which was determined before by applying a two dimensional Gaussian fit to the atom column´s intensity profile. The intensities of the atom columns are then plotted in a histogram, which describes the intensity distribution of each sublattice, as shown in figure 1b. For the determinationof the bin width, the Freedman-Diaconis rule[50] was chosen.

The histogram representation of the sublattice intensities allows a determination of the mean intensity value μ and the standard deviation σ, which represents the scatter of the mean column intensities and thus the broadness of the distribution. We highlighted the position of μ_{III} and μ_V by dashed lines in figure 1b. For this example we find μ_{III}= (5.95± 0.12)% and μ_V= (6.60± 0.25)%, respectively. The standard deviations from the mean values underline the evidence of a narrow group III intensity distribution, which corresponds to a pure mean Ga intensity and a broader group V intensity distribution, which is extended to higher intensities due to the different amount of Bi per group V atom column.

For a quantitative interpretation of our experimental results, we carried out the same evaluation for a HAADF simulation using a Ga($As_{0.952}Bi_{0.048}$) supercell with the size of 5.7 nm × 5.7 nm in x-y plane and 24.4 nm in z direction, consisting of 3.2×10^4 atoms. The cell was relaxed by VFF and simulated in the frozen lattice approach. The same microscope parameters as for the experiment were chosen for the simulation. Since the effect of a finite source size[51] is not regarded in the coherent simulation, experimental image and simulation have to be matched. Therefore we determined the mean atom column width in the experiment by measuring the standard deviation σ_{2D} of a two dimensional Gaussian fit. This process step yields a mean σ_{2D} of six pixels (47 pm). This σ_{2D} value was used to apply a Gaussian broadening to the atom columns in the simulated image afterwards. The final result is depicted in figure 2a. Afterwards, the same evaluation steps were performed for the simulated image as described for the experimental case. This provides the results, which are shown in figure 2b, where the intensity distribution of 613 atom columns is shown. The figure shows a narrow group III (Ga) intensity distribution with μ_{III}= (5.51± 0.08)%. The group V intensity distribution is significantly broader with μ_V= (6.47± 0.37)%, which originates from the incorporation of the Bi atoms on group V sites as it has been emphasized in the experimental intensity distribution. A comparison with the experiment proves good

agreement between both results, although the standard deviation from μ_V is slightly higher in the theoretical case than in the experimental one, what is very surprising. We conclude that this may be an indication for a local non-statistical distribution of Bi atoms in the experimental case and the result of a statistical group V column intensity distribution in the theoretical case. This will be discussed afterwards. It, however, is also obvious that the Ga intensity distribution is 1.5 times broader in the experimental case than in the theoretical one and has a lower mean value μ_{III}. The smaller mean value can be explained by the slightly different crystal thicknesses ($\Delta t \approx 4$ nm) used for experiment and simulation. Therefore also the relative frequencies (numbers of occurrence) of the single column intensities are smaller in the experiment compared to simulation. Of course, the simulation result (figure 2b) provides always a perfect image without any experimental noise due to the scanning process (figure 1a). This leads to the difference in Ga intensity distribution between simulation and experiment. The simulation yields a Gaussian like Ga intensity distribution instead of a single peak due to the VFF relaxation of the supercell and the frozen lattice formalism used for the simulation. The former introduces static atomic displacements of Ga atoms (due to different atomic parameters of Bi) and therefore slightly different Ga column positions compared to a perfect crystal, while the frozen lattice formalism introduces lattice vibrations and therefore an additional thermal scattering background. This reproduces the experiment, which has been conducted at room temperature, best. The similarity of group V intensities between simulation and experiment is remarkable. Also the larger width of the distribution by alloying with Bi is reflected in the theoretical image.

A huge advantage of the simulation is that we know the distribution of the Bi atoms in the supercell. Thus we can quantify the integer amount of Bi atoms per group V column and the corresponding group V column intensity. The yellow, green and red boxes in figure 2b define regions of group V column intensities, which contain one Bi atom, two Bi atoms and three Bi atoms, respectively. The group V intensities below the yellow box do not contain any Bi atom and thus can be referred to as pure As columns. The highest intensity bar (not colour coded) corresponds to a group V column containing four Bi atoms. An unexpected result is that there is no overlap between the intensity regions but a discrete division between the intensities of the atom columns with different Bi content. This outcome expresses a greater impact of Bi on the atom columns intensities than intensity fluctuations originating due to lattice vibrations and static atomic displacements, as it is reflected in the Ga intensity distribution of the simulated image. In contrast to the theoretical results, we do not expect a discrete division of the group V intensities depending on the amount of Bi atoms per atom column in the experimental image, because the experimental Ga intensity distribution provides a 1.5 times larger standard deviation (due to experimental noise) than the theoretical one. This of course becomes more crucial when the TEM sample thickness increases. The comparison between the theoretical and experimental results will form the basis for the evaluation part, where the detection of Bi chains in the experimental HR HAADF images takes place.

Detection of Bi chains via Hough transform

In the previous part, we have determined the range of column intensities, which correspond to group V columns containing three Bi atoms. We use this result as a starting point for our method to detect Bi clustering in our measurements. Judging from the simulation, we know that most of the group V columns contain at least one Bi atom (for x = 0.048). Since we are investigating Bi ordering, it is worth to investigate group V column intensities with a higher (three and more) number of Bi atoms. Therefore, we select experimental intensities above the mean column intensity μ_V=7% and plot the corresponding group V column positions. The result is a group V intensity map for the most intense group V columns, displayed in figure 3a. The color code corresponds to the mean column intensities. From this image it can be qualitatively seen that the Bi atoms tend to order in chain-like features in <010> and <101>-directions.

The quantitative detection method for the atomic ordering itself is based on the so-called Hough transform[22], which allows to identify straight lines in an image. The Hough transform is defined as:

$$\rho = \cos\theta \times x_i + \sin\theta \times y_i \quad (1),$$

where x_i and y_i are the (x,y) position of each image pixel i, ρ is the distance of the (x,y) position from the origin and θ is the angle between the distance line |ρ| and the x axis.

For the Bi ordering detection, we make use of the center positions (peak positions) of the group V columns shown in figure 3a as (x,y) points. With this set of points we create the Hough space by using a MATLAB routine. The resulting ρ-θ diagram is depicted in figure 4, where the blue squares represent the detected local maxima, i.e. the Hough-peaks.

By selecting a certain angular range, namely θ= {0°; 90°; ±45°}, chains along specific crystallographic direction can be detected. A linear transformation of (1) to:

$$y = -\left(\frac{\cos\theta}{\sin\theta}\right) \times x + \left(\frac{\rho}{\sin\theta}\right) \quad (2)$$

allows for the back transformation of the Hough peaks and thus the detection of straight lines in the x-y plane, which correspond directly to <100> (figure 3b) and <101> directions (figure 3c).

We performed this detection method on four $Ga(As_{1-x}Bi_x)$ layers with different Bi content x and counted the number and length of chains in every single HR HAADF image. Afterwards the number of occurrence of each chain length was detected and normalized by the amount of investigated group V atomic columns. This allows us to compare the data from every HR HAADF image independently from the number of group V atomic columns in the image. The result is a relative number of occurrence versus chain length plot (Figure 5) for different Bi contents (color coded squares) and different directions, i.e. <100> (fig. 5a) and <101> (fig.

5b). It can be clearly seen that the Bi chain length as well as the amount of chains increases with increasing Bi fraction. We also compared our results from experiment with simulation, to decide whether this chain-like arrangement corresponds to a random distribution of Bi atoms present in the experimental samples. The data points of the simulation are represented by grey bars in figure 5. There is a significant difference between simulation and experiment for the same Bi fraction x = 0.048. The simulation provides about 7.5 % of group V columns, which have a chain length of one (which means no chain) and only a small amount of chains with two or three atoms in a chain. Whereas the amount of chains with a length of two and more atoms is significantly higher in the experiment than in simulation. Moreover, the highest Bi fraction (black squares) provides consistently a higher amount of Bi pairs than chains with length of one in all four investigated directions, which is definitely not the case in the simulation and which shows once more the ordering of Bi atoms on a local scale (in the nanometer range). Consequently, in the experimental images are less single Bi atoms. This proves that Bi ordering in form of chains/clusters along <100> and <101> directions takes place in MOVPE grown Ga(AsBi) layers. This is true even under optimized growth conditions where Bi seems to be distributed homogeneously on length scales above 10 nm. The ordering along <100> directions has to be distinguished from the CuPt-ordering, because Ga atoms are surrounded by Bi pairs or tetramers (described in the part below) and thus it is rather a clustering effect than an ordering on {111} planes like in the CuPt case. However, the detected Bi ordering along <101> directions, especially the detection of parallel lines next to each other in fig. 3c, is directly referring to CuPt ordering. Since the sample was prepared in [010] zone axis, {111} lattice planes proceed in the electron beam's direction and therefore become "invisible" in the projected image.

To understand this why the observed Bi chains are formed during the growth, electronic structure calculations will be performed in the following.

Computational results on bond strength in Bi clusters

The bond strength of Ga-Bi bonds in $Ga(As_{1-x}Bi_x)$ has been studied for dispersed and clustered arrangements of Bi atoms in a $3 \times 3 \times 3$ supercell with two, three and four As atoms replaced by Bi, corresponding to x = 0.03125, 0.04688 and 0.0625, respectively. For the dispersed arrangements, the Bi atoms were placed at maximum distance to each other, while being bonded to a shared Ga atom in the clustered case. The differences in total energy are negligible for different configurations at a given concentration[21]. The integrated COHP up to the Fermi energy (ICOHP) is used as an indicator for bond strength (Figure 6) and shows significant differences in bonding.[45–47]

The limiting cases for the bond strength of Ga to Group V-atoms As and Bi are given by binary compounds GaAs (ICOHP(Ga-As) = -4.508 eV/bond) and hypothetical GaBi (ICOHP(Ga-Bi) = -3.892 eV/bond). It is found that all ICOHP-values in Ga(AsBi) are close to the values in binary GaAs (-4.438 to -4.554 eV/bond) and much stronger than in GaBi. The bond strength

for dispersed Bi atoms slightly increases with the Bi concentration (x = 3.125/4.688/6.25%; ICOHP = -4.438/-4.440/-4.446 eV/bond) and is generally smaller compared to the clustered arrangements of the same Bi concentration in Fig. 6b-d.

For clustered Bi atoms, bonds to Ga within the same plane as the shared one parallel to the Bi atoms (*in plane*, ICOHP = -4.489/-4.490/-4.492 eV/bond) are stronger than bonds to Ga atoms in other crystallographic planes (*out of plane*, ICOHP = -4.439/-4.438 eV/bond).

For the Bi pair (Fig. 6b), the bond to the shared Ga atom (-4.449 eV/bond) is rather weak but still stronger compared to the dispersed case (-4.438 eV/bond). The Bi triangle (Fig. 6c) shows a slight increase in Ga-Bi bond strength (-4.485 eV/bond) compared to the dispersed case (-4.440 eV/bond). The strongest Ga-Bi bond studied here can be found for the Bi tetrahedron with a bond strength of -4.554 eV/bond, exceeding the Ga-As bond strength in binary GaAs. For this cluster, all exterior Ga-Bi bonds show the typical strength of bonds to in-plane Ga atoms.

These findings support the HR HAADF based observation of clustering being favored over random dispersion. Specifically, the paired arrangement and the tetrahedral cluster correspond to a two atom chain in the <100> direction and two interconnected chains, respectively. While a preference of chains over other clustered configurations cannot be inferred from the COHP calculations so far, the chemical bonding perspective indicates clusters of Bi atoms in Ga(As,Bi) being stabilized by stronger bonds to shared Ga atoms and to in-plane Ga atoms compared to isolated Bi atoms.

Conclusions

The actual distribution of Bi atoms within the crystal influences the optical properties of Ga(BiAs) layers. We use atomic resolution HAADF imaging to reveal a non statistical distribution of Bi. Via a statistical evaluation utilizing the Hough transform, we find chain-like ordering of Bi atoms along the <100> and <101> crystallographic directions. The formation of these structures can be explained by electronic structure calculations, which show the energetical favorability of these configurations over isolated Bi atoms.

Acknowledgement

Support of the German Science Foundation in the framework of GRK 1782 (“Functionalization of Semiconductors”) is gratefully acknowledged. PR and RT acknowledge computational resources from the HRZ Marburg, CSC Frankfurt and HLR Stuttgart.

References

[1] Alberi K, Wu J, Walukiewicz W, Yu K M, Dubon O D, Watkins S, Wang C, Liu X, Cho Y-J and Furdyna J 2007 Valence-band anticrossing in mismatched III-V semiconductor alloys *Phys. Rev. B* **75** 045203

[2] Francoeur S, Seong M-J, Mascarenhas A, Tixier S, Adamcyk M and Tiedje T 2003 Band gap of GaAs[sub 1−x]Bi[sub x], 0<x<3.6% *Appl. Phys. Lett.* **82** 3874

[3] Ludewig P, Knaub N, Hossain N, Reinhard S, Nattermann L, Marko I P, Jin S R, Hild K, Chatterjee S, Stolz W, Sweeney S J and Volz K 2013 Electrical injection Ga(AsBi)/(AlGa)As single quantum well laser *Appl. Phys. Lett.* **102** 242115

[4] Marko I P, Ludewig P, Bushell Z L, Jin S R, Hild K, Batool Z, Reinhard S, Nattermann L, Stolz W, Volz K and Sweeney S J 2014 Physical properties and optimization of GaBiAs/(Al)GaAs based near-infrared laser diodes grown by MOVPE with up to 4.4% Bi *J. Phys. D. Appl. Phys.* **47** 345103

[5] Fuyuki T, Yoshioka R, Yoshida K and Yoshimoto M 2013 Long-wavelength emission in photo-pumped GaAs1−xBix laser with low temperature dependence of lasing wavelength *Appl. Phys. Lett.* **103** 202105

[6] Lewis R B, Beaton D A, Lu X and Tiedje T 2009 GaAsBi Light Emitting Diodes *J. Cryst. Growth* **311** 1872–5

[7] Lu X, Beaton D A, Lewis R B, Tiedje T and Whitwick M B 2008 Effect of molecular beam epitaxy growth conditions on the Bi content of GaAs1-x Bix *Appl. Phys. Lett.* **92**

[8] Ptak A J, France R, Beaton D A, Alberi K, Simon J, Mascarenhas A and Jiang C S 2012 Kinetically limited growth of GaAsBi by molecular-beam epitaxy *J. Cryst. Growth* **338** 107–10

[9] Ludewig P, Knaub N, Stolz W and Volz K 2013 MOVPE growth of Ga(AsBi)/GaAs multi quantum well structures *J. Cryst. Growth* **370** 186–90

[10] Forghani K, Anand A, Mawst L J and Kuech T F 2013 Low temperature growth of GaAs1−yBiy epitaxial layers *J. Cryst. Growth* **380** 23–7

[11] Ludewig P, Bushell Z L, Nattermann L, Knaub N, Stolz W and Volz K 2014 Growth of Ga(AsBi) on GaAs by continuous flow MOVPE *J. Cryst. Growth* **396** 95–9

[12] Forghani K, Guan Y, Wood A W, Anand A, Babcock S E, Mawst L J and Kuech T F 2014 Self-limiting growth when using trimethyl bismuth (TMBi) in the metal-organic vapor phase epitaxy (MOVPE) of GaAs 1 À y Bi y *J. Cryst. Growth* **395** 38–45

[13] Norman A G, France R and Ptak A J 2011 Atomic ordering and phase separation in MBE GaAs[sub 1−x]Bi[sub x] *J. Vac. Sci. Technol. B Microelectron. Nanom. Struct.* **29** 03C121

[14] Reyes D F, Bastiman F, Hunter C J, Sales D L, Sanchez A M, David J P R and González D 2014 Bismuth incorporation and the role of ordering in GaAsBi/GaAs structures. *Nanoscale Res. Lett.* **9** 23

[15] Sales D L, Guerrero E, Rodrigo J F, Galindo P L, Yáñez A, Shafi M, Khatab A, Mari R H, Henini M, Novikov S V., Chisholm M F and Molina S I 2011 Distribution of bismuth atoms in epitaxial GaAsBi *Appl. Phys. Lett.* **98** 101902

[16] Wu M, Luna E, Puustinen J, Guina M and Trampert A 2014 Observation of atomic

ordering of triple-period-A and -B type in GaAsBi *Appl. Phys. Lett.* **105** 041602

[17] Puustinen J, Wu M, Luna E, Schramm a., Laukkanen P, Laitinen M, Sajavaara T and Guina M 2013 Variation of lattice constant and cluster formation in GaAsBi *J. Appl. Phys.* **114**

[18] Wu M, Luna E, Puustinen J, Guina M and Trampert A 2014 Formation and phase transformation of Bi-containing QD-like clusters in annealed GaAsBi. *Nanotechnology* **25** 205605

[19] Punkkinen M P J, Laukkanen P, Kuzmin M, Levämäki H, Lång J, Tuominen M, Yasir M, Dahl J, Lu S, Delczeg-Czirjak E K, Vitos L and Kokko K 2014 Does Bi form clusters in GaAs 1 − x Bi x alloys? *Semicond. Sci. Technol.* **29** 115007

[20] Shakfa M K, Jandieri K, Wiemer M, Ludewig P, Volz K, Stolz W, Baranovskii S D and Koch M 2015 Energy scale of compositional disorder in Ga(AsBi) *J. Phys. D. Appl. Phys.* **48** 425101

[21] Bannow L C, Rubel O, Rosenow P, Badescu S C, Hader J, Moloney J V., Tonner R and Koch S W 2016 Configuration Dependence of Band Gap Narrowing and Localization in Dilute GaAs_{1-x} Bi_x Alloys

[22] HOUGH P V C 1962 Method and means for recognizing complex patterns *U.S. Patent, no.3069654*

[23] Hart P E 2009 How the Hough transform was invented [DSP History] *IEEE Signal Process. Mag.* **26** 18–22

[24] Knaub N, Beyer A, Wegele T, Ludewig P and Volz K 2016 Quantification of Bi distribution in MOVPE-grown Ga(AsBi) via HAADF STEM *J. Cryst. Growth* **433** 89–96

[25] Tixier S, Adamcyk M, Tiedje T, Francoeur S, Mascarenhas A, Wei P and Schiettekatte F 2003 Molecular beam epitaxy growth of GaAs[sub 1 - x]Bi[sub x] *Appl. Phys. Lett.* **82** 2245–7

[26] Wang S Q and Ye H Q 2003 First-principles study on elastic properties and phase stability of III–V compounds *Phys. status solidi* **240** 45–54

[27] Pennycook S and Jesson D 1991 High-resolution Z-contrast imaging of crystals *Ultramicroscopy* **37** 14–38

[28] Jones L, Yang H, Pennycook T J, Marshall M S J, Aert S Van, Browning N D, Castell M R and Nellist P D 2015 Smart Align — a new tool for robust non-rigid registration of scanning microscope data *Adv. Struct. Chem. Imaging* 1–16

[29] He D S and Li Z Y 2014 A practical approach to quantify the ADF detector in STEM *J. Phys. Conf. Ser.* **522** 012017

[30] Kirkland E J 2010 *Advanced Computing in Electron Microscopy* (Boston, MA: Springer US)

[31] Rosenauer A and Schowalter M 2008 STEMSIM - A New Software Tool for Simulation of STEM *Microsc. Semicond. Mater. 2007* **120** 170–2

[32] Kresse G and Hafner J 1993 Ab initio molecular dynamics for liquid metals *Phys. Rev. B* **47** 558–61

[33] Kresse G and Hafner J 1994 Ab initio molecular-dynamics simulation of the liquid-

metal-amorphous-semiconductor transition in germanium *Phys. Rev. B* **49** 14251

[34] Kresse G and Furthmüller J 1996 Efficiency of ab-initio total energy calculations for metals and semiconductors using a plane-wave basis set *Comp. Mat. Sci.* **6** 15

[35] Kresse G and Furthmüller J 1996 Efficient iterative schemes for ab initio total-energy calculations using a plane-wave basis set *Phys. Rev. B* **54** 11169

[36] Becke A D and Johnson E R 2006 A simple effective potential for exchange *J. Chem. Phys.* **124** 221101

[37] Tran F and Blaha P 2009 Accurate Band Gaps of Semiconductors and Insulators with a Semilocal Exchange-Correlation Potential *Phys. Rev. Lett.* **102** 226401

[38] Perdew J P, Burke K and Ernzerhof M 1996 Generalized gradient approxiamtion made simple *Phys. Rev. Lett.* **77** 3865

[39] Perdew J P, Burke K and Ernzerhof M 1997 Erratum: Generalized gradient approxiamtion made simple *Phys. Rev. Lett.* **78** 1396

[40] Grimme S, Antony J, Ehrlich S and Krieg H 2010 A consistent and accurate ab initio parametrization of density functional dispersion correction (DFT-D) for the 94 elements H-Pu *J. Chem. Phys.* **132** 154104

[41] Grimme S, Ehrlich S and Goerigk L 2011 Effect of the Damping Funtion in Dispersion Corrected Density Functional Theory *J. Comput. Chem.* **32** 1456–65

[42] Blöchl P E 1994 Projector augmented-wave method *Phys. Rev. B* **50** 17953–79

[43] Kresse G and Joubert D 1999 From ultrasoft pseudopotentials to the projector augmented-wave method *Phys. Rev. B* **59** 1758

[44] Monkhorst H J and Pack J D 1976 Special points for Brillouin-zone integrations *Phys. Rev. B* **13** 5188

[45] Dronskowski R and Blöchl P E 1993 Crystal Orbital Hamilton Populations (COHP). Energy-Resolved Visualization of Chemical Bonding in Solids Based on Density-Functional Calculations *J. Phys. Chem* **97** 8617–24

[46] Deringer V L, Tchougr A L and Dronskowski R 2011 Crystal Orbital Hamilton Population (COHP) Analysis As Projected from Plane-Wave Basis Sets *J. Phys. Chem. A* **115** 5461–6

[47] Maintz S, Deringer V L, Tchougréeff A L and Dronskowski R 2013 Analytic Projection From Plane-Wave and PAW Wavefunctions and Application to Chemical-Bonding Analysis in Solids *J. Comp. Chem.* **34** 2557–67

[48] Koga T, Kanayama K, Watanabe S and Thakkar A J 1998 Analytical Hartree-Fock Wave Functions Subject to Cusp and Asymptotic Constraints : He to Xe , Li+ to Cs+ , H- to I- *ICQC* **71** 491–7

[49] Koga T, Kanayama K, Watanabe T, Imai T and Thakkar A J 2000 Analytical Hartree-Fock wave functions for the atoms Cs to Lr *Theor. Chem. Acc.* **104** 411–3

[50] Freedman D and Diaconis P 1981 On the histogram as a density estimator:L 2 theory *Zeitschrift für Wahrscheinlichkeitstheorie und Verwandte Gebiete* **57** 453–76

[51] Dwyer C, Erni R and Etheridge J 2008 Method to measure spatial coherence of subangstrom electron beams *Appl. Phys. Lett.* **93** 021115

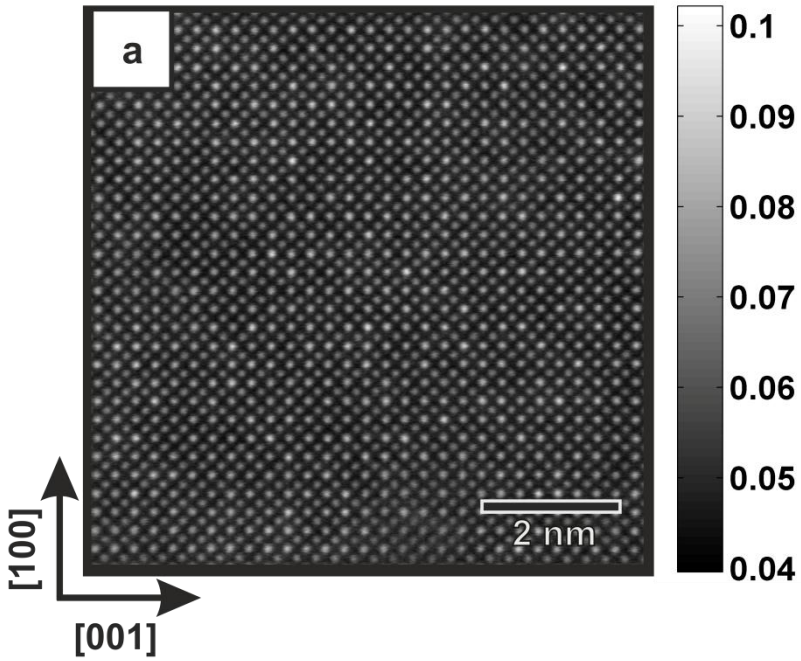

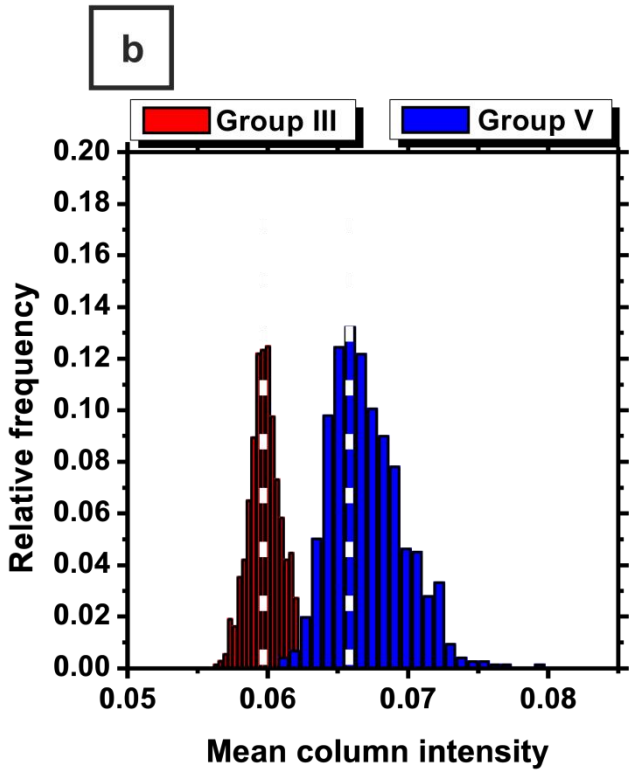

Figure 1: (a) Non-rigidly aligned [010] HR HAADF image of a Ga($As_{0.952}Bi_{0.048}$) layer. (b) Intensity distribution plot of the separated group III and group V atom column intensities. The dashed lines represent the mean intensity values μ_{III} and μ_V.

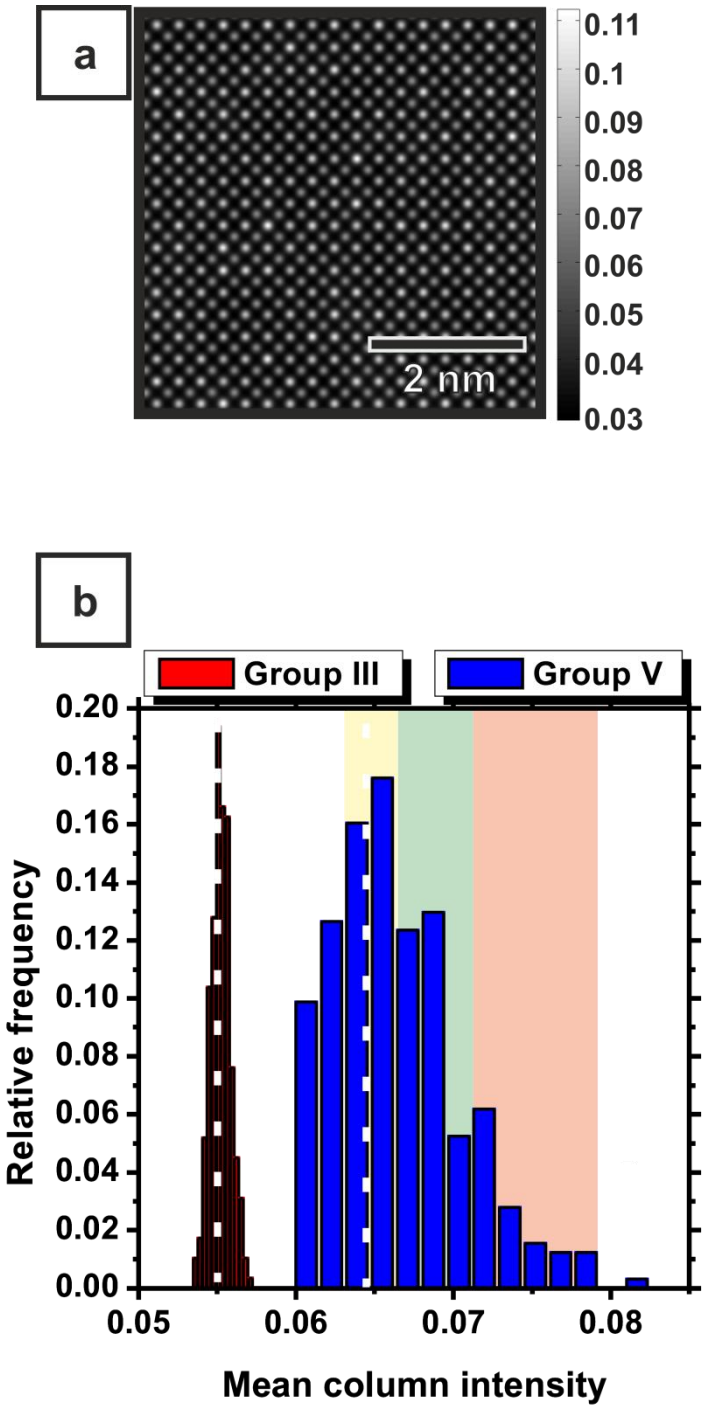

Figure 2: (a) Simulated HAADF STEM image of a relaxed Ga($As_{0.952}Bi_{0.048}$) supercell simulated in frozen lattice approach. (b) Intensity distribution plot of the separated group III and group V atomic column intensities. The yellow, green and red boxes represent the intensity values of group V columns containing one, two and three Bi atoms, respectively.

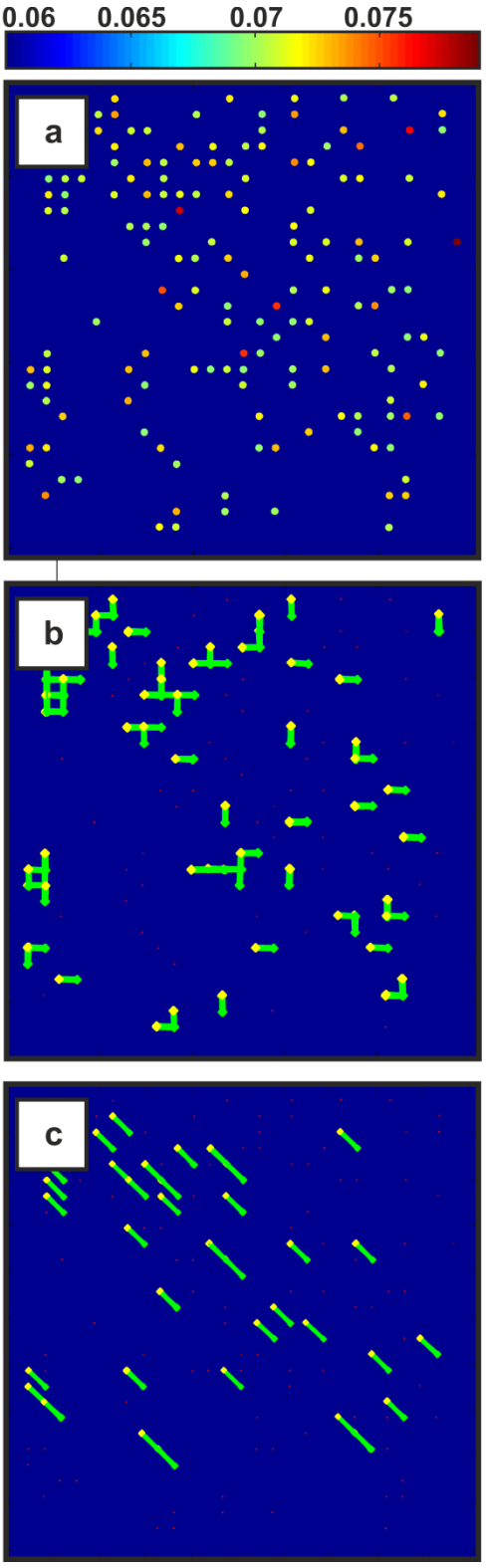

Figure 3: (a) Group V intensity map of the HR image depicted in figure 1a. Intensity values above 7% were taken into account. The color bar describes the increasing mean column intensity. (b) Back transformation of Hough peaks found in fig. 4 at 0° and -90°. The green lines represent the ordering of Bi atoms along the <100> directions. (c) Back transformation of Hough peaks found in fig. 4 at -45°. The green lines represent the ordering of Bi atoms along the [-101] direction.

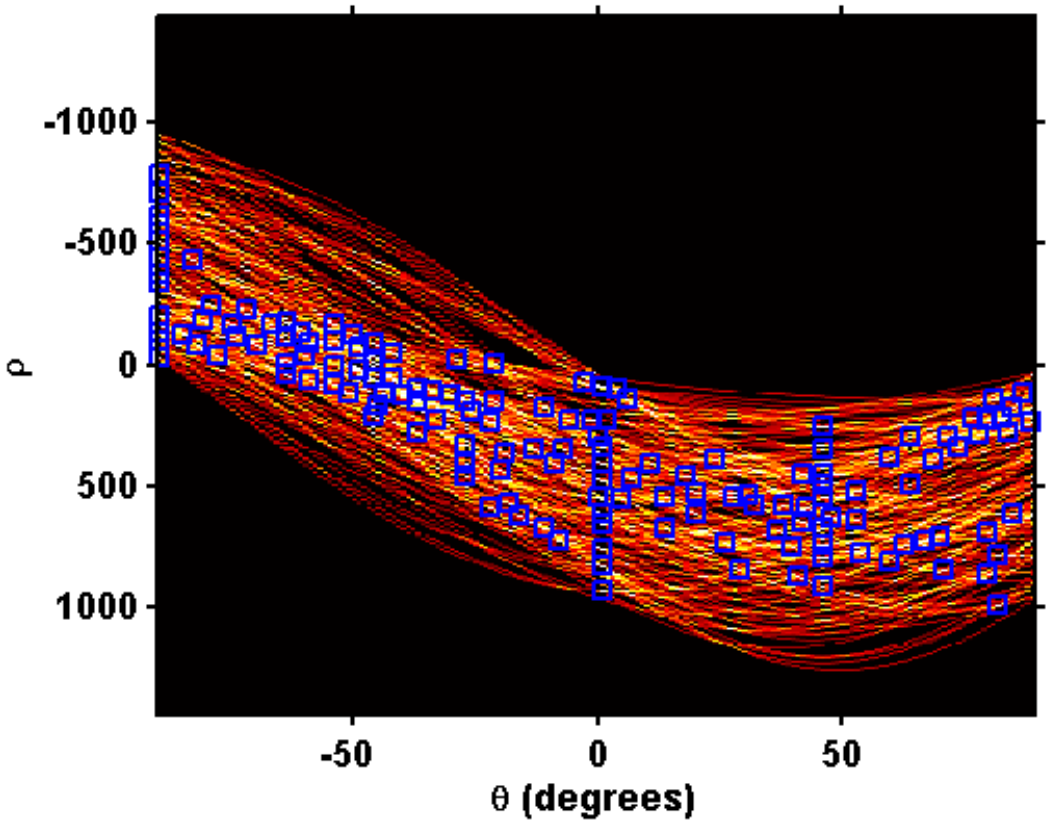

Figure 4: Hough transform (ρ-θ diagram) of the intensity map depicted in fig. 3a. The blue squares represent the detected Hough-peaks.

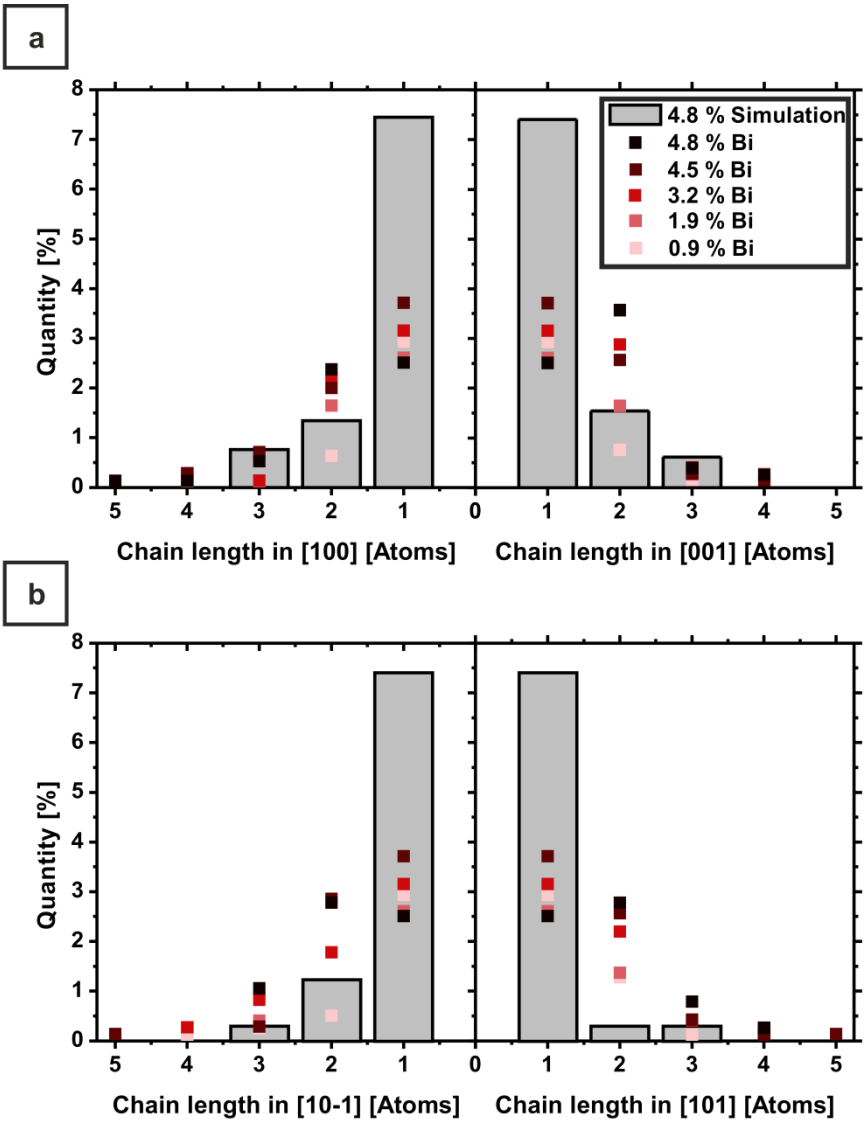

Figure 5: Relative number of occurrence of Bi chains in % versus chain length plot for experimental $Ga(As_{1-x}Bi_x)$ samples with different Bi fractions in (a) <100>- and (b) <101> direction. The data represented by grey bars correspond to the frozen lattice HAADF simulation of a relaxed Ga $Ga(As_{1-x}Bi_x)$ supercell wit x = 0.048, where the Bi had been distributed randomly.

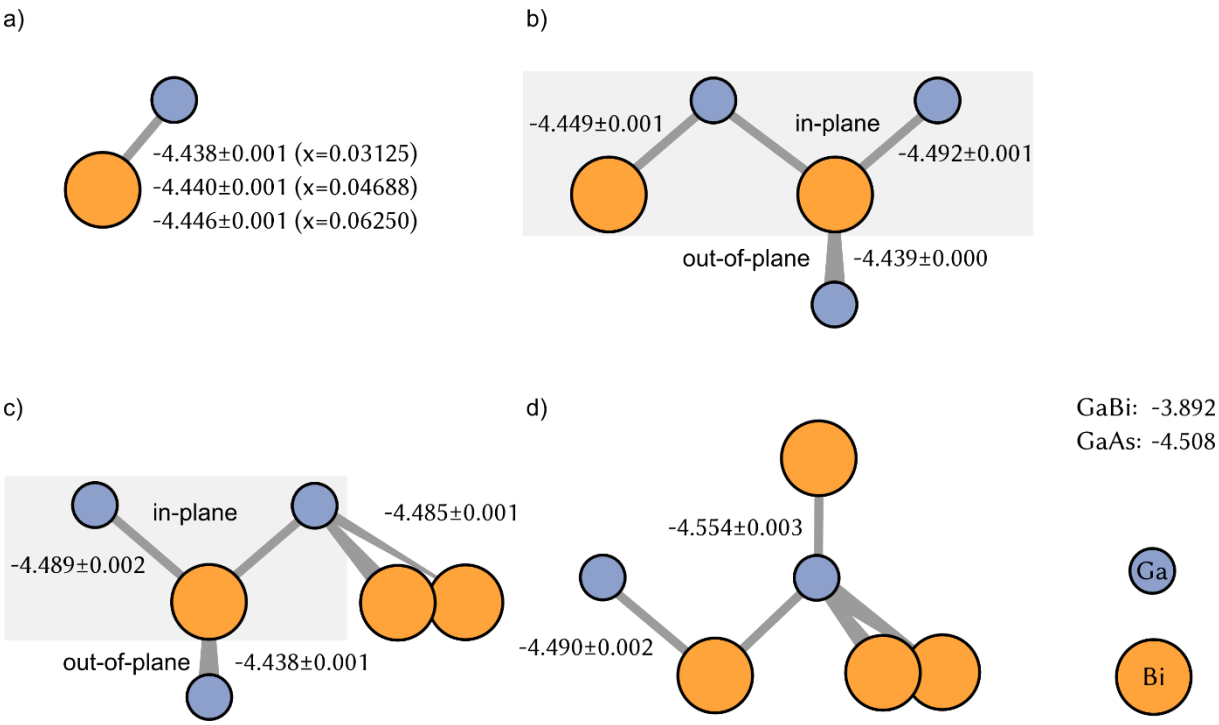

Figure 6: Schematic representation of structural motifs investigated computationally of dispersed (a) and clustered (b) Bi_2, c) Bi_3 and d) Bi_4) arrangements of Bi atoms in $Ga(As_{1-x}Bi_x)$ supercells. Averaged ICOHP values are given for equivalent bonds in eV per bond together with the standard deviation. For the clustered arrangements bonds to Ga in the same (in plane) and in other crystallographic planes (out of plane) can be distinguished.

6.3 Investigation of the microstructure of metallic droplets on Ga(AsBi)/GaAs[1]

E. Sterzer, N. Knaub, P. Ludewig, R. Straubinger, A. Beyer, K. Volz, *Investigation of the microstructure of metallic droplets on Ga(AsBi)/GaAs*, Journal of Crystal Growth **408**, 71 (2014). DOI: 10.1016/j.jcrysgro.2014.09.006

Abstract

Low Bi content GaAs is a promising material for new optical devices with less heat production. The growth of such devices by metal organic vapor phase epitaxy faces several challenges. This paper summarizes results of the formation of metallic droplets during the epitaxial growth of Ga(AsBi) using all-liquid group III and V precursors. The samples that are grown, investigated by atomic force microscopy and scanning electron microscopy, show a different metal droplet distribution over the surface depending on the growth temperature and the V/III ratio of the precursors. Investigations with energy dispersive X-ray analysis and selective etching prove the appearance of phase separated Ga-Bi and pure Bi droplets at growth temperatures between 375 °C and 425 °C, which is explainable by the phase diagram of Ga-Bi. Since the pure Bi droplets show a preferred orientation on the surface after cool-down, transmission electron microscopy measurements were done by using the dark field imaging mode in addition to electron diffraction and high resolution imaging. These experiments show the single crystalline structure of the Bi droplets. The comparison of experimental diffraction patterns with image simulation shows a preferred alignment of Bi {10-1} lattice planes parallel to GaAs {202} lattice planes with the formation of a coincidence lattice. Thus it is possible to derive a model of how the Bi droplets evolve on the GaAs surface.

The Authors contribution

My contribution to this work was the TEM sample preparation and TEM investigations of the droplets' crystal structure. Furthermore I did the evaluation and interpretation of the TEM measurements. Peter Ludewig carried out the sample growth via MOVPE and Eduard Sterzer performed the SEM and AFM measurements. All co-authors also helped Eduard Sterzer and me to interpret the data and to improve the first draft of the manuscript.

1 Reprinted from *Journal of Crystal Growth **408** (2014) 71-77*, Copyright 2014, with permission from Elsevier.

Journal of Crystal Growth 408 (2014) 71–77

Contents lists available at ScienceDirect

Journal of Crystal Growth

journal homepage: www.elsevier.com/locate/jcrysgro

Investigation of the microstructure of metallic droplets on Ga(AsBi)/GaAs

E. Sterzer [1], N. Knaub [1], P. Ludewig, R. Straubinger, A. Beyer, K. Volz *

Materials Science Center and Faculty of Physics, Philipps-Universität Marburg, Marburg 35032, Germany

ARTICLE INFO

Article history:
Received 3 April 2014
Received in revised form
1 September 2014
Accepted 4 September 2014
Communicated by C. Caneau
Available online 19 September 2014

Keywords:
A1. Atomic force microscopy
A1. Electron microscopy
A1. Recrystallization
A3. Metal organic vapor phase epitaxy
B1. Bismuth compounds
B2. Semiconducting III–V materials

ABSTRACT

Low Bi content GaAs is a promising material for new optical devices with less heat production. The growth of such devices by metal organic vapor phase epitaxy faces several challenges. This paper summarizes results of the formation of metallic droplets during the epitaxial growth of Ga(AsBi) using all-liquid group III and V precursors. The samples that are grown, investigated by atomic force microscopy and scanning electron microscopy, show a different metal droplet distribution over the surface depending on the growth temperature and the V/III ratio of the precursors. Investigations with energy dispersive X-ray analysis and selective etching prove the appearance of phase separated Ga–Bi and pure Bi droplets at growth temperatures between 375 °C and 425 °C, which is explainable by the phase diagram of Ga–Bi. Since the pure Bi droplets show a preferred orientation on the surface after cool-down, transmission electron microscopy measurements were done by using the dark field imaging mode in addition to electron diffraction and high resolution imaging. These experiments show the single crystalline structure of the Bi droplets. The comparison of experimental diffraction patterns with image simulation shows a preferred alignment of Bi {10−1} lattice planes parallel to GaAs {202} lattice planes with the formation of a coincidence lattice. Thus it is possible to derive a model of how the Bi droplets evolve on the GaAs surface.

1. Introduction

The development of low bismuth (Bi) content gallium arsenide (GaAs) promises new devices with less heat generation [1] and a less temperature sensitive band gap [2,3]. First optically pumped [4], then electrically pumped lasing at room temperature [5] has been already demonstrated for dilute Bi containing devices grown by metal organic vapor phase epitaxy (MOVPE). Ga(AsBi) alloys with high Bi fractions above 10% have been grown; however, only by molecular beam epitaxy (MBE) and at growth temperatures around 200 °C [6]. In the case of MOVPE growth it is more challenging to achieve such high Bi fractions, since growth temperatures above 350 °C are required for the decomposition of the precursor chemicals. Because of the large covalent radius of the Bi atoms in comparison to the arsenic (As) atoms, the incorporation of Bi in GaAs causes local strain which makes this ternary material system highly metastable. Therefore, the crystal rejects the offered Bi, which segregates towards the surface and causes the formation of metallic droplets [7,8]. The understanding of the droplet formation is an important point for the growth improvement of Ga(AsBi)/GaAs alloys with high Bi concentration. A first theoretical description of Ga/GaAs core–shell structure formation during Ga-liquid droplet epitaxy on GaAs based on kinetic Monte Carlo simulations has been discussed in [9]. The mechanisms described in that paper can also take place in the growth of Ga(AsBi), where liquid Ga as well as liquid Bi droplets might be present at the surface due to the highly non-equilibrium growth conditions used.

There is already a first experimental description of droplet formation in MBE grown Ga(AsBi) thin films by atomic force microscopy (AFM), scanning electron microscopy (SEM), energy dispersive X-ray analysis (EDX) and reflection high energy electron diffraction (RHEED) [10], which shows Ga–Bi droplet formation for the Ga-rich Ga(AsBi) growth regime.

Since there are no crystallographic descriptions of Bi droplets on the Ga(AsBi) surface and no studies for MOVPE-grown samples yet, we will show the results of MOVPE-grown droplet containing Ga(AsBi) samples. This is interesting, as a decisive difference between MBE and MOVPE growth is the growth temperature compared to critical temperatures in the Ga–Bi phase diagram: Bi from Ga–Bi liquid mixtures solidifies at temperatures of 221.7 °C [11]. This temperature is above the MBE growth temperature of Ga(AsBi) in most cases, but below the MOVPE growth temperature of Ga(AsBi). We used SEM

* Corresponding author.
E-mail address: kerstin.volz@physik.uni-marburg.de (K. Volz).
[1] Both authors contributed equally.

http://dx.doi.org/10.1016/j.jcrysgro.2014.09.006
0022-0248/

combined with EDX as well as cross-section transmission electron microscopy (TEM). This allowed us not only to characterize the droplets and to get the structural information but also to gain crystallographic information, e.g. the crystallographic relationship between droplet and Ga(AsBi) layer surface normal, by evaluating the TEM diffraction pattern.

2. Experimental procedure

The investigated Ga(AsBi) samples were grown by MOVPE on GaAs (001) substrates in a commercially available AIX 200-GFR reactor with Pd-purified H_2 as carrier gas using a low reactor pressure of 50 mbar. The Ga precursor used was triethylgallium (TEGa), while tertiarybutylarsine (TBAs) and trimethylbismuth (TMBi) were used as group V precursors for As and Bi respectively. The growth temperature of the Ga(AsBi) alloys was chosen between 375 °C and 450 °C; we also varied TBAs/TEGa from 3.2 to 5 and TMBi/TBAs from 0.1 to 0.3 resulting in a V/III ratio from 6 to 7.35. A table with growth parameters and layer thicknesses of the investigated samples shown here is depicted in the Appendix. Our growth of droplet free Ga(AsBi) layers has been described in detail in [7, 12]. Sample surface characterization has been carried out in a Hitachi S-4100 SEM equipped with an Oxford Instruments EDX detector for composition determination. Further investigations of the surface were performed by using a Nanoscope IIIa AFM under atmospheric pressure to get a better understanding of the topology of the droplets on the surface. The droplets at the surface very often contain Ga as well as Bi. To further determine whether the droplets contain Bi or Ga a peculiar chemically selective etching process was also carried out. The samples were etched with hydrochloric acid (HCl, 30%) which only etches Ga and does not attack Bi, while sulfuric acid (H_2SO_4, 96%) was used to selectively etch Bi and not to attack Ga. After etching, either using both etchants or only one, the samples were again examined by AFM. Besides the topology we also investigated the crystallographic relation of the droplets with the GaAs substrate by using TEM. TEM samples were prepared in [010] cross-section conventionally by mechanical grinding, followed by Ar-ion milling with a Gatan PIPS. The microscopic investigations have been carried out in a JEOL JEM 3010 conventional TEM operating at 300 kV, as well as in a double C_s-corrected JEOL 2200FS scanning TEM, operating at 200 kV. The TEM methods used to investigate the Bi droplets in cross-section were dark field imaging and high resolution TEM as well as electron diffraction, which allowed to judge whether the metallic Bi droplets have a single crystalline or a polycrystalline structure.

3. Results and discussion

In this paper we will show the appearance of metallic droplets on the surface of Ga(AsBi) layers grown on GaAs under non-optimized conditions. Under optimized growth conditions [7,12], droplet formation can be avoided and thus will not be discussed here. It must be mentioned that under the growth conditions used here, we do not see metallic droplets when growing GaAs only. This shows that the metal droplet formation is a property of the Ga–As–Bi material system.

The SEM/EDX investigations show different arrangements of metallic droplets on the surface. We not only find droplets which form groups on the surface (clustering) but also detect droplets uniformly distributed across the surface. The droplet arrangement depends on the growth conditions. The temperature has a significant influence on the formation of metal droplet clusters as it is shown in Fig. 1a and b. The lower the growth temperature, the more clustering of metal droplets on the surface is observed. At low temperatures the decomposition of the metal organic precursors as well as the diffusivity of the atoms is lower compared to higher growth temperatures. We assume that a catalytic decomposition of the precursors takes place wherever a metal droplet is formed already. At these positions on the surface further metal droplets can hence form. As the diffusivity is low, the metal droplets are not evenly distributed on the surface, but cluster in groups (Fig. 1b). At higher growth temperatures a larger amount of metal organic precursor is decomposed and hence more evenly distributed metal droplets form (Fig. 1a).

Moreover we can correlate the size of the droplets and their density with the amount of group III precursor available in the reactor. The more group III precursor is available the bigger the droplets are, but the density of the droplets on the surface shrinks. The same results are obtained by reducing the As precursors partial pressure, which can be seen in the SEM images in Fig. 2a. Here, large Ga–Bi droplets form due to less As being available and the resulting Ga rich surface. Fig. 2b depicts smaller Bi droplets, containing much less Ga, but a surface more densely covered with droplets, because a higher As precursor partial pressure compared to the sample depicted in Fig. 2a was used here.

We will first determine the droplet composition for these two samples, before we look into their formation process during growth and cool-down.

Detailed SEM and EDX investigations of the droplets shown in Fig. 2a and b yield the chemical compositions of the different droplets. We found droplets containing Ga and Bi (Fig. 3a corresponding to Fig. 2a) or Bi mainly (Fig. 3b corresponding to Fig. 2b). The figures depict SEM images with an EDX spectrum for element analysis. Since the EDX measurements were performed at 20 keV the signal penetration depth for pure GaAs is up to 1.7 μm; therefore some signal is also detected from the underlying layer and substrate, in this case of GaAs. In Fig. 3a one can see that under these growth conditions the droplets are split, consisting in one part of Ga and in the other part of Bi. On top of the Bi-part, one can also find small Ga droplets (white arrows). A miscible liquid Ga–Bi mixture at growth temperature in the range 375–425 °C separates into a liquid Ga and a solid Bi phase at temperatures below 221.7 °C, i.e. during cool-down of the sample to room temperature. At 29.77 °C the liquid Ga solidifies. Therefore, the droplets develop into their final shape and compositional profile most likely during cool-down of the sample from growth temperature (above 300 °C) to room temperature, where the AFM and SEM/EDX measurements were made. Since we know the cool-down process of our reactor, one can indirectly say how long a wafer needs to cool down to the temperature at which Bi solidifies. In the case of the samples grown at 425 °C, the wafer takes about 14 min to cool down to the solid Bi phase (below 221.7 °C). The Bi metal solidifies first and all Ga is repelled from its lattice, as there is no solubility of Ga in solid Bi. This can also be seen in the droplets' morphology, as they often show faceted crystal regions where Bi is found and round Ga droplets aside or on top of the Bi (Fig. 3a). The droplet movement and their coalescence, which will be discussed in the following, take place at higher temperatures. In contrast to Fig. 3a, we see mainly pure Bi droplets if we use a higher As precursor partial pressure (Fig. 3b).

As the droplets' size increases and their density decreases when the layers are grown thicker (SEM images not shown here), the effect of droplet coalescence can be explained by Ostwald-ripening [13]. At the beginning, Bi only acts as a surfactant on the GaAs surface. By offering more and more Bi, a certain Bi fraction is incorporated into the growing Ga(AsBi) layer, while a planar metal film is on the growth surface. When a certain critical metal film thickness exceeds on the surface, metal droplets form as described before [7,12]. This happens possibly due to the increasing surface

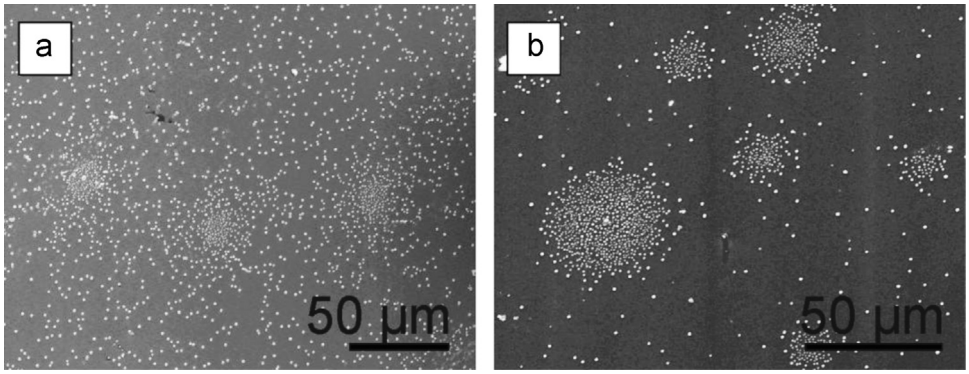

Fig. 1. (a) SEM image of a Ga(AsBi) sample grown at 400 °C. Three metal droplet clusters with pure Bi droplets are visible. There are additional droplets distributed uniformly between the clusters. (b) SEM image of a Ga(AsBi) sample grown at 375 °C. All other growth conditions were the same as for the sample shown in (a). In comparison to (a) the droplets evolve mainly in clusters; few droplets distributed between the clusters can be seen.

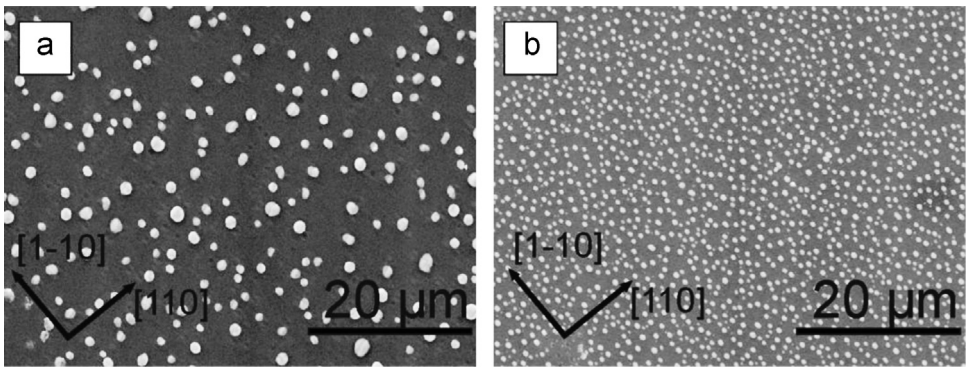

Fig. 2. (a) SEM image of a Ga(AsBi) sample surface covered with Ga–Bi droplets grown at 425 °C. The droplets are spatially separated and randomly distributed (TBAs partial pressure: 0.045 mbar). Compared to lower growth temperatures, larger droplets can be observed, but their density is lower. (b) SEM image of a sample grown using higher TBAs partial pressure compared to the one used for the sample shown in (a) (0.07 mbar). The surface is covered with droplets containing mainly Bi which are oriented along the [1–10] Ga-polar direction. In comparison to (a) the density of the droplets is higher.

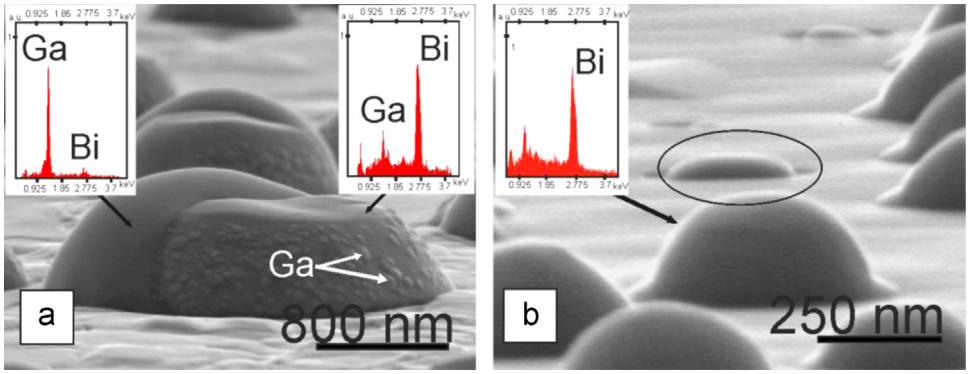

Fig. 3. (a) SEM image of the surface of a bulk Ga(AsBi)/GaAs sample grown at 425 °C (same sample as shown in Fig. 2a). The EDX spectra, shown as inset, show the composition of the droplet, which is separated in a Ga and a Bi part. The surface of the Bi part is covered by small Ga droplets. Due to the moving of droplets the surface is rough. (b) SEM image of a Ga(AsBi) surface containing droplets, made of mainly Bi (same sample depicted in Fig. 2b). The encircled droplet seems to extend into the layer which also indicates that the droplets are forming during the growth. The foot of the droplet is also mainly Bi.

tension of the planar film. However, the finding of an Ostwald ripening process also poses questions on the movement and formation of droplets on the surface during growth. Therefore, we investigated the sample surface (of the sample shown in Figs. 2a and 3a) before and after an etching process with sulfuric acid and hydrochloric acid. The results are shown in the SEM image in Fig. 4a (before etching) andb (AFM micrograph after the etching process with sulfuric acid). Both observations were performed on the same sample, but in slightly different positions. The SEM image in Fig. 4a shows clearly the appearance of Ga–Bi droplets. Moreover one can see holes (some are encircled) close to the droplets. The growth mechanism of the ring-like, elevated structure, consisting of GaAs and surrounding the area where the droplets were, is most probably similar to the one described in [9]. The appearance of holes in unetched samples leads to the assumption that smaller droplets were formed during growth and might form bigger ones by coalescence afterwards on the surface. A possible proof for this assumption is shown in Fig. 4c. This AFM micrograph is an enlarged image of the area which is marked by the black box in Fig. 4b. Here, one can see three holes (encircled positions) where probably three smaller droplets were before. A possible scenario could be the following: at temperatures where Bi is liquid, the three droplets moved towards the center of the image (moving direction is marked with black arrows) where

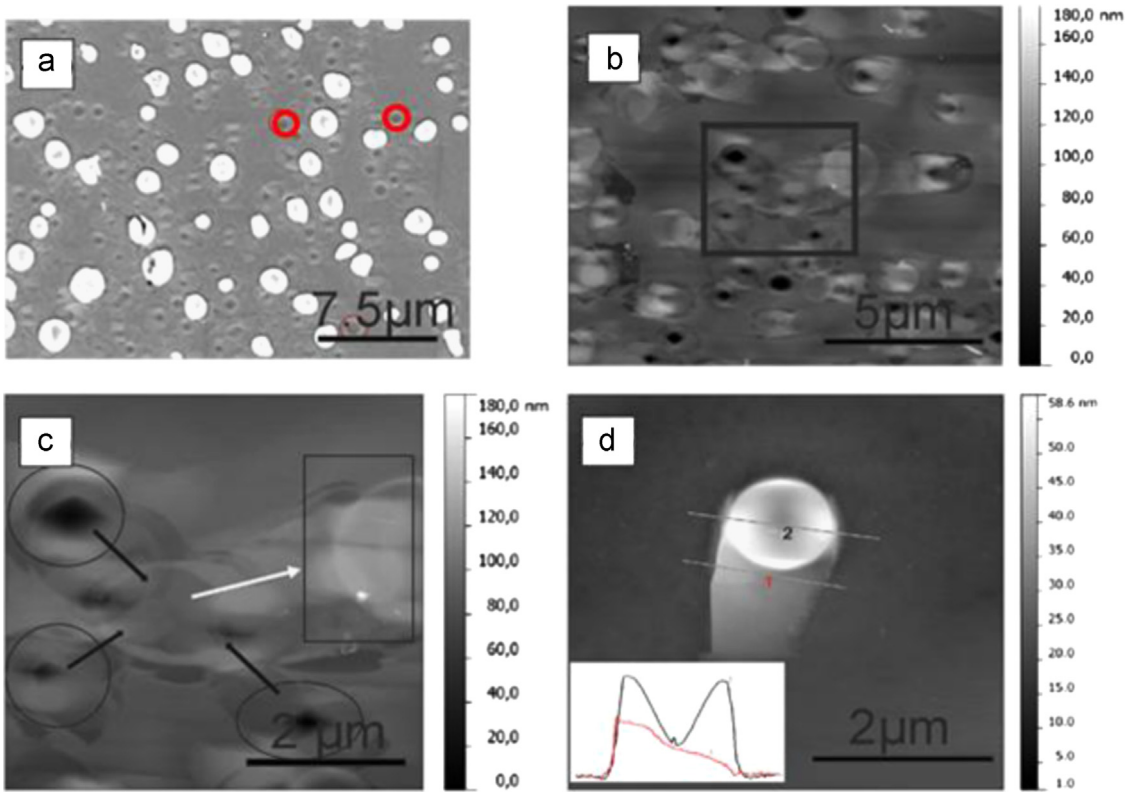

Fig. 4. (a) SEM image of a surface belonging to the same sample as shown in Fig. 3a. One can see Ga–Bi droplets distributed over the surface as well as some holes (two are encircled in red) close to them. The holes occur probably during growth and indicate positions where droplets were before they moved and coalesced, since the image was taken before an etching process. The image was intentionally overexposed to show the surface morphology better. (b) AFM micrograph of the same sample surface as shown in (a) but after etching with sulfuric acid. (c) Enlarged image of the squared area depicted in (b). The circles mark the holes where it is assumed that smaller droplets were before they moved towards the middle of the image (as marked with black arrows) and coalesce into a bigger droplet. Afterwards the bigger droplet probably moved (white arrow) to the area which is marked with the box. This droplet was then etched away before the AFM image was taken. (d) AFM micrograph of the same sample as shown in (a) and (b) after etching with sulfuric acid and hydrochloric acid. The position of a droplet as well as a trail behind it can be seen. The lines marked 1 and 2 represent the positions of the line profiles which are depicted as an inset in this figure. (For interpretation of the references to color in this figure legend, the reader is referred to the web version of this article.)

they formed a bigger droplet. The bigger droplet then moved on the surface (moving direction is marked with white arrow) until it finally stopped at the position which is marked (box). This droplet was etched away prior to taking the AFM image. Our assumption that the bigger droplet moved on the surface is based on the fact that a movement trace is still visible on the sample surface. Another hint for droplet moving is depicted in Fig. 4d. This AFM micrograph of the same sample as described in Fig. 4a and b was recorded after the etching process with sulfuric acid and hydrochloric acid. The micrograph depicts the former droplet position on the surface, but more important is the clearly visible trace left behind during the droplet movement. The inset in Fig. 4d depicts the line profiles across the trail of the droplet, marked in the figure with 1 and 2. The line marked as 1 shows the profile of the area of the droplet trail, while the second line represents the GaAs height profile at the position where the Ga–Bi droplet was etched away. The profile points out that the depth of the hole does not reach the underlying substrate and that the hole is surrounded by a mound on either side. Since the etches we used were to only attack either Ga or Bi and there is still a mound left around the hole after etching, one can assume a mound containing GaAs; as will be seen later this GaAs mound contains a small Bi fraction. A possible explanation for this could be a recrystallization process which took place as was simulated in [9]. The property where droplets move and coalesce on the surface has for our growth conditions only been found for droplets containing a large amount of Ga, which is liquid down to room temperature. Droplet movement could not be found for samples having Bi droplets only, as will be shown in the following. It should be noted that movement of metallic droplets on semiconductor surfaces (e.g. GaAs) has been observed before [14] and its driving force has been explained by different surface chemical potentials, which for our samples can easily occur due to surface composition fluctuations.

Fig. 5a shows an AFM micrograph of a sample surface (sample shown in Figs. 2b and 3b, having mainly Bi metal droplets), etched with sulfuric acid to remove Bi only and leaving Ga unetched. We observe holes in the Ga(AsBi) surface where the Bi droplets were before. This indicates that the metal droplets extend into the semiconductor layer under these growth conditions and hence also that mainly Bi-containing droplets are formed during the growth. The very peculiar morphology of the holes, especially their raised edges (Fig. 5b), also leads to the conclusion that liquid phase epitaxy (LPE) is taking place at growth temperature in the Bi–GaAs system studied here. Again, similar phenomena have been described using kinetic Monte Carlo simulations in [9] looking at the Ga–GaAs system. In addition to the holes left by the etched Bi, one can see small Ga droplets all over the surface, which could be removed by etching with HCl (depicted in Fig. 5c).

It is already known that Bi as a surfactant enhances the lateral growth rate of GaAs growth as well as for Ga(AsBi) growth [10,15] whereas the formation of pure Bi droplets on the surface is undesirable and hinders the growth of homogeneous Ga(AsBi) layers. The SEM image of the intact structure in Fig. 2b as well as the AFM image of the etched sample depicted in Fig. 5a shows a preferred alignment of the droplets on the surface. By investigating the droplets with respect to the known crystallographic

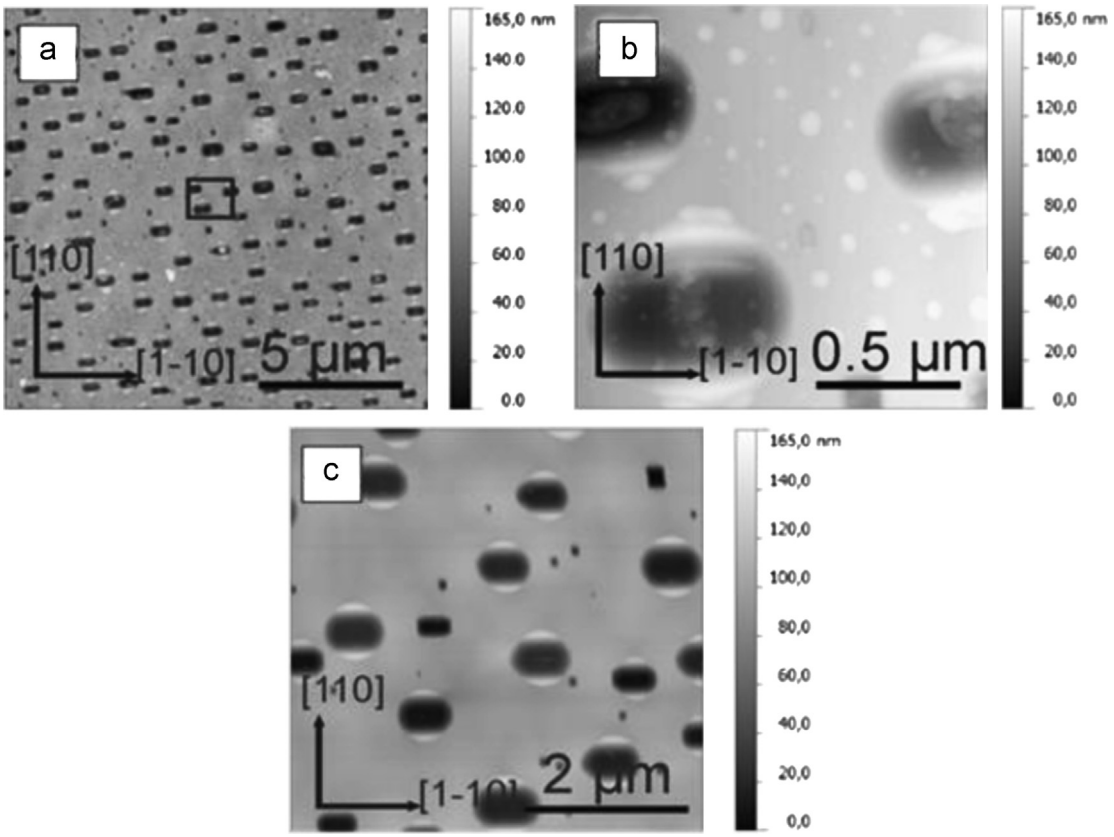

Fig. 5. (a) This AFM image confirms the preferred orientation of droplets, shown in Figs. 2b and 3b already, with their long axis along the Ga-polar [1–10] direction. The sample has been etched with sulfuric acid which is selective against Bi. Therefore holes remain where Bi droplets had been before. (b) The enlarged image of (a) reveals small droplets on the surface which are probably Ga. (c) AFM micrograph of the same sample depicted in (a) and (b) after a further etching process with hydrochloric acid which is selective against Ga. After this process the small droplets disappear.

direction of the substrate, we find that the long axis of the droplets is along the [1–10] Ga-polar direction of the GaAs substrate. The Bi droplets hence have a preferred orientation with respect to the surface. Therefore, we assume a crystallographic relationship between the metal Bi and the semiconductor crystal structure. To get a better understanding of why the Bi droplets form like that, we have performed cross-section investigation of the droplets in TEM.

Fig. 6a shows the bright field image of a 400–500 nm large Bi droplet on a Ga(AsBi) layer grown on GaAs. One can see the shape of the droplet and also some facets due to its crystalline structure. Since bright field imaging does not allow to derive crystallographic information on the sample, we also performed dark field imaging of the same droplet. The 002-diffraction spot of the cubic zinc-blende GaAs has been used for the dark field imaging. This reflection is chemically sensitive for the cubic zinc-blende lattice, and the measured intensity is proportional to the square of the absolute value of the structure factor of the investigated material. In this kind of imaging Ga(AsBi) appears brighter than GaAs. The higher the Bi content of the material, the brighter the Ga(AsBi) layer with respect to GaAs. One can see clearly the inhomogeneous Bi composition in the Ga(AsBi) layer in Fig. 6b. The composition depth profile is again very peculiar, pointing towards a LPE process taking place during growth, as has also been theoretically described in [9] and is now shown here experimentally with the example of a ternary material. We observe a Bi-poor region directly underneath the Bi droplet, which is sandwiched between two Ga(AsBi) layers on the sides. During LPE Bi can act as a catalyst for GaAs growth, as it is described in [16]. This leads to the conclusion that once a small droplet is formed during growth, the droplet is fed with the Bi from the underlying Ga(AsBi) layer until only GaAs remains, which can be recognized in the dark field images by nearly the same intensity as pure GaAs.

To get a better understanding of the Bi droplet's crystal structure and the possibility of pure Bi droplet formation in general we simulated the diffraction pattern of the Bi droplet depicted in Fig. 6c (using the electron diffraction simulation software JEMS [17]). The results are overlaid to the experimental pattern. The spots surrounded by circles belong to the typical GaAs [010] diffraction pattern, and the additional diffraction spots, which are surrounded by squares, belong to the Bi droplet. Judging from the spotty appearance of the diffraction pattern, as well as from the bright field image discussed before, one can say that the Bi droplet has a single crystalline structure assuming the pure Bi crystal structure, which is rhombohedral (space group R-3m). Due to the threefold symmetry of the Bi crystal structure we got the solution $\langle -1-13\rangle$ for the droplet orientation. In this case the diffraction spots of the Bi lattice planes parallel to GaAs {202} planes are Bi {10–1}. By simulating a rhombohedral Bi diffraction pattern with JEMS one can derive the lattice plane distance of Bi $\{10-1\}=0.2273$ nm, which is close to the known lattice plane distance of GaAs $\{202\}=0.2$ nm. This corresponds to a lattice mismatch of 12%. To accommodate this mismatch, a coincidence lattice of GaAs and Bi could form when the condition $7\times$ Bi $\{10-1\}\approx 8\times$ GaAs {202} is fulfilled, as it is shown in the ball and stick model of the Bi droplet on the GaAs surface in Fig. 6d, which was created with the free available software VESTA [18]. The model displays the crystallographic relationship between the lattice planes of Bi and GaAs which we experimentally found, and also shows which planes constitute the droplet's facets. To confirm

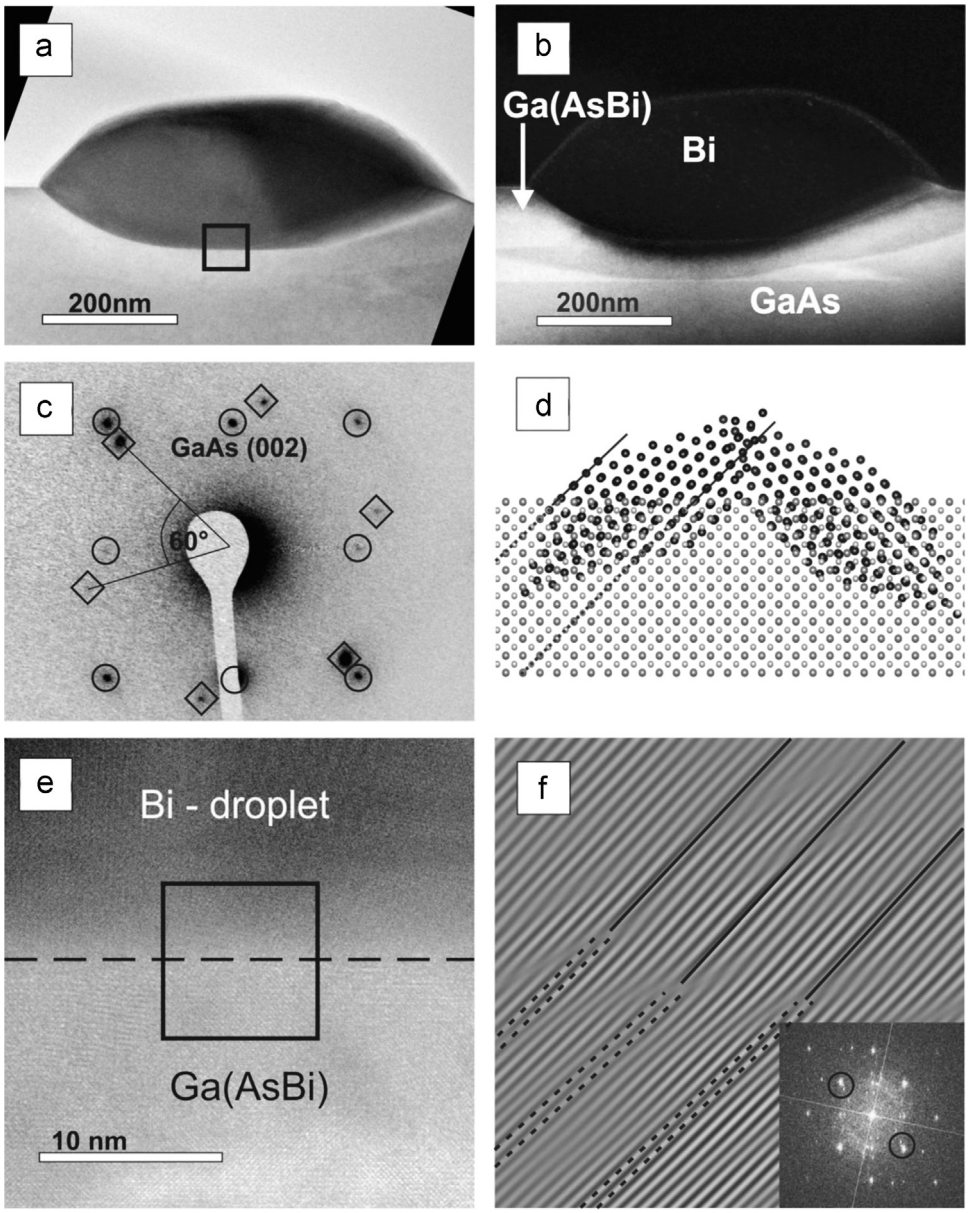

Fig. 6. (a) Cross-sectional [010] TEM bright field image of a 400–500 nm large Bi-droplet (dark) on Ga(AsBi) surface. The squared area represents the region where high resolution measurements were carried out. (b) TEM (002) dark field image of the same droplet as in (a). Under these imaging conditions the Ga(AsBi) layer appears brighter than pure GaAs. The Ga(AsBi) layer underneath and surrounding the droplet has inhomogeneous chemical composition. (c) Diffraction pattern of the Bi droplet on GaAs from (a). The encircled diffraction spots highlight the GaAs diffraction, while the squared ones highlight the Bi droplet diffraction. One can see the Bi (10–1) diffraction spots parallel to GaAs (202). The Bi crystal structure assumed for the simulation of this diffraction pattern is rhombohedral. (d) Ball and stick model of the investigated Bi droplet (black atoms) on GaAs (gray atoms). The dashed lines represent the {202} lattice planes of GaAs, while the black ones belong to the {10 − 1} planes of Bi. Every 7th Bi {10 − 1} lattice plane fits to every 8th GaAs {202} lattice plane. By the formation of this coincidence lattice the crystal accommodates its lattice mismatch from 12% to 0.6%. (e) High resolution TEM measurement of the region depicted in (a). The dashed line represents the interface of the Bi-droplet and the Ga(AsBi) layer. (f) Bragg-filtered region of the squared area in (e). The encircled spots in the Fourier transform mark the spots which were taken for the Bragg-filtering process. The filtered image highlights the additional zinc-blende {202} lattice planes (dashed lines) at each 7th Bi {10 − 1} lattice plane (straight lines).

Table 1
Growth parameters of the four investigated samples.

Sample	Sample shown in Fig.	T_{growth} [C°]	TEGa partial pressure [mbar]	TBAs/TEGa	TMBi/TBAs	Thickness [nm]	Growth scheme (pulsed gowth mode) #pulses
A	1a	400	0.014	3.6	0.2	32	300
B	1b	375	0.014	3.6	0.2	13	300
C	2a, 3a, 4a, 4b, 4c, 4d	425	0.014	3.2	0.194	91	250
D	2b, 3b, 5a, 5b, 5c, 6a, 6b, 6e	425	0.014	5	0.1	160	250

this model we carried out high resolution TEM measurement of the Bi-droplet/Ga(AsBi) interface depicted in Fig. 6e. Afterwards, we performed a fast Fourier transformation (FFT) of the image (inset in Fig. 6f) and a Bragg-filtering process of the GaAs {202} lattice planes. The result of the inverse FFT is shown in Fig. 6f, which is the filtered image of the squared region in Fig. 6e. Here

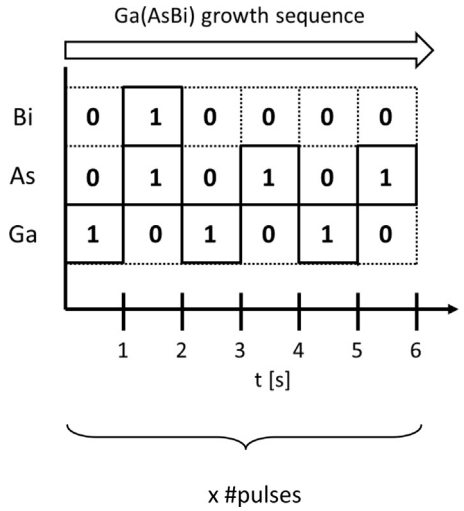

Fig. A1. Growth scheme.

one can see for every 7th Bi-droplet {10−1} lattice plane (straight line) an additional GaAs {202} lattice plane (dashed line). Hence, a coincidence lattice is formed, which significantly reduces the strain from 12% to 0.6%. With these results it is possible to explain the preferred orientation of the pure Bi droplets, which can form under certain growth conditions during the growth of Ga(AsBi) layers on GaAs by the accommodation of the droplets' lattice mismatch.

4. Summary

We have shown how metallic droplets (Bi and Ga–Bi) can evolve and behave on the Ga(AsBi) surface by using several investigation techniques like AFM, SEM/EDX and TEM. The SEM investigation combined with EDX measurements revealed the tendency that droplets can arrange on the surface uniformly or in clusters and be droplets of pure Bi or a mixture of Ga and Bi (Ga–Bi), depending on the As precursor as well as on the Bi precursor partial pressure. The arrangement of the droplets depends on the temperature due to the diffusivity of the Ga and Bi atoms and catalytic decomposition of the group III and group V precursors. After etching selectively (HCl 30% for Ga- and H_2SO_4 for Bi-etching) we could show that the droplets move on the surface during growth and that their morphology as well as the morphology and the composition of the surrounding semiconductor layers is determined by an LPE process taking place during growth. A preferred orientation of Bi droplets with respect to the GaAs lattice has been discovered in AFM/SEM images and further investigated in TEM by using dark and bright field imaging, as well as electron diffraction. The evaluation of a Bi droplet on GaAs diffraction pattern yields to the following arrangement of Bi {10−1} planes: Bi {10−1}||GaAs {202}. A ball and stick model of the recorded dark field image allows to visualize how a metallic Bi droplet can crystallize on the cubic zinc-blende structure of GaAs and additional high resolution TEM measurements confirm this model experimentally. Finally the results of this paper contribute to the understanding of why metallic (especially Bi) droplets with single crystal structure are formed on a semiconductor material under specific growth conditions.

Acknowledgments

This work was founded by the German Science Foundation (GRK 1782) and the European Union Project no. BIANCHO (FP7-257974).

Appendix A

See Table 1 and Fig. A1.

References

[1] K. Alberi, O.D. Dubon, W. Walukiewicz, K.M. Yu, K. Bertulis, A. Krotkus, Appl. Phys. Lett. 91 (5) (2007) 051909. http://dx.doi.org/10.1063/1.2768312.
[2] S.Sweeney, in: Proceedings of the 22nd IEEE International, Semiconductor Laser Conference (ISLC), 2010, pp. 111–112.
[3] M. Usman, C.A. Broderick, A. Lindsay, E.P. O'Reilly, Phys. Rev. B 84 (2011) 245202. http://dx.doi.org/10.1103/PhysRevB.84.245202.
[4] Y. Tominaga, K. Oe, M. Yoshimoto, Appl Phy Express 3 (6) (2010) 062201. http://dx.doi.org/10.1143/APEX.3.062201.
[5] P. Ludewig, N. Knaub, N. Hossein, S. Reinhard, L. Nattermann, I.P. Marko, S.R. Jin, K. Hild, S. Chatterjee, W. Stolz, S.J. Sweeney, K. Volz, Appl. Phys. Lett. 102 (24) (2013) 242115. http://dx.doi.org/10.1063/1.4811736.
[6] K. Oe, H. Okamoto, Jpn. J. Appl. Phys. 37 (Part 2, No. 11A) (1998) L1283–L1285. http://dx.doi.org/10.1143/JJAP.37.L1283.
[7] P. Ludewig, N. Knaub, W. Stolz, K. Volz, J. Cryst. Growth 370 (2013) 186–190. http://dx.doi.org/10.1016/j.jcrysgro.2012.07.002.
[8] X. Lu, D.A. Beaton, R.B. Lewis, T. Tiedje, M.B. Whitwick, Appl. Phys. Lett. 92 (2008) 192110. http://dx.doi.org/10.1063/1.2918844.
[9] K. Reyes, P. Smereka, D. Nothern, J. Mirecki Millunchick, S. Bietti, C. Somaschini, S. Sanguinetti, C. Frigeri, Phys. Rev. B 87 (2013) 165406. http://dx.doi.org/10.1103/PhysRevB.87.165406.
[10] G. Vardar, S.W. Paleg, M.V. Warren, M. Kang, S. Jeon, R.S. Goldman, Appl. Phys. Lett. 102 (4) (2013) 042106. http://dx.doi.org/10.1063/1.4789369.
[11] D. Manasijevic, D. Minić, D. Živković, I. Katayama, J. Vřešťál, D. Petković, J. Phys. Chem. Solids 70 (9) (2009) 1267–1273. http://dx.doi.org/10.1016/j.jpcs.2009.07.010.
[12] P. Ludewig, Z. Bushell, L. Nattermann, N. Knaub, W. Stolz, K. Volz, J. Cryst. Growth 396 (2014) 95–99. http://dx.doi.org/10.1016/j.jcrysgro.2014.03.041.
[13] C. Wagner, Z. Elektrochem. 65 (718) (1961) 581–591.
[14] W.-X. Tang, C.-X. Zheng, Z.-Y. Zhou, D.E. Jesson, J. Tersoff, IBM J. Res. Dev. 55 (4) (2011) 10:1–10:7. http://dx.doi.org/10.1147/JRD.2011.2158762.
[15] R.R. Wixom, L.W. Rieth, G.B. Stringfellow, J. Cryst. Growth 265 (3–4) (2004) 367–374. http://dx.doi.org/10.1016/j.jcrysgro.2004.02.019.
[16] M. Panek, M. Ratuszek, M. Tłaczała, J. Cryst. Growth 74 (3) (1986) 568–574. http://dx.doi.org/10.1016/0022-0248(86)90203-4.
[17] P. Stadelmann, Ultramicroscopy 21 (2) (1987) 131–145. http://dx.doi.org/10.1016/0304-3991(87)90080-5.
[18] K. Momma, F. Izumi, J. Appl. Crystallogr. 44 (6) (2011) 1272–1276. http://dx.doi.org/10.1107/S0021889811038970.

6.4 MOVPE growth of Ga(AsBi)/GaAs multi quantum well structures[1]

P. Ludewig, N. Knaub, W. Stolz, K. Volz, Journal of Crystal Growth **370**, 186 (2013). DOI: 10.1016/j.jcrysgro.2012.07.002.

Abstract

This paper summarizes results of the epitaxial growth of Ga(AsBi) by metal organic vapor phase epitaxy (MOVPE) using all-liquid group V precursors. Ga(AsBi)/GaAs multi quantum well (MQW) samples are grown on GaAs (001) substrates at temperatures as low as 375 °C and 400 °C using triethylgallium (TEGa), tertiarybutylarsine (TBAs) and trimethylbismuth (TMBi) as precursors. High resolution x-ray diffraction (HR-XRD), transmission electron microscopy (TEM) as well as atomic force microscopy (AFM) measurements show that MQW structures with good crystalline quality are realized. Under specific growth conditions, the Bi droplet formation can be avoided completely. The incorporated Bi-content is limited depending on the growth temperature used. Surplus Bi segregates at the surface and incorporates into the subsequent GaAs barrier when the Bi supply is stopped. The MQW samples show room temperature photoluminescence (PL) already after growth. A redshift and a decreasing PL signal intensity with increasing Bi fraction is observed.

The Authors contribution

My contribution to this work was the TEM sample preparation and the TEM measurements. Furthermore, I helped Peter Ludewig with the interpretation of the gained TEM results.

1 Reprinted from *Journal of Crystal Growth **370** (2013) 186-190*, Copyright 2012, with permission from Elsevier.

Journal of Crystal Growth 370 (2013) 186–190

Contents lists available at SciVerse ScienceDirect

Journal of Crystal Growth

journal homepage: www.elsevier.com/locate/jcrysgro

MOVPE growth of Ga(AsBi)/GaAs multi quantum well structures

P. Ludewig *, N. Knaub, W. Stolz, K. Volz

Material Science Center and Faculty of Physics, Philipps-Universität Marburg, Hans Meerwein Straße 6, 02D34, 35032 Marburg, Germany

ARTICLE INFO

Available online 16 July 2012

Keywords:
A3. Metalorganic vapor phase epitaxy
B1. Bismuth compounds
B2. Semiconducting III–V materials

ABSTRACT

This paper summarizes results of the epitaxial growth of Ga(AsBi) by metal organic vapor phase epitaxy (MOVPE) using all-liquid group V precursors. Ga(AsBi)/GaAs multi quantum well (MQW) samples are grown on GaAs (001) substrates at temperatures as low as 375 °C and 400 °C using triethylgallium (TEGa), tertiarybutylarsine (TBAs) and trimethylbismuth (TMBi) as precursors. High resolution x-ray diffraction (HR-XRD), transmission electron microscopy (TEM) as well as atomic force microscopy (AFM) measurements show that MQW structures with good crystalline quality are realized. Under specific growth conditions, the Bi droplet formation can be avoided completely. The incorporated Bi-content is limited depending on the growth temperature used. Surplus Bi segregates at the surface and incorporates into the subsequent GaAs barrier when the Bi supply is stopped. The MQW samples show room temperature photoluminescence (PL) already after growth. A redshift and a decreasing PL signal intensity with increasing Bi fraction is observed.

1. Introduction

Due to band anticrossing (BAC) in the valance band (VB), replacing a small amount of As by Bi highly reduces the bandgap of GaAs while the spin–orbit splitting is increased [1]. If the Bi fraction is more than 10.5% the spin–orbit splitting becomes higher the bandgap [2,3]. Hence, Bi containing laser-diodes with an increased efficiency could be realized, since Auger loss processes could be suppressed. Furthermore, the temperature sensitivity of the bandgap of dilute bismide Ga(AsBi) is reduced compared to conventional III/V semiconductors [4]. Therefore devices with increased temperature stability become possible [5].

The epitaxial growth of the metastable Ga(AsBi) is still a challenge and very low growth temperatures are required. In molecular beam epitaxy (MBE) the successful deposition of Ga(AsBi) on GaAs with Bi fractions of more than 10% has been reported [6,7]. Furthermore Ga(AsBi)/GaAs multi quantum well (MQW) structures were successfully grown[8]. The photoluminescence signal of those samples is very sensitive to the Bi content as well as the applied growth conditions [6,9]. Using metal organic vapor phase epitaxy (MOVPE) lower Bi fractions of 2.4% at reduced pressure and 3.7% at atmospheric pressure were realized since higher growth temperatures (>350 °C) are required for the decomposition of the precursors [10,11]. Furthermore the appearance of Bi droplets or whiskers at the surface could not be suppressed yet. A limited Bi content in Ga(AsBi) depending on the growth conditions was observed at atmospheric pressure MOVPE [11] as well as MBE [6,12].

In this paper we will present the successful growth of Ga(AsBi)/GaAs MQWs with up to 4.2% of Bi by MOVPE and discuss the growth mechanism as well as the structural and optical properties of the MQWs. Those Ga(AsBi)/GaAs MQW could act as active region of a high efficiency IR laser diode.

2. Experimental procedure

Ga(AsBi)/GaAs MQW structures were grown on GaAs (001) substrates by MOVPE. The samples shown in the following are 3x or 5x QW structures that were ended with a GaAs barrier. A commercially available AIX 200-GFR reactor system with Pd-purified H_2 as carrier gas at a reduced reactor pressure of 50 mbar was used. The applied growth temperatures were 375 °C and 400 °C. Triethylgallium (TEGa) was used as Gallium precursor, tertiarybutylarsine (TBAs) and trimethylbismuth (TMBi) as group V precursors since low growth temperatures were required. The growth rates were 0.88 μm/h at 400 °C and 0.41 μm/h at 375 °C, respectively, due to reduced decomposition of Ga precursor. Those were determined by the layer thicknesses in the growth regime where no segregation is observed and the growth rate of GaAs and Ga(AsBi) are the same within the accuracy of the measurement. The TBAs/TEGa ratio was varied from 1.1 to 3.6 and the TMBi/TEGa ratio was varied in the range of 2.3E-3 to 0.13 at a constant TEGa supply of 7E-3 mbar for all samples. The Ga(AsBi) QWs were all grown by pulsed growth mode supplying group III and group V precursors alternating for 1 s without any pause in between. In contrast the GaAs barriers were grown under a continuous

* Corresponding author. Tel.: +49 6421 28 25713; fax: +49 6421 28 28935.
E-mail address: peter.ludewig@physik.uni-marburg.de (P. Ludewig).

0022-0248/$ - see front matter © 2012 Elsevier B.V. All rights reserved.
http://dx.doi.org/10.1016/j.jcrysgro.2012.07.002

precursor flow. High resolution X-ray diffraction (HR-XRD) omega-2theta scans around the GaAs (004) reflection in combination with dynamical modeling of the experimental pattern was used to determine the Bi content and the layer thicknesses. The parameters of GaBi were taken from [13] and [14]. Cross-sectional transmission electron microscopy (TEM) dark field (DF) (002) images were taken in order to investigate the crystalline quality, the homogeneity of the composition as well as the layer thicknesses in more detail. The (002) reflection is chemically sensitive in III/V semiconductors with zinc-blende structures. The TEM samples were prepared conventionally, using Ar-ion milling as last preparation step. Imaging took place in a JEOL JEM 3010, which was operated at 300 keV. The surface morphology and the presence of Bi droplets were studied by atomic force microscopy (AFM). Room temperature photoluminescence spectroscopy (PL) was performed to analyze optical properties of the MQWs. The PL measurements were carried out using a continuous-wave (cw) Ar-ion laser at a wavelength of 514 nm for excitation. The PL signal was dispersed in a 1 m grating monochromator (THR 1000, Jobin-Yvon) and collected by a cooled germanium detector applying the standard lock-in technique.

3. Results and discussion

First we will discuss the influence of the V/V ratio on the growth of Ga(AsBi) by MOVPE. Therefore the TBAs partial pressure was changed with constant TMBi and TEGa supply. Following, the TBAs and TEGa partial pressures were held constant varying the TMBi supply. Furthermore the Bi incorporation in dependency of the growth temperature is discussed and finally the influence of the Bi incorporation on the optical properties.

Fig. 1(a) shows HR-XRD (004) patterns of Ga(AsBi)/GaAs 5xQWs. In all cases the growth temperature was 400 °C with constant TEGa and TMBi supply (TMBi/TEGa=0.09). Only the TBAs partial pressure was varied in order to change the V/V ratio. In case of TBAs/TEGa=1.1 the diffraction pattern shows no MQW profile. A single Ga(AsBi) layer of about 60 nm thickness and Bi content of 2% was found instead of a 5xQW. The surface of this sample is covered by Ga droplets as determined by energy dispersive X-ray spectroscopy (EDX) in scanning electron microscopy (SEM) (not shown here) indicating a too low V/III ratio. If the TBAs/TEGa ratio is increased to 2.1 the diffraction pattern of a 5xQW with a Bi fraction of 2.7% is found. The pendellösung fringes are clearly resolved indicating good crystalline structure and sharp hetero interfaces. This is no longer the case when the TBAs partial pressure is further raised to TBAs/TEGa=3.6. In this case the pendellösung fringes are broadened and TEM investigations of this sample shows that the topmost barrier is missing. Dynamical modeling of the XRD profiles show that the shift of the zero order peak which occurs by increasing the TBAs/TEGa from 2.1 to 3.6 only results from an increased GaAs barrier thickness (31 nm instead of 25 nm). The reason for this behavior as well as the missing topmost barrier is not understood so far. However the Bi content (2.7%) is not changed by the increased TBAs supply. This demonstrates that the structure of the Ga(AsBi)/GaAs MQWs is very sensitive to the chosen TBAs/TEGa ratio due to the required low growth temperatures while the Bi incorporation cannot be raised by decreasing the TBAs partial pressure under the growth conditions used here.

Fig. 1(b) shows the HR-XRD (004) patterns of Ga(AsBi)/GaAs 5xQWs where the V/V ratio was only changed by varying the TMBi supply. The TBAs/TEGa ratio was set to 2.1 following the discussion before. In this case all three profiles show clearly resolved pendellösung fringes indicating that there is no change in the layer sequence of these samples. Dynamical modeling of these patterns shows that the layer thicknesses of these samples differ.

This is shown in Fig. 2 in more detail. The QW-, barrier and super lattice (SL) thicknesses, as well as the Bi fraction of several 5xQW structures are plotted versus the TMBi/(TMBi+TBAs) ratio with constant TBAs and TEGa supply (TBAs/TEGa=2.1). The graph

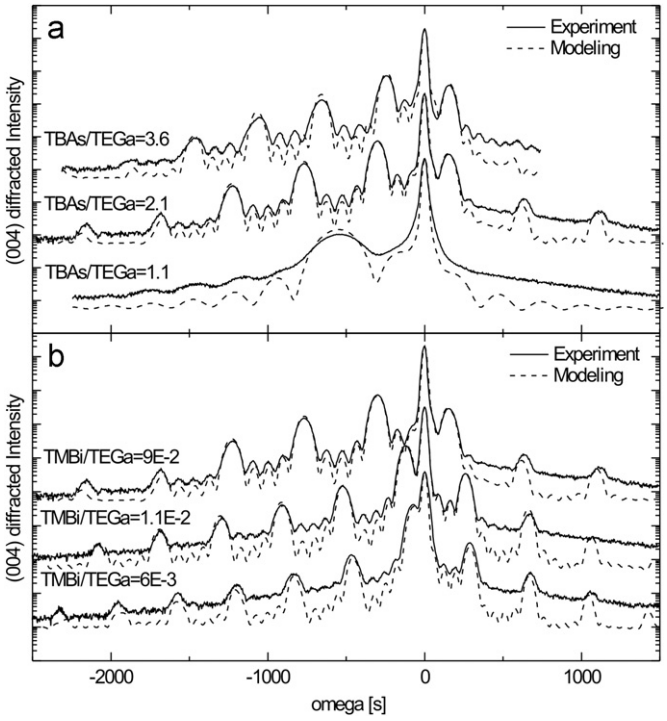

Fig. 1. HR XRD (004) pattern of Ga(AsBi)/GaAs MQWs grown with different TBAs/TEGa ratios (a) and different TMBi/TEGa ratios (b). (a) T_{growth} = 400°C TMBi/TEGa = 0.09, (b) T_{growth} = 400°C TBAs/TEGa = 2.1.

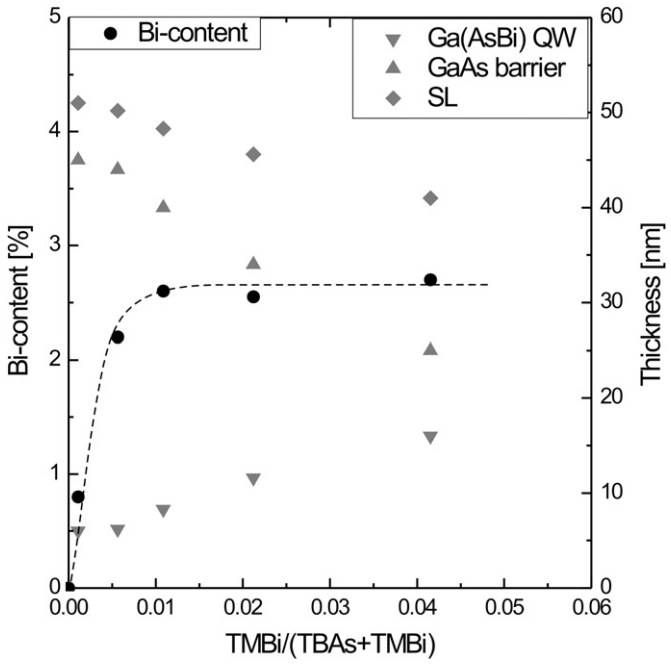

Fig. 2. Thicknesses and Bi fraction of several Ga(AsBi)/GaAs MQWs depending on the TMBi partial pressure. Above a TMBi/V ratio of 0.005 surpluses Bi segregates at the surface and incorporates into the subsequent GaAs barrier. The dashed line is only a guide to the eye.

shows, that an increasing TMBi partial pressure leads in the beginning to an increasing Bi content. At a TMBi/(TMBi+TBAs) ratio of approximately 5E-3 a saturation of the Bi content occurs at about 2.7%. At this point, where the saturation of the Bi content sets in, the thickness of the QWs increases linearly with the TMBi partial pressure while the barrier as well as the SL thickness decreases. Obviously only a given amount of Bi can be incorporated into GaAs under the chosen growth conditions. Since there is no desorption of Bi expected at that low growth temperatures, surplus Bi segregates at the surface and then incorporates in the subsequent GaAs barriers when TMBi is no longer supplied. As soon as the Bi surface coverage falls below a certain value the incorporation stops immediately and Bi acts as a surfactant; so pure GaAs can be grown. Hence only the QW and barrier thicknesses are affected by raising the Bi supply. Furthermore the growth rate of the MQWs is reduced when there is too much Bi at the surface, since the SL thickness is decreasing and the growth times are not changed. This indicates that the Ga does not reach the GaAs growth front effectively anymore. The limitation of the Bi content was already discussed in [11] for AP-MOVPE and [15] for MBE growth. Our studies show that this limitation does not occur from the formation of a liquid Bi phase at the surface as proposed in [11] but from the metastability of the material leading to the formation of a liquid Bi phase and Bi droplets as the result.

The surface morphologies of some of these samples are shown in Fig. 3. In Fig. 3(a) there is no segregation of surpluses Bi so this sample shows a very smooth surface (topmost GaAs barrier). If the TMBi flow is raised (Fig 3(b)) and segregation sets in, small dots at the surface can be found, which are a hint for the formation of Bi droplets. Further increasing the TMBi partial pressure leads to less but much bigger droplets (Fig. 3(c)) which could be ascribed to Ostwald ripening of the droplets. Fig. 3(d) shows the surface morphology of a sample with a Bi fraction of 4.2% that was grown at 375 °C. In this case also droplet free surfaces are possible. The RMS roughnesses of the droplet free samples are in the range of 0.25 nm.

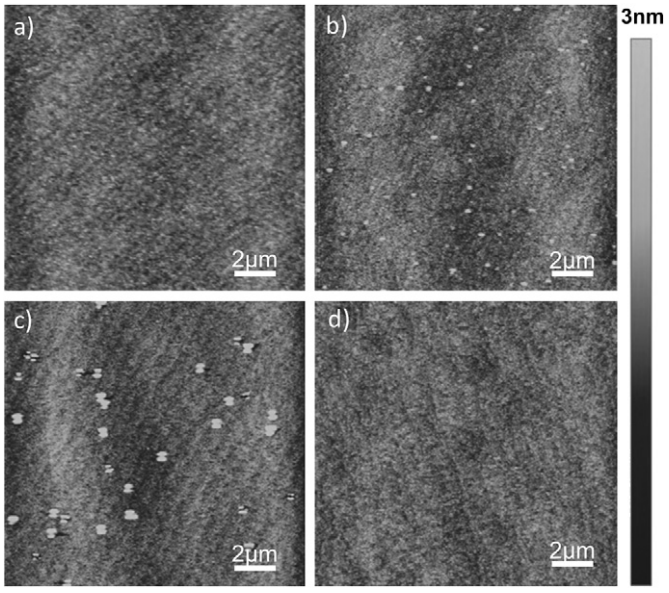

Fig. 3. Surface morphology of the Ga(AsBi)/GaAs MQWs depending on the TMBi partial pressure and the growth temperature. (a)–(c) were grown at a temperature of 400 °C with TMBi/V ratios of (a) 0.0056; (b) 0.021 and (c) 0.042. (d) was grown at a reduced temperature of 375 °C. For low TMBi/V ratio smooth surfaces with no droplet formation were observed. If the TMBi partial pressure is increased Bi droplets occur. For the low temperature growth with a Bi concentration of 4.2% also droplet free surfaces were realized.

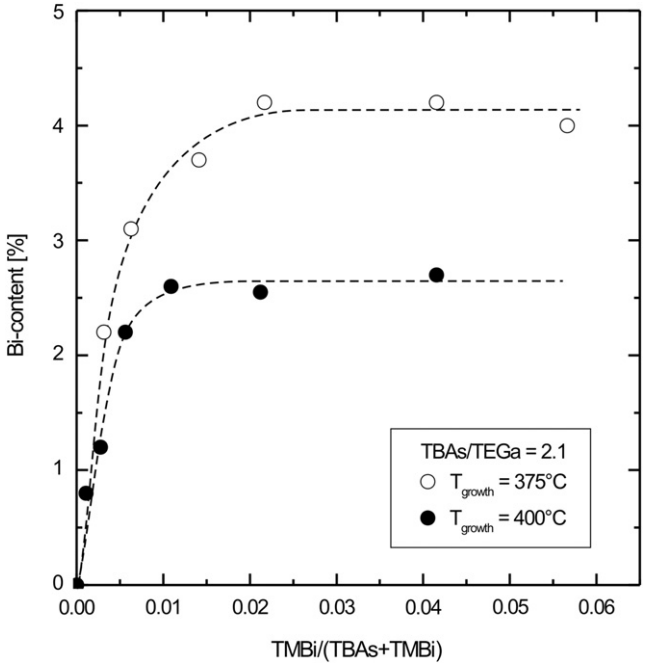

Fig. 4. Bi fraction depending on the TMBi partial pressure for samples grown at 375 °C and 400 °C. If the temperature is only reduced by 25 °C the Bi fraction can be raised from 2.7% to 4.2%. The dashed lines are again only guides to the eye.

In Fig. 4 the Bi fraction of Ga(AsBi)/GaAs MQW is plotted versus the TMBi/V ratio for growth temperatures of 400 °C and 375 °C, respectively. The TBAs supply and the TEGa supply were not changed (TBAs/TEGa=2.1). The results are consistent with the assumption of a limited Bi fraction in Ga(AsBi) which is independent of the TMBi supply. This limitation can be raised from 2.7% of Bi to 4.2% by reducing the temperature from 400 °C to 375 °C. More experiments will be done here to extrapolate an activation energy.

Fig. 5 displays TEM DF (002) images in [010] direction of two Ga(AsBi)/GaAs 3xQWs. The sample shown in Fig. 5(a) was grown at 400 °C with a TMBi partial pressure of 3.3E-4 mbar (TMBi/(TMBi+TBAs)=0.011) and a Bi fraction of 2.7% while the sample shown in Fig. 5(b) was grown at 375 °C with a much higher TMBi supply of 1.3E-3 mbar and a Bi fraction of 4.2%. In both cases the interfaces from GaAs barriers (dark) to Ga(AsBi) QWs (bright) are very smooth while the upper ones seems to be a little smeared out which is a hint for a gradient of the Bi fraction. Perpendicular to the growth direction Bi gets incorporated very homogeneously for layers with 2.7% of Bi as well as for 4.2%. The comparison of the QW thicknesses in Fig. 5(a) confirms the assumption, that a certain coverage of Bi is needed before the Bi incorporation starts, as the first QW is much thinner than the other two. When TMBi is supplied in the first place it takes some time until this critical surface coverage is reached and Bi incorporates which leads to a delay of the Ga(AsBi) growth. After the TMBi supply is stopped, surplus Bi still incorporates as demonstrated before, until the Bi coverage is again below this critical surface coverage. Hence a certain amount of Bi stays on the surface and acts as a surfactant during the growth of the first barrier. When now TMBi is again supplied for the second QW the critical amount of Bi at the surface is reached immediately and therefore the growth of Ga(AsBi) starts without delay. This assumption is supported by Fig. 5(b). In this case the TMBi supply is four times higher while the growth rate is less than the half due to the lower applied temperature. So in this case the critical coverage of Bi is reached much faster and no difference in the QW thicknesses is observed. In addition the gradient of the Bi fraction at the upper interfaces

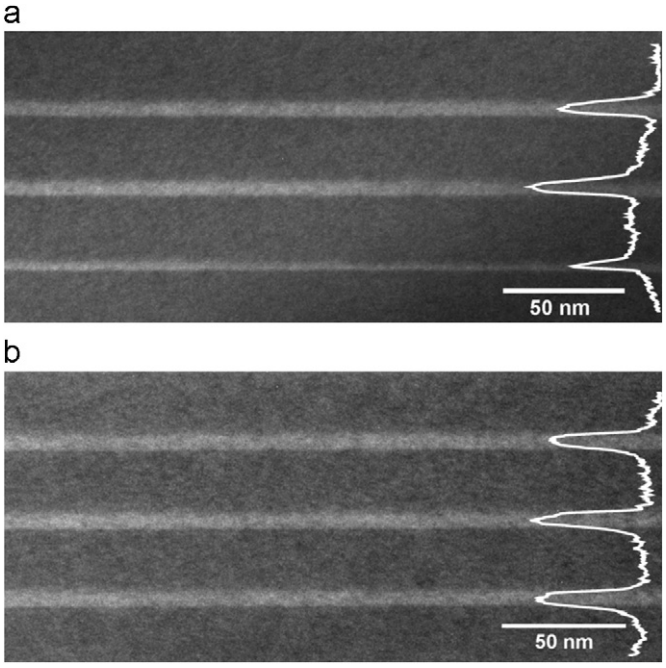

Fig. 5. Cross-sectional TEM DF (002) images of Ga(AsBi)/GaAs 3xQWs grown at 400 °C with a small TMBi supply (a) and at 375 °C with a higher TMBi supply (b). The Ga(AsBi) QWs appear brighter than the GaAs barriers in the DF images.

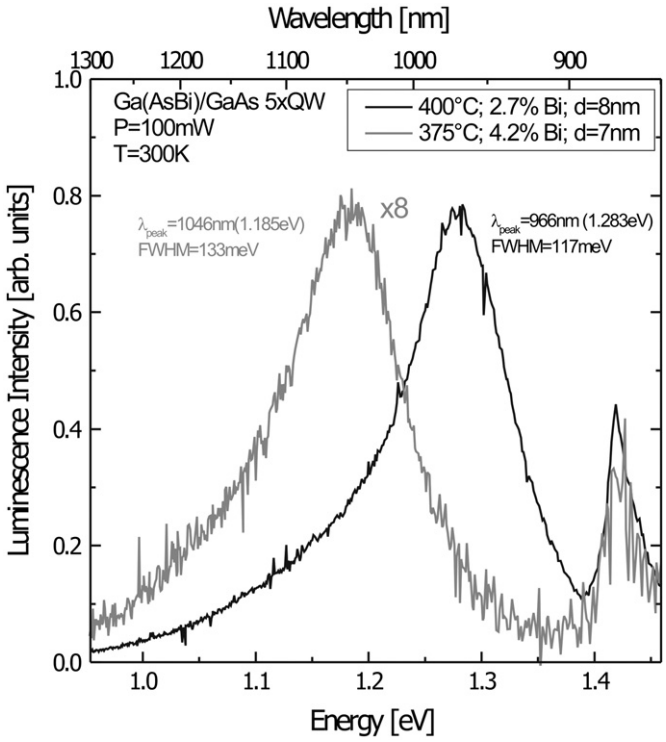

Fig. 6. Room-temperature photoluminescence spectra of Ga(AsBi)/GaAs 5xQWs with Bi fractions of 2.7% and 4.2%.

can be explained since during the time where the TMBi supply stops and the time where the surface coverage of Bi falls below the critical Bi coverage, the Bi fraction decreases.

Fig. 6 shows room temperature photoluminescence spectra of a sample with a Bi content of 2.7% grown at 400 °C and a sample

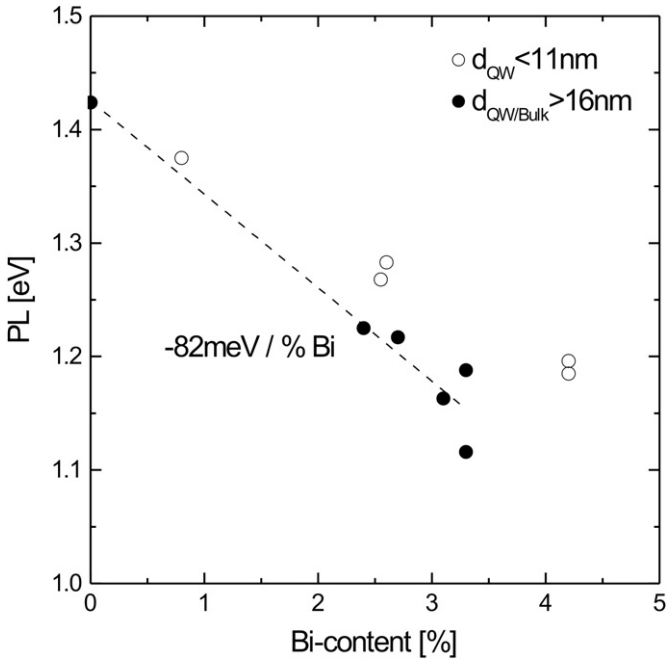

Fig. 7. Dependency of the photoluminescence peak on the Bi content.

with 4.2% of Bi grown at 375 °C. Both are as grown 5xQWs with QW thickness of 8 nm (2.7% Bi) and 7 nm (4.2% Bi). The PL peak position shifts from 1.283 eV to 1.185 eV when the Bi fraction is raised from 2.7% to 4.2%. Furthermore the integrated photoluminescence intensity decreases by more than one order of magnitude which is explained by Bi related defects as well as by the lower growth temperature. Especially for the sample with a Bi fraction of 2.7% a defect level in the range of 1.1 eV can be found which might be due to Bi clusters. The large line width of the emission of these MQWs is comparable to the literature [9]. This broadening might be due to Bi clusters and inhomogeneity of the Bi incorporation especially at the QW to barrier interfaces as discussed before.

The PL peak position of several MQW and bulk layers is shown in Fig. 7 in dependency of the Bi fraction. In this case one has to distinguish between thick layers where no quantization takes place (filled circles) and thinner layers where quantization effects have to be taken into account (empty circles). For the bulk and thick MQW layers a reduction of the emission energy of about 82 meV with 1% of Bi can be found which is in good agreement with the literature [16]. In case of the QW samples this effect is much lower which is due to the quantization.

4. Summary

We have demonstrated the growth of droplet free Ga(AsBi)/GaAs MQW on GaAs (001) substrates by MOVPE with Bi contents of up to 4.2%. Under optimized growth parameters layers with good crystalline quality are realized. The TMBi/TEGa and TBAs/TBAs ratios have to be adjusted very carefully in order to avoid Ga droplets (too low TBAs/TEGa ratio) as well as Bi droplets (too high TMBi/TEGa ratio). A limitation of the Bi content was found that is independent on V/III and V/V ratio but can be increased by reducing the growth temperature. In order to grow Ga(AsBi) a critical Bi coverage of the surface is needed whereas surplus Bi segregates at the surface and leads to a carry-over into the subsequent GaAs barriers. Room temperature photoluminescence

was observed where the peak position shifts to lower energy and the integrated PL signal drops by increasing the Bi fraction.

Acknowledgments

This work was founded by the European Union Project No. BIANCHO (FP7-257974) and the German Science Foundation (DFG: VO805/4 and VO/805/5).

References

[1] K. Alberi, O.D. Dubon, W. Walukiewicz, K.M. Yu, K. Bertulis, A. Krotkus, Applied Physics Letters 91 (5) (2007) 051909.
[2] S. Sweeney, In Semiconductor Laser Conference (ISLC), 2010 22nd IEEE International, 111 –112, Sept. (2010).
[3] M. Usman, C.A. Broderick, A. Lindsay, E.P. O'Reilly, Physical Review B 84 (245202) (2011).
[4] K. Oe, H. Okamoto, Japanese Journal of Applied Physics 37 (Part 2, No. 11A) (1998) L1283–L1285.
[5] Y. Tominaga, K. Oe, M. Yoshimoto, Applied Physics Express 3 (6) (2010) 062201.
[6] X. Lu, D.A. Beaton, R.B. Lewis, T. Tiedje, Y. Zhang, Applied Physics Letters 95 (4) (2009) 041903.
[7] A. Ptak, R. France, D. Beaton, K. Alberi, J. Simon, A. Mascarenhas, C.-S. Jiang, Journal of Crystal Growth 338 (1) (2012) 107–110.
[8] Y. Tominaga, Y. Kinoshita, K. Oe, M. Yoshimoto, Applied Physics Letters 93 (13) (2008) 131915.
[9] A.R. Mohmad, F. Bastiman, C.J. Hunter, J.S. Ng, S.J. Sweeney, J.P.R. David, Applied Physics Letters 99 (4) (2011) 042107.
[10] K. Oe, Journal of Crystal Growth 237-239 (Part 2(0)) (2002) 1481–1485.
[11] H. Fitouri, I. Moussa, A. Rebey, A. Fouzri, B.E. Jani, Journal of Crystal Growth 295 (2) (2006) 114–118.
[12] F. Bastiman, A. Mohmad, J. Ng, J. David, S. Sweeney, Journal of Crystal Growth 338 (1) (2012) 57–61.
[13] S. Tixier, M. Adamcyk, T. Tiedje, S. Francoeur, A. Mascarenhas, P. Wei, F. Schiettekatte, Applied Physics Letters 82 (14) (2003) 2245–2247.
[14] S.Q. Wang, H.Q. Ye, Physica Status Solidi (B) 240 (1) (2003) 45–54.
[15] X. Lu, D.A. Beaton, R.B. Lewis, T. Tiedje, M.B. Whitwick, Applied Physics Letters 92 (19) (2008) 192110.
[16] S. Francoeur, M.-J. Seong, A. Mascarenhas, S. Tixier, M. Adamcyk, T. Tiedje, Applied Physics Letters 82 (22) (2003) 3874–3876.

6.5 Electrical injection Ga(AsBi)/(AlGa)As single quantum well laser[1]

P. Ludewig, N. Knaub, N. Hossain, S. Reinhard, L. Nattermann, I. P. Marko, S.R. Jin, K. Hild, S. Chatterjee, W. Stolz, S.J. Sweeney, K. Volz, Applied Physics Letters **102**, 242115 (2013). DOI: 10.1063/1.4811736.

Abstract

The Ga(AsBi)material system opens opportunities in the field of high efficiency infrared laser diodes. We report on the growth, structural investigations, and lasing properties of dilute bismide Ga(AsBi)/(AlGa)As single quantum well lasers with 2.2% Bi grown by metal organic vapor phase epitaxy on GaAs (001) substrates. Electrically injected laser operation at room temperature is achieved with a threshold current density of 1.56 kA/cm^2 at an emission wavelength of 947 nm. These results from broad area devices show great promise for developing efficient IR laser diodes based on this emerging materials system.

The Authors contribution

My contribution to this work was the TEM sample preparation and the STEM HAADF measurements which also included a determination of the Ga(AsBi) quantum well layer thickness. Furthermore, I was involved the interpretation of the STEM measurements.

1 Reprinted with permission from *Applied Physics Letters **102** (2013) 242115.* Copyright 2013, AIP Publishing LLC.

Electrical injection Ga(AsBi)/(AlGa)As single quantum well laser

P. Ludewig,[1] N. Knaub,[1] N. Hossain,[2] S. Reinhard,[1] L. Nattermann,[1] I. P. Marko,[2] S. R. Jin,[2] K. Hild,[2] S. Chatterjee,[1] W. Stolz,[1] S. J. Sweeney,[2] and K. Volz[1,a)]
[1]*Material Sciences Center and Faculty of Physics, Philipps-Universität Marburg, 35032 Marburg, Germany*
[2]*Advanced Technology Institute and Department of Physics, University of Surrey, Guildford, Surrey GU2 7XH, United Kingdom*

(Received 9 April 2013; accepted 6 June 2013; published online 20 June 2013)

The Ga(AsBi) material system opens opportunities in the field of high efficiency infrared laser diodes. We report on the growth, structural investigations, and lasing properties of dilute bismide Ga(AsBi)/(AlGa)As single quantum well lasers with 2.2% Bi grown by metal organic vapor phase epitaxy on GaAs (001) substrates. Electrically injected laser operation at room temperature is achieved with a threshold current density of 1.56 kA/cm^2 at an emission wavelength of ~947 nm. These results from broad area devices show great promise for developing efficient IR laser diodes based on this emerging materials system. © *2013 AIP Publishing LLC*. [http://dx.doi.org/10.1063/1.4811736]

Dilute bismide Ga(AsBi) based lasers diodes are promising candidates for high efficiency infrared (IR) light sources. The incorporation of only a small amount of Bi into GaAs causes a large reduction in the band gap due to valence band anti-crossing[1] and, in addition, decreases the temperature sensitivity of the emission wavelength compared to conventional III/V semiconductors,[2] making temperature stabilization more straightforward. Furthermore, for Bi fractions above approximately 10%, the spin-orbit splitting becomes larger than the bandgap.[3–6] Under such conditions it is expected that troublesome hot-hole generating Auger recombination and inter-valence band absorption (IVBA) processes may be suppressed leading to higher efficiencies and more temperature stable power output of lasers for optical communications applications.[6–8] Ga(AsBi) light-emitting diodes (LEDs)[9,10] and optically pumped laser diodes[11] have been demonstrated with promising optical material qualities. In order to exploit the beneficial properties of this metastable material system, which has to be grown under highly non-equilibrium growth conditions, it is however necessary to demonstrate that electrically pumped lasing at room temperature can be achieved.

In this work we will present an electrically pumped Ga(AsBi)/(AlGa)As laser with a Bi fraction of 2.2% in the active material. Single quantum well (SQW) laser devices as well as Ga(AsBi)/(AlGa)As multi QW test structures were grown by metal organic vapor phase epitaxy (MOVPE) on exact GaAs (001) substrates. A commercially available AIX 200-GFR reactor system with Pd-purified H_2 as carrier gas at a reduced reactor pressure of 50 mbar was used. Trimethylaluminum (TMAl) and triethylgallium (TEGa) were used as group III precursors, tertiarybutylarsine (TBAs), and trimethylbismuth (TMBi) as group V precursors since low growth temperatures were required. Diethyl tellurium (DETe) and diethyl zinc (DEZn) were used as n- and p-type dopants, respectively. Furthermore p-type doping with carbon was realized by a reduced V/III ratio in the p-contact (AlGa)As layer.

Adding Bi to GaAs mainly affects the valence band and for low Bi concentration, the conduction band (CB) offset is small; we estimate the e1-CB(GaAs)-separation to be 12 meV. Therefore, to provide a suitable electron confinement (AlGa)As barriers were used. Adding Al into the barriers improves the electron confinement; however, this leads to a lower refractive index contrast relative to the cladding and hence causes poorer optical confinement. A reasonable compromise was found to be to use 20% Al in the barriers which significantly increases e1-CB($Al_{0.2}Ga_{0.8}As$) to approximately 144 meV. The quantum well was selected to be thick enough to avoid inhomogeneity effects. A schematic of the layer structure of the laser diode grown on n^+ substrate is given in Figure 1. The 6.4 nm thick Ga($AsBi_{0.022}$) QW is embedded between 150 nm thick ($Al_{0.2}Ga$)As barriers for electrical confinement in the active region. The 1.4 μm thick ($Al_{0.4}Ga$)As:Te and ($Al_{0.4}Ga$)As:C layers serve as waveguides as well as n and p contact layers, respectively. 250 nm of highly p-doped GaAs:Zn were grown on top of the structure to improve the metal-semiconductor contact. All (AlGa)As and GaAs layers were grown at 625 °C, adjusting the Al fraction by the ratio of the group III vapor pressures. In contrast, the Ga($AsBi_{0.022}$) QW was deposited at 400 °C using a pulsed growth mode where group III and group V precursors were alternately supplied to the reactor for 1 s without any pause in between. Subsequently, TEGa and TBAs were supplied for a few seconds with continuous precursor flow in order to consume the segregated Bi. This growth methodology of Ga(AsBi) QW structures using MOVPE was described earlier in more detail.[12] The temperature changes applied before and after the growth of the QW were performed during TBAs stabilized growth interruptions. It is assumed that the segregated Bi that is left at the surface after the QW growth is stopped gets evaporated during the heating to 625 °C. So far no influence of segregated Bi on the growth of the (AlGa)As barrier was found which supports this assumption.

To form broad area laser structures, 50 μm and 100 μm wide Au/Cr metal stripes were deposited on the top contact, and an Au/AuGe/Cr-based contact was deposited on the substrate backside. The sample was alloyed at 400 °C for ohmic contact formation. To avoid current spreading the GaAs:Zn-contact layer was etched-off using the metal stripes as mask. Since the device was grown on GaAs-substrates the laser

a)E-mail: kerstin.volz@physik.uni-marburg.de

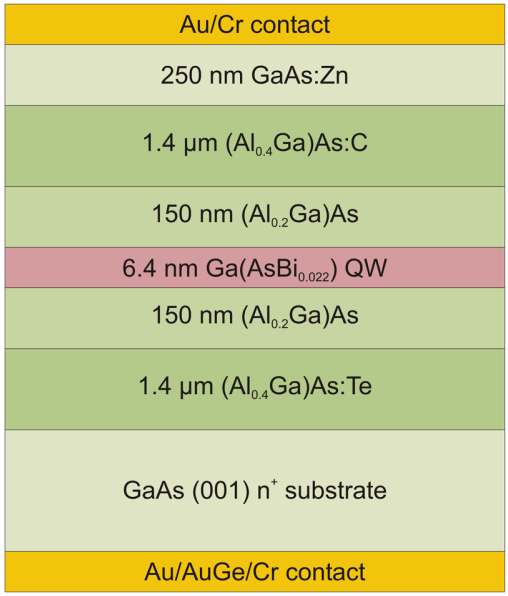

FIG. 1. Schematic view of the electrically pumped Ga($AsBi_{0.022}$)/(AlGa)As SQW laser diode.

facets were cleaved using standard techniques with a cavity length of 1 mm. The devices were measured *as-cleaved*.

Figure 2 shows high resolution X-ray diffraction (HR-XRD) omega-2theta scans around the GaAs (004) reflection, which were performed to investigate a Ga(AsBi)/(AlGa)As 5 × QW test structure that was grown under the same growth conditions as the active region of the device. Dynamical modeling of the experimental pattern allowed the determination of the Bi-fraction to 2.2% and layer thickness of 6.4 nm of the QW assuming GaBi lattice constant of 6.33 Å.[13]

Cross-sectional [-110] scanning transmission electron microscopy (STEM) high angle annular dark field (HAADF) images were taken in order to investigate the crystalline quality, the homogeneity of the composition, as well as the

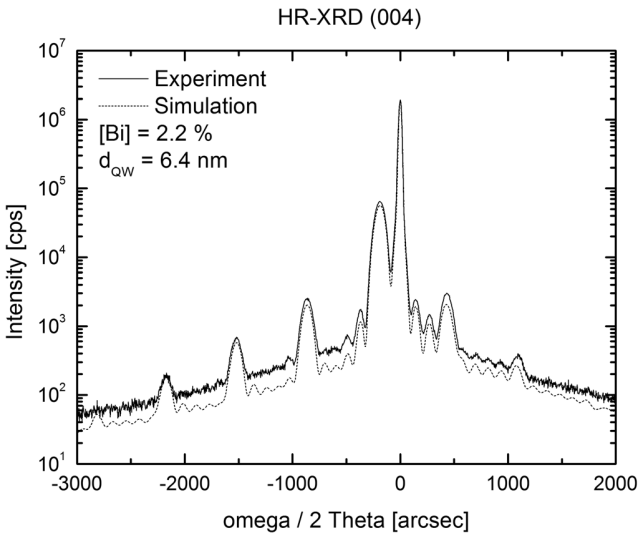

FIG. 2. HR-XRD (004) pattern of a Ga(AsBi)/(AlGa)As 5 × QW. The diffraction pattern is in good agreement with the dynamical simulation of a 5 × QW structure with a Bi fraction of 2.2 and a Ga(AsBi) layer thickness of 6.4 nm. The (AlGa)As barriers contain about 20% Al with a thickness of 22 nm, the sample is capped by a 7 nm thin GaAs layer.

layer thicknesses of the laser in more detail. Imaging took place with a JEOL JEM 2200 FS, which was operated at 200 keV using an aberration corrector for the probe. Figure 3 shows an overview HAADF [-110] STEM image of the laser device (a) as well as a high resolution image of the Ga(AsBi) QW (b). Since the contrast in the STEM HAADF mode is highly sensitive to the chemical composition of the layer (Z-contrast) a very high chemical homogeneity of the quantum well can be concluded from these investigations. In addition, the Ga(AsBi)/(AlGa)As transition can be clearly seen, indicating good control of the growth process. Furthermore, it is obvious that there is no degradation of the crystalline structure occurring during the TBAs stabilized growth interruptions that were applied during changes of the growth temperature.

Room temperature photoluminescence (PL) spectroscopy was performed using a continuous-wave (cw) 100 mW Ar-ion laser at a wavelength of 514 nm for excitation. The PL signal was dispersed in a 1 m grating monochromator (THR 1000, Jobin-Yvon) and collected by a cooled germanium detector applying standard lock-in techniques. The PL spectra of two 5 × QWs samples with Ga(AsBi) QW grown under the same growth conditions are shown in Figure 4. In contrast to the laser test structure with (AlGa)As barriers (black line), the sample with GaAs barriers was completely grown at 400 °C (grey line). The blue shift of the PL signal is explained by a thinner QW thickness using ($Al_{0.2}Ga$)As barriers since the growth is interrupted and the sample heated to ($Al_{0.2}Ga$)As growth temperature before all segregated Bi is consumed. Furthermore the higher confinement of the ($Al_{0.2}Ga$)As barriers compared to GaAs lead to a blue shift.

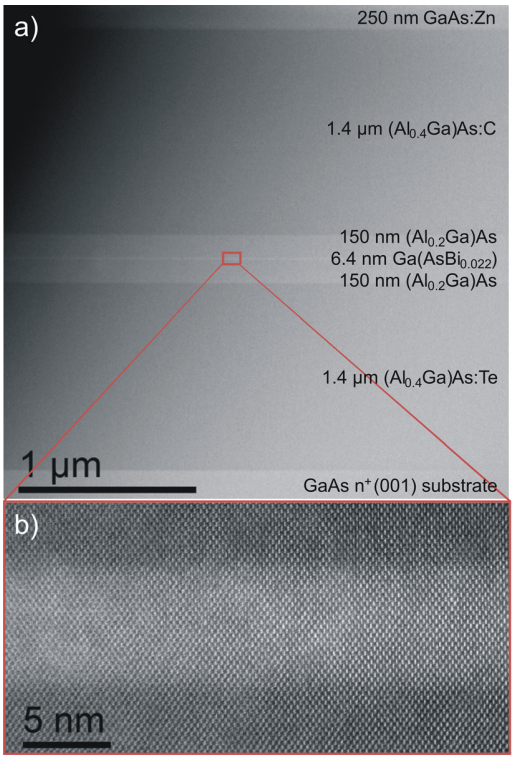

FIG. 3. (a) STEM HAADF overview image of the laser structure. (b) High resolution STEM image of the Ga(AsBi) QW showing smooth interfaces and a high chemical homogeneity.

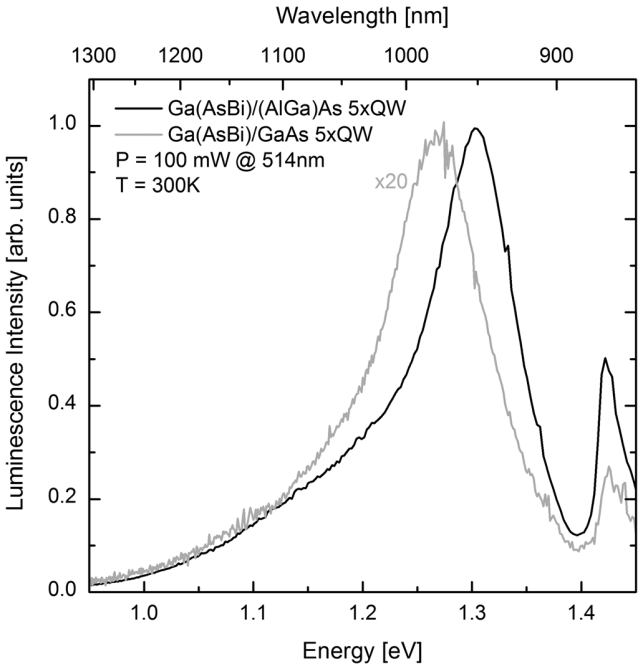

FIG. 4. Photoluminescence spectra of a Ga(AsBi)/GaAs and a Ga(AsBi)/(AlGa)As 5 × QW as test structure for the SQW laser diode.

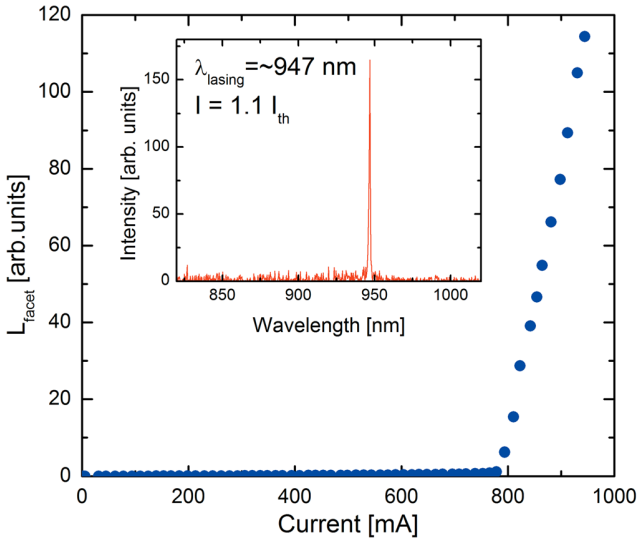

FIG. 5. L-I curve for a 50 × 1000 μm Ga(AsBi)/(AlGa)As SQW laser diode at room temperature and corresponding lasing spectrum (inset).

The integrated PL intensity is increased by a factor of 20 using $(Al_{0.2}Ga)As$ barriers. This is most likely due to improved carrier confinement and an annealing effect of the Ga(AsBi) QW due to the higher growth temperature of the $(Al_{0.2}Ga)As$ barrier. The relatively large full width at half maximum (FWHM) of about 120 meV might be related to disorder within the QW; however, comparable values were observed before in the Ga(AsBi) material system.[13,14]

The devices were measured as-cleaved under pulsed operation (200 ns long pulses at a frequency of 10 kHz) in order to reduce current heating effects. RT measurements were carried out on a probe station, where the facet emission was detected with a large area (InGa)As detector. Figure 5 shows the light-current (L-I) characteristic and the laser emission spectrum (inset) recorded at an injection current of ~1.1 J_{th} (where J_{th} is the threshold current density) at RT. Clear threshold behavior of the integrated emission intensity as a function of drive current is observed at RT as shown in Figure 5. This threshold behavior also corresponds to a pronounced spectral narrowing of the facet emission above threshold (as shown in the inset of Figure 5) providing further verification of laser action. J_{th} for the broad area SQW devices was measured to be ~1.56 kA/cm^2 with a lasing wavelength of 947 nm at RT. The voltage drop across devices at threshold was measured to be approximately 2 V. The J_{th} of these devices is relatively high compared to the standard (InGa)As lasers. However, we believe that room temperature lasing in such a complex material system, for which only one quantum well provides optical gain, is encouraging. This shows great promise for developing efficient IR lasers with this materials system. Investigations are currently underway to determine the cause of the high threshold currents; however, we expect that the device performance is affected by non-radiative defect-related recombination due to unoptimised low temperature growth.

In summary, we have developed high optical quality Ga(AsBi) (2.2% Bi) quantum well material using the MOVPE growth technique. Based upon this material development we have gone on to demonstrate electrically pumped lasing at room temperature with a threshold current density of 1.56 kA/cm^2 at an emission wavelength of 947 nm. These initial results show great promise for this material in laser applications, and further research is now focused on demonstrating longer wavelength lasers where higher bismuth fractions are expected to eliminate some of the major losses plaguing lasers in the near-infrared.

This work was funded by the European Union Framework 7 Project BIANCHO (FP7-257974), the Engineering and Physical Sciences Research Council (EPSRC), UK (EP/H005587/1 and EP/G064725/01), and the German Science Foundation (DFG: GRK1782 and VO805/4).

[1]K. Alberi, O. D. Dubon, W. Walukiewicz, K. M. Yu, K. Bertulis, and A. Krotkus, Appl. Phys. Lett. **91**, 051909 (2007).
[2]K. Oe, Jpn. J. Appl. Phys. **41**, 2801 (2002).
[3]S. J. Sweeney, "Bismide-alloys for higher efficiency infrared semiconductor lasers," in *22nd IEEE International Semiconductor Laser Conference (ISLC)*, 2010, pp. 111–112.
[4]Z. Batool, K. Hild, T. J. C. Hosea, X. Lu, T. Tiedje, and S. J. Sweeney, J. Appl. Phys. **111**, 113108 (2012).
[5]M. Usman, C. A. Broderick, A. Lindsay, and E. P. O'Reilly, Phys. Rev. B **84**, 245202 (2011).
[6]S. J. Sweeney and S. R. Jin, J. Appl. Phys. **113**, 043110 (2013).
[7]S. J. Sweeney, patent W02010/149978 (2010).
[8]A. F. Phillips, S. J. Sweeney, A. R. Adams, and P. J. A. Thijs, IEEE J. Sel. Top. Quantum Elect. **5**, 401 (1999).
[9]R. Lewis, D. Beaton, X. Lu, and T. Tiedje, J. Cryst. Growth **311**, 1872 (2009).
[10]N. Hossain, I. P. Marko, S. R. Jin, K. Hild, S. J. Sweeney, R. B. Lewis, D. A. Beaton, and T. Tiedje, Appl. Phys. Lett. **100**, 51105 (2012).
[11]Y. Tominaga, K. Oe, and M. Yoshimoto, Appl. Phys. Express **3**, 62201 (2010).
[12]P. Ludewig, N. Knaub, W. Stolz, and K. Volz, J. Cryst. Growth **370**, 186 (2013).
[13]S. Tixier, M. Adamcyk, T. Tiedje, S. Francoeur, A. Mascarenhas, P. Wei, and F. Schiettekatte, Appl. Phys. Lett. **82**, 2245 (2003).
[14]I. Moussa, H. Fitouri, Z. Chine, A. Rebey, and B. El Jani, Semicond. Sci. Technol. **23**, 125034 (2008).

6.6 Growth of Ga(AsBi) on GaAs by continuous flow MOVPE[1]

P. Ludewig, Z. L. Bushell, L. Nattermann, N. Knaub, W. Stolz, K. Volz, Journal of Crystal Growth **396**, 95 (2014). DOI: 10.1016/j.jcrysgro.2014.03.041.

Abstract

In this paper we discuss the epitaxial growth of Ga(AsBi) on GaAs under continuous precursor gas supply by metal organic vapor phase epitaxy (MOVPE). Due to the required low growth temperatures the all liquid precursors triethylgallium (TEGa), tertiarybutylarsine (TBAs) and trimethylbismuth (TMBi) were chosen. The influence of several growth parameters such as V/V and V/III ratio, the applied growth temperature and growth rate on the Bi incorporation was investigated. Layers containing up to 5% Bi with good chemical homogeneity and smooth Ga(AsBi)/GaAs hetero interfaces without metallic droplet formation were realized and beyond that incorporation of more than 7% Bi was shown. Furthermore it was found, that Bi acts as surfactant during the growth, reducing the growth rate and impurity incorporation and improving the integrated photoluminescence signal by several orders of magnitude.

The Authors contribution

My contribution to this work was the preparation of the Ga(AsBi) TEM samples and the investigation of them by means of STEM. Besides layer thickness determination, the investigation of the samples surfaces was part of the STEM investigation. Furthermore, I helped the author to interpret the STEM measurements.

1 Reprinted from *Journal of Crystal Growth **396** (2014) 95-99*, Copyright 2014, with permission from Elsevier.

Journal of Crystal Growth 396 (2014) 95–99

Contents lists available at ScienceDirect

Journal of Crystal Growth

journal homepage: www.elsevier.com/locate/jcrysgro

Growth of Ga(AsBi) on GaAs by continuous flow MOVPE

P. Ludewig [a,*], Z.L. Bushell [a,b], L. Nattermann [a], N. Knaub [a], W. Stolz [a], K. Volz [a]

[a] Material Science Center and Faculty of Physics, Philipps-Universität Marburg, Hans-Meerwein-Straße, Mehrzweckgebäude 02D34, 35032 Marburg, Germany
[b] Advanced Technology Institute and Department of Physics, University of Surrey, Guildford, Surrey GU2 7XH, United Kingdom

ARTICLE INFO

Article history:
Received 30 January 2014
Received in revised form
23 March 2014
Accepted 24 March 2014
Communicated by: C. Caneau
Available online 1 April 2014

Keywords:
A3. Metalorganic vapor phase epitaxy
B1. Bismuth compounds
B2. Semiconducting III–V materials
B2. Semiconducting gallium arsenide
B2. Semiconducting ternary compounds

ABSTRACT

In this paper we discuss the epitaxial growth of Ga(AsBi) on GaAs under continuous precursor gas supply by metal organic vapor phase epitaxy (MOVPE). Due to the required low growth temperatures, liquid precursors triethylgallium (TEGa), tertiarybutylarsine (TBAs) and trimethylbismuth (TMBi) were chosen. The influence of several growth parameters such as TMBi/V and V/III ratios, the applied growth temperature and growth rate on the Bi incorporation was investigated. Layers containing up to 5% Bi with good chemical homogeneity and smooth Ga(AsBi)/GaAs hetero-interfaces without metallic droplet formation were realized and beyond that incorporation of more than 7% Bi was shown. Furthermore it was found that Bi acts as surfactant during the growth, reducing the growth rate and impurity incorporation and improving the integrated photoluminescence signal by several orders of magnitude.

1. Introduction

The strong impact of Bi on the band structure of GaAs makes the Ga(AsBi) material system of interest for several applications, especially high efficiency infra red light sources. For Bi fractions exceeding approximately 10% the band gap becomes smaller than the spin–orbit splitting; hence Auger loss processes and intervalance band absorption involving transitions to the spin–orbit band could be suppressed [1,2]. Furthermore, it was shown that the temperature sensitivity of the band gap of this alloy is reduced with respect to the one of GaAs [3], allowing better control of the emission wavelength. However, the growth of high quality Ga(AsBi) crystals is still challenging. Recently we reported on room temperature lasing operation of a $Ga(As_{0.978}Bi_{0.022})$ single quantum well (SQW) laser diode [4]. Optical pumped lasing has already been demonstrated on $Ga(As_{0.941}Bi_{0.059})$ grown by molecular beam epitaxy (MBE) [5]. In MBE, growth Bi fractions $>10\%$ were already reported but growth temperatures as low as 200 °C are required. In metal organic vapor phase epitaxy (MOVPE) much higher growth temperatures (>350 °C) are needed in order to decompose the metal organic precursors; hence only Bi fractions up to 4% were reported so far [6–9]. In addition, the formation of metallic Bi droplets causes problems since surplus Bi segregates to the surface but does not desorb due to the low temperatures. In earlier studies we presented the growth of droplet free Ga(AsBi)/GaAs multi-quantum well structures that were grown in a pulsed growth mode [8]. In this case surplus Bi was consumed during the growth of the nominally Bi free GaAs barriers. However, the growth rate is limited to one monolayer per pulse and the control of the layer thickness as well as the deposition of bulk layers is very challenging. Furthermore this growth mode, where the Bi surface coverage changes all the time, is not recommendable for the deposition of quaternary material systems as e.g. Ga(NAsBi) and (GaIn)(AsBi) which extend the usage of the dilute bismides [1,2,10,11].

In the present work we will discuss the MOVPE growth of Ga(AsBi) layers where all growth parameters are adjusted very carefully and therefore continuous growth of high quality and droplet free bulk structures is possible. This not only enables investigations of Bi incorporation and the optical properties depending on several parameters but also analysis of the impact of Bi on the growth rate and the impurity incorporation.

2. Experimental procedure

Ga(AsBi) single layers of about 50–100 nm thickness were grown by MOVPE on exact GaAs (001) substrates. Growth took place in a commercially available horizontal reactor system with gas flow rotation (AIX 200-GFR-reactor) at a reduced reactor pressure of 50 mbar using Pd purified H_2 as carrier gas. Due to the required low growth temperatures of 375 °C and 400 °C, liquid precursors triethylgallium (TEGa), tertiarybutylarsine (TBAs) and

* Corresponding author. Tel.: +49 6421 2825713.
E-mail address: peter.ludewig@physik.uni-marburg.de (P. Ludewig).

http://dx.doi.org/10.1016/j.jcrysgro.2014.03.041
0022-0248/

trimethylbismuth (TMBi) were chosen. Most of the samples were heated to 625 °C under TBAs stabilization after the Ga(AsBi) deposition in order to grow a 20 nm thick GaAs capping layer. The heating process takes about 2 min and enables desorption of surplus Bi from the surface. In contrast to our earlier studies, where the segregated Bi is also incorporated during the growth of the subsequent GaAs layers that were grown at the same temperature as that of the Ga(AsBi) layer [8], here one can be sure that the Bi is incorporated only in the nominal Ga(AsBi) layers and therefore determine the growth rates. It was already shown before that the Ga(AsBi) material is not negatively affected by these temperature changes and sharp Ga(AsBi)/GaAs hetero-interfaces can be realized [4]. The Bi fraction and layer thickness were determined by modeling the high resolution x-ray diffraction (HR-XRD) pattern around the (004) GaAs substrate peak assuming 6.33 Å as GaBi lattice constant [12]. In some cases cross sectional scanning transmission electron microscopy (STEM) investigations were carried out to confirm these measurements and to analyze the homogeneity of the Bi incorporation as well as the Ga(AsBi)/GaAs interfaces. Surface morphologies and the presence of metal droplets were studied by atomic force microscopy (AFM). Room temperature photoluminescence (PL) measurements were then performed to relate the optical properties of the samples to the composition and the applied growth conditions. The PL measurements were carried out using a continuous-wave (cw) Ar-ion laser at a wavelength of 514 nm for excitation. The PL signal was dispersed in a 1 m grating monochromator and collected by a cooled germanium detector applying the standard lock-in technique.

3. Results and discussion

First the Bi incorporation and growth rate using optimized continuous growth conditions will be discussed in relation to the TMBi/V and V/III ratios as well as the temperature. Then we will address the structural quality and finally the effect of Bi as a surfactant on the carbon incorporation and the optical properties.

The filled circles in Fig. 1 show the dependence of the Bi fraction of the Ga(AsBi) layers on the TMBi/V ratio when only TMBi was changed. All samples were grown at 400 °C and capped with GaAs at 625 °C; the Ga(AsBi) layer thickness varies between 50 nm and 80 nm. Compared to the samples discussed in [8] the growth parameters were optimized to reduce Bi segregation and enable the growth of thick single layer samples under continuous precursor supply. The TEGa partial pressure here was increased to 0.042 mbar, which corresponds to a GaAs growth rate of 0.43 nm/s at 400 °C and the TBAs/TEGa ratio was slightly reduced to 1.9. As for the pulsed growth of the MQW structures the Bi fraction first increases with the amount of TMBi in the reactor and then levels out at about 3.8% in the present case. Since the GaAs cap is grown at 625 °C where the segregated Bi is not incorporated into the crystal it is possible to determine the Ga(AsBi) growth rate directly from its layer thickness and growth time (open circles Fig. 1). We find that with increasing TMBi the growth rate is reduced by about 33% and levels out as the Bi fraction does. As the growth rate is usually determined only by the group III precursor, we assume that the presence of Bi or the not yet fully decomposed TMBi at the surface either reduces the decomposition of TEGa or hinders it from sticking to the surface. Gas phase reactions seem unlikely here since the maximum applied TMBi/TEGa ratio is only 0.031.

In order to investigate the influence of the applied V/III ratio the TBAs partial pressure was varied starting from the sample with TMBi/V = 0.02 and TBAs/TEGa = 1.9 in Fig. 1, where the Bi limitation has already set in (marked with *). The determined Bi fractions and growth rates of this series are plotted in Fig. 2 (black circles). We observe that the Bi fraction increases nearly linearly up to 4.4% with decreasing TBAs, which is due to the fact that As and Bi are in competition for the group V sublattice places. When the TBAs gets too low the Bi fraction decreases again, which could be related to the low V/III (< 1) ratio leading to a Ga rich surface. At this point it needs to be pointed out that the given numbers are the gas phase ratios of the precursors, which are not necessarily the same as the pure metal ratios at the surface since the decomposition characteristics need to be taken into account at these low growth temperatures. Besides the increasing Bi fraction the growth rate is reduced even more than observed from the variation of the TMBi. The sample with the maximum Bi fraction of 4.4% has a growth rate of only 25% of that of the pure GaAs sample. This underlines the assumption that the more Bi or TMBi rich the surface the less the decomposition of TEGa or sticking to the surface; however, an influence of the low V/III ratio is not excluded. On the other hand, if the TBAs supply is too high (here TBAs/TEGa > 2.5) the growth rate drops along with the Bi fraction. This behavior is not yet understood and still under investigation but was also observed for

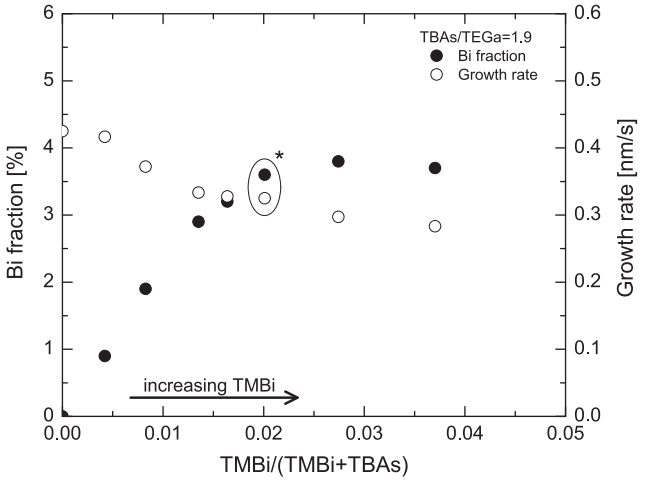

Fig. 1. Bi fraction (filled circles) and growth rate (open circles) of Ga(AsBi) samples grown at 400 °C where only the TMBi partial pressure was varied. Under the given growth conditions the Bi fraction levels out at about 3.8%. In addition, one can see that the growth rate decreases with increasing amount of TMBi.

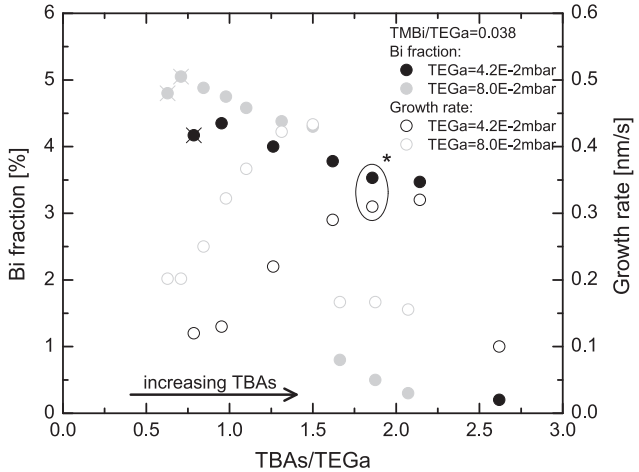

Fig. 2. Bi fraction (filled circles) and growth rate (open circles) of Ga(AsBi) samples grown at 400 °C where only the TBAs partial pressure was varied. In a narrow range of TBAs/TEGa ratios the Bi fraction increases while the growth rate decreases. Outside this range the Bi incorporation drops. The same behavior is observed for higher growth rates (gray circles) where the Bi fraction rises up to 5%. Data points of samples with volcano-like structures at the surface are crossed.

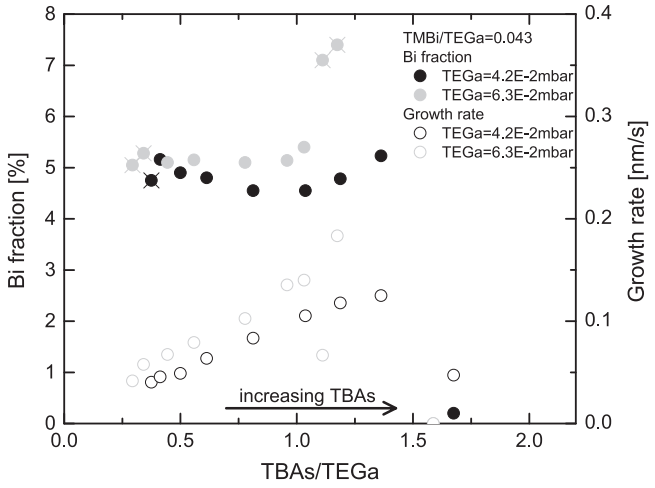

Fig. 3. Bi fraction (filled circles) and growth rate (open circles) of Ga(AsBi) samples grown at 375 °C where only the TBAs partial pressure was varied. We observe the same trend as that at 400 °C (Fig. 2). In addition, there is a small range where the higher growth rate due to the higher TBAs partial pressure leads to again increasing Bi fraction of up to 7.4%. Data points of samples with Bi droplets at the surface are crossed.

several sets of other samples. The gray circles in Fig. 2 show a series where the amount of all precursors given to the reactor was increased by a factor of 1.9. (Within the range of conditions of our study, we found a clear linear relation between the amount of TEGa in the reactor and the growth rate under a given TMBi/V ratio.) The growth rate and Bi incorporation behave in the same manner for the lower precursor flows but are shifted to lower TBAs/TEGa ratio. Increasing the growth rate also increases the Bi fraction for the same V/III ratio, as expected for this metastable material since there is less time for the Bi to escape the crystal.

Further investigations on the Ga(AsBi) growth were carried out at a reduced growth temperature of 375 °C. Fig. 3 summarizes the results of the TBAs variation for partial pressure of TEGa =0.042 mbar (black circles) and the 1.5 times higher value of 0.063 mbar (gray circles). The TMBi partial pressure is again chosen such that the Bi incorporation is in the saturated regime. The trend is very similar to what was observed for the growth at 400 °C: the growth rate decreases with decreasing TBAs supply and also drops at too high TBAs values (here TBAs/TEGa > 1.5) and the Bi fraction increases at low TBAs values and then decreases at approximately TBAs/TEGa < 0.4. However, in contrast to the observation at 400 °C the Bi fraction shows differing behavior for higher TBAs/TEGa ratios in the range of 1–1.5. In this growth regime we find a very narrow window where the Bi incorporation rises to values above 7% before it is suppressed by too much As. An explanation would be that in this regime the increasing growth rate, which supports the Bi incorporation, overbalances the higher amount of As that would suppress the Bi incorporation. In contrast to all other samples discussed so far, in this growth regime the samples show very inhomogeneous Bi distributions, especially those with Bi fractions higher than 7%. Whereas the plotted values were determined in the center region of the 50 mm wafer of 15–20 mm diameter, the outer area shows no presence of Ga(AsBi). Either no growth takes place at all in the outer area or no Bi gets incorporated. The reasons might be small changes in the gas phase composition and temperature across the wafer that lead to disadvantageous growth conditions as in the range of TBAs/TEGa > 1.5.

The surface morphologies of all samples discussed above were investigated by atomic force microscopy. For the series where only the amount of TMBi was varied, all samples up to TMBi/V=0.027 show smooth surfaces of the GaAs cap (Fig. 4(a)). In case of the sample with TMBi/V=0.037 we find volcano-like structures at the surface (Fig. 4(b)) which originate most likely from evaporated Bi droplets that leave holes behind. The structures consist of GaAs as confirmed by STEM investigations (not shown here) and arise most probably by crystallization of liquid Ga that was dissolved in the evaporated Bi droplets and As that is used for group V stabilization [13]. These structures are observed also in the sample series where the TBAs is varied (Fig. 2) on those samples with low V/III-ratios where the Bi fraction slightly decreases again. The sample series at 375 °C (Fig. 3) was grown without GaAs cap, and we find Bi droplets not only for this low V/III regime but also for the high V/III region, for the samples with Bi fractions above 7%. The surface morphologies of the samples in between these ranges do not show any indication of metallic droplet formation during the growth. In Fig. 4(c) the high angle annular dark field (HAADF) STEM image in [−110] direction of a sample with about 5% Bi is shown. The sample was grown at 400 °C in the TMBi/V regime, where the growth rate levels out, the Bi incorporation has its maximum (see Fig. 2) and already small amounts of the volcano-like structures appear at the surface. The contrast in this imaging mode is dependent on the atomic number Z of the atoms, making those group V columns with Bi atoms appear brighter than pure As columns. We find smooth and abrupt heterointerfaces between the Ga(AsBi) and GaAs layers showing again the stability of this material system versus the change of the growth temperature from 400 °C to 625 °C. In addition the contrast in the Ga(AsBi) layer is homogenous and no signs of Bi clustering could be found. Overall this structural analysis shows that at least up 5% Bi can be incorporated into GaAs by MOVPE growth with high crystalline quality.

One main issue that occurs in low temperature MOVPE is the unintentional incorporation of C into the crystal from the organic groups of the precursors. In order to determine the amount of C in the Ga(AsBi) layers, secondary ion mass spectroscopy (SIMS) measurements were carried out on structures containing different amounts of Bi. The results for five samples from the series where the solid Bi fraction was adjusted by the TMBi partial pressure (see Fig. 1) including the Bi free sample, are plotted in Fig. 5. Interestingly the highest amount of C with about 5×10^{19} C atoms/cm^2 was found in the low temperature (LT) GaAs sample, which shows that the main C doping seems to come from the TEGa precursor since an incorporation of C from the tertiarybutyl-group of the TBAs is very unlikely. The more the Bi added to the surface during the growth, the lower the amount of C incorporated in the epilayer. For the sample with the highest TMBi/V ratio of 0.0275, which was grown in the Bi saturation regime, the C level is only 2×10^{16} C atoms/cm^2 (close to the detection limit) in the layer and therefore more than three orders of magnitude lower than in the LT GaAs sample. This might be related to the fact that the segregated Bi occupies the group V sites at the surface during growth and with that hinders the incorporation of C, which is incorporated on group V lattice sites in GaAs [14]. Only at the lower interface could a C doping of about 10^{18} C atoms/cm^2 be detected since it takes some time at the beginning of the Ga(AsBi) layer growth until a certain Bi coverage is reached [8].

In addition, room temperature photoluminescence (PL) measurements of these samples were performed to investigate their optical properties (Fig. 6(a)). With increasing TMBi partial pressure the integrated PL signal monotonically increases by several orders of magnitude even though the Bi fraction again decreases for the highest TMBi/V ratio. These investigations show that the often observed effect of improved PL intensity with increasing Bi fraction [16,17] is most probably not related to the Bi fraction in the crystal, but instead to the larger amount of Bi at the surface during growth that is needed for higher Bi incorporation. The Bi

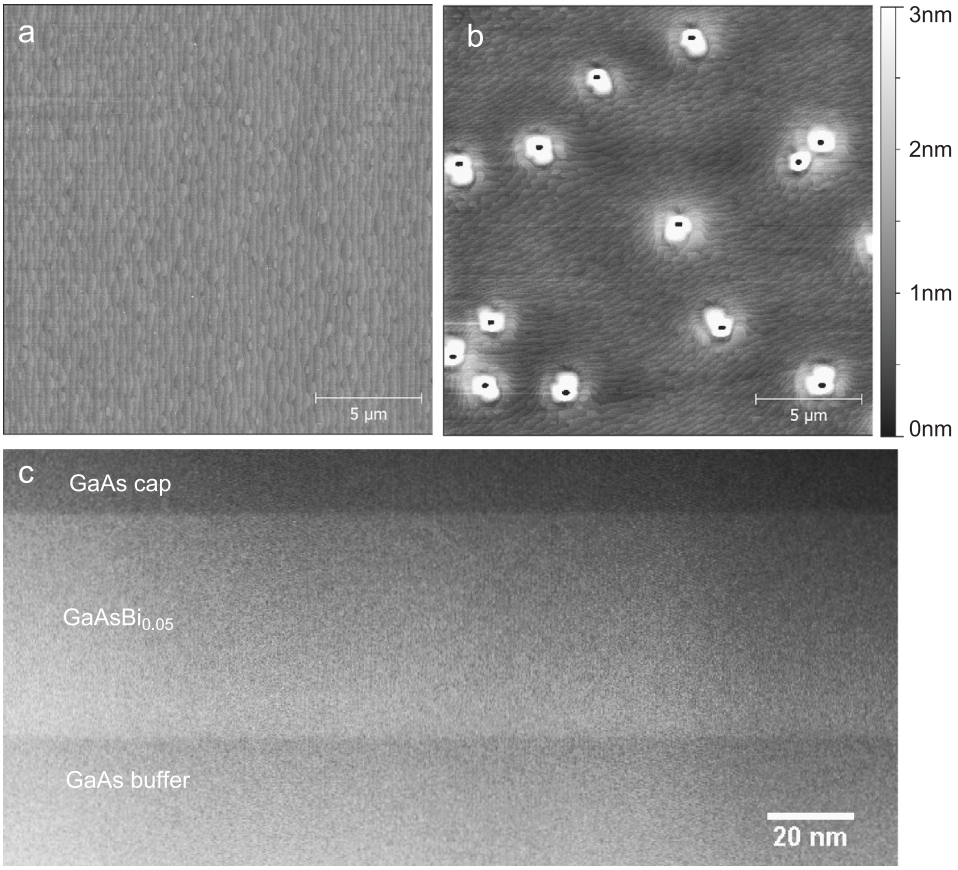

Fig. 4. Surface morphologies of the GaAs cap of the sample with TMBi/V=0.027 (a) and TMBi/V=0.037 (b) from the series in Fig. 1 where only TMBi was varied. While in (a) no signs of metallic droplets can be found, the volcano-like structures in (b) form when Bi droplets are evaporated at the higher temperatures. The cross section HAADF-STEM image in [−110] direction of a sample with 5% Bi (c) shows smooth interfaces and high chemical homogeneity.

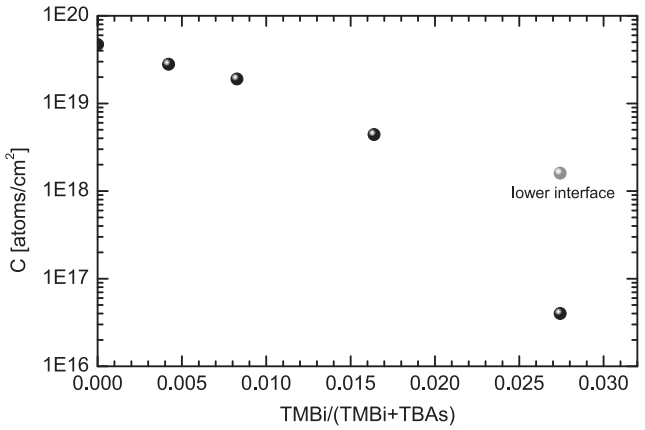

Fig. 5. Carbon incorporation dependence on the TMBi partial pressure. With increasing amount of Bi on the surface during the growth, the unintentional C incorporation decreases by several orders of magnitude.

acts as a surfactant and hence reduces the amount of defects such as antisites or vacancies and also the incorporation of C, which then leads to an improved PL intensity.

The PL peak energy of several samples discussed above is plotted in Fig. 6(b). We find a very good agreement of our measurements with calculations of the Ga(AsBi) bandgap taken from [15] (dashed line) which confirms the investigation of the composition by HR-XRD. In addition the linewidth (full width at half maximum, FWHM) of the PL spectra is plotted versus the Bi fraction. Here we find quite high values in the low Bi fraction regime (< 3.5%) of about 130–140 meV. These values might be due to the superposition of the PL signal coming from the Ga(AsBi) layer with the signal from a defect level at roughly 0.97 eV that is observed in Fig. 6(a). This defect level also appears in the PL spectrum of a Bi free GaAs sample that was grown at the same conditions as those of the Ga(AsBi) samples; hence it must be related to a defect occurring in the low temperature growth of GaAs such as e.g. antisites or vacancies. For higher Bi fractions the Ga(AsBi) peak becomes more intense and therefore the defect level has less influence on the PL spectra and the linewidth shrinks to about 80–90 meV which is often observed in this material system [16–18] and is most probably due to the disorder.

4. Summary

The growth of Ga(AsBi) by MOVPE applying continuous precursor flows is dominated by the surface Bi. The Bi fraction increases with the amount of Bi at the surface, reaching a maximum value depending on the applied growth conditions. This maximum increases with the growth rate and increases with decreasing temperature and TBAs supply. Applying relatively high growth rates and V/III ratios in the range of 0.5–2, we were able to deposit homogenous Ga(AsBi) layers with up to 5% Bi and smooth Ga(AsBi)/GaAs heterointerfaces. There is a very narrow growth regime at 375 °C where even more than 7% of Bi was incorporated but at the cost of homogeneity and morphology. It was also found that besides the Bi incorporation, the growth rate of the Ga(AsBi) depends on the TMBi partial pressure, which is most likely related to a suppressed TEGa decomposition due to the

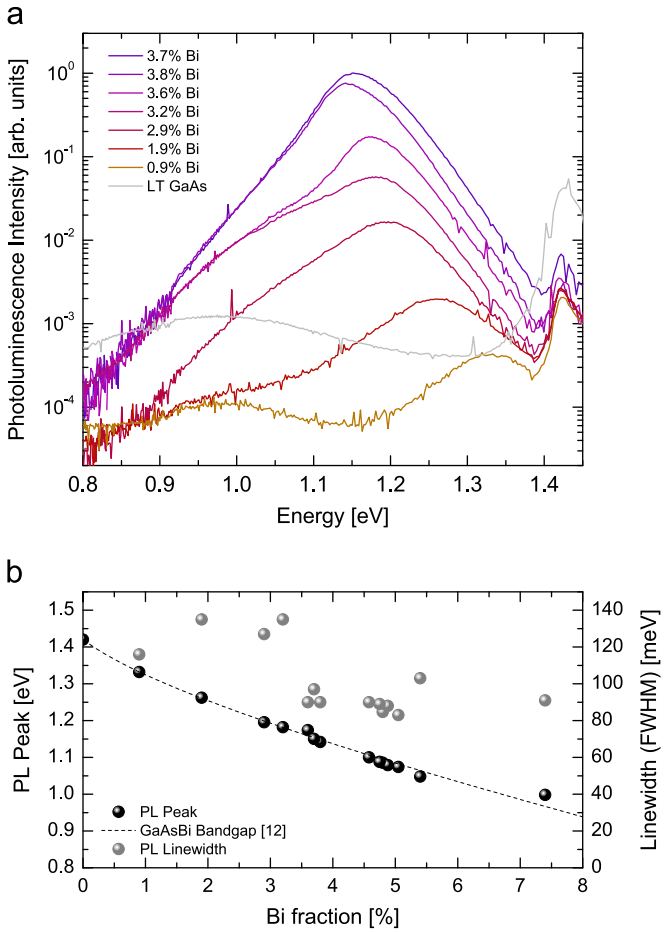

Fig. 6. Room temperature photoluminescence spectra (a) of the Ga(AsBi) samples plotted in Fig. 1. The integrated PL intensity does not scale with the Bi fraction but with the applied TMBi partial pressure due the surfactant effect of Bi. The peak positions (b) of the samples are in very good agreement with the calculated values taken from [15]. The quite high linewidth of the PL spectra for samples with low Bi fraction could be due to a superposition of the PL of the Ga(AsBi) layer and an additional peak at about 0.97 eV. This peak is most likely due to a defect level such as antisites or vacancies since it is also observed in the spectra of a GaAs sample that was grown under the same conditions as those of the Ga(AsBi) samples but without TMBi (LT GaAs).

presence of (TM)Bi at the surface. Bi acts as a surfactant during the growth and improves the photoluminescence signal and quenches the C incorporation.

Acknowledgments

This work was funded by the European Union Framework 7 Project BIANCHO (FP7-257974) and the German Science Foundation (DFG: VO805/4 and DFG: GRK1782). Z.L. Bushell acknowledges financial support from an ERASMUS grant through the European Commission Lifelong Learning Programme.

References

[1] C.A. Broderick, M. Usman, S.J. Sweeney, E.P. O'Reilly, Semicond. Sci. Technol. 27 (2012) 094011, http://dx.doi.org/10.1088/0268-1242/27/9/094011.
[2] S.J. Sweeney, S.R. Jin, J. Appl. Phys. 113 (2013) 043110, http://dx.doi.org/10.1063/1.4789624.
[3] K. Oe, H. Okamoto, Japn. J. Appl. Phys. 37 (1998) L1283–L1285, http://dx.doi.org/10.1143/JJAP.37.L1283.
[4] P. Ludewig, N. Knaub, N. Hossain, S. Reinhard, L. Nattermann, I.P. Marko, S.R. Jin, K. Hild, S. Chatterjee, W. Stolz, S.J. Sweeney, K. Volz, Appl. Phys. Lett. 102 (2013) 242115, http://dx.doi.org/10.1063/1.4811736.
[5] T. Fuyuki, R. Yoshioka, K. Yoshida, M. Yoshimoto, Appl. Phys. Lett. 103 (2013) 202105, http://dx.doi.org/10.1063/1.4830273.
[6] K. Oe, J. Cryst. Growth 239 (2002) 1481–1485, http://dx.doi.org/10.1016/S0022-0248(01)02301-6.
[7] I. Moussa, H. Fitouri, A. Rebey, B. El Jani, Thin Solid Films 516 (2008) 8372–8376, http://dx.doi.org/10.1016/j.tsf.2008.04.062.
[8] P. Ludewig, N. Knaub, W. Stolz, K. Volz, J. Cryst. Growth 370 (2013) 186–190, http://dx.doi.org/10.1016/j.jcrysgro.2012.07.002.
[9] K. Forghani, A. Anand, L.J. Mawst, T.F. Kuech, J. Cryst. Growth 380 (2013) 23–27, http://dx.doi.org/10.1016/j.jcrysgro.2013.05.033.
[10] I.P. Marko, Z. Batool, K. Hild, S.R. Jin, N. Hossain, T.J.C. Hosea, J.P. Petropoulos, Y. Zhong, P.B. Dongmo, J.M.O. Zide, S.J. Sweeney, Appl. Phys. Lett. 101 (2012) 221108, http://dx.doi.org/10.1063/1.4768532.
[11] Z.L. Bushell, P. Ludewig, N. Knaub, Z. Batool, K. Hild, W. Stolz, S.J. Sweeney and K. Volz, Growth and characterisation of Ga(NAsBi) alloy by metal organic vapour phase epitaxy, J. Cryst. Growth. http://dx.doi.org/10.1016/j.jcrysgro.2014.03.038, in press.
[12] S. Tixier, M. Adamcyk, T. Tiedje, S. Francoeur, A. Mascarenhas, P. Wei, F. Schiettekatte, Appl. Phys. Lett. 82 (2003) 2245–2247, http://dx.doi.org/10.1063/1.1565499.
[13] K. Reyes, P. Smereka, D. Nothern, J.M. Millunchick, S. Bietti, C. Somaschini, S. Sanguinetti, C. Frigeri, Phys. Rev. B 87 (2013) 165406, http://dx.doi.org/10.1103/PhysRevB.87.165406.
[14] T.F. Kuech, M.a. Tischler, P.-J. Wang, G. Scilla, R. Potemski, F. Cardone, Appl. Phys. Lett. 53 (1988) 1317, http://dx.doi.org/10.1063/1.100008.
[15] C.A. Broderick, M. Usman, E.P. O'Reilly, Semicond. Sci. Technol. 28 (2013) 125025, http://dx.doi.org/10.1088/02681242/28/12/125025.
[16] A.R. Mohmad, F. Bastiman, C.J. Hunter, J.S. Ng, S.J. Sweeney, J.P.R. David, Appl. Phys. Lett. 99 (2011) 42107, http://dx.doi.org/10.1063/1.3617461.
[17] X. Lu, D.A. Beaton, R.B. Lewis, T. Tiedje, Y. Zhang, Appl. Phys. Lett. 95 (2009) 41903, http://dx.doi.org/10.1063/1.3191675.
[18] A.R. Mohmad, F. Bastiman, J.S. Ng, S.J. Sweeney, J.P.R. David, Appl. Phys. Lett. 98 (2011) 122107, http://dx.doi.org/10.1063/1.3565244.

6.7 Growth and characterisation of Ga(NAsBi) alloy by metal organic vapour phase epitaxy[1]

Z. L. Bushell, P. Ludewig, N. Knaub, Z. Batool, K. Hild, W. Stolz, S. J. Sweeney, K. Volz, Journal of Crystal Growth **396**, 79 (2014). DOI: 10.1016/j.jcrysgro.2014.03.038.

Abstract

This paper summarises results of the epitaxial growth of Ga(NAsBi) by metal organic vapour phase epitaxy (MOVPE) and the subsequent optical and structural characterisation of the samples. Ga(NAsBi)/GaAs multi quantum well (MQW) samples are grown at 400 °C and single layers at 450 °C on GaAs (001) substrates. Triethylgallium (TEGa), tertiarybutylarsine (TBAs), trimethylbismuth (TMBi) and unsymmetrical dimethylhydrazine (UDMHy) are used as precursors. Secondary ion mass spectrometry (SIMS) shows that the Bi content is independent of the N content in the alloy. It is found that the N content depends on both UDMHy and TMBi supply during growth. High resolution X-ray diffraction (HR-XRD), scanning transmission electron microscopy (STEM) and atomic force microscopy (AFM) measurements show that samples with good crystalline quality can be realised. For samples containing 1.8% Bi and up to 1.8% N grown at 450 °C, photoreflectance spectroscopy (PR) shows a decrease in the band gap with increasing N content of -141±22 meV/%N.

The Authors contribution

My contribution part of this work was the preparation of Ga(NAsBi) MQW samples for STEM HAADF investigations. The investigations of the Ga(NAsBi) MQW structure via STEM included the determination of each Ga(NAsBi) QW layer thickness for confirming the results from HR-XRD measurements. Moreover, I helped Zoe Bushell with the interpretation of the STEM images.

1 Reprinted from *Journal of Crystal Growth **396** (2014) 79-84*, Copyright 2014, with permission from Elsevier.

Journal of Crystal Growth 396 (2014) 79–84

Contents lists available at ScienceDirect

Journal of Crystal Growth

journal homepage: www.elsevier.com/locate/jcrysgro

Growth and characterisation of Ga(NAsBi) alloy by metal–organic vapour phase epitaxy

Z.L. Bushell [a,b,*], P. Ludewig [a], N. Knaub [a], Z. Batool [b], K. Hild [b], W. Stolz [a], S.J. Sweeney [b], K. Volz [a]

[a] Material Science Center and Faculty of Physics, Philipps-Universität Marburg, 35032 Marburg, Germany
[b] Advanced Technology Institute and Department of Physics, University of Surrey, Guildford, Surrey GU2 7XH, United Kingdom

ARTICLE INFO

Article history:
Received 31 January 2014
Received in revised form
21 March 2014
Accepted 25 March 2014
Communicated by: C. Caneau
Available online 1 April 2014

Keywords:
A3. Metal–organic vapour phase epitaxy
B1. Bismuth compounds
B1. GaNAsBi
B1. Nitrides
B2. Semiconducting III–V materials
B2. Semiconducting quaternary alloys

ABSTRACT

This paper summarises results of the epitaxial growth of Ga(NAsBi) by metal–organic vapour phase epitaxy (MOVPE) and the subsequent optical and structural characterisations of the samples. Ga(NAsBi)/GaAs multi-quantum well (MQW) samples are grown at 400 °C and single layers at 450 °C on GaAs (001) substrates. Triethylgallium (TEGa), tertiarybutylarsine (TBAs), trimethylbismuth (TMBi) and unsymmetrical dimethylhydrazine (UDMHy) are used as precursors. Secondary ion mass spectrometry (SIMS) shows that the Bi content is independent of the N content in the alloy. It is found that the N content depends on both UDMHy and TMBi supply during growth. High resolution X-ray diffraction (HR-XRD), scanning transmission electron microscopy (STEM) and atomic force microscopy (AFM) measurements show that samples with good crystalline quality can be realised. For samples containing 1.8% Bi and up to 1.8% N grown at 450 °C, photoreflectance spectroscopy (PR) shows a decrease in the band gap with increasing N content of 141 ± 22 meV/% N.

1. Introduction

The III–V alloy Ga(NAsBi) has several important properties that make it an interesting material for infrared photonic devices. Band anticrossing (BAC) interactions in both the conduction band and valence band due to the incorporation of dilute amounts of nitrogen and bismuth, respectively, into GaAs lead to a strong reduction in the bandgap [1]. Due to the compensation in strain between the relatively small N atoms and relatively large Bi atoms, it is predicted to be possible to cover a range of bandgaps from 0.2 eV to 1.4 eV whilst keeping the strain on GaAs to within ± 1.5% [1]. The incorporation of bismuth also increases the spin–orbit splitting [2], which could allow suppression of Auger recombination and inter-valence band absorption [3]. The bandgap of Ga(NAsBi) is also less temperature sensitive than conventional III–V alloys [4], which offers the potential for devices with improved temperature stability.

The growth of Ga(AsBi) has been demonstrated by both molecular beam epitaxy (MBE) and metal–organic vapour phase epitaxy (MOVPE), with Bi content of more than 10% in MBE growth [5,6] and up to 7.4% by MOVPE [7]. For successful growth of the metastable Ga(AsBi), growth conditions must be carefully controlled within a narrow range with low growth temperatures and low V/III ratios required [7–9]. Ga(NAsBi) bulk layers have previously been grown successfully by MBE [10,11] but there have been no previous reports on growth by MOVPE. In this paper we present the successful growth of Ga(NAsBi) MQWs and single layers by MOVPE and discuss their structural and optical properties.

2. Experimental procedure

Ga(NAsBi)/GaAs multi-quantum well (MQW) and single layer samples were grown on semi-insulating GaAs (001) substrates by MOVPE. Growth took place in a commercially available AIX 200-GFR horizontal reactor system, using Pd-purified H_2 carrier gas at a reduced reactor pressure of 50 mbar. Triethylgallium (TEGa), tertiarybutylarsine (TBAs), trimethylbismuth (TMBi) and unsymmetrical dimethylhydrazine (UDMHy) were used as precursors for Ga, As, Bi and N respectively, since these decompose at the low growth temperatures required. Growth temperatures of 400 °C and 450 °C were used for the Ga(NAsBi) layers and 625 °C for GaAs. Temperature changes before and after the Ga(NAsBi) growth were performed during TBAs stabilised growth interruptions. The UDMHy/TBAs ratio was varied up to a maximum of 1.0 and the TMBi/TBAs ratio was varied in the range of 7.7×10^{-3} – 3.0×10^{-2}.

* Corresponding author.
E-mail address: zb00031@surrey.ac.uk (Z.L. Bushell).

http://dx.doi.org/10.1016/j.jcrysgro.2014.03.038
0022-0248/

The MQW samples grown at 400 °C had a constant TEGa supply of 4.2×10^{-2} mbar and TBAs/TEGa ratio of 1.2 and the growth rate was around 1 μm/h. The single layer samples grown at 450 °C had a constant TEGa supply of 3.2×10^{-2} mbar and TBAs/TEGa ratio of 1.9 and the growth rate was in the range of 2–3 μm/h in order to incorporate sufficient Bi at the higher growth temperature.

Dynamical modelling to fit the experimental results from high resolution X-ray diffraction (HR-XRD) omega–2theta scans around the GaAs (004) reflection was used to determine the layer thicknesses and relationship between Bi and N contents. Two samples containing Ga(NAsBi) and Ga(AsBi) layers were also analysed by secondary ion mass spectrometry (SIMS) to investigate the relative Bi and N contents of the layers. Cross-sectional [010] scanning transmission electron microscopy (STEM) high angle annular dark field (HAADF) images were obtained using a JEOL JEM 2200 FS in order to investigate the crystalline quality and layer thicknesses in more detail. In the STEM HAADF mode the intensity is sensitive to the chemical composition of the layer (Z-contrast) so it can be used to investigate chemical homogeneity in the material. STEM samples were prepared conventionally, using Ar-ion milling as the final preparation step. Atomic force microscopy was used to study the surface morphology. Room temperature (RT) photoluminescence spectroscopy (PL) and photomodulated reflectance (PR) were performed to analyse the optical properties of the samples. The PL measurements were carried out using the 514 nm line of a continuous-wave Ar-ion laser for excitation. The PL signal was dispersed in a 1 m grating monochromator (THR 1000, Jobin-Yvon) and collected by a cooled germanium detector applying the standard lock-in technique. In addition to PL, PR, a form of modulation spectroscopy [12], is a very useful non-destructive technique to determine the band gap and other critical points in the band structure of semiconductors. To modulate the sample dielectric function a 514 nm argon ion laser chopped at a frequency of 333 Hz with output power of 113 mW was used, illuminating the same spot on the sample where a monochromatic probe beam was reflected off the sample. The output PR signal, the fractional change in the reflectivity $\Delta R/R$, was measured with a lock-in amplifier connected to an InGaAs detector.

3. Results and discussion

In this section the influence of N content on Bi incorporation in Ga(NAsBi) is first discussed. The influence of both UDMHy and TMBi supply on the growth of Ga(NAsBi) MQWs at 400 °C is then investigated and the structural properties are examined by STEM. Finally, the growth of Ga(NAsBi) single layers at 450 °C is investigated and the optical properties are discussed.

Dynamical modelling of HR-XRD results can only determine a linear relationship between Bi and N contents in the quaternary alloy, not the absolute values of each. Therefore a sample was produced for SIMS analysis with both Ga(AsBi) and Ga(NAsBi) ~30 nm layers separated by a 100 nm GaAs barrier. Both layers were grown under identical conditions at 400 °C apart from the addition of N to the Ga(NAsBi) layer with UDMHy/TBAs = 1. The results of the SIMS analysis are shown in Fig. 1. It can be seen that the Bi content of the two layers is approximately equal, independent of the addition of N. It is therefore assumed when performing subsequent fitting of dynamical modelling to the HR-XRD results that the Bi content of Ga(NAsBi) is the same as that of an equivalent N-free sample grown under the same conditions.

3.1. Growth of Ga(NAsBi) MQW samples at 400 °C

Starting from a Ga(AsBi)/GaAs MQW sample with Bi content of 3.5%, as determined from HR-XRD, a set of samples (#1–4 in Table 1) were grown varying only the UDMHy supply. A second

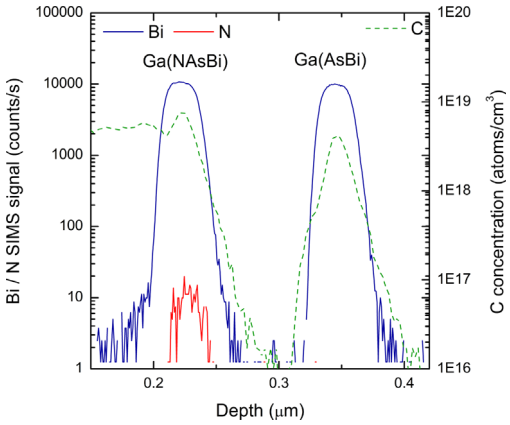

Fig. 1. SIMS profile of Ga(NAsBi) and Ga(AsBi) layers grown at 400 °C surrounded by GaAs barriers.

set of samples (#5–8 in Table 1) were also produced with increasing UDMHy supply, but in this case with Bi content of 2.6%. Fig. 2(a) and (b) shows the experimental HR-XRD (004) patterns (solid lines) of these sets of Ga(NAsBi) MQW samples along with the best fit simulations (dashed lines). The main features of the XRD patterns identified in Fig. 2 are as follows: (1) GaAs substrate peak and (2) broad peak from Ga(NAsBi) QWs, superimposed with fringes due to the layer thicknesses. It is possible to achieve a good fit of the simulated curve to the experimental result in all cases, allowing for accurate determination of the layer compositions and thicknesses. Further detail on the dynamical theory of XRD and interpretation of the XRD profiles for multi-layer structures can be found, for example, in Ref. [13]. In all cases the diffraction patterns show a 3 × QW profile with clearly resolved pendellosung fringes, indicating good crystalline quality and sharp heterointerfaces. It can be seen that with increasing UDMHy supply, the samples change from being compressively strained (broad QW peak on left, lower angle side of substrate peak), through almost lattice matched to GaAs for the sample with UDMHy/TBAs = 0.75, towards tensilely strained (broad QW peak on right, larger angle side of substrate peak).

The resulting N content, as determined from dynamical modelling of the HR-XRD results assuming that the Bi content is independent of N, for these two sets of samples is plotted in Fig. 3(a). Details of all samples are also summarised in Table 1 for reference. It can be seen that there is a linear increase in the N content with increasing UDMHy supply during growth. In contrast to the Bi incorporation, which is independent of N, it is found that for a given UDMHy/TBAs ratio the N content is higher in the sample with lower Bi content. In order to investigate this further, additional samples (#9–10 in Table 1) were grown with a constant UDMHy/TBAs ratio of 0.75 and the TMBi/TBAs ratio was instead varied. Fig. 3(b) shows the resulting N content in these samples and it can be seen that there is an approximately linear decrease in the N content with increasing TMBi supply. The growth rate of these Ga(NAsBi) layers, also plotted in Fig. 3(b), decreases with increasing TMBi supply as has previously been observed in the growth of Ga(AsBi) QWs [8]. This suggests that there is increased Bi surface coverage that may be reducing the rate of diffusion of atoms to the growth surface or reducing decomposition of the precursors, and this could be inhibiting the N incorporation. There may also be more chance for N desorption from the surface at lower growth rates, as is observed in the growth of (GaIn)(NAs) where the N content approximately doubles as growth rate is doubled [14]. In addition there is increased competition between Bi and N atoms for group V lattice sites, which could lead to reduced N incorporation.

Table 1
Summary of properties for all samples discussed in this work.

Sample #	QW/single layer	T_{growth} (°C)	UDMHy/TBAs	TMBi/TBAs	Bi (%)	N (%)
1	3QW	400	0.00	0.030	3.5	0.0
2	3QW	400	0.50	0.030	3.5	1.3
3	3QW	400	0.75	0.030	3.5	1.8
4	3QW	400	1.00	0.030	3.5	2.7
5	3QW	400	0.00	0.015	2.6	0.0
6	3QW	400	0.50	0.015	2.6	2.0
7	3QW	400	0.75	0.015	2.6	2.7
8	3QW	400	1.00	0.015	2.6	3.7
9	3QW	400	0.75	0.008	1.4	3.5
10	3QW	400	0.75	0.000	0.0	4.1
11	Single layer	450	0.00	0.008	1.8	0.0
12	Single layer	450	0.30	0.008	1.8	0.6
13	Single layer	450	0.61	0.008	1.8	1.2
14	Single layer	450	1.00	0.008	1.8	1.8
SIMS	4× 30 nm Ga(NAsBi) layers grown under the same conditions as *A*: 2, *B*: 9, *C*: 4, and *D*: 7					

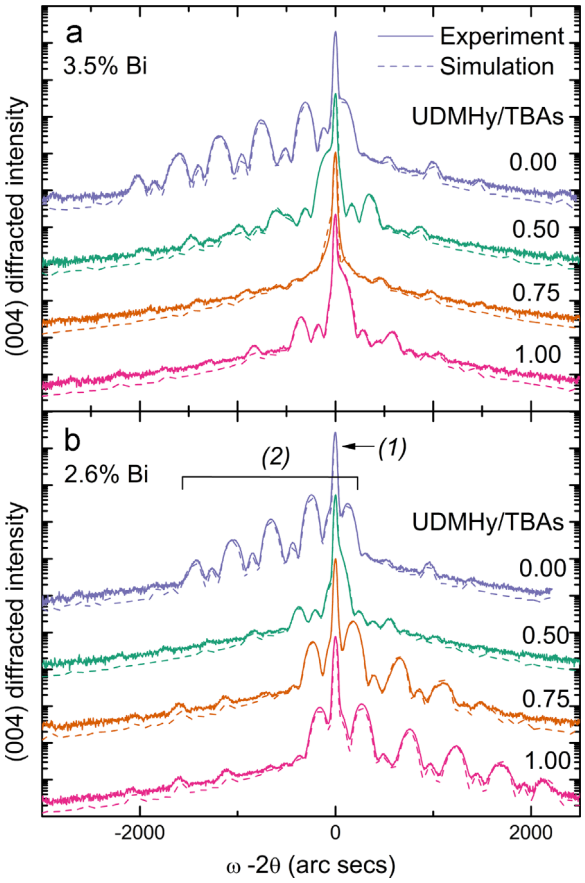

Fig. 2. HR-XRD (004) patterns of Ga(NAsBi)/GaAs MQWs grown at 400 °C with different UDMHy/TBAs ratios for (a) TMBi/TBAs=0.03, 3.5% Bi and (b) TMBi/TBAs=0.015, 2.6% Bi. The features (1) and (2) are the GaAs substrate peak and broad Ga(NAsBi) QW peak, respectively.

A second sample was investigated with SIMS analysis, which contained four ~30 nm Ga(NAsBi) layers, grown under the same conditions as (*A*): #2, (*B*): #9, (*C*): #4, and (*D*): #7 as listed in Table 1 and labelled in Fig. 3, separated by 100 nm GaAs barriers. The SIMS depth profile is shown in Fig. 4(a) and in Fig. 4(b) the average SIMS signal from the Bi (N) in each layer is plotted against the expected Bi (N) content as determined from HR-XRD of the MQW sample grown under the same conditions. There is a clear linear relationship between the Bi (N) signal and Bi (N) content, which provides additional evidence that composition as

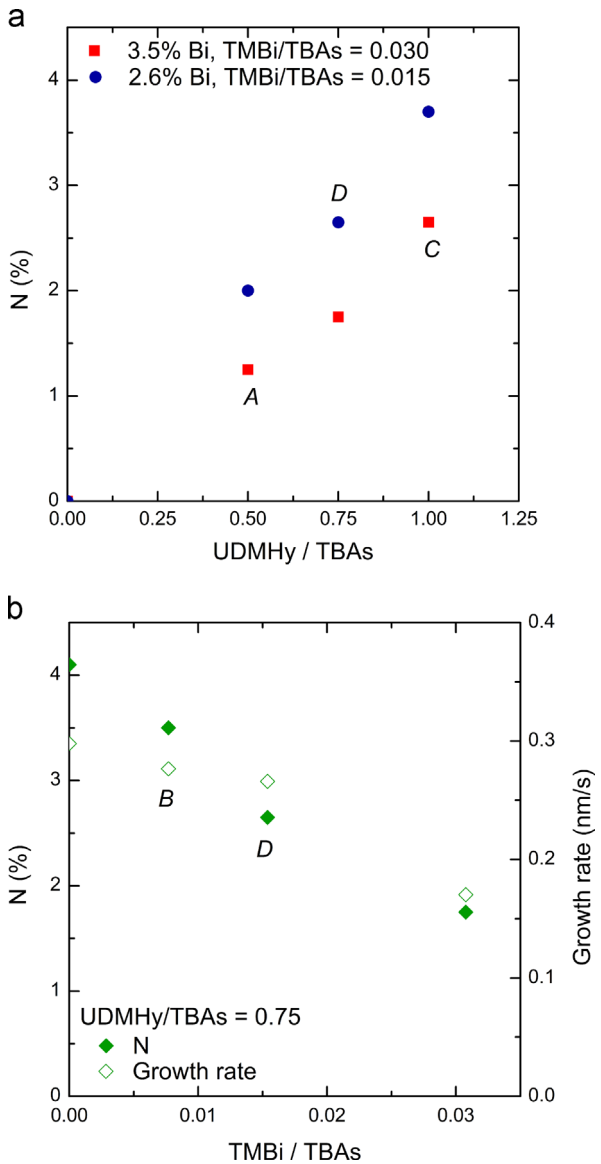

Fig. 3. (a) Dependence of N content of Ga(NAsBi)/GaAs MQWs grown at 400 °C on UDMHy/TBAs ratio. Red squares: TMBi/TBAs=0.030, 3.5% Bi, blue circles: TMBi/TBAs=0.015, 2.6% Bi. (b) Dependence of N content (filled markers) and growth rate (open markers) on TMBi/TBAs ratio for constant UDMHy/TBAs=0.75. (For interpretation of the references to colour in this figure legend, the reader is referred to the web version of this article.)

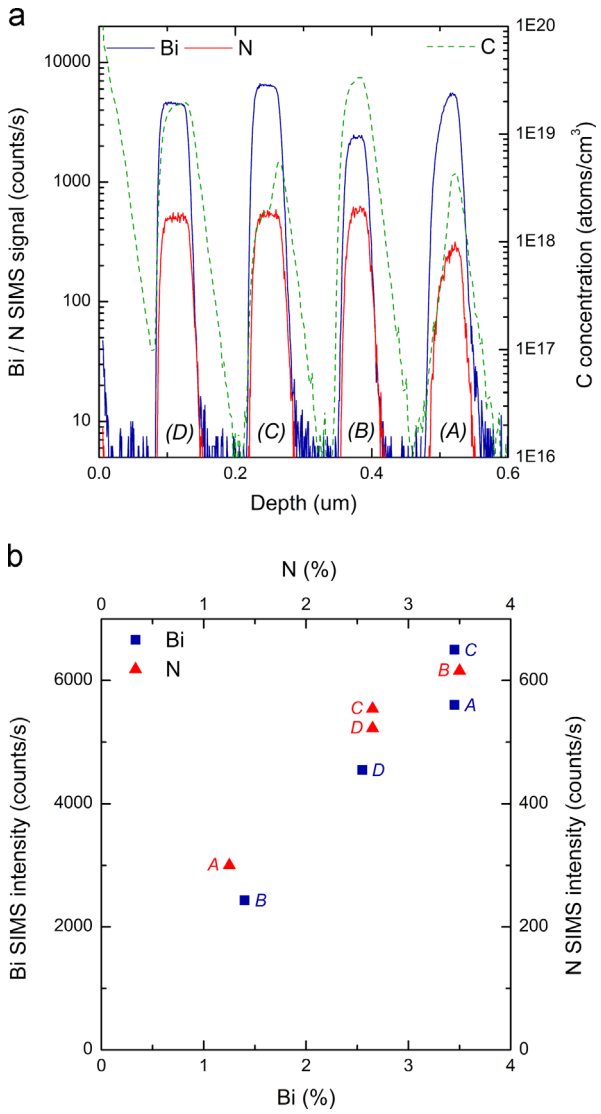

Fig. 4. (a) SIMS profile of Ga(NAsBi) layers with (A) 3.5% Bi, 1.2% N, (B)1.4% Bi, 3.6% N, (C)3.5% Bi, 2.7% N and (D) 2.6% Bi, 2.7% N. (b) Average intensity of Bi (N) SIMS signal plotted against Bi (N) content as determined from XRD.

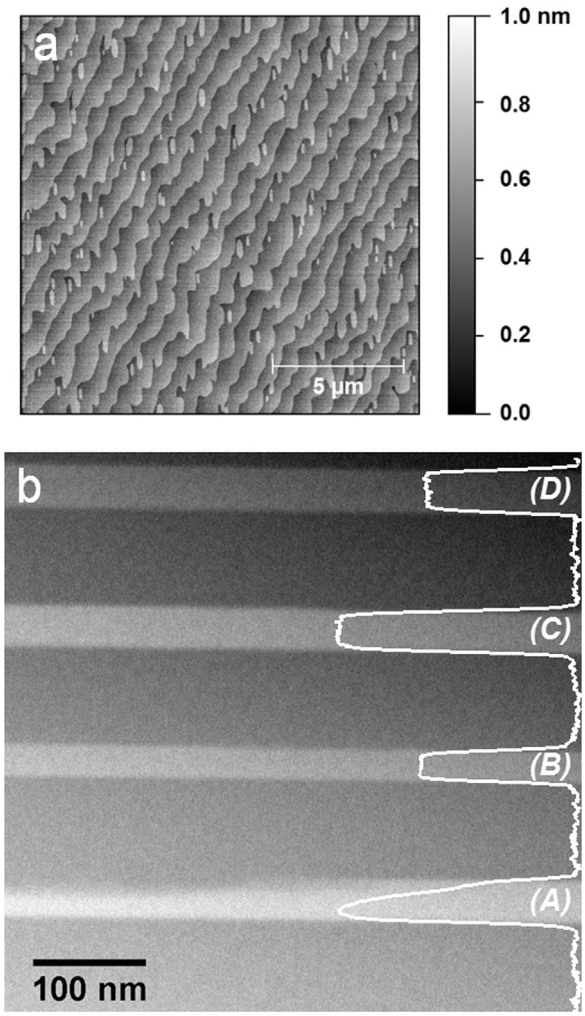

Fig. 5. (a) 15 × 15 μm AFM image showing the surface morphology of the GaAs cap layer on sample #4. (b) STEM HAADF image of Ga(NAsBi)/GaAs SIMS sample.

determined by HR-XRD is correct and the Bi content does indeed remain the same as in an equivalent N-free sample. In particular, layers (*C*) and (*D*) have different Bi contents but are expected to have the same N content and from the SIMS analysis it can be seen that the N content is approximately equal in the two layers.

Atomic force microscopy was used to study the surface morphology of the GaAs cap layer on all of the MQW samples. It was found that all samples had very low surface roughness, comparable to Ga(AsBi)/GaAs samples reported in Ref. [7], and no Bi droplets were present. An example AFM image of sample #4 is shown in Fig. 5(a) for a $15 \times 15\ \mu m^2$ area. To investigate the internal structure, STEM HAADF images were made of the SIMS sample from Fig. 4 and an overview is shown in Fig. 5(b). The Ga(NAsBi) layers appear brighter than the GaAs barriers due to the presence of Bi atoms with higher atomic number. Since the contrast is highly sensitive to the atomic number, uniform brightness within a layer indicates good chemical homogeneity in the material. The layers (*B*), (*C*) and (*D*) all have very good homogeneity in composition and thickness with relatively sharp interfaces, demonstrating that it is possible to grow Ga(NAsBi) with good crystalline quality by MOVPE. Layer (*A*), however, has significant variations in thickness at different positions, which is also reflected in the SIMS results where there is a gradient in Bi and N contents at the upper interface. Since this is one of the layers with higher TMBi supply, it is thought this may be due to the Bi surface coverage increasing during the growth time and possibly becoming too great, causing the formation of Bi droplets on the surface. Layer (*C*), which has the same TMBi supply, does not suffer from such problems showing that it is possible to successfully produce material with higher Bi content so further investigation will be required to achieve this over a wider range of compositions.

Attempts were made to measure room temperature PL from the Ga(NAsBi)/GaAs MQW samples (#1–10) but no signal could be detected with the apparatus. It is thought that the incorporation of N into the crystal has introduced non-radiative defects such as N interstitials and Ga vacancies that significantly reduce the PL intensity, as also occurs in other N containing materials such as Ga(NAs) and (GaIn)(NAs) [15–18]. Another factor which acts to decrease PL intensity is unintentional incorporation of carbon from the metal–organic precursors. It has previously been found in MOVPE growth of Ga(NAs) and (GaIn)(NAs) that the C content increases strongly with decreasing growth temperature and is significantly higher than that in GaAs due to the strength of the C–N bond [19]. The directly comparable Ga(AsBi) and Ga(NAsBi) layers grown under identical conditions apart from the addition of N, for which the SIMS profile is plotted in Fig. 1, provide some evidence of increased C incorporation with approximately twice as

much C in the N containing layer. Note that the high C concentration in the left-most GaAs barrier in the figure occurs because this was grown at 400 °C instead of the usual 625 °C to check C incorporation in GaAs at this temperature. The SIMS analysis of the other Ga(NAsBi) layers, shown in Fig. 4(a), found them to have C concentrations of 5×10^{18}–4×10^{19} atoms/cm^3, whereas previous SIMS analysis of Ga(AsBi) layers with a similar range of Bi contents showed them to have typically 5×10^{16}–2×10^{19} atoms/cm^3 depending on TMBi supply [7]. Although there is slightly greater C incorporation in the Ga(NAsBi) material, it is still of the same order of magnitude as for Ga(AsBi) samples from which good RT PL can be detected, so it is unlikely to have a significant effect on the PL intensity from the Ga(NAsBi) samples. It is therefore thought that other non-radiative defects introduced by the presence of N are the dominant reason for the absence of RT PL.

3.2. Ga(NAsBi) single layer growth at 450 °C

Other N containing materials, such as Ga(NAs) and (GaIn)(NAs), are typically grown at higher temperatures of 500–600 °C [20–22] so it was thought that by increasing the growth temperature of Ga(NAsBi) it may be possible to improve the material quality through decreasing non-radiative defects and also carbon incorporation. The higher temperature presents a problem for Bi incorporation, however, which requires a low growth temperature. Previous investigations of the MOVPE growth of Ga(AsBi) have focused on growth at 400 °C and 375 °C [8], so it was first necessary to perform initial investigations on the growth of Ga(AsBi) at 450 °C. After some optimisation of precursor partial pressures, the growth of a sample with 1.8% Bi and a droplet free surface was achieved so this was used as the starting point for the growth of Ga(NAsBi) samples. All 450 °C samples (#11–14 in Table 1) are single layers with thickness in the range 40–70 nm, capped with 20 nm GaAs. The results of N content determined from simulation of the XRD data are shown in Fig. 6. A linear increase in N content with UDMHy supply is again observed, as it was at 400 °C.

Room temperature PL measurements were performed and the spectra are shown in Fig. 7. There is a clear redshift in the PL peak from 1.27 eV for the Ga(AsBi) sample to 1.19 eV for the Ga(NAsBi) sample with the lowest N content of 0.6%. The peak intensity also decreases significantly with the addition of N, which could be explained by the presence of N-related defects and increased C incorporation. It is interesting to note that the PL intensity from

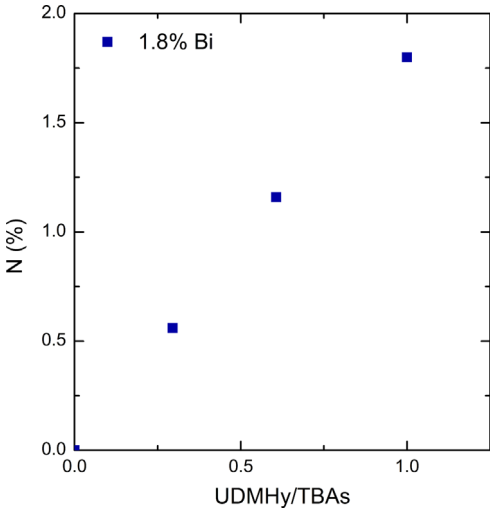

Fig. 6. Dependence of N content of Ga(NAsBi) single layers with 1.8% Bi grown at 450 °C on UDMHy/TBAs ratio.

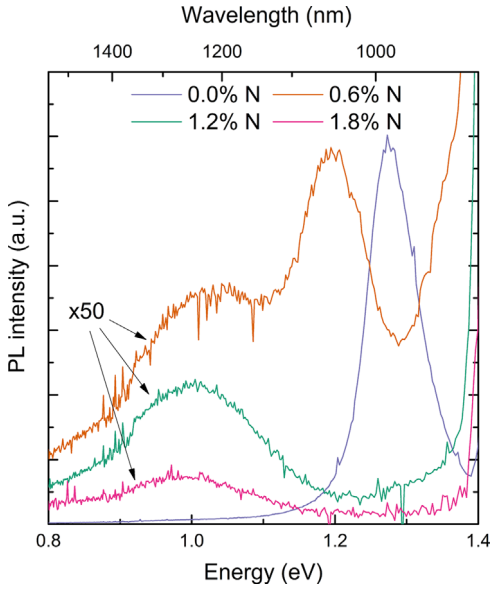

Fig. 7. Room temperature photoluminescence spectra of Ga(NAsBi) single layers with 1.8% Bi grown at 450 °C. PL intensity ×50 for N-containing samples.

the N-free sample is an order of magnitude greater than for previous Ga(AsBi) samples with similar Bi content grown at 400 °C [7]. This suggests that there is an improvement in material quality and probable reduction in C incorporation at the higher growth temperature. All spectra have a broad peak at ~1 eV, which is thought to be related to a defect and is also observed in pure GaAs grown at 400 °C by MOVPE [7]. According to theoretical calculations, the samples with 1.2% and 1.8% N are expected to have band gaps that lie within the broad feature around 1 eV and as such it is not possible to distinguish a separate peak due the Ga(NAsBi).

In order to determine the band gap in all samples even where there is no clear PL peak, RT photoreflectance spectroscopy (PR) was also performed. PR spectra were analysed by a third derivative functional form (TDFF) to determine the energy transition values [23] as shown in Fig. 8(a). The band gap as determined by PR of the four samples as a function of N content is plotted in Fig. 8(b). There is a reduction in band gap of 141 ± 22 meV/% N over the range studied, which is in good agreement with the redshift in PL peak energy of 130 meV/% N measured previously for MBE-grown samples with up to 4.5% Bi and 2% N [4] and smaller than the 180 meV decrease in band gap for 1% N in GaAs [24]. In other dilute nitride materials, as well as MBE grown Ga(NAsBi), previous investigations have shown that annealing can significantly improve PL intensity [17,25,26]. It is therefore planned to carry out annealing studies on this material in future, with the expectation that this may improve the optical properties of the material.

4. Summary

We have discussed the growth by MOVPE of Ga(NAsBi)/GaAs MQWs and Ga(NAsBi) single layers on GaAs (001) substrates using growth temperatures of 400 °C and 450 °C. Beginning from Ga(AsBi) samples with known Bi content, it was found that N incorporation can easily be controlled by varying UDMHy supply during growth with a linear relationship between UDMHy supply and N content over the range investigated, whilst Bi content remains constant. Samples have been shown to have good chemical homogeneity and relatively sharp Ga(NAsBi)/GaAs interfaces can be achieved. By increasing the growth temperature to 450 °C it

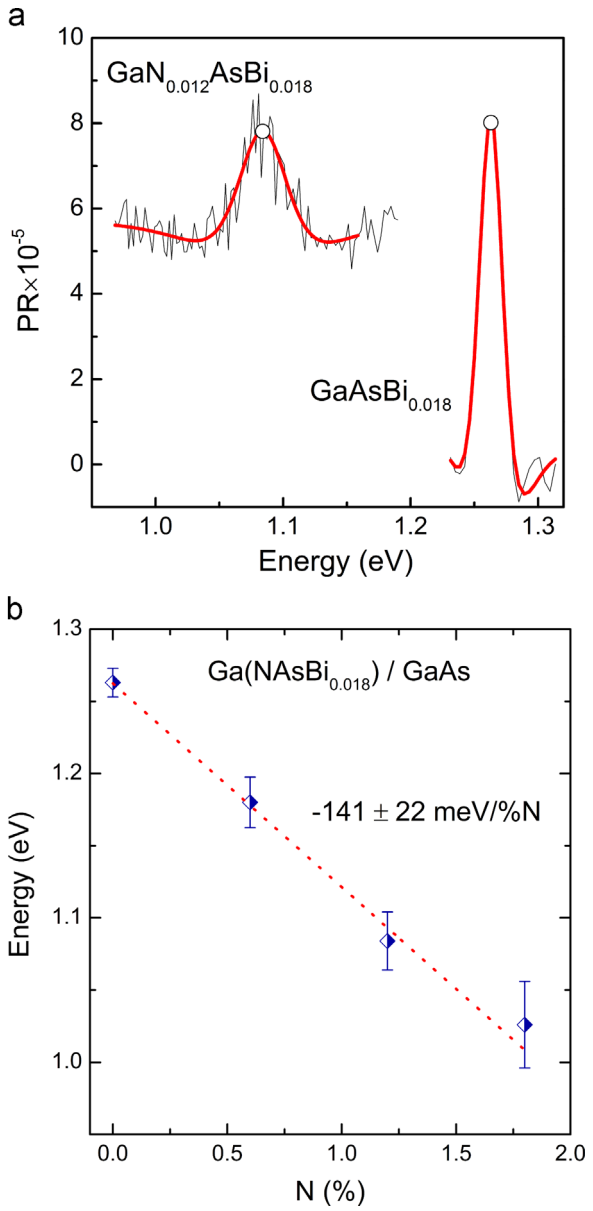

Fig. 8. (a) PR spectra (black lines) and corresponding fits (red lines) for a sample without and with 1.2% N (both containing 1.8% Bi). The open circles denote the position of the band gap energy as determined by the fitting. (b) Dependence of band gap on N content for Ga(NAsBi) single layers with 1.8% Bi as measured by PR. (For interpretation of the references to colour in this figure legend, the reader is referred to the web version of this article.)

was possible to detect RT photoluminescence from a Ga(NAsBi) sample with 0.6% N. Photoreflectance spectroscopy showed a decrease in the band gap of 141 ± 22 meV/% N for Ga(NAsBi) single layer samples with 1.8% Bi and up to 1.8% N. These preliminary results illustrate the potential of Ga(NAsBi) alloys for infrared band gap materials that can be lattice-matched to GaAs with applications in photonic devices.

Acknowledgements

This work was funded by the European Union Framework 7 Project BIANCHO (FP7-257974), the German Science Foundation (DFG: VO805/4 and DFG: GRK1782) and EPSRC-UK Projects EP/H005587/1 and EP/G064725/1. Z.L. Bushell acknowledges financial support from an ERASMUS grant through the European Commission Lifelong Learning Programme. Z. Batool is grateful to the Kwan Trust and the Islamia University of Bahawalpur, Pakistan for supporting her Ph.D. studentship.

References

[1] S.J. Sweeney, S.R. Jin, Bismide–nitride alloys: promising for efficient light emitting devices in the near- and mid-infrared, J. Appl. Phys. 113 (2013) 043110.
[2] B. Fluegel, S. Francoeur, A. Mascarenhas, S. Tixier, E. Young, T. Tiedje, Giant spin–orbit bowing in $GaAs_{1-x}Bi_x$, Phys. Rev. Lett. 97 (2006) 067205.
[3] M. Usman, C.A. Broderick, A. Lindsay, E.P. O'Reilly, Tight-binding analysis of the electronic structure of dilute bismide alloys of GaP and GaAs, Phys. Rev. B 84 (2011) 245202.
[4] M. Yoshimoto, W. Huang, G. Feng, K. Oe, New semiconductor alloy GaNAsBi with temperature-insensitive bandgap, Phys. Status Solidi 243 (2006) 1421–1425.
[5] X. Lu, D.A. Beaton, R.B. Lewis, T. Tiedje, Y. Zhang, Composition dependence of photoluminescence of $GaAs_{1-x}Bi_x$ alloys, Appl. Phys. Lett. 95 (2009) 041903.
[6] A.J. Ptak, R. France, D.A. Beaton, K. Alberi, J. Simon, A. Mascarenhas, et al., Kinetically limited growth of GaAsBi by molecular-beam epitaxy, J. Cryst. Growth 338 (2012) 107–110.
[7] P. Ludewig, Z.L. Bushell, L. Nattermann, N. Knaub, W. Stolz, K. Volz, Growth of Ga(AsBi) on GaAs by continuous flow MOVPE, J. Cryst. Growth. http://dx.doi.org/10.1016/j.jcrysgro.2014.03.041, accepted for publication.
[8] P. Ludewig, N. Knaub, W. Stolz, K. Volz, MOVPE growth of Ga(AsBi)/GaAs multiquantum well structures, J. Cryst. Growth 370 (2012) 186–190.
[9] K. Oe, Metalorganic vapor phase epitaxial growth of metastable $GaAs_{1-x}Bi_x$ alloy, J. Cryst. Growth 237–239 (2002) 1481–1485.
[10] S. Tixier, S.E. Webster, E.C. Young, T. Tiedje, S. Francoeur, A. Mascarenhas, et al., Band gaps of the dilute quaternary alloys $GaN_xAs_{1-x-y}Bi_y$ and $Ga_{1-y}In_yN_xAs_{1-x}$, Appl. Phys. Lett. 86 (2005) 112113.
[11] M. Yoshimoto, W. Huang, Y. Takehara, J. Saraie, A. Chayahara, Y. Horino, et al., New semiconductor GaNAsBi alloy grown by molecular beam epitaxy, Jpn. J. Appl. Phys. 43 (2004) L845–L847.
[12] F.H. Pollak, in: T.S. Moss (Ed.), Handbook on Semiconductors, 2nd ed., Elsevier, Amsterdam, 1994, p. 527.
[13] P.F. Fewster, Analysis of nearly perfect semiconductor multi-layer structures, X-Ray Scattering from Semiconductors, 2nd ed., Imperial College Press, London (2003) 200–247.
[14] K. Volz, J. Koch, F. Hohnsdorf, B. Kunert, W. Stolz, MOVPE growth of dilute nitride III/V semiconductors using all liquid metalorganic precursors, J. Cryst. Growth 311 (2009) 2418–2426.
[15] W. Li, M. Pessa, T. Ahlgren, J. Decker, Origin of improved luminescence efficiency after annealing of Ga(In)NAs materials grown by molecular-beam epitaxy, Appl. Phys. Lett. 79 (2001) 1094.
[16] N.Q. Thinh, I.A. Buyanova, W.M. Chen, H.P. Xin, C.W. Tu, Formation of nonradiative defects in molecular beam epitaxial GaN_xAs_{1-x} studied by optically detected magnetic resonance, Appl. Phys. Lett. 79 (2001) 3089.
[17] S.G. Spruytte, C.W. Coldren, J.S. Harris, W. Wampler, P. Krispin, K. Ploog, et al., Incorporation of nitrogen in nitride–arsenides: origin of improved luminescence efficiency after anneal, J. Appl. Phys. 89 (2001) 4401.
[18] J. Toivonen, T. Hakkarainen, M. Sopanen, H. Lipsanen, J. Oila, K. Saarinen, Observation of defect complexes containing Ga vacancies in GaAsN, Appl. Phys. Lett. 82 (2003) 40.
[19] K. Volz, T. Torunski, B. Kunert, O. Rubel, S. Nau, S. Reinhard, et al., Specific structural and compositional properties of (GaIn)(NAs) and their influence on optoelectronic device performance, J. Cryst. Growth 272 (2004) 739–747.
[20] F. Hohnsdorf, J. Koch, C. Agert, W. Stolz, Investigations of (GaIn)(NAs) bulk layers and (GaIn)(NAs)/GaAs multiple quantum well structures grown using tertiarybutylarsine (TBAs) and 1,1-dimethylhydrazine (UDMHy), J. Cryst. Growth 195 (1998) 391–396.
[21] T. Miyamoto, T. Kageyama, S. Makino, D. Schlenker, F. Koyama, K. Iga, CBE and MOCVD growth of GaInNAs, J. Cryst. Growth 209 (2000) 339–344.
[22] A. Moto, S. Tanaka, N. Ikoma, T. Tanabe, S. Takagishi, Metalorganic vapor phase epitaxial growth of GaNAs using tertiarybutylarsine (TBA) and dimethylhydrazine (DMHy), Jpn. J. Appl. Phys. 38 (1999) 1015–1018.
[23] D.E. Aspnes, Third-derivative modulation spectroscopy with low-field electroreflectance, Surf. Sci. 37 (1973) 418–442.
[24] J. Wu, W. Shan, W. Walukiewicz, Band anticrossing in highly mismatched III–V semiconductor alloys, Semicond. Sci. Technol. 17 (2002) 860–869.
[25] K. Volz, D. Lackner, I. Németh, B. Kunert, W. Stolz, C. Baur, et al., Optimization of annealing conditions of (GaIn)(NAs) for solar cell applications, J. Cryst. Growth 310 (2008) 2222–2228.
[26] G. Feng, K. Oe, M. Yoshimoto, Influence of thermal annealing treatment on the luminescence properties of dilute GaNAs–bismide alloy, Jpn. J. Appl. Phys. 46 (2007) L764–L766.

Zusammenfassung (Summary in German)

Für die Entwicklung von neuen technischen Anwendungen, spielt die Energieeffizienz eine tragende Rolle. So ist die Nachfrage nach neuartigen energieeffizienten optoelektronischen Bauelementen sehr groß, vor allem im Bereich des Internet-Datentransfers und der dafür benötigten Laserdioden mit einer Emissionswellenlänge von 1,55 µm. Ein vielversprechendes Materialsystem, welches sich zur Herstellung von hocheffizienten Bauelementen eignet, ist der verdünnt Bi-haltige Verbindungshalbleiter Ga(AsBi). Es ist bekannt, dass der geringe Einbau von Bi in GaAs die Bandlücke sowie die Temperaturabhängigkeit der Emissionswellenlänge reduziert und zur Unterdrückung von nichtstrahlenden Rekombinationsprozessen beiträgt, was mit Hilfe des sogenannten Valenzband Anticrossing Models beschrieben werden kann. In der Praxis konnte somit zum ersten Mal ein elektrisch gepumpter Breitstreifen Ga(AsBi) Quantum-well (QW) Laser realisiert werden.
Diese Arbeit beschäftigt sich mit der Strukturanalyse von Ga(AsBi), Ga(PAsBi) und Ga(NAsBi), welche mittels der metallorganischen Gasphasenepitaxie (MOVPE, *metal organic vapour phase epitaxy*) hergestellt wurden, wobei das Wachstum der Materialsysteme nicht Teil dieser Arbeit war. Die strukturellen Untersuchungen erfolgten mit Hilfe von sphärische Aberration korrigierter Rastertransmissionselektronenmikroskopie (STEM, *scanning transmission electron microscopy*). Die Auswertung und Interpretation der STEM Messungen erfolgte unter anderem mit Hilfe von Simulationsrechnungen, die an Ga(AsBi) Superzellen durchgeführt wurden sowie mittels weiterer Datenverarbeitung. Diese erfolgte mit der MATLAB-Software, welche die Trennung der Kristalluntergitter in Hochauflösungsaufnahmen ermöglichte sowie zur statistischen Auswertung der Atomsäulenintensitäten diente.
Zu Beginn der Arbeit wurden Ga(AsBi) Proben, mit hoher Anzahl an metallischen Tropfen auf der Oberfläche, mittels der TEM in [010] Zonenachse untersucht (siehe Section 6.3). Dabei konnte mit Hilfe von TEM Beugungsbildern gezeigt werden, dass es sich überwiegend um Bi Einkristalle handelt. Die Auswertung von zusätzlichen Hochauflösungsaufnahmen ergab außerdem, dass sich die $\{10\bar{1}\}$ Netzebenen der Bi Einkristalle parallel zu den $\{202\}$ Netzebenen von GaAs anordnen und somit ein Koinzidenzgitter bilden. Dadurch kann die Gitterfehlanpassung zwischen Tropfen und GaAs Oberfläche von 12% auf 0,6% reduziert werden.
Des Weiteren wurden auch tropfenfreie Ga(AsBi)-QW Strukturen mit unterschiedlich

nominellen Bi Gehalten ($0{,}9\% \leqslant x \leqslant 4{,}8\%$) in [010] Zonenachse untersucht und mit Hilfe von STEM Simulationsrechnungen quantifiziert (siehe Section 6.1). Dabei wurden Ga(AsBi) Superzellen mit unterschiedlichen Bi Gehalten ($1\% \leqslant x \leqslant 5\%$) simuliert und deren Intensität mit der von niedrigaufgelösten STEM Messungen von Ga(AsBi)-QW Strukturen verglichen. Die dadurch ermittelten Bi Gehalte waren in guter Übereinstimmung mit den Werten, die mittels Sekundärinonenmassenspektrometrie (SIMS, *secondary ion mass spectrometry*) und hochauflösender Röntgendiffraktometrie (HR-XRD, *high resolution x-ray diffraction*) bestimmt wurden. Weiterhin konnte mit Hilfe von STEM Simulationsrechnungen verifiziert werden, dass die detektierte Streuintensität sich eher proportional zu $Z^{1.6}$ anstatt zu Z^2 verhält. Zusätzlich wurde eine Methode angewandt (nicht in dieser Arbeit entwickelt), die es erlaubt STEM Intensitätsfluktuationen innerhalb der Ga(AsBi)-QW Strukturen zu messen und so ein Maß für die Kompositionsfluktuationen zu erhalten. Es ergaben sich Ga(AsBi) Kompositionsfluktuationen, die vergleichbar mit der von GaAs sind, wodurch von einer homogenen Bi Verteilung im Bereich von 10 nm und größer für alle untersuchten Ga(AsBi)-QW Strukturen ausgegangen werden konnte. Für die Untersuchung der Ordnung von Bi Atomen oder der Inhomogenitäten auf atomarer Skala wurden zusätzliche hochaufgelöste STEM Messungen von Ga(AsBi)-QW Strukturen in [010] Zonenachse durchgeführt (siehe Section 6.2). Außerdem wurde eine Ga(AsBi) Superzelle mit einem Bi Gehalt von 4,8% im sogenannten *frozen-lattice* Formalismus simuliert und mit den experimentellen Messungen verglichen. Bei den hochaufgelösten Aufnahmen wurden in kurzer Aufnahmezeit sieben Messungen hintereinander von einem Bereich in den jeweiligen Ga(AsBi)-QW Strukturen durchgeführt und mittels des MATLAB-Programms *SmartAlign* zu jeweils einer Aufnahme zusammengefügt, wobei die Drift der Probe während der Messungen berücksichtigt werden musste. Die Vorteile, die sich dadurch ergeben, spiegeln sich in einem deutlich verbesserten Signal-zu-Rauschverhältnis sowie weniger Aufnahmeartefakte wider, die während der STEM Hochauflösungsaufnahmen entstehen. Außerdem ergaben statistische Auswertungen der Atomsäulenintensitäten von experimenteller Messung und entsprechender Simulationsrechnung ein vergleichbares Ergebnis. Dadurch war die Möglichkeit gegeben die Anzahl der Bi Atome in den Gruppe V Atomsäulen zu quantifizieren und sie entsprechenden Intensitäten zuzuordnen. Im weiteren Verlauf wurden in den Auswertungen der experimentellen Messungen die Intensitäten betrachtet, die einer höheren Anzahl an Bi Atomen (drei und höher) pro Atomsäule entsprechen. Zusätzlich wurde eine Positionskarte der entsprechenden Gruppe V Atomsäulen erzeugt und mittels der sogenannten *Hough-Transformation* konnten atomare Bi Ordnungseffekte in Form von "Ketten" entlang der kristallographischen Richtungen $\langle 100 \rangle$ und $\langle 101 \rangle$ detektiert werden. Der Vergleich mit einer entsprechend ausgewerteten Simulationsrechnung (zufällige Bi Verteilung) zeigt, dass der Anteil der "kettenartigen" Bi Ordnung in der Simulation deutlich geringer ausfällt bzw. nicht vorhanden ist. Dadurch konnte verifiziert werden, dass atomare Bi Ordnung in Ga(AsBi)-QW Strukturen vorliegt, obwohl diese eine homogene Bi Verteilung im Bereich von 10 nm und größer aufweisen.

Weiterhin wurden die quaternären Materialsysteme Ga(NAsBi) und Ga(PAsBi) auf homogenen Einbau von Bi und N bzw. P anhand von Intensitätsfluktuationsmessungen untersucht. Die Ergebnisse sind vergleichbar mit denen der Ga(AsBi)-QW Strukturen, wobei im Ga(PAsBi) eine etwas höhere Intensitätsfluktuation ermittelt werden konnte. Mittels hochaufgelösten STEM Messungen wurde außerdem die sogenannte $CuPt_B$ Ordnung und zusätzliche Clusterformationen in Ga(PAsBi)-QW Strukturen detektiert. Vor allem in Ga(PAsBi) Proben, die nach dem Wachstum thermischen Ausheizprozessen unterzogen wurden, wurden vermehrt Clusterformationen detektiert. Erste Hinweise für die chemische Zusammensetzung der Clusterformationen konnte die energiedispersive Röntgenspektroskopie (EDX, *energy dispersive x-ray spectroscopy*) liefern, welche parallel zu den STEM Messungen durchgeführt wurde. Dadurch konnten die Clusterformationen als Bi-reiche Regionen innerhalb der Ga(PAsBi) Struktur identifiziert werden. Im Zusammenhang mit der Formation von Bi-reichen Clustern könnte das thermische Ausheizen stehen, weil dadurch dem System zusätzliche Energie zugeführt wird, was die Ansammlung von Bi fördern könnte.
Daher ist es erforderlich die MOVPE Wachstumsbedingungen für Ga(PAsBi) weiter zu optimieren, wodurch chemisch homogene Ga(PAsBi) Strukturen realisiert werden könnten. Darüber hinaus können systematische (S)TEM Untersuchungen der Clusterformationen dabei helfen deren Ursprung besser zu erforschen und somit optimale MOVPE Wachstumsparameter zu gewährleisten.
Des Weiteren haben STEM Simulationsrechnungen von dünnen Ga(AsBi) Superzellen (5 nm) und deren statistische Intensitätsauswertung gezeigt, dass lokale Verzerrungseffekte in Ga Atomsäulen detektiert werden können, die auf benachbarte Bi Atome zurückzuführen sind. Dies zeigt, dass generell die Möglichkeit besteht mit Hilfe von hochaufgelösten STEM Messungen lokale Verzerrungen zu quantifizieren. Jedoch ist es von Vorteil wenn die zu untersuchten Proben eine Dicke von etwa 5 nm in Durchstrahlrichtung aufweisen. Dies ist mit der konventionellen Probenpräparation, die in dieser Arbeit verwendet wurde, nicht zu realisieren. Der wesentliche Grund dafür liegt darin, dass die Proben mit Hilfe von Argon Ionen auf eine Zieldicke zwischen 15 und 30 nm gedünnt werden, was zu einem Einbau von Fremdatomen in den Proben sowie zu Schäden an deren Oberfläche (Amorphisierung) führt. Daher empfiehlt es sich auf Präparationssysteme zurückzugreifen, die nur auf mechanisches Dünnen zurückgreifen und somit ohne Ionendünnung auskommen. Aber auch hier ist viel Erfahrung im Umgang mit solchen Präparationssystemen notwendig, um Probendicken im Bereich von einigen Nanometern zu realisieren.
Insgesamt zeigen die Resultate dieser Arbeit, dass die Rastertransmissionselektronenmikroskopie aus der Strukturanalyse und der Charakterisierung von neuartigen Halbleitern nicht wegzudenken bzw. notwendig ist. Außerdem zeigen die Ergebnisse auch, dass Bi haltige Halbleitermaterialien ein hohes Maß an chemischer Homogenität aufweisen, was die Realisierung von neuen energieeffizienten Halbleiterbauelementen erlauben könnte.

Bibliography

[1] "The Nobel Prize in Physics 2014". Nobelprize.org. Nobel Media AB 2014. Web. 19 Apr 2016.

[2] I. Akasaki and H. Amano, Japanese J. Appl. Physics, Part 1 Regul. Pap. Short Notes Rev. Pap. **45**, 9001 (2006).

[3] K. Oe and H. Okamoto, Jpn. J. Appl. Phys. **37**, L1283 (1998).

[4] K. Oe, Jpn. J. Appl. Phys. **41**, 2801 (2002).

[5] S. Tixier, M. Adamcyk, T. Tiedje, S. Francoeur, A. Mascarenhas, P. Wei and F. Schiettekatte, Appl. Phys. Lett. **82**, 2245 (2003).

[6] S. Francoeur, M.-J. Seong, A. Mascarenhas, S. Tixier, M. Adamcyk and T. Tiedje, Appl. Phys. Lett. **82**, 3874 (2003).

[7] B. Fluegel, S. Francoeur, A. Mascarenhas, S. Tixier, E. Young and T. Tiedje, Phys. Rev. Lett. **97**, 067205 (2006).

[8] V. Pačebutas, K. Bertulis, L. Dapkus, G. Aleksejenko, A. Krotkus, K. M. Yu and W. Walukiewicz, Semicond. Sci. Technol. **22**, 819 (2007).

[9] P. Ludewig, *Growth and characterization of dilute bismide GaAs based alloys for high efficiency infra red laser diodes*, PhD thesis, Philipps Universität Marburg, 2014.

[10] A. G. Norman, R. France and A. J. Ptak, J. Vac. Sci. Technol. B Microelectron. Nanom. Struct. **29**, 03C121 (2011).

[11] M. Wu, E. Luna, J. Puustinen, M. Guina and A. Trampert, Appl. Phys. Lett. **105** (2014).

[12] G. Ciatto, E. C. Young, F. Glas, J. Chen, R. A. Mori and T. Tiedje, Phys. Rev. B - Condens. Matter Mater. Phys. **78**, 1 (2008).

[13] G. Ciatto, M. Thomasset, F. Glas, X. Lu and T. Tiedje, Phys. Rev. B - Condens. Matter Mater. Phys. **82**, 1 (2010).

[14] D. L. Sales, E. Guerrero, J. F. Rodrigo, P. L. Galindo, A. Yáñez, M. Shafi, A. Khatab, R. H. Mari, M. Henini, S. V. Novikov, M. F. Chisholm and S. I. Molina, Appl. Phys. Lett. **98**, 101902 (2011).

[15] M. Wu, E. Luna, J. Puustinen, M. Guina and A. Trampert, Nanotechnology **25**, 205605 (2014).

[16] N. Knaub, A. Beyer, T. Wegele, P. Ludewig and K. Volz, J. Cryst. Growth **433**, 89 (2015).

[17] N. Knaub, A. Beyer, P. Rosenow, K. Jandieri, P. Ludewig, S. W. Koch, R. Tonner and K. Volz.

[18] E. Sterzer, N. Knaub, P. Ludewig, R. Straubinger, A. Beyer and K. Volz, J. Cryst. Growth **408**, 71 (2014).

[19] P. Ludewig, N. Knaub, W. Stolz and K. Volz, J. Cryst. Growth **370**, 186 (2013).

[20] P. Ludewig, N. Knaub, N. Hossain, S. Reinhard, L. Nattermann, I. P. Marko, S. R. Jin, K. Hild, S. Chatterjee, W. Stolz, S. J. Sweeney and K. Volz, Appl. Phys. Lett. **102**, 242115 (2013).

[21] Z. Bushell, P. Ludewig, N. Knaub, Z. Batool, K. Hild, W. Stolz, S. Sweeney and K. Volz, J. Cryst. Growth **396**, 79 (2014).

[22] P. Ludewig, Z. Bushell, L. Nattermann, N. Knaub, W. Stolz and K. Volz, J. Cryst. Growth **396**, 95 (2014).

[23] http://www.ioffe.ru/SVA/NSM/Semicond/GaAs/bandstr.html.

[24] http://www.ioffe.ru/SVA/NSM/Semicond/GaAs/basic.html.

[25] K. Alberi, O. D. Dubon, W. Walukiewicz, K. M. Yu, K. Bertulis and A. Krotkus, Appl. Phys. Lett. **91**, 051909 (2007).

[26] K. Alberi, J. Wu, W. Walukiewicz, K. M. Yu, O. D. Dubon, S. Watkins, C. Wang, X. Liu, Y.-J. Cho and J. Furdyna, Phys. Rev. B **75**, 045203 (2007).

[27] S. Imhof, C. Bückers, A. Thränhardt, J. Hader, J. V. Moloney and S. W. Koch, Semicond. Sci. Technol. **23**, 125009 (2008).

[28] P. Carrier and S.-H. Wei, Phys. Rev. B **70**, 035212 (2004).

[29] M. Silver, E. P. O'Reilly and A. R. Adams, IEEE J. Quantum Electron. **33**, 1557 (1997).

[30] S. J. Sweeney, A. F. Phillips, A. R. Adams, E. P. O'Reilly and P. J. A. Thijs, IEEE Photonics Technol. Lett. **10**, 1076 (1998).

[31] T. Higashi, S. J. Sweeney, A. F. Phillips, A. R. Adams, E. P. O'Reilly, T. Uchida and T. Fujii, IEEE J. Sel. Top. Quantum Electron. **5**, 413 (1999).

[32] S. J. Sweeney and S. R. Jin, J. Appl. Phys. **113**, 043110 (2013).

[33] C. A. Broderick, M. Usman, S. J. Sweeney and E. P. O'Reilly, Semicond. Sci. Technol. **27**, 094011 (2012).

[34] D. Manasijević, D. Minić, D. Živković, I. Katayama, J. Vřeštál and D. Petković, J. Phys. Chem. Solids **70**, 1267 (2009).

[35] A. Janotti, S.-H. Wei and S. Zhang, Phys. Rev. B **65**, 115203 (2002).

[36] T. G. Ramesh and S. Ramaseshan, Acta Crystallogr. Sect. A **27**, 569 (1971).

[37] P. N. P. Keating, Phys. Rev. **145**, 637 (1966).

[38] L. Pauling, J. Am. Chem. Soc. **69**, 542 (1947).

[39] A. Allred, J. Inorg. Nucl. Chem. **17**, 215 (1961).

[40] S. B. Zhang and A. Zunger, Appl. Phys. Lett. **71**, 677 (1997).

[41] W. Shan, W. Walukiewicz, J. Ager, E. Haller, J. Geisz, D. Friedman, J. Olson and S. Kurtz, Phys. Rev. Lett. **82**, 1221 (1999).

[42] S. G. Spruytte, C. W. Coldren, J. S. Harris, W. Wampler, P. Krispin, K. Ploog and M. C. Larson, J. Appl. Phys. **89**, 4401 (2001).

[43] M. Yoshimoto, W. Huang, Y. Takehara, J. Saraie, A. Chayahara, Y. Horino and K. Oe, Jpn. J. Appl. Phys. **43**, L845 (2004).

[44] W. Huang, K. Oe, G. Feng and M. Yoshimoto, J. Appl. Phys. **98**, 053505 (2005).

[45] K. Forghani, Y. Guan, M. Losurdo, G. Luo, D. Morgan, S. E. Babcock, A. S. Brown, L. J. Mawst and T. F. Kuech, Appl. Phys. Lett. **105**, 111101 (2014).

[46] E. Rutherford, Philos. Mag. **92**, 379 (2012).

[47] S. J. Pennycook, Ultramicroscopy **30**, 58 (1989).

[48] S. Pennycook and D. Jesson, Ultramicroscopy **37**, 14 (1991).

[49] P. Hartel, Ultramicroscopy **63**, 93 (1996).

[50] G. B. Stringfellow, J. Cryst. Growth **128**, 503 (1993).

[51] G. B. Stringfellow, *Organometallic vapor-phase epitaxy: theory and practice*, Academic Press, 2 edition, 1998.

[52] J. M. Lebeau and S. Stemmer, Ultramicroscopy **108**, 1653 (2008).

[53] O. Scherzer, Zeitschrift für Phys. **101**, 593 (1936).

[54] O. Scherzer, J. Appl. Phys. **20**, 20 (1949).

[55] M. Haider, Ultramicroscopy **75**, 53 (1998).

[56] O. Krivanek, N. Dellby and A. Lupini, Ultramicroscopy **78**, 1 (1999).

[57] M. Haider, Ultramicroscopy **81**, 163 (2000).

[58] R. Erni, M. Rossell, C. Kisielowski and U. Dahmen, Phys. Rev. Lett. **102**, 1 (2009).

[59] O. L. Krivanek, M. F. Chisholm, V. Nicolosi, T. J. Pennycook, G. J. Corbin, N. Dellby, M. F. Murfitt, C. S. Own, Z. S. Szilagyi, M. P. Oxley, S. T. Pantelides and S. J. Pennycook, Nature **464**, 571 (2010).

[60] E. Okunishi, H. Sawada and Y. Kondo, Micron **43**, 538 (2012).

[61] R. Ishikawa, E. Okunishi, H. Sawada, Y. Kondo, F. Hosokawa and E. Abe, Nat. Mater. **10**, 278 (2011).

[62] D. Van Dyck and M. Op de Beeck, Ultramicroscopy **64**, 99 (1996).

[63] J. M. Cowley and Y. Huang, Ultramicroscopy **40**, 171 (1992).

[64] K. Huang, Proc. R. Soc. A Math. Phys. Eng. Sci. **190**, 102 (1947).

[65] V. Grillo and F. Rossi, J. Cryst. Growth **318**, 1151 (2011).

[66] E. J. Kirkland, *Advanced Computing in Electron Microscopy*, Springer US, Boston, MA, 2010.

[67] J. M. Cowley and A. F. Moodie, Acta Crystallogr. **10**, 609 (1957).

[68] E. J. Kirkland, R. F. Loane and J. Silcox, **23**, 77 (1987).

[69] K. Ishizuka, Ultramicroscopy **90**, 71 (2002).

[70] R. F. Loane, P. Xu and J. Silcox, Acta Crystallogr. Sect. A Found. Crystallogr. **47**, 267 (1991).

[71] Z. L. Wang, Acta Crystallogr. Sect. A Found. Crystallogr. **54**, 460 (1998).

[72] Z. L. Wang, Micron **34**, 141 (2003).

[73] S. K. Sinha, CRC Crit. Rev. Solid State Sci. **3**, 273 (1973).

[74] A. Rosenauer and M. Schowalter, STEMSIM-a New Software Tool for Simulation of STEM HAADF Z-Contrast Imaging, in *Microsc. Semicond. Mater. 2007*, pages 170–172, Springer Netherlands, Dordrecht, 2007.

[75] M. Schowalter, A. Rosenauer, J. T. Titantah and D. Lamoen, Acta Crystallogr. Sect. A Found. Crystallogr. **65**, 5 (2009).

[76] P. L. Galindo, S. Kret, A. M. Sanchez, J.-Y. Laval, A. Yáñez, J. Pizarro, E. Guerrero, T. Ben and S. I. Molina, Ultramicroscopy **107**, 1186 (2007).

[77] D. Freedman and P. Diaconis, Zeitschrift für Wahrscheinlichkeitstheorie und Verwandte Gebiete **57**, 453 (1981).

[78] P. Voyles, D. Muller and E. Kirkland, Microsc. Microanal. **10**, 291 (2004).

[79] T. Wegele, A. Beyer, P. Ludewig, P. Rosenow, L. Duschek, K. Jandieri, R. Tonner, W. Stolz and K. Volz, J. Phys. D. Appl. Phys. **49**, 075108 (2016).

[80] M. P. J. Punkkinen, P. Laukkanen, M. Kuzmin, H. Levämäki, J. Lång, M. Tuominen, M. Yasir, J. Dahl, S. Lu, E. K. Delczeg-Czirjak, L. Vitos and K. Kokko, Semicond. Sci. Technol. **29**, 115007 (2014).

[81] M. Panek, M. Ratuszek and M. Tłaczała, J. Cryst. Growth **74**, 568 (1986).

[82] K. Sakamoto, H. Matsuhata, K. Kyoya, K. Miki and T. Sakamoto, Jpn. J. Appl. Phys. **33**, 2307 (1994).

[83] S. Tixier, M. Adamcyk, E. Young, J. Schmid and T. Tiedje, J. Cryst. Growth **251**, 449 (2003).

[84] I. Németh, *Transmission electron microscopic investigations of heteroepitaxial III/V semiconductor thin layer and quantum well structures*, PhD thesis, Philipps Universität Marburg, 2008.

Appendix

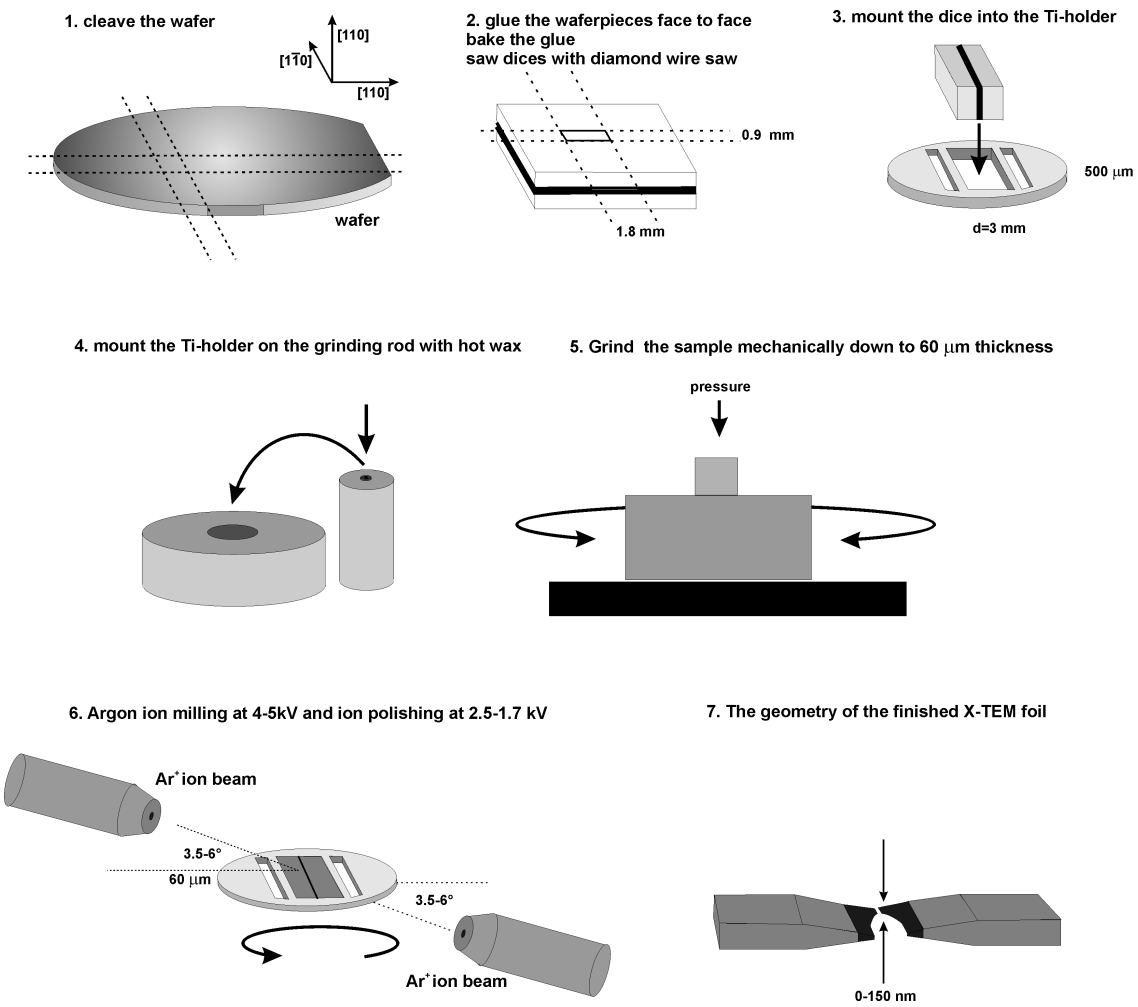

Figure 6.1: Single steps for conventional sample preparation in cross section, like it was applied for the Bi containing samples in this work. Cited from Ref. 84.

Danksagung

Abschließend möchte ich hier die Gelegenheit ergreifen und allen Personen danken, die mir das Zustandekommen dieser Arbeit ermöglicht und mich während der gesamten Zeit unterstützt haben.
Als erstes gilt mein Dank Frau Prof. Dr. Kerstin Volz für die durchgehend wunderbare Betreuung sowie die interessanten und lehrreichen Diskussionen. Danke für das entgegengebrachte Verständnis und dafür, dass Ihre Tür stets offen für mich war. Außerdem danke ich Frau Prof. Dr. Kerstin Volz und Herrn Dr. habil. Wolfgang Stolz für die Möglichkeit in ihrer Arbeitsgruppe forschen zu dürfen sowie für deren ständige Bereitschaft auf Fragen einzugehen.
Herrn Dr. Ralf Tonner möchte ich für die freundliche Übernahme des Zweitgutachtens danken.
Der Deutschen Forschungsgemeinschaft (DFG) danke ich für die finanzielle Unterstützung in Form eines Promotionsstipendiums im Rahmen des Graduiertenkollegs *Funktionalisierung von Halbleitern* (GRK 1782).
Ein großes Dankeschön geht auch an meine Korrekturleser Dr. Andreas Beyer (Addi), Jürgen Belz (Jorge) und Rita Joseph. Vor allem Dr. Andreas Beyer und Jürgen Belz danke ich für die vielen Diskussionen rund um MATLAB sowie für deren stets großes Interesse und Unterstützung an meinem Themengebiet.
Ein spezieller Dank geht an dieser Stelle an Dr. Kakhaber Jandieri für seine interessanten Gespräche sowie die unzähligen Superzellenrelaxationen, die er für mich durchgeführt hat.
Außerdem möchte ich meinen Bürokollegen Tatjana Wegele und Dr. Peter Ludewig für die tolle Zeit danken und dafür, dass sie es mit mir so lange aushalten mussten. Besonders Dr. Peter Ludewig möchte ich für die Diskussionen und Fragen rund um die MOVPE und die Vielzahl an Proben danken, die er zum Teil extra nur für TEM Untersuchungen hergestellt hat.
An dieser Stelle gilt auch ein großes Dankeschön an unsere Techniker Thomas Ochs, Stefan Reinhard und Celina Becker, die dafür gesorgt haben, dass alle Geräte funktioniert haben bzw. wieder zu funktionieren hatten. Vor allem Celina Becker gilt ein großes Dankeschön für die Instandhaltung des (S)TEMs und für die Präparation der ein oder anderen TEM Probe.
Ein ganz besonderer Dank geht an das Sekretariat, bestehend aus Isabell Kimmel, Marina

Koch und Elke Vaupel für deren tägliche Organisationsarbeit, die für uns übernommen wird.
Ich danke allen anderen Bachelor-und Master-Studenten sowie Doktoranden und Postdocs, die ich hier nicht erwähnt habe, für die tolle Zeit und die interessanten aber nicht immer ernst gemeinten Gespräche.
Außerdem danke ich meiner Familie, die mir meine schulische und universitäre Ausbildung ermöglicht und mich durch diese begleitet und immer unterstützt haben.
Zu guter Letzt geht das größte Dankeschön an meine wunderbare Freundin Ekaterina, die mich durch die ganze Doktorarbeit begleitet und mir vieles erleichtert hat. Ich danke Dir, dass Du mir immer wieder den Mut und die Motivation gegeben hast, die ich in dieser Zeit des Öfteren gebraucht habe. Ich bin froh, dass wir uns kennengelernt haben und Du ein Teil von meinem Leben geworden bist.
Vielen Dank, dass es Dich gibt!